School of Earth and Planetary Science

Sulphur isotope and trace element signatures within mineralised occurrences in the Fraser Zone, Western Australia

Alexander Thomas Walker

This thesis is presented for the Degree of

Doctor of Philosophy

of

Curtin University

November 2019

Declaration

To the best of my knowledge and belief this thesis contains no material previously published by any other person except where due acknowledgement has been made.

This thesis contains no material which has been accepted for the award of any other degree or diploma in any university.

This thesis contains published and co-authored works as outlined in the authorship agreement form. Copyright for those published works resides with the copyright holder(s).

Signature:

Date: 23/04/2020

Authorship Agreement Form

The Curtin University Authorship, Peer Review and Publication of Research Findings Policy and Procedures[1] which references the Australian Code for the Responsible Conduct of Research[2], provides clear guidelines regarding attribution of authorship. This form is to assist researchers in capturing discussions around intended publications arising from joint work. It does not replace copyright or certification forms required by publishers.

1. Research

Project Title:	Mineral systems on the margin of Cratons: Albany-Fraser Orogen / Eucla Basement case study: Sulphur isotope and trace element signatures within mineralised occurrences in the Fraser Zone, Western Australia		
Project identifier (if applicable)	RES-SE-DAG-CK-56052 (MRIWA: M470)		
Principal Investigator	Katy Evans		
Other named investigator/s#	Alexander Walker	**Role**	PhD Candidate
Other researcher/s#	Christopher Kirkland	**Role**	Investigator

Insert additional rows if required

2. Publications/Outputs – the intended outputs from the above research are identified below

Pub#	**Description (e.g. method paper)**	**Publication Type (Conference, journal article etc)**
1	Walker, A.T., Evans, K.A., Kirkland, C.L., Martin, L., Kiddie, O.C., Spaggiari, C.V., 2019. Tracking mineralisation with in situ multiple sulphur isotopes: a case study from the Fraser Zone, Western Australia. Precambrian Research, 332.	Journal article (published)
2	Walker, A.T., Evans, K.A., Kirkland, C.L. Novel applications of image analysis to interpret trace element distributions in magmatic sulphides. Lithos, *in revision*	Journal article (in revision)
3	An Archaean sulfur source for Proterozoic VMS-style mineralisation: a case study from the Fraser Zone, Western Australia. *In preparation*	Journal article (in preparation)

Insert additional rows if required

3. Proposed order of authors

(add rows as required for additional authors and/or if authorship will differ between multiple outputs)

Pub*	**Author****	**Contribution**
1	1. Alexander T. Walker	Principal author, undertook sample collection & preparation, sample analysis and data interpretation; wrote the manuscript with discussion and input from Katy Evans, Christopher Kirkland, Laure Martin and Catherine Spaggiari.
1	2. Katy A. Evans	Provided additional data for interpretation and assisted with sample collection and preparation; key contributor to idea generation, discussion, writing and revision of manuscript.
1	3. Christopher L. Kirkland	Key contributor to idea generation, discussion, writing and revision of manuscript.

---

[1] http://policies.curtin.edu.au/findapolicy/#A

[2] https://www.nhmrc.gov.au/guidelines-publications/r39

1	4. Laure Martin	Assisted with sample preparation and analysis; provided information for manuscript methodology section and editorial comments.
1	5. Oliver C. Kiddie	Provided additional data and arranged access to sample material.
1	6. Catherine V. Spaggiari	Provided editorial comments and contributed to revision of manuscript.
2	1. Alexander T. Walker	Principal author; undertook sample collection, sample preparation, sample analysis, data reduction and interpretation. Wrote the manuscript with discussion and input from Katy Evans and Christopher Kirkland.
2	2. Katy A. Evans	Key contributor to idea generation, discussion, writing and revision of manuscript; assisted with sample collection.
2	3. Christopher L. Kirkland	Key contributor to idea generation, discussion, writing and revision of manuscript.
3	1. Alexander T. Walker	Principal author; undertook sample collection, sample analysis and data interpretation. Wrote the manuscript with discussion and input from Katy Evans and Christopher Kirkland.
3	2. Katy A. Evans	Key contributor to idea generation, discussion, writing and revision of manuscript; assisted with sample collection.
3	3. Christopher L. Kirkland	Key contributor to idea generation, discussion, writing and revision of manuscript; assisted with sample collection.
1	Named Acknowledgement:	

* If multiple publications are intended under table 2, and author inclusion and order is the same, then insert "All"

** Attribution of authorship, and role of corresponding author, may have some discipline differences, however, in all cases, inclusion must be based upon substantive intellectual contribution as defined under the Policy. Acceptance should also be sought where intending to name an individual in the acknowledgements.

4. Confirmation of agreement

(add rows as required)

Author Name and Affiliation (if other than Curtin)	Author Signature	Date
Katy A. Evans		22/10/2019
Christopher L. Kirkland		28/10/2019
Laure Martin (UWA-CMCA)		28/10/2019
Oliver C. Kiddie (Creasy Group)		24/10/2019
Catherine V. Spaggiari (GSWA)		31/10/2019

All authors should maintain a copy of this completed form for their reference.

Abstract

The Palaeoproterozoic to Mesoproterozoic Albany-Fraser Orogen (AFO) extends along the southern and south-eastern margins of the Archaean Yilgarn Craton in Western Australia. The Orogen has a complex tectonothermal history and incorporates several distinct lithotectonic domains that represent reworking of Yilgarn material and variable juvenile mantle input. The Fraser Zone is a belt of metagabbroic, ultramafic, granitic and paragneissic rocks within the AFO; it is primarily prospective for magmatic sulphide mineralisation, and exploration efforts have increased substantially in the area in recent years. Much of the Fraser Zone geology lies under thick cover which increases the challenges faced by mineral explorers. The objectives of this project were, by using laser ablation mass spectrometry and in-situ secondary ion mass spectrometry techniques, to collect sulphide trace element and sulphur isotope data, to place constraints on mineralising processes within the Fraser Zone, and to help identify prospective environments for mineralisation.

Sulphide δ^{34}S data from mineralised magmatic sulphide prospects in the Fraser Zone record variable assimilation of the local sulphur bearing metasediments of the Snowys Dam Formation. The characteristic sulphur isotope signatures of each locality reveal a link between mineralisation and the quantity of external sulphur assimilated; the more intensely mineralised prospect is associated with greater degrees of assimilation. Δ^{33}S data indicates an absence of Archaean sulphur within analysed material, at odds with the Archaean Yilgarn heritage of the Fraser Zone. This implies that sulphur is decoupled from other geochemical and isotopic systems. This is consistent with the recyling of Archaean sulphur from detrital material incorporated into the Fraser Zone during uplift, erosion and sedimentary transport.

Laser ablation mapping of sulphide breccia material from the Octagonal prospect in the Fraser Zone indicates post-formation modification of ore, including fluid-facilitated alteration. Element concentrations show that the primary sulphide assemblage of pyrrhotite, pentlandite and chalcopyrite that crystallised from a sulphide liquid was modified, with pyrrhotite replaced by pyrite and magnetite during alteration. Powerful co-localisation techniques were tested and used to measure spatial relationships between elemental distributions and fractures quantitatively; the results show that Mn and some Ag content was mobile within the fracture networks during fluid assisted remobilisation. This work links post-mineralisation modification processes and depletion of metal contents with destruction of mineralised horizons within Octagonal, with broader implications for the development of ore deposits worldwide.

By the end of 2019, mineral explorers identified several new prospects within the Fraser Zone, including Andromeda; a joint Creasy Group-IGO venture. Andromeda is novel in a region prospective for magmatic sulphide mineralisation, with observed sulphide assemblages more akin to Volcanogenic Massive Sulphide (VMS) mineralisation. A majority of *in-situ* δ^{34}S sulphur isotopic measurements from analysed sulphides are 4.50–6.70‰, which are characteristic of VMS deposits worldwide. The Δ^{33}S values record the presence of Archaean sulphur at Andromeda, in contrast to other results in Fraser Zone magmatic sulphide prospects. The presence of Archaean sulphur is attributed to the tapping of a cryptic Archaean reservoir by fluids linked to the hydrothermal system from which Andromeda is derived, possibly by the transfer of Archaean sulphur from the Yilgarn craton or Biranup Zone via the Fraser Shear Zone.

Together, the sulphur isotope and trace element data imply that the Fraser Zone hosts complex and highly variable mineralising environments. The assimilation of local sulphur-rich material appears to be crucial to economic magmatic sulphide mineralisation in the Fraser Zone, with the Snowys Dam Formation providing the only currently known source of sulphur-rich sedimentary material. The essential nature of the Snowys Dam Formation to mineralisation provides a significant spatial constraint on the environments prospective for magmatic sulphides and suggests explorers should focus their efforts on areas in proximity to the Snowys Dam Formation when pursuing this deposit style. The absence of Archaean sulphur within Fraser Zone magmatic sulphide prospects, and the entrainment of Archaean sulphur at Andromeda, serve to illustrate the complex manner by which sulphur has cycled through the Fraser Zone from a broad range of sources. The necessity of an extensional tectonic setting for the formation of the VMS deposit at Andromeda fits with our current understanding of the geodynamic setting of the Fraser Zone, which likely formed within an extensional rift or back-arc environment. The removal of Archaean sulphur from incorporated cratonic material highlights a fundamental process by which Archaean sulphur signatures, previously considered to be ‘indelible’, can be stripped from the geological record, with broader implications for our understanding of the crustal sulphur cycle. Post-mineralisation modification of ore associated with metamorphism can is quantifiable with the development of element-feature co-localisation analysis. This modification has resulted in metal depletion and destruction of primary sulphide assemblages within the Octagonal prospect and is likely to have occurred within other deposits in the Fraser Zone. Despite this, the region remains highly prospective for economic mineralisation, and an open-minded approach to exploration will aid the discovery of a diverse range of mineralisation styles.

Acknowledgements

The road to the end of this thesis has been long and exhausting, and yet has also passed in the blink of an eye. Its completion would not have been possible without the help and support of many people.

First, I would like to thank my supervisor Katy Evans. When I first started my PhD, I had been four years out of university, with much of my undergraduate learning forgotten and certainly no background in sulphur isotope geochemistry. I owe a great deal to Katy's willingness to share her broad knowledge of geology, her undoubtedly hard-worn patience, and her readiness to help me. I am very grateful for her warmth and her boundless enthusiasm for just about any topic, for giving me the freedom to develop my thesis in line with my interests, and for inviting me along on the annual undergraduate Albany-Fraser field trips.

My co-supervisor Chris Kirkland also deserves thanks for much of the same. Amongst many opportunities, he involved me with the CCFS network, and his expertise and extensive knowledge of the Albany-Fraser Orogen have been essential to the development of my thesis.

I am very grateful to Allison Dugdale, both for inviting me to help her teach undergraduates the fundamentals of ore deposits and for providing fresh and exciting viewpoints on a wide range of geological topics. The experience has helped me to understand geology in new and different ways and has given me a very positive outlook on teaching.

Many other individuals at Curtin University need to be acknowledged. I want to thank Noreen Evans and Brad McDonald for their assistance with LA-ICP-MS analyses and data reduction. I am grateful to Andy Wieczorek for his help with sampling equipment and the countless occasions he helped me find practical solutions to problems. I thank Kelly Merigot for her assistance with TIMA analysis and sample preparation, in addition to answering many questions about the best ways to polish sulphides.

I want to thank Catherine Spaggiari, Mark Munro, Raphael Quentin de Gromard and Hugh Smithies at the Geological Survey of Western Australia (GSWA). Between them, I was afforded many fantastic opportunities including presenting at the GSWA 2019 Open Day and several fieldwork trips. Their provision of samples and willingness to share their comprehensive knowledge of the Albany-Fraser Orogen was also invaluable.

I am grateful for the assistance of Laure Martin with sample preparation and sulphur isotope analyses at the Centre for Microscopy, Characterisation and Analysis. Always friendly and willing to help, she made sure I got the most out of my samples and somehow managed to find me extra analytical time in the busiest of periods.

I want to thank Richard England for so willingly sharing his time and experience on many topics relevant to this thesis. Casual questions on a sample or two often became day-long investigations, with Richard providing invaluable insight.

This project would not have been possible without financial support from several sources. I thank Curtin University for its financial support, including the provision of a Curtin International Postgraduate Research Scholarship, and would also like to thank the Minerals Research Institute of Western Australia, the GSWA and Creasy Group for their financial support. I am sincerely grateful to Oliver Kiddie for the opportunities to visit both Octagonal and Nova-Bollinger for sample collection, in addition to providing the information I needed.

I am also grateful to my friends and colleagues for their humour and support; Mike, Kate, Rick, Ruairidh, Sam, Margaret, Julian and Sarah, amongst many others. Thank you for reminding me there is a life outside a PhD.

I want to thank Dani for providing her unwavering patience, love and support, particularly in the last months of this thesis when I worked almost to the exclusion of all else.

Finally, I would like to thank my family for their unwavering support and love. From my first step into geology my mother has been there and willing to help in any way possible, as I left first for Leicester to commence my undergraduate studies, then New Zealand, and finally Australia for this PhD. I couldn't have gotten this far without you.

Contents

List of Tables

List of Figures

Chapter 1

Introduction

99.6% of the Earth's continental crust (by mass) is comprised of ten elements (O, Si, Al, Fe, Ca, Mg, Na, K, Ti and H) (Rudnick and Gao, 2003). The remaining 0.4% includes all other elements also considered essential to human society and industry today (e.g. Ni, Cu, Co, platinum group elements (PGE) and rare earth elements), dispersed throughout the crust at low (<1000 ppm) concentrations (Heinrich and Candela, 2014). Mineral deposits may be defined as abnormal concentrations of minerals within the crust containing these scarce elements (Atkinson and Edwards, 1986), with the term ore deposit further defining mineral deposits in which the grade (bulk concentration of valuable elements) and tonnage (quantity of ore) allow economic extraction of said elements (Heinrich and Candela, 2014).

In recent years there has been a growing perception that greenfield exploration has become increasingly unsuccessful with many of the "easily found" ore deposits already located (Hagemann et al., 2016). In response to this an approach to understanding mineral deposits called the mineral systems concept was introduced by Wyborn et al. (1994) in an attempt to place ore formation within larger scale geological systems. Within the mineral systems concept, ore deposits are the foci of a range of earth processes occurring at different temporal and spatial scales, representing zones of focused mass and energy flux within often complex geological systems (McCuaig et al., 2010; McCuaig and Hronsky, 2014). Within this concept there are four elements essential to the genesis of mineral systems: whole lithospheric architecture, transient favourable geodynamics, fertility and preservation of the primary depositional zone (McCuaig and Hronsky, 2014) (Fig. 1.1).

This approach emphasises ore-forming processes common to a range of ore deposit models, linking these ore systems and relating them in a predictive context to larger scale geodynamic context (McCuaig and Hronsky, 2014). In doing so mineral exploration is refocused on mapping these four critical elements of mineral systems at different scales

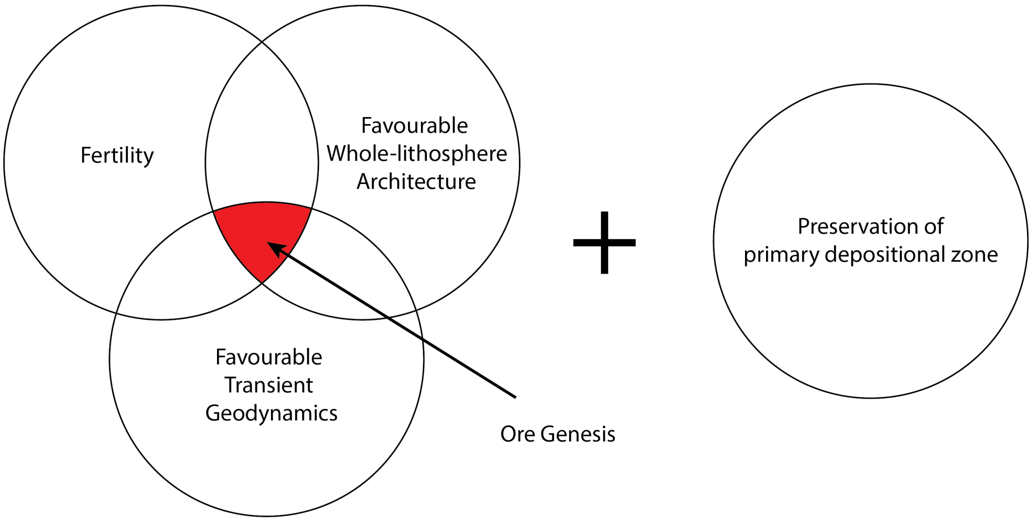

Figure 1.1: The mineral systems concept (modified after McCuaig and Hronsky, 2014)

to better advise exploration decisions.

This thesis focuses on the “Fertility” component of the mineral systems concept. Ore deposits contain significant concentrations of metal and sulphur in the form of sulphide minerals. Sulphur is a critical ligand within mineralising systems that transports and concentrates gold in hydrothermal fluids (Loucks and Mavrogenes, 1999) and concentrates base metals such as Ni, Cu, and Co in magmatic sulphide deposits due to their highly chalcophile nature (Naldrett, 2004). Identification of sources of metals and sulphur involved in economic mineralisation can be difficult but may significantly aid exploration efforts by delineating regions or geological intervals that are fertile and therefore prospective for mineralisation. Multiple sulphur isotopes (δ^{34}S, Δ^{33}S, Δ^{36}S and trace element signatures may be used to fingerprint specific metal and sulphur reservoirs and characterise geological processes in mineralising systems.

1.1 Magmatic sulphide deposits

Magmatic sulphide deposits provide a significant quantity of the world’s Ni, Cu, Co, Rh, Rh, Ru, Pd, Re, Os, Ir, Pt, Cr, Ti and V, with much of the demand for the platinum group elements (PGE), especially Pt and Pd, accommodated by South Africa’s Bushveld complex alone (Mungall and Naldrett, 2008; Schulz et al., 2010; Barnes and Ripley, 2016; Peck and Huminicki, 2016) (Table 1.1). In Western Australia the Ni and base metal mineral sectors are significant components of the economy valued at AU$1.6 billion and AU$514 million respectively (Department of Mines, Industry Regulation and Safety, 2018).

Many of these deposits owe their metal endowment to melting of fertile mantle or lower

Deposit/camp	Ni	Cu	Co	Pt	Pd	Rh	Ru	Ir	Os	Total	Ore (US$/t)	PGE (%)
Noril'sk	191870	77101	18029	49864	59734	4591	352	98	135	401774	307	29
Sudbury	163548	29367	13972	15765	5998	1682	210	91	38	230670	140	10
Duluth	66160	39600	17033	12093	12224	500	78	31	34	147753	37	17
Jinchuan	45146	6415	2238	1354	316	46	15	15	17	55562	108	3
Pechenga	33080	3548	3420	847	366	34	7	4	6	41312	122	3
Thompson	28828	402	1555	310	502	126	31	14	18	31786	212	3
Mt Keith	23718	95	1506	-	-	-	-	-	-	25319	53	-
Voisey's Bay	17975	1917	2768	212	82	12	3	1	1	22971	168	1
Kambalda	16069	237	3123	417	175	79	38	9	19	20166	301	4
Perseverance (Agnew)	8171	82	-	-	-	-	-	-	-	8252	159	0
Raglan	5556	286	298	421	349	68	27	5	6	7015	284	12
Bushveld	126332	11353	-	684404	139811	65035	18008	3344	1800	1040086	90	87

Table 1.1: Value of ore resources (millions US$), value of ore (US$ per tonne) and proportion (%) that PGE contribute total value (after Naldrett, 2004)

crust, igneous fractionation, and segregation of sulphide liquids (Candela, 2003), and are typically associated with mafic and ultramafic magmas (Naldrett, 2004).

Deposits can be divided into three broad groups: laterally extensive but narrow reef or stratiform deposits (e.g., the Bushveld Complex), deposits of variable width at the margins of intrusions, termed contact deposits (e.g. the Platreef of the Bushveld Complex) and Ni-Cu-sulphide deposits (Barnes and Ripley, 2016). Deposits within the Sudbury district in Ontario, Canada are an exception to this classification, because they are associated with a meteorite impact-related melt sheet (Naldrett, 2004). The magmatic sulphide mineralisation within the Fraser Zone falls within the Ni-Cu-sulphide category.

1.1.1 Processes controlling mineralisation within Ni-Cu-sulphide deposits

Ore minerals in Ni-sulphide deposits consist of base metal sulphides (BMS) with sulphide assemblages primarily comprised of pyrrhotite (Fe_7S_8), pentlandite ($[FeNi]_9S_8$), chalcopyrite ($FeCuS_2$) and, commonly, magnetite. Other BMS, including cubanite (Fe_2CuS_3), mooihookite ($Cu_9Fe_9S_{16}$) and talnakhite ($Cu_9[Fe,Ni_8]S_{16}$), may also be present (Barnes and Lightfoot, 2005). Separation of an immiscible sulphide phase is required to focus the dispersed metal concentration in a magma, a process that requires sulphide saturation in the silica melt (Ripley and Li, 2003; Naldrett, 2004; Schulz et al., 2010). The sulphur content of the upper mantle is low (approx. 400 ppm; von Gehlen, 1992), so mantle-derived melts are typically sulphur undersaturated. Further, sulphur solubility increases with decreasing pressure, implying that mafic magmas emplaced at shallow crustal levels are unlikely to reach sulphide saturation without introduction of external sulphur, extensive fractional crystallization, or increases in the SiO_2 content of the magma (Mavrogenes and O'Neill, 1999; Naldrett, 2004; Ripley and Li, 2013). Increases in the SiO_2 content can be caused by assimilation of silica-rich country rock or more felsic melts (Irvine, 1975; Li and Ripley, 2005). Introduction of external sulphur via assimilation of sulphur rich crustal rocks is thought to be a key factor in the formation of several Ni-sulphide deposits including the Duluth Complex, Noril'sk and Voisey's Bay (e.g. Grinenko, 1985; Lesher and Burnham, 2001; Ripley and Li, 2003; Naldrett, 2004; Ripley and Li, 2013).

Once sulphide saturation is reached, droplets of sulphide liquid precipitate and segregate from the silicate liquid at approximately 1200°C (Naldrett, 2004 and references therein). Chalcophile elements in adjacent silicate melt then partition into the sulphide liquid. Iron-rich monosulphide solution (MSS) crystallises from the sulphide liquid as it cools from approximately 1180 to 950°C, followed by iron oxides and then Cu-rich Intermediate Solid Solution (ISS) at approximately 900°C (Naldrett, 1969, 2004; Barnes and Ripley, 2016). Below 900°C, MSS and ISS are unstable; MSS decomposes to form pyrrhotite + pentlandite ± pyrite, while ISS forms chalcopyrite ± cubanite ± pyrite ±

pentlandite (Barnes and Ripley, 2016; Mansur et al., 2019).

Partition coefficients dictate the distribution of metals between MSS, ISS and derived sulphides. Nickel is initially incompatible within MSS and concentrates within the Cu-rich liquids, becoming more compatible in MSS as fS_2 increases from approximately 0.2 to 1 and temperature decreases between 1100–900°C (Li et al., 1996; Barnes et al., 1997; Makovicky, 2002; Liu and Brenan, 2015; Barnes and Ripley, 2016). When MSS decomposes, Ni and its elemental partner, Co, are concentrated within pentlandite, and to a lesser extent pyrrhotite (Barnes and Lightfoot, 2005). The PGE partition, to a limited extent, into the BMS but commonly form separate platinum group minerals (PGM) in association with Te, Se, Bi, As and Sb (Helmy et al., 2007). Rhenium, Ir, Os, Pd, Ru and Rh occur within pyrrhotite and pentlandite if not sequestered in PGM. Platinum, Ag and Au are incompatible within the products of MSS and ISS, and tend to reside within the PGM (Barnes et al., 1994; Mungall et al., 2005; Godel and Barnes, 2008; Barnes et al., 2008; Barnes and Ripley, 2016).

Sulphide saturation is only one of several steps required for economic magmatic sulphide mineralisation. The concentrations of base metals and PGE within mantle-derived melts are very low due to their sequestration into the Earth's core, occurring at earliest within approximately 34 Ma of solar system formation (Barnes and Lightfoot, 2005 and references therein; Kleine and Walker, 2017)(Table 1.2). The relatively low concentrations of the PGE in the mantle require significant levels of enrichment to be economically extractable; an enrichment factor of approximately 10,000 for instance is required to elevate an average Pt concentration of 0.4 ppb in the crust to an economic concentration of approximately 4 ppm in Pt ore (Mungall and Naldrett, 2008). Consequently, high degrees of partial melting within the mantle are required to produce fertile magmas. These volumes of magma must be transported into the crust with minimal olivine fractionation and sulphide extraction to avoid metal depletion during either olivine crystallisation or early sulphide formation (Barnes and Lightfoot, 2005).

	Ni	Cu	Co	Os	Ir	Ru	Rh	Pt	Pd	Au
Bulk earth	18220	60	880	900	900	1300	240	1900	1000	160
Prim. mantle	1960	30	105	3.4	3.4	5	0.95	7	4	1
Bulk crust	105	75	29	0.1	0.1+	0.2	0.14	5	5	3+
Upper cont. crust	20+	25+	10+	0.02	0.02+	0.04	0.02	2	2	1.8+

Table 1.2: Concentrations of base metals (ppm) and PGE (ppb) within bulk earth, mantle and crust (from Barnes and Lightfoot, 2005)

Once within a mineralising system, the concentration of metal in a sulphide liquid (C_S) is controlled by the metal concentration of the silicate melt (C_L), elemental partition coefficients between the sulphide and silicate liquids (D), and the ratio of silicate to sulphide liquid (R) (Campbell and Naldrett, 1979) as described in the following equation:

$$C_S = C_L \cdot D(R+1)/(R+D) \tag{1.1}$$

This allows the calculation of the volume of magma from which sulphides segregated (Barnes et al., 1993). The extremely high R factors (>10000) required for PGE-rich sulphides imply large magmatic bodies and/or very dynamic magmatic systems within which several voluminous magmas are processed and with which sulphides can interact, or possibly suspension of sulphide droplets within a magma to maximise metal enrichment (Lesher and Keays, 2002).

Once sulphide saturation and metal enrichment have occurred, a mechanism is required to concentrate precipitated sulphides to form sulphide ore; should this not occur then the result is the formation of large volumes of disseminated sulphides at grades insufficient for economic extraction. Sulphides may concentrate in slurries at the base of magmatic intrusions under the influence of gravity (Barnes and Lightfoot, 2005), within structural traps (e.g. folds) or in flow dynamic traps (e.g. intersections between feeder conduits and larger chambers).

1.2 Sulphur isotope geochemistry

Sulphur isotope geochemistry has been developing since the late 1940s (e.g. Thode et al., 1949), with applications in the geological sciences ranging from identification of natural abundances of sulphur isotopes within terrestrial and extraterrestrial bodies, to characterisation of the temporal evolution of the terrestrial sulphur isotope signature (Hulston and Thode, 1965; Farquhar et al., 2003).

The atomic number of an element is equal to the number of protons that exist within atomic nuclei of the element in question. Isotopes represent different forms of the same element in which the number of protons remain the same but the number of neutrons differ, allowing definition of isotopes by their differing atomic masses (the sum of protons and neutrons present). Five naturally occurring isotopes of sulphur exist on Earth today. Those isotopes that are stable include ^{32}S, ^{33}S, ^{34}S and ^{36}S with approximate abundances of 95%, 0.75%, 4.20% and 0.017%, respectively (MacNamara and Thode, 1950). The last, ^{35}S, is the unstable product of cosmic ray spallation of ^{40}Ar (Peters, 1959), shortlived (λ = 87 days) and consequently of limited use in geological science.

Sulphur isotope geochemistry focuses on relative differences in the ratios of sulphur isotopes rather than the absolute quantities present within substances, and the processes that drive these differences. Variations in sulphur isotopic abundance are most often considered in terms of the abundance ratios of ^{34}S/^{32}S and ^{33}S/^{32}S, however in recent years ^{36}S/^{32}S ratios have been used to identify Archaean sulphur (e.g. LaFlamme et al., 2018). There are several processes that alter, or fractionate, the ratios of sulphur isotopes present in a substance. The most important are redox processes, which produce oxidized species enriched in ^{34}S, and reduced species depleted in ^{34}S (Seal, 2006). As these changes in isotopic ratios are generally very minor, isotopic compositions are measured in delta (δ) notation in per mil (‰, per thousand). The ^{34}S/^{32}S composition of a substance may be defined as:

$$\delta^{34}S(‰) = \frac{(^{34}S/^{32}S)_{sample} - (^{34}S/^{32}S)_{reference}}{(^{34}S/^{32}S)_{reference}} \tag{1.2}$$

The reference material is Vienna Canyon Diablo Troilite (VCDT) meteoritic material with a δ^{34}S composition of 0.0‰, which is thought to approximate the bulk sulphur isotope composition of the Earth (Seal, 2006). Other than meteoritic sulphur, measurement of δ^{34}S has allowed identification of multiple terrestrial sulphur reservoirs that record fractionation process (or processes) (Fig 1.2).

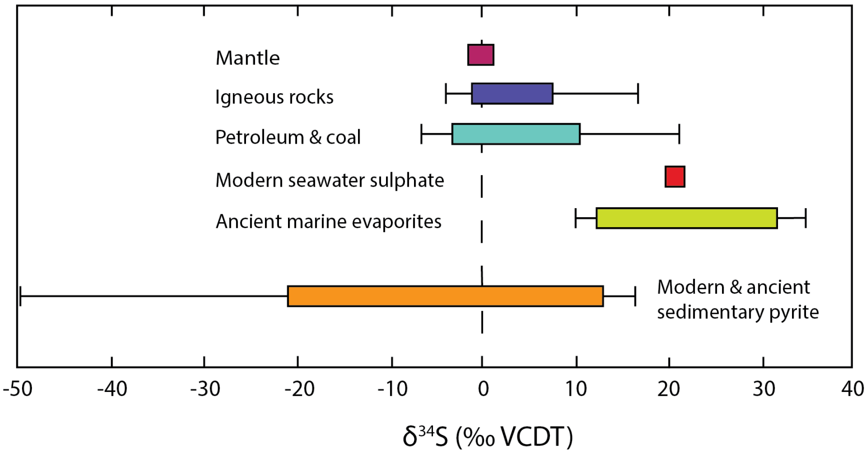

Figure 1.2: δ^{34}S values characterising common terrestrial sulphur reservoirs (From Walker et al., 2019 after Seal, 2006)

Sulphur from two or more of these reservoirs may interact and mix within a range of geological scenarios, with ore deposits the most relevant to this work. Assimilation of external sulphur is essential for the formation of many magmatic sulphide deposits, and δ^{34}S isotopic compositions are a powerful tool that can identify the sources of sulphur incorporated within these deposits (e.g. Ding et al., 2012).

During many equilibrium and non-equilibrium processes, fractionation between the different sulphur isotopes in sulphur-bearing compounds is coupled and the extent is proportional to the difference in mass of the isotopes. This process is called mass-dependent fractionation (MDF). Processes that exhibit MDF include isotopic exchange between substances at equilibrium and disequilibrium. Examples of disequilibrium exchange include bacterial sulphate reduction, evaporation and diffusion (O'Neil, 1986; Seal, 2006). As the term suggests, changes in isotopic compositions due to MDF are controlled by relative differences in mass between sulphur isotopes; within any given sample variations in δ^{33}S will be approximately half of that measured by δ^{34}S, as determined by a difference in atomic mass of one between ^{33}S/^{32}S versus two in ^{34}S/^{32}S (Hulston and Thode, 1965). Sulphur isotopic compositions that show mass-dependent fractionation form a linear array on plots of their ratios or on δ^{34}S versus δ^{33}S. This array is called the mass-fractionation line. The slope of this line is equal to the mass difference between the isotopic ratios. On a δ^{34}S vs δ^{33}S plot the mass-fractionation line is described by the equation:

$$\delta^{33}S(‰) = 0.515 \times \delta^{34}S \tag{1.3}$$

In addition to MDF there are processes that impart anomalous fractionation to sulphur isotopes, termed mass-independent fractionation (MIF). This results in isotopic compositions that deviate from mass fractionation lines, with the deviation measured by Δ^{33}S for δ^{34}S vs δ^{33}S space, and δ^{36}S in δ^{34}S vs δ^{36}S space as defined by:

$$\Delta^{33}S = \delta^{33}S - 1000 \cdot \left[\left(1 - \frac{\delta^{34}S}{1000}\right)^{0.515} - 1\right] \tag{1.4}$$

and

$$\Delta^{36}S = \delta^{36}S - 1000 \cdot \left[\left(1 - \frac{\delta^{34}S}{1000}\right)^{1.91} - 1\right] \tag{1.5}$$

respectively. Prior to the c. 2.4 Ga Great Oxygenation Event (GOE) sulphur underwent photodissociation while exposed to UV radiation within the Archaean atmosphere (Farquhar et al., 2000). Atmospheric sulphur-bearing compounds (e.g. SO, SO_2) introduced by volcanic activity dissociated to elemental sulphur (S_8) and H_2SO_4 aerosols, imparting positive and negative Δ^{33}S anomalies, respectively (Farquhar et al., 2003). Elemental sulphur was subsequently incorporated into sediments, passing on a positive Δ^{33}S character to sedimentary sulphides; negative Δ^{33}S bearing sulphates dissolved into the oceanic sulphate reservoir (Farquhar et al., 2003).

A sharp change in the magnitude of Δ^{33}S anomalies is observed after c. 2.4 Ga. Sulphur-bearing minerals that formed after this time show a more limited range of

$\Delta^{33}S$ (and $\Delta^{36}S$) values between -0.5‰ and 0.7‰ (Savarino et al., 2003; Bekker et al., 2004) (Fig. 1.3). Two primary hypotheses have been advanced to account for this, including the onset of oxidative weathering and onset of oxygenation of what had been an atmosphere dominated by CH_4 and CO_2 (Farquhar et al., 2003 and references therein). The former explanation describes oxidative weathering of a substantial reservoir of positive $\Delta^{33}S$ continental sulphide to sulphate in tandem with oxygenation of the atmosphere, ending atmospheric photodissociation processes. Oceanic sulphate produced by weathering would retain the average $\Delta^{33}S$ of Archaean reduced sulphur of c. 0.5‰, within the range of $\Delta^{33}S$ values that characterise younger sulphur (Farquhar et al., 2002, 2003). The second hypothesis invokes an increase in atmospheric oxygen and concomitant development of an ozone layer hindering sulphur photolysis, with oxygen levels eventually reaching concentrations sufficient to effectively end atmospheric MIF-inducing processes (Seal, 2006 and references therein). This change facilitates easy differentiation of Archaean sulphur from younger (<2.4 Ga) sulphur via sulphur isotopic analysis, where that Archaean sulphur possesses $\Delta^{33}S$ values beyond -0.5‰ and 0.7‰. MIF sulphur anomalies imparted to Archaean sulphur have proven to be robust, $\Delta^{33}S$ values, once formed, cannot be modified except by dilution by other non-MIF bearing sulphur reservoirs which serves only to reduce the magnitude of $\Delta^{33}S$ anomalies (e.g. Wacey et al., 2015).

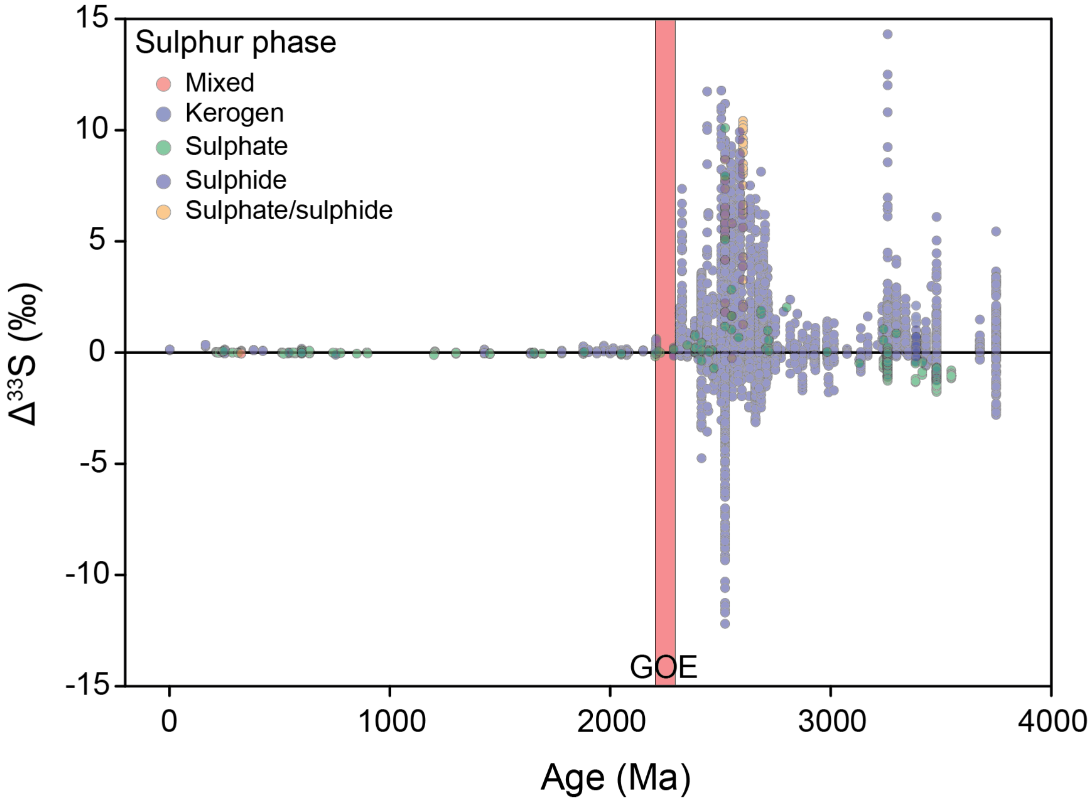

Figure 1.3: Evolution of the global $\Delta^{33}S$ record through time. Data from the CET Global Sedimentary Sulphur Database (Selvaraja et al., 2017)

Small MIF anomalies can be generated by dominantly MDF processes, with values traditionally defined to be within the range of 0 ± 0.2‰ (Farquhar et al., 2003). More recently, MDF- induced MIF has been more accurately defined (LaFlamme et al., 2018) as described by the equation:

$$\Delta^{33}S_{MDF} = 1000 \times \left(\left(\frac{\delta^{34}S}{1000} + 1 \right)^{\lambda} - 1 \right) - 1000 \times \left(\left(\frac{\delta^{34}S}{1000} + 1 \right)^{0.515} - 1 \right) \tag{1.6}$$

Equilibrium reactions typically result in a mass-dependent relationship between δ^{33}S and δ^{34}S (λ^{33}) where $\lambda^{33} = 0.515$ however λ^{33} in kinetically-controlled reactions is 0.508–0.519 (Hulston and Thode, 1965; Ono et al., 2006; Leavitt et al., 2014; LaFlamme et al., 2018). If $\lambda^{33} = 0.508$ rather than $\lambda^{33} = 0.515$, each 1.0‰ variation in δ^{34}S is associated with a maximum MDF-induced MIF of 0.007‰ (LaFlamme et al., 2018). This new finding allows more precise discrimination between MDF-induced MIF and low magnitude Archaean MIF anomalies.

1.3 Study area

This project focuses on Western Australia's Albany–Fraser Orogen, specifically the Proterozoic geology of the Fraser Zone. The Fraser Zone has emerged as a region of particular significance in the Albany-Fraser Orogen in recent years, with the discovery of the Nova-Bollinger Ni-Cu deposit in 2012 (Bennett et al., 2014) and other mineralised localities attesting to a significant and relatively untapped mineral potential. Much of the basement geology of the Orogen is concealed beneath extensive cover sequences, however, and the Fraser Zone is no exception to this, adding a further hurdle to exploration efforts. One of the objectives of this thesis was to assess the benefits of applications of stable isotope geochemistry and trace element analysis to exploration under cover.

1.4 Research objectives

The main aim of this thesis is to provide trace element and sulphur isotopic constraints on the processes that formed and modified mineralisation within the Fraser Zone. The objectives were to:

- Characterise multiple sulphur isotopic signatures (δ^{34}S, Δ^{33}S) within footwall and sulphide-rich lithologies in variably mineralised localities within the Fraser Zone.
- Assess the sulphur sources and pathways involved in mineralisation to help direct exploration efforts towards prospective environments.

- Identify the trace element signature of mineralised occurrences and recognize elemental tracers of mineralizing processes.

1.5 Thesis structure

This thesis comprises a published article (Chapter 3) and two manuscripts (Chapters 4 and 5) prepared for submission to peer-reviewed journals. These chapters are presented in chronological order of completion. Text and figures from published work and prepared manuscripts are reproduced in full or as published but have been reformatted for consistency in this work. This leads to unavoidable repetition in places, particularly with regards to geological background and methodologies.

Chapter 2 provides an overview of the geology of the Albany-Fraser Orogen and a summary of published sulphur isotopic and magmatic sulphide research undertaken in the region.

Chapter 3 reports *in-situ* sulphur isotopic work undertaken at the Octagonal, Plato and NRM localities in the Fraser Zone for this thesis. Magmatic sulphide mineralisation is linked to assimilation of local sulphur-rich lithologies, with a notable absence of Archaean sulphur.

The chapter is published as: Walker, A.T., Evans, K.A., Kirkland, C.L., Martin, L., Kiddie, O.C., Spaggiari, C.V., 2019. Tracking mineralisation with in-situ multiple sulphur isotopes: a case study from the Fraser Zone, Western Australia. Precambrian Research, 332.

Chapter 4 presents data and conclusions drawn from image analysis of sulphide trace element maps of samples from the Octagonal prospect in the Fraser Zone. Elemental remobilisation and replacement of primary sulphide assemblages are associated with metamorphism and fluid-facilitated alteration.

This work forms a manuscript entitled “A novel application of image analysis to interpret trace element distributions in magmatic sulphides” that has been submitted to Lithos and is currently in revision.

Chapter 5 reports *in-situ* sulphide sulphur isotopic measurements from recently discovered mineralisation at the Andromeda prospect in the Fraser Zone. Textural observations and sulphur isotopic compositions at Andromeda are more similar to VMS-style mineralisation than magmatic sulphide mineralisation, and the sulphur records an Archaean signature that is thought to be inherited from Archaean Biranup material, via fluid flow along the Fraser Shear Zone.

This is a manuscript in preparation for submission entitled “An Archaean sulphur source for Proterozoic VMS-style mineralisation: a case study from the Fraser Zone, Western Australia".

Chapter 6 draws together the findings of the thesis and discusses the implications for prospectivity and mineralisation within the Fraser Zone.

1.6 References

Atkinson, K., Edwards, R., 1986. Ore deposit geology and its influence on mineral exploration. London; New York: Chapman and Hall.

Barnes, S.-J., Couture, J.-F., Sawyer, E. W., Bouchaib, C., 1993. Nickel-copper occurrences in the Belleterre-Angliers Belt of the Pontiac Subprovince and the use of Cu-Pd ratios in interpreting platinum-group element distributions. Economic Geology 88 (6), 1402–1418.

Barnes, S.-J., Lightfoot, P. C., 2005. Formation of magmatic nickel-sulfide ore deposits and processses affecting their copper and platinum-group element contents. Economic Geology 100th Anniversary, 179–213.

Barnes, S.-J., Makovicky, E., Karup-Moller, S., Makovicky, M., Rose-Hansen, J., 1994. Partition coefficients for Ni, Cu, Pd, Pt, Rh, and Ir between monosulphide solid solution and sulphide liquid and the implications for the formation of compositionally zoned Ni-Cu sulphide bodies by fractional crystallization of sulphide liquid. Mineralogical Magazine 58, 51–52.

Barnes, S.-J., Makovicky, E., Makovicky, M., Rose-Hansen, J., Karup-Moller, S., 1997. Partition coefficients for Ni, Cu, Pd, Pt, Rh, and Ir between monosulfide solid solution and sulfide liquid and the formation of compositionally zoned Ni–Cu sulfide bodies by fractional crystallization of sulfide liquid. Canadian Journal of Earth Sciences 34 (4), 366–374.

Barnes, S.-J., Prichard, H. M., Cox, R. A., Fisher, P. C., Godel, B., 2008. The location of the chalcophile and siderophile elements in platinum-group element ore deposits (a textural, microbeam and whole rock geochemical study): Implications for the formation of the deposits. Chemical Geology 248 (3-4), 295–317.

Barnes, S.-J., Ripley, E. M., 2016. Highly siderophile and strongly chalcophile elements in magmatic ore deposits. Reviews in Mineralogy and Geochemistry 81 (1), 725–774.

Bekker, A., Holland, H., Wang, P.-L., Rumble Iii, D., Stein, H., Hannah, J., Coetzee, L., Beukes, N., 2004. Dating the rise of atmospheric oxygen. Nature 427 (6970), 117.

Bennett, M., Gollan, M., Staubmann, M., Bartlett, J., 2014. Motive, means, and opportunity: key factors in the discovery of the Nova–Bollinger magmatic nickel–copper sulfide deposits in Western Australia. Building Exploration Capability for the 21st Century. Society of Economic Geologists, Special Publications 18, 301–320.

Campbell, I., Naldrett, A., 1979. The influence of silicate: sulfide ratios on the geochemistry of magmatic sulfides. Economic Geology 74 (6), 1503–1506.

Candela, P., 2003. Ores in the earths crust. Treatise on geochemistry 3, 659.

Department of Mines, Industry Regulation and Safety, 2018. Latest statistics release. `http://dmp.wa.gov.au/About-Us-Careers/Latest-Statistics-Release-4081.aspxm`, [Online; accessed 25-July-2019].

Ding, X., Ripley, E. M., Shirey, S. B., Li, C., 2012. Os, Nd, O and S isotope constraints on country rock contamination in the conduit-related Eagle Cu–Ni–(PGE) deposit, Midcontinent Rift system, Upper Michigan. Geochimica et Cosmochimica Acta 89, 10–30.

Farquhar, J., Bao, H., Thiemens, M., 2000. Atmospheric influence of earth's earliest sulfur cycle. Science 289 (5480), 756–758.

Farquhar, J., Johnston, D. T., Wing, B. A., Habicht, K. S., Canfield, D. E., Airieau, S., Thiemens, M. H., 2003. Multiple sulphur isotopic interpretations of biosynthetic pathways: implications for biological signatures in the sulphur isotope record. Geobiology 1 (1), 27–36.

Farquhar, J., Wing, B., McKeegan, K., Harris, J., Cartigny, P., Thiemens, M., 2002. Mass-independent sulfur of inclusions in diamond and sulfur recycling on early earth. Science 298 (5602), 2369–2372.

Godel, B., Barnes, S.-J., 2008. Platinum-group elements in sulfide minerals and the whole rocks of the JM Reef (Stillwater Complex): Implication for the formation of the reef. Chemical Geology 248 (3-4), 272–294.

Grinenko, L., 1985. Sources of sulfur of the nickeliferous and barren gabbro-dolerite intrusions of the northwest Siberian platform. International Geology Review 27 (6), 695–708.

Hagemann, S. G., Lisitsin, V., Huston, D., 2016. Mineral system analysis: Quo vadis. Ore Geology Reviews 76, 504–522.

Heinrich, C. A., Candela, P. A., 2014. Fluids and ore formation in the earth's crust. In: Treatise on Geochemistry (Second Edition). Vol. 13. Elsevier, pp. 1–28.

Helmy, H. M., Ballhaus, C., Berndt, J., Bockrath, C., Wohlgemuth-Ueberwasser, C., 2007. Formation of Pt, Pd and Ni tellurides: experiments in sulfide–telluride systems. Contributions to Mineralogy and Petrology 153 (5), 577–591.

Hulston, J., Thode, H., 1965. Variations in the S33, S34, and S36 contents of meteorites and their relation to chemical and nuclear effects. Journal of Geophysical Research 70 (14), 3475–3484.

Irvine, T., 1975. Crystallization sequences in the muskox intrusion and other layered intrusions—ii. origin of chromitite layers and similar deposits of other magmatic ores. In: Irvine, T. (Ed.), Chromium: its Physicochemical Behavior and Petrologic Significance. Pergamon, pp. 991 – 1020.

Kleine, T., Walker, R. J., 2017. Tungsten isotopes in planets. Annual Review of Earth and Planetary Sciences 45 (1), 389–417.

LaFlamme, C., Jamieson, J. W., Fiorentini, M. L., Thébaud, N., Caruso, S., Selvaraja, V., 2018. Investigating sulfur pathways through the lithosphere by tracing mass independent fractionation of sulfur to the Lady Bountiful orogenic gold deposit, Yilgarn Craton. Gondwana Research 58, 27–38.

Leavitt, W. D., Cummins, R., Schmidt, M. L., Sim, M. S., Ono, S., Bradley, A. S., Johnston, D. T., 2014. Multiple sulfur isotope signatures of sulfite and thiosulfate reduction by the model dissimilatory sulfate-reducer, Desulfovibrio alaskensis str. G20. Frontiers in microbiology 5, 591.

Lesher, C., Keays, R. R., 2002. Komatiite-associated Ni-Cu-PGE deposits: Geology, mineralogy, geochemistry and genesis. In: The geology, geochemistry, mineralogy and Mineral beneficiation of the platinum-group elements. Canadian Institute Mineral Metallurgy Petroleum, pp. 579–618.

Lesher, C. M., Burnham, O. M., 2001. Multicomponent elemental and isotopic mixing in Ni–Cu–(PGE) ores at Kambalda, Western Australia. The Canadian Mineralogist 39 (2), 421–446.

Li, C., Barnes, S.-J., Makovicky, E., Rose-Hansen, J., Makovicky, M., 1996. Partitioning of nickel, copper, iridium, rhenium, platinum, and palladium between monosulfide solid solution and sulfide liquid: effects of composition and temperature. Geochimica et Cosmochimica Acta 60 (7), 1231–1238.

Li, C., Ripley, E. M., 2005. Empirical equations to predict the sulfur content of mafic magmas at sulfide saturation and applications to magmatic sulfide deposits. Mineralium Deposita 40 (2), 218–230.

Liu, Y., Brenan, J., 2015. Partitioning of platinum-group elements (PGE) and chalcogens (Se, Te, As, Sb, Bi) between monosulfide-solid solution (MSS), intermediate solid solution (ISS) and sulfide liquid at controlled fO_2–fS_2 conditions. Geochimica et Cosmochimica Acta 159, 139–161.

Loucks, R. R., Mavrogenes, J. A., 1999. Gold solubility in supercritical hydrothermal brines measured in synthetic fluid inclusions. Science 284 (5423), 2159–2163.

MacNamara, J., Thode, H., 1950. Comparison of the isotopic constitution of terrestrial and meteoritic sulfur. Physical Review 78 (3), 307.

Makovicky, E., 2002. Ternary and quaternary phase systems with PGE. In: Geology, Geochemistry, Mineralogy and Mineral Beneficiation of Platinum-group Elements. Canadian Institute of Mining, Metallurgy and Petroleum, pp. 131–175.

Mansur, E. T., Barnes, S.-J., Duran, C. J., Sluzhenikin, S. F., 2019. Distribution of chalcophile and platinum-group elements among pyrrhotite, pentlandite, chalcopyrite and cubanite from the Noril'sk-Talnakh ores: implications for the formation of platinum-group minerals. Mineralium Deposita, 1–18.

Mavrogenes, J. A., O'Neill, H. S., 1999. The relative effects of pressure, temperature and oxygen fugacity on the solubility of sulfide in mafic magmas. Geochimica et Cosmochimica Acta 63 (7), 1173 – 1180.

McCuaig, T. C., Beresford, S., Hronsky, J., 2010. Translating the mineral systems approach into an effective exploration targeting system. Ore Geology Reviews 38 (3), 128–138.

McCuaig, T. C., Hronsky, J. M., 2014. The mineral system concept: the key to exploration targeting. Society of Economic Geologists Special Publication 18, 153–175.

Mungall, J. E., Andrews, D. R., Cabri, L. J., Sylvester, P. J., Tubrett, M., 2005. Partitioning of Cu, Ni, Au, and platinum-group elements between monosulfide solid solution and sulfide melt under controlled oxygen and sulfur fugacities. Geochimica et Cosmochimica Acta 69 (17), 4349–4360.

Mungall, J. E., Naldrett, A. J., 2008. Ore deposits of the platinum-group elements. Elements 4 (4), 253–258.

Naldrett, A., 1969. A portion of the system Fe–S–O between 900 and 1080°c and its application to sulfide ore magmas. Journal of Petrology 10 (2), 171–201.

Naldrett, A., 2004. Magmatic sulfide deposits: Geology, geochemistry and exploration. Springer Science & Business Media.

O'Neil, J. R., 1986. Theoretical and experimental aspects of isotopic fractionation. Reviews in Mineralogy 16, 1–40.

Ono, S., Wing, B., Johnston, D., Farquhar, J., Rumble, D., 2006. Mass-dependent fractionation of quadruple stable sulfur isotope system as a new tracer of sulfur biogeochemical cycles. Geochimica et Cosmochimica Acta 70 (9), 2238–2252.

Peck, D., Huminicki, M., 2016. Value of mineral deposits associated with mafic and ultramafic magmatism: Implications for exploration strategies. Ore Geology Reviews 72, 269–298.

Peters, B., 1959. Cosmic-ray produced radioactive isotopes as tracers for studying large-scale atmospheric circulation. Journal of Atmospheric and Terrestrial Physics 13 (3-4), 351–370.

Ripley, E. M., Li, C., 2003. Sulfur Isotope Exchange and Metal Enrichment in the Formation of Magmatic Cu-Ni-(PGE) Deposits. Economic Geology 98 (3), 635.

Ripley, E. M., Li, C., 2013. Sulfide Saturation in Mafic Magmas: Is External Sulfur Required for Magmatic Ni-Cu-(PGE) Ore Genesis? Economic Geology, v. 108, 45–58.

Rudnick, R. L., Gao, S., 2003. Composition of the continental crust. Treatise on geochemistry 3, 659.

Savarino, J., Romero, A., Cole-Dai, J., Bekki, S., Thiemens, M. H., 2003. Uv induced mass-independent sulfur isotope fractionation in stratospheric volcanic sulfate. Geophysical Research Letters 30 (21).

Schulz, K. J., Chandler, V. W., Nicholson, S. W., Piatak, N., Seal, R. R., Woodruff, L. G., Zientek, M. L., 2010. Magmatic sulfide-rich nickel-copper deposits related to picrite and (or) tholeiitic basalt dike-sill complexes: A preliminary deposit model. US Department of the Interior, US Geological Survey.

Seal, II, R. R., 2006. Sulfur isotope geochemistry of sulfide minerals. Reviews in Mineralogy and Geochemistry 61 (1), 633.

Selvaraja, V., Caruso, S., Fiorentini, M. L., LaFlamme, C., 2017. The Global Sedimentary Sulfur Isotope Database.
URL http://www.cet.edu.au/research-projects/special-projects/gssid-global-sedimentary-sulfur-isotope-database

Thode, H., Macnamara, J., Collins, C., 1949. Natural variations in the isotopic content of sulphur and their significance. Canadian journal of research 27 (4), 361–373.

von Gehlen, K., 1992. Sulfur in the earth's mantle — a review. In: Schidlowski, M., Golubic, S., Kimberley, M. M., McKirdy, D. M., Trudinger, P. A. (Eds.), Early Organic Evolution: Implications for Mineral and Energy Resources. Springer Berlin Heidelberg, Berlin, Heidelberg, pp. 359–366.

Wacey, D., Noffke, N., Cliff, J., Barley, M. E., Farquhar, J., 2015. Micro-scale quadruple sulfur isotope analysis of pyrite from the 3480 Ma Dresser Formation: New insights into sulfur cycling on the early Earth. Precambrian Research 258, 24–35.

Walker, A., Evans, K., Kirkland, C., Martin, L., Kiddie, O., Spaggiari, C., 2019. Tracking mineralisation with in situ multiple sulphur isotopes: a case study from the Fraser Zone, Western Australia. Precambrian Research 332.

Wyborn, L., Heinrich, C., Jaques, A., 1994. Australian proterozoic mineral systems: essential ingredients and mappable criteria. In: The AusIMM Annual Conference. Vol. 1994. AusIMM Darwin, pp. 109–115.

Chapter 2

Geological Background

2.1 A geological synthesis of the Albany-Fraser Orogen

The Albany–Fraser Orogen (AFO) is a Palaeoproterozoic to Mesoproterozoic orogenic belt located on the southern and south eastern margins of the Archaean Yilgarn Craton in Western Australia (Spaggiari et al., 2015). It is a component of the West Australian Craton (WAC), separated from the South Australian Craton (SAC) by the Madura and Coompana Provinces, and the North Australian Craton (NAC) by the Musgrave Province (Quentin de Gromard et al., 2017).

As a component of the WAC, the AFO is interpreted to be part of the larger Australo–Antarctic, Albany–Fraser Wilkes Orogen prior to the breakup of Gondwana (Fitzsimons, 2003) (Fig. 2.1). The Windmill Islands region in Antarctica preserves two major periods of orogenesis that correlate with Stages I and II of the Albany-Fraser Orogeny. It is these events that produced the predominant tectonic and metamorphic features seen in the AFO today (Post et al., 1997; Fitzsimons, 2003). Significant detrital zircon populations in the Windmills Island region record clusters of ages at c. 1800 Ma, 1600 Ma and 1400 Ma (Zhang et al., 2012; Morrissey et al., 2017), which broadly correlate to magmatic ages in the AFO and adjacent Madura, Coompana and Musgrave Provinces (Clark et al., 2000; Kirkland et al., 2011, 2015a; Spaggiari and Smithies, 2015; Howard et al., 2015; Smithies et al., 2015).

The AFO is bounded by the Yilgarn Craton to the west and the Rodona Shear Zone to the east (Fig. 2.2) (Spaggiari et al., 2012, 2015). The orogen includes Palaeoproterozoic to Mesoproterozoic igneous and metamorphic rocks formed over an extensive and cryptic tectonic history, which includes reworking of Archaean crust and modification by variable degrees of mantle-derived magmatism (Smithies et al., 2015; Spaggiari et al., 2015).

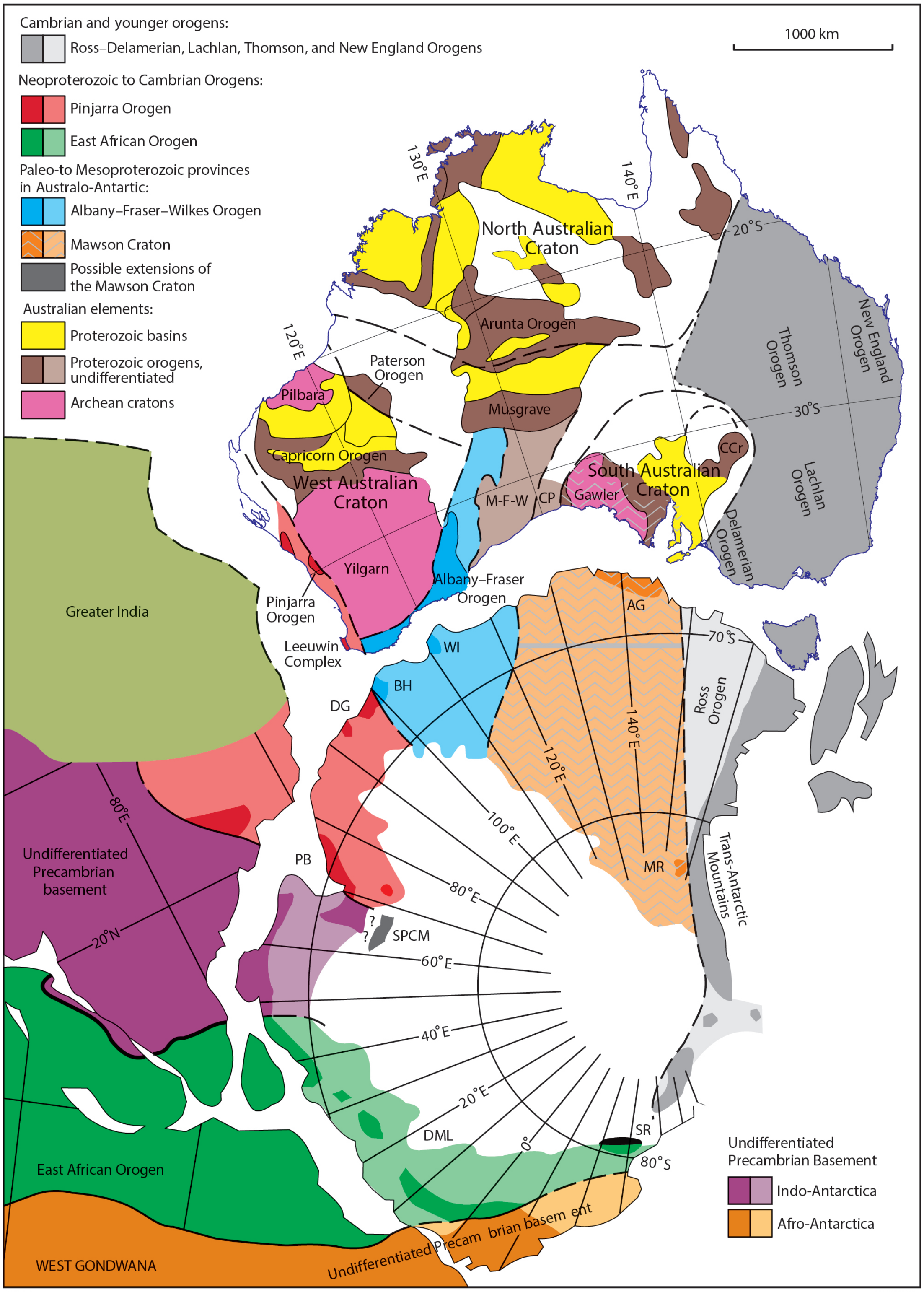

CS79b

09.08.11

Figure 2.1: Palaeogeographic reconstruction of the AFO in relation to crustal elements of easternmost Gondwana (from Spaggiari et al., 2011)

2.1.1 Tectonic subdivisions of the Albany-Fraser Orogen

The AFO is divided into several distinct lithotectonic domains (Fig. 2.2); the Northern Foreland, Tropicana Zone (which we consider here to be part of the Northern Foreland, Biranup Zone, Fraser Zone and the Nornalup Zone).

Northern Foreland

The Northern Foreland has been defined "as the portion of the Yilgarn Craton reworked during the Albany-Fraser Orogen, thereby reflecting it's proximity to the collisional orogenic belt" (Spaggiari et al., 2011), and comprises greenschist to lower amphibolite facies Yilgarn material modified by Palaeoproterozoic to Mesoproterozoic magmatism (Spaggiari et al., 2015; Quentin de Gromard et al., 2017) (Fig. 2.2). It includes the granitic Munglinup Gneiss; a higher grade and more significantly reworked component than the rest of the Northern Foreland (Spaggiari et al., 2011). The Northern Foreland is thought to be derived from Archaean precursor lithologies and records at least four stages of granitic magmatism with crystallisation ages between c. 2720–2630 Ma (Spaggiari et al., 2011). Numerous shear zones and faults separate the Northern Foreland from the adjacent Yilgarn Craton and Biranup Zone, and the intensity of Proterozoic deformation increases away from the Craton and towards the Biranup Zone (Spaggiari et al., 2009, 2011).

Tropicana Zone

The Tropicana Zone is the most north-easterly domain of the AFO and comprises rocks of Yilgarn affinity with a geological evolution distinct to the adjacent Yilgarn Craton (Quentin de Gromard et al., 2017). The zone is dominated by the c. 2720 Ma amphibolite to granulite facies Archaean Tropicana Gneiss and Hercules Gneiss, which are overlain by metasedimentary rocks of the Lindsay Hill Formation and intruded by Palaeoproterozoic granitic rocks (Occhipinti et al., 2014, 2018; Kirkland et al., 2015b; Spaggiari et al., 2015). The Tropicana Gneiss comprises amphibolite to granulite facies quartzofeldspathic gneiss that includes tonalitic, quartz-syenogranitic, syenitic and monzo-granitic compositions, mafic to ultramafic gneiss, metachert and meta-iron formations (Occhipinti et al., 2014; Doyle et al., 2014, 2015). The Hercules Gneiss is made up predominantly of 2692 ± 16 Ma sanukitoids that are interpreted to be a likely source of gold in the Tropicana Zone (Kirkland et al., 2015b), with intrusion interpreted to have started during granulite facies metamorphism associated with the 2718–2554 Ma Atlantis Event (Occhipinti et al., 2018 and references therein).

The Tropicana Zone hosts the Tropicana gold deposit. Gold mineralisation is interpreted to have formed after the Atlantis Event under greenschist facies conditions (Doyle et al., 2014, 2015) and located primarily within K-feldspar rich quartzo-feldspathic orthogneiss or pegmatitic rocks (Doyle et al., 2009, 2015).

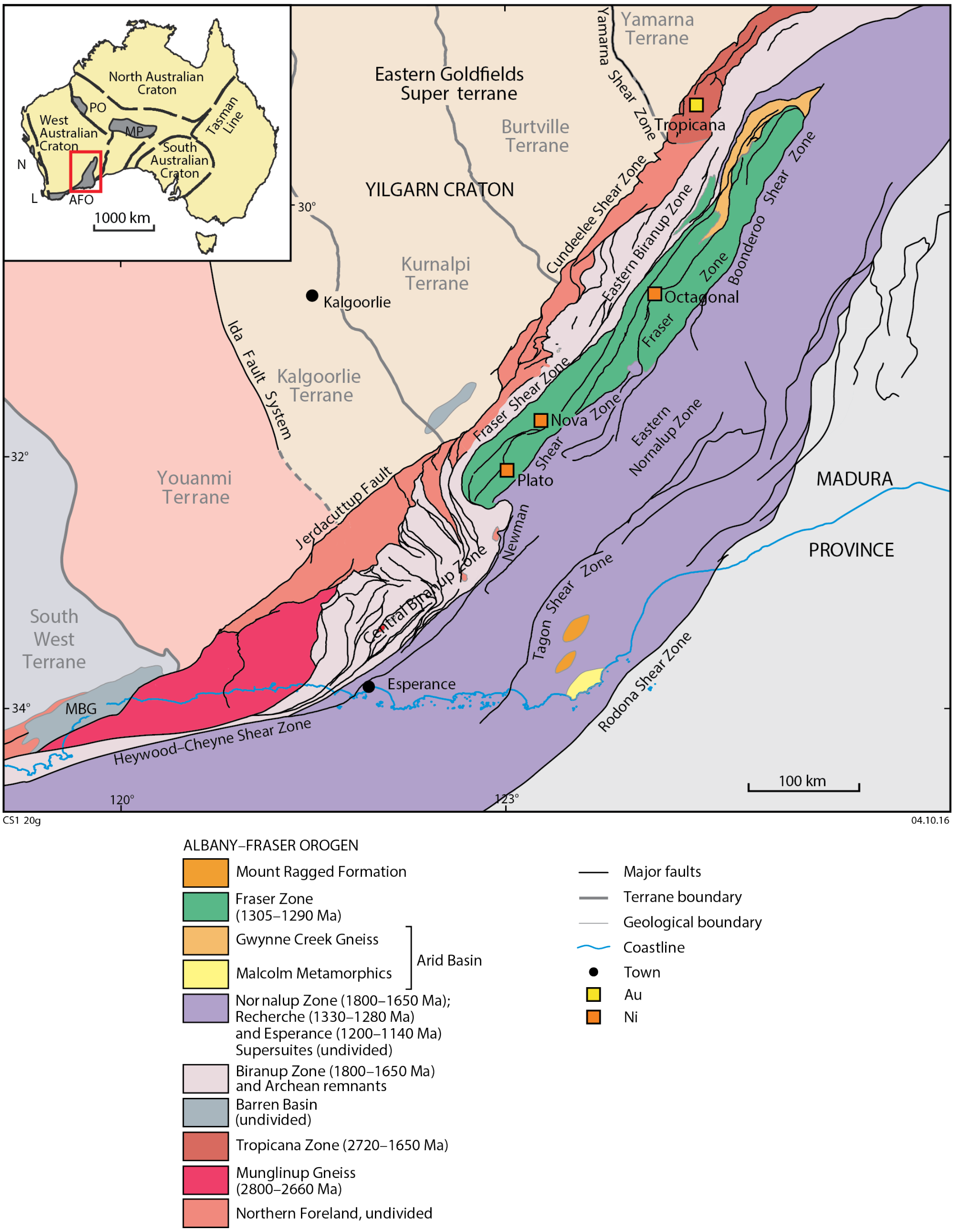

Figure 2.2: Simplified geological overview of the AFO (modified after Spaggiari et al., 2011)

Biranup Zone

The Biranup Zone is a belt of predominantly mid-crustal rocks extending along the length of the AFO (Spaggiari et al., 2011), abutting the Northern Foreland to the west and the Nornalup and Fraser Zones to the east across shear zones (Fig. 2.2). The south-eastern end of the Biranup Zone, where Biranup Zone rocks are tectonically interlayered with those of the Northern Foreland, has come to be called the “S bend” for its apparent S-fold geometry (Spaggiari et al., 2011; Munro et al., 2017). Biranup Zone geology is dominated by deformed orthogneiss with interpreted protolith crystallisation ages between 1815–1625 Ma (Nelson et al., 1995; Spaggiari et al., 2011; Kirkland et al., 2014a), with subordinate metagabbro and paragneiss. The majority of Biranup Zone magmas were emplaced during the 1710–1650 Ma Biranup Orogeny, with a younger generation of granitic and gabbroic rocks emplaced at c. 1665 ± 4 Ma (Kirkland et al., 2011). In addition to magmatic material the Biranup Zone incorporates Palaeoproterozoic metasedimentary rocks of the Barren Basin (See Section 2.1.2) that have been intruded by Palaeoproterozoic granites (Spaggiari et al., 2015).

Due to a lack of evidence for a Palaeoproterozoic magmatic event of origin, the Biranup Zone has previously been interpreted to be exotic to the Albany-Fraser Orogen (e.g. Spaggiari et al., 2009). More recently, Nd and Hf isotopic datasets have since shown that the Biranup Zone likely formed autochthonously along the margin of the Yilgarn Craton (Kirkland et al., 2011). The Lu-Hf character of the Biranup Zone encompasses values that include more evolved values of a Yilgarn-like affinity in addition to more juvenile values (Kirkland et al., 2011). A temporal trend to these values is interpreted to represent the progressive dilution of an older Archaean Hf signature by the addition of more depleted juvenile input via more recent magmatism. Additional Lu-Hf data from magmatic zircon analyses are consistent with reworking of material with a crustal residence age of c. 2.0–2.5 Ga (Kirkland et al., 2011, 2014a). In a geodynamic context this is compatible with the extensive magmatic reworking of the Biranup Zone.

Nornalup Zone

The Nornalup Zone is the southern and southeasternmost portion of the AFO, separated from the Biranup Zone by the Newman Shear Zone, the Fraser Zone by the Boonderoo Fault and the Madura province by the Rodona Shear Zone (Fig. 2.2) (Spaggiari et al., 2011). Supracrustal geology of the Nornalup Zone includes the Mesoproterozoic Malcolm Metamorphics and paragneisses belonging to the Arid Basin, in addition to sediments of the Ragged Basin. Much of the basement of the Nornalup Zone is concealed by the voluminous Recherche and Esperance Supersuites (Spaggiari et al., 2011). This basement includes migmatitic metatonalitic gneiss with a magmatic crystallisation age of 1809 ± 8 Ma (Kirkland et al., 2014b) and granitic gneiss with a magmatic crystallisation age of 1763 ± 11 Ma (Kirkland et al., 2012). These ages suggest that the basement of the Nornalup Zone contains Palaeoproterozoic granites comparable to those in the Biranup Zone (Quentin de Gromard et al., 2017).

Recherche Supersuite

The 1330–1280 Ma (Nelson et al., 1995; Clark et al., 2000; Smithies et al., 2015) Recherche Supersuite was emplaced during Stage I of the Albany-Fraser Orogeny and comprises amphibolite to granulite facies granites with subordinate synmagmatic intermediate and mafic intrusives, with rocks often including gneissose fabrics (Spaggiari et al., 2011; Smithies et al., 2015). These granitic rocks show a wide range of silica contents and have been classified as granodiorite (SiO_2 <64 wt %), monzogranite (SiO_2 64–70.5 wt%) and syenogranite (SiO_2 >70.5 wt%); these are collectively referred to as the 1330–1283 Ma Gora Hill Suite (Smithies et al., 2015). The Gora Hill Suite is suggested to represent variable mixing between mantle derived gabbroic magmas, such as those now exposed in the Fraser Zone, and existing felsic crust (Smithies et al., 2013, 2015).

A separate group (SiO_2 >72 wt%) exhibiting HFSE, REE, Th and U depletions relative to other granitic rocks in the Recherche Supersuite has been named as the 1320–1287 Ma Southern Hills Suite (Smithies et al., 2015). Major and trace element compositions of these granitic rocks are typical of highly evolved, small degree anatectic melts derived from felsic or quartzofeldspathic sources (Smithies et al., 2015). Although the Suite extends beyond the Fraser Zone into the Biranup and Nornalup Zones, field relationships and the peraluminous nature of the Southern Hills Suite suggest that these rocks represent anatectic melts of the Snowys Dam Formation metasedimentary rocks into which the Fraser gabbro intruded (Smithies et al., 2015).

Esperance Supersuite

Emplacement of the 1200–1140 Ma Esperance Supersuite occurred during Stage II of the Albany-Fraser Orogeny. The Esperance Supersuite is voluminous within the Nornalup Zone, but shows a poorly defined extent across the rest of the orogen (Spaggiari et al., 2011) and includes voluminous greenschist to amphibolite facies metagranites which are less pervasively deformed than rocks of the Recherche Supersuite (Spaggiari et al., 2011; Smithies et al., 2015). The discovery of granites with similar ages within the Madura Province indicates that magmatism associated with the Esperance Supersuite was not confined to the Albany-Fraser Orogen (Smithies et al., 2015).

A subset of ferroan, alkali-calcic to alkali granitic rocks define the Booanya Suite of granites within the Esperance Supersuite and occur primarily within the Nornalup Zone (Smithies et al., 2015). The Truslove Suite comprises a more widespread range of granites within the Nornalup and Biranup Zones; these rocks represent low degree partial melts of primarily local Biranup magmatic rocks (Smithies et al., 2015).

Fraser Zone

Located between the Biranup and Nornalup Zones (Fig. 2.2), the Fraser Zone is characterised by a strong NE-SW trending gravity anomaly approximately 425 km long by 50 km wide, attributed to significant volumes of mafic and ultramafic material (Fig. 2.3) (Maier et al., 2016b). It exhibits a v-shaped geometry with a depth of c. 15km, bounded by the Fraser, Newman and Boonderoo Shear Zones (Spaggiari et al., 2014b; Brisbout, 2015). The Fraser Zone is dominated by voluminous sheeted metagabbro (Fraser gabbro) intercalated with more minor granitic gneiss and paragneiss (Smithies et al., 2013; Maier et al., 2016b). Minor ultramafic material occurs within some metagabbroic sills and larger cumulate bodies such as those seen at the Nova-Bollinger Ni-Cu deposit (Maier et al., 2016b). These magmatic components intruded metasediments of the Snowys Dam Formation. The Snowys Dam Formation forms part of the Mesoproterozoic Arid Basin with a maximum depositional age of 1332 ± 21 Ma (Spaggiari et al., 2015) and comprises a sequence of amphibolite to granulite facies pelitic, semipelitic, calcic, locally iron- and sulphide-rich metasedimentary rocks (Spaggiari et al., 2015; Quentin de Gromard et al., 2017). Relative abundances of these magmatic and sedimentary lithologies vary spatially, and the Fraser Zone can be subdivided into north-western and south-eastern domains along the Browns Dam Shear Zone (Munro et al., 2017). Interlayered paragneiss, metagabbro and metagranite dominate the north-western domain, while the south-eastern domain primarily comprises metagabbro (Munro et al., 2017). Upper amphibolite to granulite facies metamorphism of these rocks at c. 1334–1280 Ma led to the formation of the Fraser Range Metamorphics (Spaggiari et al., 2009, 2011), with intense folding, shearing and interlayering observable at all scales (Munro et al., 2017; Quentin de Gromard et al., 2017).

At many localities there is clear evidence for incorporation of metasedimentary country rock within metagabbroic intrusions, with metasedimentary inclusions, stringers and mingling textures commonplace (Maier et al., 2016b). As such, Fraser Zone metagabbro can be broadly divided into "main" and "hybrid" gabbro; hybrid gabbro describes those metagabbroic rocks exhibiting physical and geochemical evidence for contamination or hybridisation with more felsic material, while main gabbro describes metagabbro showing no evidence of contamination (Smithies et al., 2013; Maier et al., 2016b). Hybrid metagabbro typically exhibits elevated SiO_2 content and lower Mg # relative to main gabbro and can be further subdivided into Groups 1 and 2 based on Th vs La, Pb and K geochemical trends (Smithies et al., 2013).

Emplacement of magmatic components of the Fraser Zone began with the initiation of coeval mafic and felsic magmatism between 1310–1283 Ma (Spaggiari et al., 2015) in association with Stage I of the Albany-Fraser Orogeny. Igneous crystallisation of Fraser Zone mafic components has been dated at between 1305–1290 Ma via zircon U-Pb geochronology (De Waele and Pisarevsky, 2008; Kirkland et al., 2011; Clark et al.,

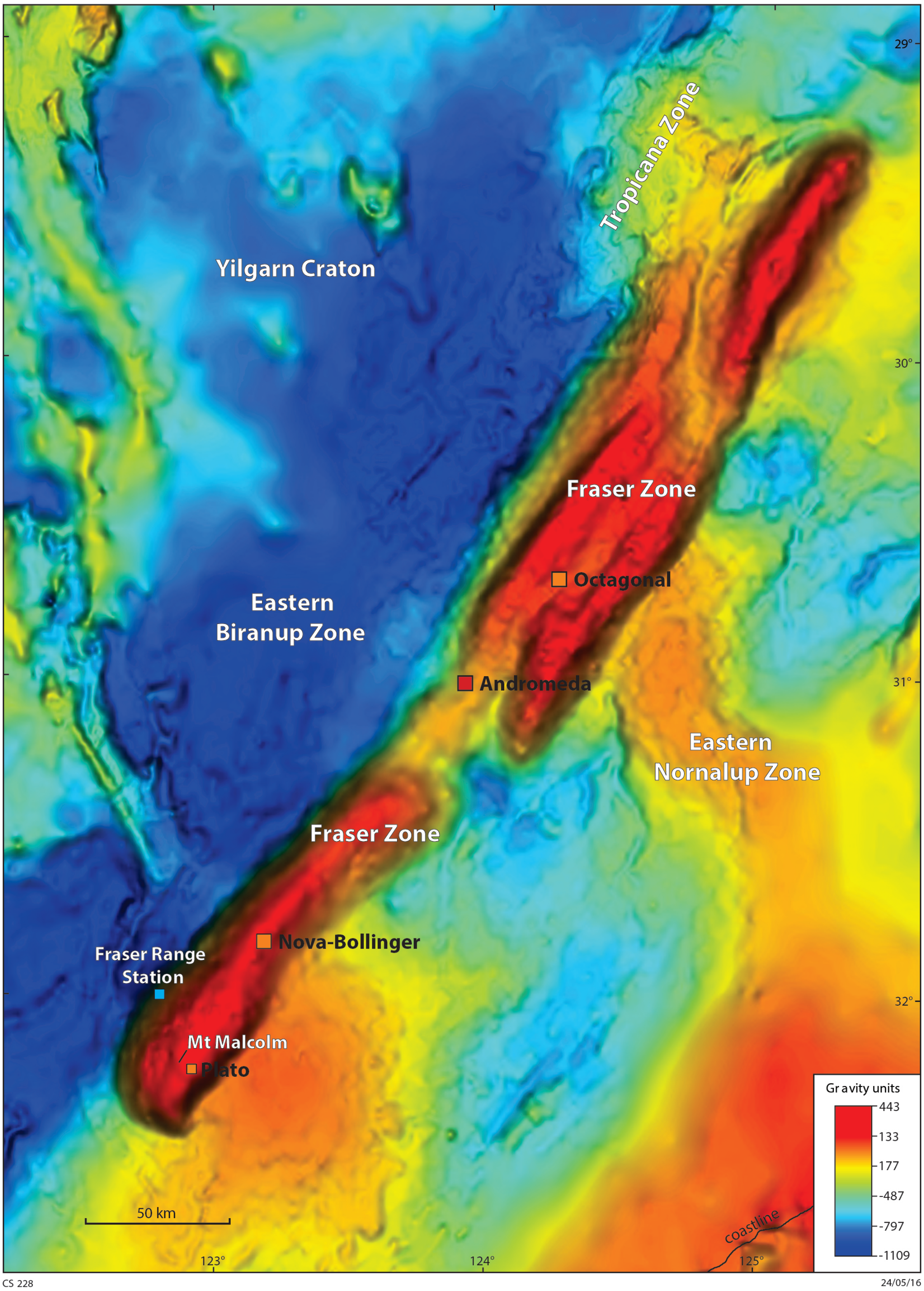

Figure 2.3: Gravity map showing the extent of the Fraser Zone (strong gravity response) and studied localities (from Maier et al., 2016b)

2014). This magmatism is part of the 1330–1280 Ma Recherche Supersuite (Section 2.1.1). Upper amphibolite to granulite facies metamorphism occurred coevally with magmatism, with the brief interval between initiation of magmatism and metamorphism implying mafic magmatism was a thermal driver for metamorphism (Clark et al., 2014). Thermodynamic modelling conducted by Clark et al. (2014) constrained metamorphic conditions imposed on metasedimentary material to 800–900 ^{o}C and 6.5–8.5 kbar, consistent with peak metamorphism at depths of 25–30 km. Further modelling by Glasson et al. (2019) on metagabbroic material estimated temperatures of 900–950 ^{o}C and pressures of approximately 7 kbar. These conditions are comparable to those provided by Clark et al, with the higher temperatures recorded by the metagabbro consistent with metagabbroic rocks being closer to the thermal driver of metamorphism as indeed they were the heat source (Glasson et al., 2019). Further, Glasson et al. (2019) constrained the duration of magmatism to c. 10–30 Ma via zircon U-Pb geochronology.

In contrast to widespread metamorphic zircon U-Pb ages associated with Stage I of the Albany-Fraser Orogeny in the Fraser Zone, a clear absence of metamorphic zircon U-Pb ages associated with Stage II is especially conspicuous when compared with the Stage II ages that dominate the adjacent Biranup Zone (Kirkland et al., 2016). Recent ^{40}Ar/^{39}Ar thermochronological work (Scibiorski et al., 2016) and U-titanite geochronology (Kirkland et al., 2016) has demonstrated that the Fraser Zone did experience Stage II-associated metamorphism. Small titanite grains from the Fraser Shear Zone record Stage II overprinting with mean U-Pb reset ages of 1205 ± 16 Ma (Kirkland et al., 2016). This is consistent with extrusion of the Fraser Zone to shallower crustal levels between 1270 Ma and 1193 Ma (Kirkland et al., 2011) prior to Stage II under geological conditions that were less than conducive to new zircon growth (Kirkland et al., 2016).

There has been protracted debate regarding the origin of the Fraser Zone. It has been argued that the Fraser Zone is exotic to the Albany-Fraser Orgen and represents the remnants of accreted oceanic arcs at c. 1300 Ma, with Fraser gabbro trace element characteristics argued to be typical of subduction-related magmatism (Condie and Myers, 1999). These trace element characteristics have since been explained by crustal underplating and concomitant assimilation of small quantities (<10 %) of crustal material with a composition analogous to a mix of Archaean granite and Munglinup Gneiss (Smithies et al., 2013). Although c. 1300 Ma magmatism dominates the Fraser Zone geochronological record, a small number of detrital and xenocrystic zircon analyses from metasedimentary and metagranitic rocks fall within a range of U-Pb ages identical to magmatic rocks within the Biranup Zone (1800–1650 Ma; Kirkland et al., 2011). This material is considered to have been inherited during emplacement of the Fraser Zone through a basement of comparable age to the Biranup Zone. Evolved Lu-Hf isotopic compositions from Fraser Zone granitic material imply the reworking of a Biranup Zone source component with a crustal residence age of 2.0–2.5 Ga (Kirkland et al., 2011, 2014a), which itself represents portions of the Yilgarn Craton modified by juvenile magmatic input (Kirkland et al., 2011, 2014a; Spaggiari et al., 2015). This combination of geochemical modelling, inherited Biranup Zone material and Lu-Hf isotopic data defines the relationship between the Fraser Zone and the AFO as unequivocally autochthonous and, furthermore, implies an extension of the Yilgarn Craton beneath the Fraser Zone.

2.1.2 Significant basin systems within the Albany-Fraser Orogen

Much of the orogen's basement geology is buried by up to 150 m of cover material (Gonzalez-Alvarez et al., 2014) comprising several basin systems within the orogen. The 1815–1600 Ma Barren Basin and 1600–1305 Ma Arid Basin are the most substantial of these systems, recording an extensional tectonic regime that has prevailed in the AFO for much of its history (Spaggiari et al., 2015).

Barren Basin

The Barren basis comprises a sequence of Palaeoproterozoic sedimentary material overlying the Yilgarn Craton, Northern Foreland, Biranup and Nornalup Zones, metamorphosed at upper amphibolite to granulite facies (Spaggiari et al., 2015). These metasediments include sandstones, siltstones, mudstones, conglomerates and rare carbonates, extending along a significant portion of the southern and south-eastern margins of the Yilgarn Craton as implied by basin analysis and geochronological data (Spaggiari et al., 2015).

Deposition within the Barren Basin was closely coupled to preceding regional magmatic events. The onset of deposition occurred at c. 1800 Ma in association with the Salmon Gums Event (Spaggiari et al., 2015). At this time extension along the southern and south-eastern margin of the Yilgarn Craton was ongoing with a significant component of detrital Yilgarn material derived from the development of a horst and graben architecture that exposed basement geology (Spaggiari et al., 2015). A second phase of deposition is linked to a shift in tectonic regime at c. 1680 Ma associated with the compressional Zanthus Event and is interpreted to indicate possible basin inversion (Spaggiari et al., 2015). A third and final phase of deposition at c. 1710–1650 Ma is associated with the latter stages of the Biranup Orogeny, with cessation of magmatism at 1627 Ma (Kirkland et al., 2010) interpreted to mark the end of basin formation associated with thermal subsidence. The Barren Basin is a product of a predominantly extensional tectonic regime, with intimate links between magmatism, uplift, erosion and deposition of detrital material (Spaggiari et al., 2014b, 2015) (Fig. 2.4).

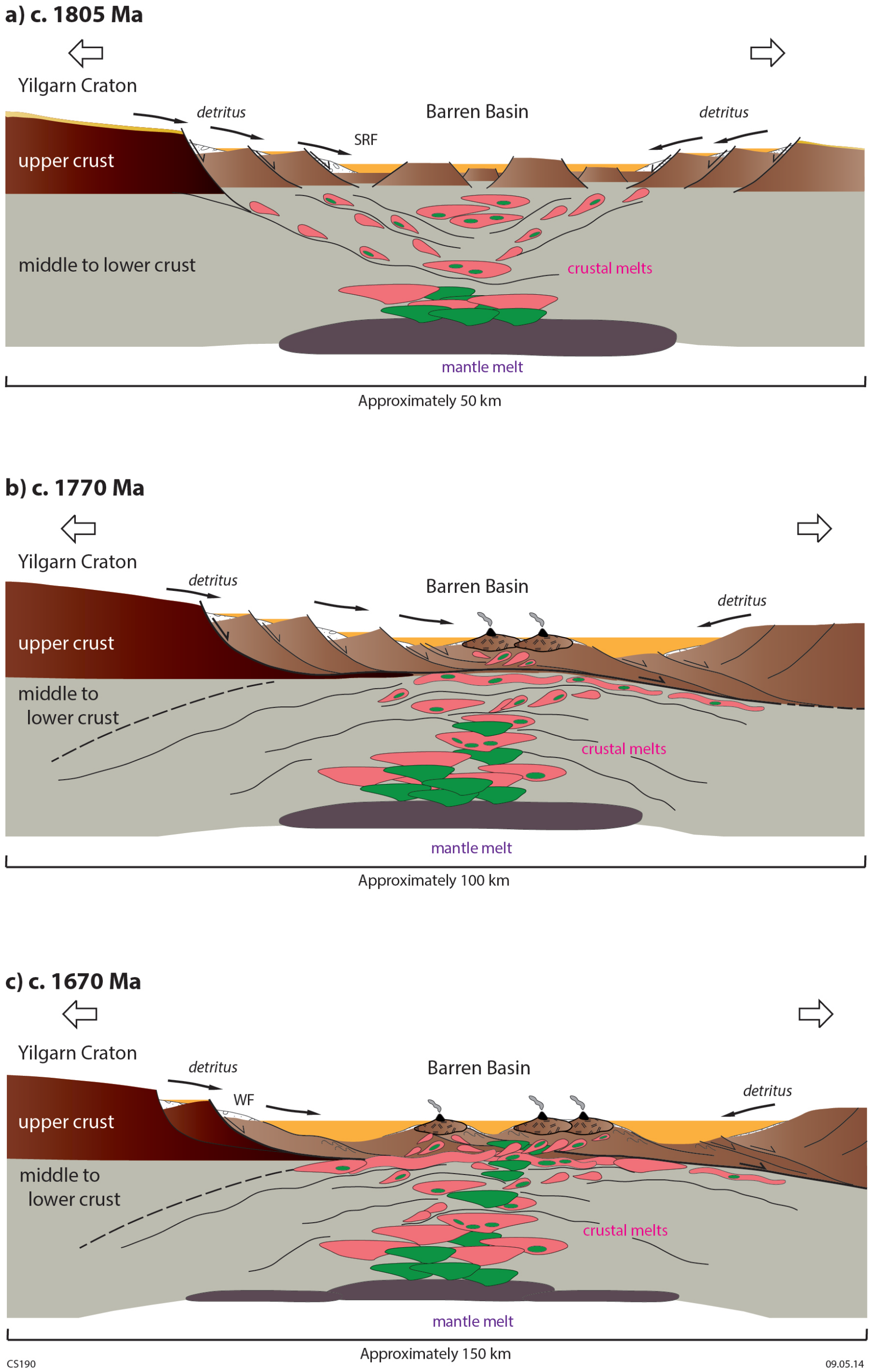

Figure 2.4: Tectonic evolution of the Barren Basin: a) Extension of the southern Yilgarn Craton by c. 1805 Ma formed a horst and graben architecture exposing basement highs. Mantle melting produced lower crustal melts and granitic intrusions along middle crustal shear zones; b) Extension and magmatism between 1780 and 1760 Ma led to doming and a core complex extension style, and basin widening. Volcanism is inferred; c) Increased magmatism during the Biranup Orogeny led to thermal subsidence, deepening of the basin, and an increased sediment load with formation of deeper depositional centres. Volcanism is inferred. Green indicates mafic/mantle component; pink indicates crustal melt/granitic component. SRF = Stirling Range Formation; WF = Woodline Formation. Large arrows indicate approximate stress field orientation. From Quentin de Gromard et al. (2017).

Arid Basin

The Arid Basin is particularly relevant to mineralisation in the Fraser Zone, including as it does the sulphide-rich Snowys Dam Formation, considered to be the primary source of external sulphur involved in magmatic sulphide mineralisation within the Fraser Zone (Maier et al., 2016b; Walker et al., 2019). Arid Basin sediments comprise mudstone, sandstone, volcanic/volcaniclastic lithologies, calcareous and iron-rich strata metamorphosed at granulite facies shortly after deposition (Spaggiari et al., 2015).

Onset of deposition is associated with the development of a marginal ocean basin from c. 1600 Ma to 1455 Ma (Fig. 2.5). Sediments were primarily derived from the Nornalup and Biranup Zones, with minor components possibly derived from more distal sources as implied by zircon U-Pb and Lu-Hf isotopes (Spaggiari et al., 2015). A change from an extensional to a convergent tectonic regime at c. 1410 Ma provided detrital material for the second phase of deposition within the Arid Basin (Spaggiari et al., 2015). This phase of deposition continued until c. 1332 Ma and the consequent start of Stage I of the Albany-Fraser Orogeny, with sediments from the accreted component of the Madura Province incorporated within the Snowys Dam Formation.

2.1.3 Tectonic events within the Albany-Fraser Orogen

The AFO has a prolonged and complex tectonic history stretching from the Neoarchaean to the Mesoproterozoic. This section summarises the most significant tectonic events modifying the AFO within the Proterozoic.

Salmon Gums Event (1815–1800 Ma)

The Salmon Gums Event comprises the earliest known Palaeoproterozoic magmatism within the AFO and is associated with the initial formation of the Barren Basin within an extensional continental rift or back-arc tectonic setting (Spaggiari et al., 2015). Granites emplaced during this event exhibit a narrow range of silica content (65.2—67.6 wt%) and geochemical characteristics that imply derivation from remelting of Archaean crust modified by juvenile mantle addition (Smithies et al., 2015).

Ngadju Event (1780–1760 Ma)

The Ngadju Event represents a second broad scale pulse of magmatism during continuing extension along the margin of the Yilgarn Craton, with associated granites and mingled co-magmatic gabbroic rocks recognised in the Tropicana, Biranup and Nornalup Zones (Spaggiari et al., 2011, 2014a). This magmatism is interpreted to have further thermally weakened already attenuating crust, accelerating extension of the Barren Basin and potentially increasing deposition within the basin system (Spaggiari et al., 2015).

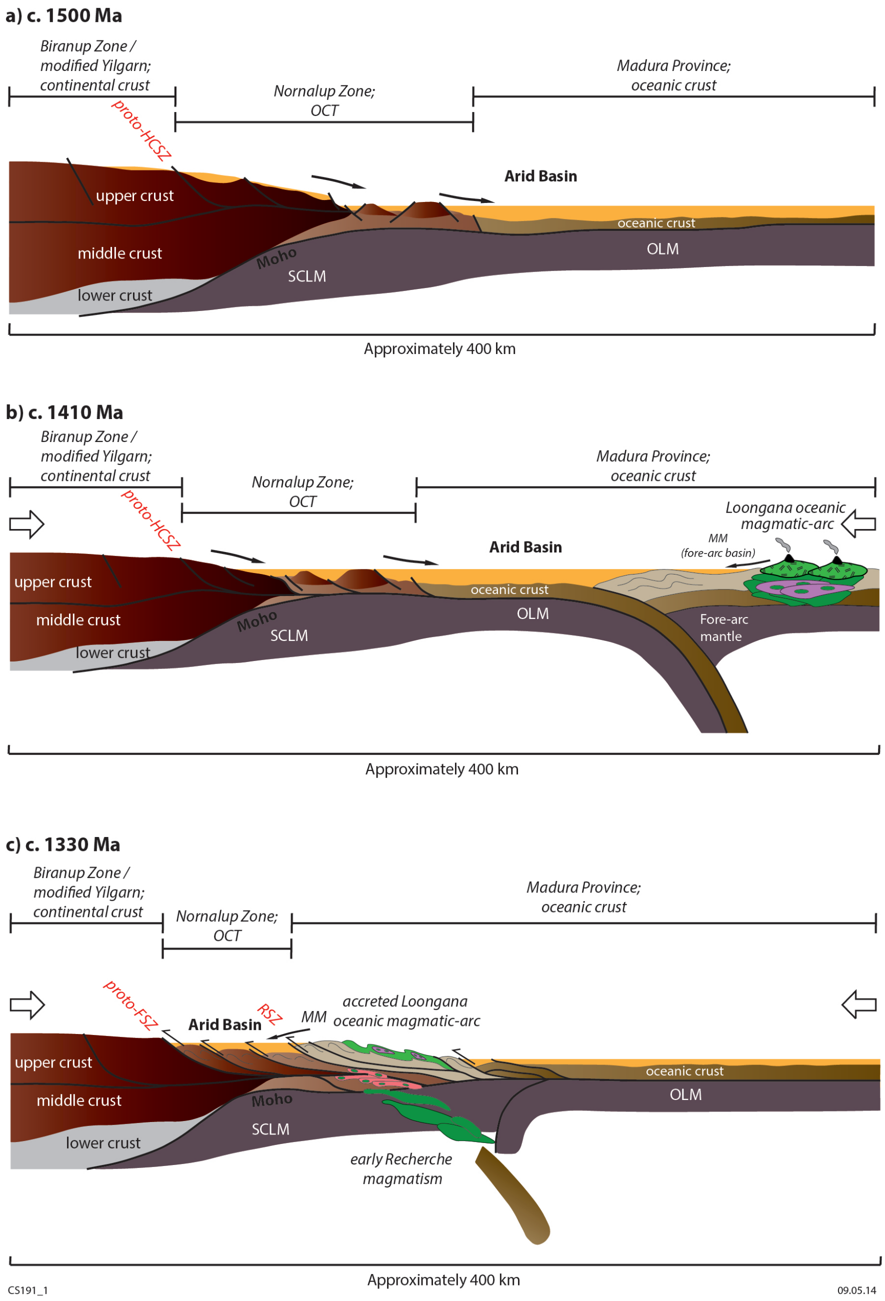

Figure 2.5: Mesoproterozoic tectonic evolution: a) At c. 1500 Ma the Arid Basin was a marginal basin outboard of the Yilgarn Craton and Biranup Zone, with the Nornalup Zone as an ocean–continent transition. These zones were part of a passive margin; b) Convergent setting and development of the Loongana oceanic magmatic-arc at c. 1400 Ma. The Malcolm Metamorphics are interpreted to be fore-arc basin deposits; c) Slab detachment and delamination results in mantle upwelling and magmatism into the Fraser Zone, in addition to westward migration of Recherche Supersuite magmatism. SCLM = sub-continental lithospheric mantle; OLM = oceanic lithospheric mantle; OCT = ocean-continent transition; MM = Malcolm Metamorphics; CSZ = Coramup Shear Zone; HCSZ= Heywood–Cheyne Shear Zone; FSZ = Fraser Shear Zone; NSZ = Newman Shear Zone; RSZ = Rodona Shear Zone; FZ = Fraser Zone. Green indicates mafic/mantle component; pink indicates crustal melt/granitic component. Large arrows indicate approximate stress field orientation. From Quentin de Gromard et al. (2017).

Biranup Orogeny (1710–1650 Ma)

The Biranup Orogeny coincided with increased deposition within the Barren Basin, with associated magmatic activity hypothesised to have resulted in thermal subsidence and deepening of the basin (Spaggiari et al., 2014b). Multiple phases of alkaline granitic magmatism record likely recycling of reworked Archaean crust mixed with juvenile mantle material (Smithies et al., 2015). The Biranup Orogeny indicates the continuation of an extensional tectonic regime until the c. 1680 Ma Zanthus event, which represents a transient compressional phase associated with basin inversion and accelerated deposition into the Barren Basin (Smithies et al., 2015).

Albany-Fraser Orogeny (1330–1140 Ma)

Divided into Stages I (1330–1260 Ma) and II (1225–1140 Ma), the Albany-Fraser Orogeny is responsible for most of the tectonic structures and metamorphic fabrics observed within the AFO.

Stage I is attributed to the collision and accretion of the Madura Province and Loongana arc onto the eastern Nornalup Zone (Spaggiari et al., 2015). Stage I was accompanied by widespread mafic and felsic magmatism of the Recherche Supersuite and is associated with upper amphibolite to granulite facies metamorphism (Bodorkos and Clark, 2004). The 1305–1290 Ma (Spaggiari et al., 2009) magmatic components of the Fraser Zone were emplaced during this event in response lithospheric delamination and mantle upwelling (Spaggiari et al., 2014b).

Stage II of the Albany-Fraser Orogeny is interpreted to represent intracontinental reworking and cratonisation of material that lies between the WAC and the SAC (Spaggiari et al., 2009; Kirkland et al., 2017), accompanied by widespread magmatism and intense deformation including craton-vergent thrusting and high temperature-moderate pressure metamorphism (Myers, 1995; Clark et al., 2000; Dawson et al., 2003; Spaggiari et al., 2009, 2011).

2.2 Previous research within the Fraser Zone

Prior to the publication of Walker et al. (2019) the sum of published magmatic sulphide and sulphur isotope research within the Fraser Zone comprised a single study by Maier et al. (2016b,a). That work examined the evolution of mafic and ultramafic rocks within the Fraser Zone and implications for magmatic sulphide mineralisation, using datasets that included whole rock element and in-situ sulphur/strontium isotopic compositions. The geological material studied included samples of Mount Malcolm main gabbro, samples from the mineralised Plato prospect proximal to Mount Malcolm, metasedimentary material of the Snowys Dam Formation from the Sunline prospect, and material from the economically mineralised Nova-Bollinger deposit; now an operating Ni-Co-Cu mine.

Mineralisation at Plato was previously described and concluded to be uneconomic in a report by Venables (2014).

Geochemical data indicate that mafic and ultramafic rocks within the Fraser Zone are all derived from the same mantle source component, slightly more depleted relative to N-MORB, with all magmas extracted from the mantle having interacted with the felsic basement to the Fraser Zone to some degree (Maier et al., 2016b). Geochemical and mineral compositions have been interpreted to indicate that the cumulates from which the Plato cumulates and Fraser Zone main gabbro formed underwent olivine and plagioclase fractionation without sulphide saturation before intrusion into the Fraser Zone (Maier et al., 2016b). Copper contents within main gabbro, hybrid gabbro and Plato cumulates average 50 ppm, below typical N-MORB values (Gale et al., 2013). Maier et al suggested that this could be explained by a) relatively small degree mantle melting ($< 20\%$) or b) the equilibration of fertile basaltic magmas with small quantities of sulphide prior to emplacement. The former explanation is favoured, as the latter is argued to be incompatible with the regional homogeneity of the Fraser Zone magmas in terms of chalcophile element depletion (Maier et al., 2016a). *In-situ* isotopic analysis of main gabbro sulphides from Mount Malcolm reveal δ^{34}S isotopic compositions between 0.0‰ to 0.4‰ (Table 2.1), overlapping with the range for mantle sulphur (Ripley, 1999).

Location	n	δ^{34}S range (‰)
Mount Malcolm	22	0.0–0.4
Nova-Bollinger	43	0.9–4.2
Sunline	2	3.6–5.2

Table 2.1: Summary of *in-situ* δ^{34}S isotopic compositions reported in Maier et al. (2016b). Mount Malcolm samples comprise main gabbro material, Sunline samples comprise metasediments of the Snowys Dam Formation

In contrast, Ni-depleted olivine compositions at Nova indicate the occurrence of sulphide saturation prior to completion of olivine crystallisation. δ^{34}S values at Nova are more positive, lying within the range of 0.9‰–4.2‰ (Table 2.1); this suggests significant assimilation of a sulphur-rich component within Nova-Bollinger, likely metasediments of the Snowys Dam Formation (Maier et al., 2016b).

Tectonic conditions during emplacement are considered to have been critical to the development of magmatic sulphide mineralisation (or lack thereof) at the localities studied. In the case of Plato and many instances of main gabbro, magmas underwent early olivine fractionation and were emplaced as thin sill-like bodies that crystallised rapidly and possessed very limited capacity to assimilate sulphur-rich country rock

(Maier et al., 2016b). At Nova, on the other hand, it is proposed that sulphide melt formed within larger magma chambers due to roof assimilation (Maier et al., 2016a). Syn-magmatic tectonic activity is thought to have driven 'seismic pumping' of sulphide-bearing silicate magmas, which subsequently formed mineralised sills (Maier et al., 2016a). Alternatively, sulphides may have descended from a magma chamber that has since been eroded (Maier et al., 2016a).

2.3 References

Bodorkos, S., Clark, D., 2004. Evolution of a crustal-scale transpressive shear zone in the Albany–Fraser Orogen, SW Australia: 2. Tectonic history of the Coramup Gneiss and a kinematic framework for Mesoproterozoic collision of the West Australian and Mawson cratons. Journal of Metamorphic Geology 22 (8), 713–731.

Brisbout, L., 2015. Determining crustal architecture in the east Albany-Fraser Orogen from geological and geophysical data. Geological Survey of Western Australia.

Clark, C., Kirkland, C. L., Spaggiari, C. V., Oorschot, C., Wingate, M. T., Taylor, R. J., 2014. Proterozoic granulite formation driven by mafic magmatism: An example from the Fraser Range Metamorphics, Western Australia. Precambrian Research 240, 1–21.

Clark, D. J., Hensen, B. J., Kinny, P. D., 2000. Geochronological constraints for a two-stage history of the Albany-Fraser Orogen, Western Australia. Precambrian Research 102 (3), 155 – 183.

Condie, K. C., Myers, J. S., 1999. Mesoproterozoic Fraser Complex: geochemical evidence for multiple subduction-related sources of lower crustal rocks in the Albany-Fraser Orogen, Western Australia. Australian Journal of Earth Sciences 46 (6), 875–882.

Dawson, G. C., Krapež, B., Fletcher, I. R., McNaughton, N. J., Rasmussen, B., 2003. 1.2 ga thermal metamorphism in the Albany–Fraser Orogen of Western Australia: consequence of collision or regional heating by dyke swarms? Journal of the Geological Society 160 (1), 29–37.

De Waele, B., Pisarevsky, S., 2008. Geochronology, paleomagnetism and magnetic fabric of metamorphic rocks in the northeast fraser belt, western australia. Australian Journal of Earth Sciences 55 (5), 605–621.

Doyle, M., Gibbs, D., Savage, J., Blenkinsop, T., 01 2009. Geology of the Tropicana Gold Project , Western Australia. pp. 50–52.

Doyle, M. G., Blenkinsop, T. G., Crawford, T., Fletcher, I., Foster, J., Fox, L., Large, R., Mathur, R., McNaughton, N., Meffre, S., Muhling, J., Occhipinti, S., Rasmussen, B., Savage, J., 2014. Tropicana deposit, Western Australia: an integrated approach to understanding granulite-hosted gold and the Tropicana Gneiss. In: Spaggiari, C., Tyler, I. (Eds.), Albany–Fraser Orogen seismic and magnetotelluric (MT) workshop 2014: extended abstracts compiled by CV Spaggiari and IM Tyler: Geological Survey of Western Australia, Record. Vol. 6. pp. 60–68.

Doyle, M. G., Fletcher, I. R., Foster, J., Large, R. R., Mathur, R., McNaughton, N. J., Meffre, S., Muhling, J. R., Phillips, D., Rasmussen, B., 2015. Geochronological Constraints on the Tropicana Gold Deposit and Albany-Fraser Orogen, Western Australia. Economic Geology 110 (2), 355.

Fitzsimons, I., 2003. Proterozoic basement provinces of southern and southwestern australia, and their correlation with antarctica. Geological Society, London, Special Publications 206 (1), 93–130.

Gale, A., Dalton, C. A., Langmuir, C. H., Su, Y., Schilling, J.-G., 2013. The mean composition of ocean ridge basalts. Geochemistry, Geophysics, Geosystems 14 (3), 489–518.

Glasson, K. J., Johnson, T. E., Kirkland, C. L., Gardiner, N. J., Clark, C., Blereau, E., Hartnady, M. I., Spaggiari, C., Smithies, H., 2019. A window into an ancient backarc? The magmatic and metamorphic history of the Fraser Zone, Western Australia. Precambrian Research 323, 55–69.

Gonzalez-Alvarez, I., Anand, R. R., Hough, R., Salama, W., Laukamp, C., Ley-Cooper, Y., Sweetapple, M. T., Sonntag, I., Lintern, M., Abdat, T., leGras, M., Walshe, J., 2014. Greenfields exploration in the Albany-Fraser Orogen and on the southeast Yilgarn cratonic margin. GSWA extended abstracts 2014, 26–28.

Howard, H., Smithies, R., Kirkland, C., Kelsey, D., Aitken, A., Wingate, M., De Gromard, R. Q., Spaggiari, C., Maier, W. D., 2015. The burning heart–the Proterozoic geology and geological evolution of the west Musgrave Region, central Australia. Gondwana Research 27 (1), 64–94.

Kirkland, C., Smithies, R., Spaggiari, C., Wingate, M., de Gromard, R. Q., Clark, C., Gardiner, N., Belousova, E., 2017. Proterozoic crustal evolution of the Eucla basement, Australia: Implications for destruction of oceanic crust during emergence of Nuna. Lithos 278, 427–444.

Kirkland, C. L., Smithies, R. H., Spaggiari, C. V., 2015a. Foreign contemporaries–unravelling disparate isotopic signatures from mesoproterozoic central and western australia. Precambrian Research 265, 218–231.

Kirkland, C. L., Spaggiari, C., Smithies, R. H., Wingate, M., Belousova, E. A., Gréau, Y., Sweetapple, M., Watkins, R., Tessalina, S., Creaser, R., 2015b. The affinity of

Archean crust on the Yilgarn—Albany–Fraser Orogen boundary: implications for gold mineralisation in the Tropicana Zone. Precambrian Research 266, 260–281.

Kirkland, C. L., Spaggiari, C. V., Johnson, T. E., Smithies, R. H., Danišík, M., Evans, N., Wingate, M. T. D., Clark, C., Spencer, C., Mikucki, E., McDonald, B. J., 2016. Grain size matters: Implications for element and isotopic mobility in titanite. Precambrian Research 278, 283 – 302.

Kirkland, C. L., Spaggiari, C. V., Pawley, M. J., Wingate, M. T. D., Smithies, R. H., Howard, H. M., Tyler, I. M., Belousova, E. A., Poujol, M., 2011. On the edge: U-Pb,Lu-Hf, and Sm-Nd data suggests reworking of the Yilgarn craton margin during formation of the Albany-Fraser Orogen. Precambrian Research 187 (3), 223 – 247.

Kirkland, C. L., Spaggiari, C. V., Smithies, R. H., Wingate, M. T. D., 2014a. Cryptic progeny of craton margins: geochronology and isotope geology of the Albany-Fraser Orogen with implications for evolution of the Tropicana Zone. Albany-Fraser Orogen seismic and magnetotelluric (MT) workshop 2014: extended abstracts compiled by CV Spaggiari and IM Tyler, Geological Survey of Western Australia, Record 2014/6, 89–101.

Kirkland, C. L., Wingate, M. T. D., Spaggiari, C. V., 2012. 194784: metamonzogranite, Newman Rock; Geochronology Record 1026. Geological Survey of Western Australia, 4p.

Kirkland, C. L., Wingate, M. T. D., Spaggiari, C. V., 2014b. 194785: metatonalite, east of Boingaring Rocks; Geochronology Record 1161. Geological Survey of Western Australia, 4p.

Kirkland, C. L., Wingate, M. T. D., Spaggiari, C. V., Pawley, M., 2010. 194736: metasyenogranite, Bartlett Bluff; Geochronology Record 849. Geological Survey of Western Australia, 4p.

Maier, W., Smithies, R., Spaggiari, C., Barnes, S., Kirkland, C., Yang, S., Lahaye, Y., Kiddie, O., MacRae, C., 2016a. Petrogenesis and Ni–Cu sulphide potential of mafic–ultramafic rocks in the Mesoproterozoic Fraser Zone within the Albany–Fraser Orogen, Western Australia. Precambrian Research 281, 27 – 46.

Maier, W. D., Smithies, R. H., Spaggiari, C. V., Barnes, S. J., Kirkland, C. L., Kiddie, O., Roberts, M. P., 2016b. The evolution of mafic and ultramafic rocks of the Mesoproterozoic Fraser Zone, Albany-Fraser Orogen, and implications for the Ni-Cu sulphide potential of the region. Geological Survey of Western Australia, Record 2016/8, 49p.

Morrissey, L. J., Payne, J. L., Hand, M., Clark, C., Taylor, R., Kirkland, C. L., Kylander-Clark, A., 2017. Linking the Windmill Islands, east Antarctica and the

Albany–Fraser Orogen: insights from U–Pb zircon geochronology and Hf isotopes. Precambrian Research 293, 131–149.

Munro, M., Quentin de Gromard, R., Spaggiari, C., 02 2017. Structural evolution of the 'S-bend' region, East Albany–Fraser Orogen. p. 4.

Myers, J. S., 1995. Geology of the Esperance 1: 1,000,000 Sheet: Sheet SI 51. Geological Survey of Western Australia.

Nelson, D., Myers, J., Nutman, A., 1995. Chronology and evolution of the middle proterozoic albany-fraser orogen, western australia. Australian Journal of Earth Sciences 42 (5), 481–495.

Occhipinti, S., Doyle, M., Spaggiari, C., Korsch, R., Cant, G., Martin, K., Kirkland, C., Savage, J., Less, T., Bergin, L., et al., 2014. Preliminary interpretation of the deep seismic reflection line 12GA-T1: northeastern Albany-Fraser Orogen. In: Albany-Fraser Orogen seismic and magnetotelluric (MT) workshop 2014: extended abstracts (Preliminary edition). Geological Survey of Western Australia, pp. 44–59.

Occhipinti, S. A., Tyler, I., Spaggiari, C., Korsch, R., Kirkland, C. L., Smithies, R. H., Martin, K., Wingate, M., 2018. Tropicana translated: a foreland thrust system imbricate fan setting for c. 2520 ma orogenic gold mineralization at the northern margin of the Albany–Fraser Orogen, Western Australia. Geological Society, London, Special Publications 453 (1), 225–245.

Post, N., Hensen, B., Kinny, P., 1997. Two metamorphic episodes during a 1340–1180 Ma convergent tectonic event in the Windmill Islands, East Antarctica. The Antarctic Region: Geological Evolution and Processes. Terra Antarctica, Sienna 157, 161.

Quentin de Gromard, R., Spaggiari, C., Munro, M., Sapkota, J., De Paoli, M., 2017. SGTSG 2017 Albany-Fraser Orogen pre-conference field trip: Transect across an Archaean craton margin to a Proterozoic ophiolite. Geological Survey of Western Australia Record 2017/14, 100p.

Ripley, E., 1999. Systematics of sulphur and oxygen isotopes in mafic igneous rocks and related cu-ni-pge mineralization. Geological Association of Canada Short Course Notes 13, 133–158.

Scibiorski, E., Tohver, E., Jourdan, F., Kirkland, C. L., Spaggiari, C., 2016. Cooling and exhumation along the curved albany-fraser orogen, western australia. Lithosphere 8 (5), 551–563.

Smithies, R. H., Spaggiari, C. V., Kirkland, C. L., 2015. Building the crust of the Albany-Fraser Orogen: constraints from granite geochemistry. Geological Survey of Western Australia, Report 150, 49p.

Smithies, R. H., Spaggiari, C. V., Kirkland, C. L., Howard, H. M., Maier, W. D., 2013. Petrogenesis of gabbros of the Mesoproterozoic Fraser Zone: constraints on the tectonic evolution of the Albany-Fraser Orogen. Geological Survey of Western Australia, Record 2013/15, 29p.

Spaggiari, C., Kirkland, C., Smithies, R., Occhipinti, S., Wingate, M., 2014a. Geological framework of the albany–fraser orogen. In: Albany–Fraser Orogen seismic and magnetotelluric (MT) workshop 2014: extended abstracts compiled by CV Spaggiari and IM Tyler: Geological Survey of Western Australia, Record. Vol. 6. pp. 12–27.

Spaggiari, C., Smithies, R., 2015. Eucla basement stratigraphic drilling results release workshop: Extended abstracts. Geological Survey of Western Australia Perth.

Spaggiari, C. V., Bodorkos, S., Barquero-Molina, M., Tyler, I. M., Wingate, M. T. D., 2009. Interpreted bedrock geology of the South Yilgarn and central Albany-Fraser Orogen, Western Australia. Geological Survey of Western Australia, Record 2009/10, 84p.

Spaggiari, C. V., Kirkland, C. L., Smithies, R. H., Wingate, M. T. D., 2011. The geology of the East Albany-Fraser Orogen - A Field Guide. Geological Survey of Western Australia, Record 2009/10, 84.

Spaggiari, C. V., Kirkland, C. L., Smithies, R. H., Wingate, M. T. D., 2012. What lies beneath - interpreting the Eucla basement. GSWA extended abstracts, 24–26.

Spaggiari, C. V., Kirkland, C. L., Smithies, R. H., Wingate, M. T. D., 2014b. Tectonic links between Proterozoic sedimentary cycles, basin formation and magmatism in the Albany-Fraser Orogen. Geological Survey of Western Australia, Report 133, 63p.

Spaggiari, C. V., Kirkland, C. L., Smithies, R. H., Wingate, M. T. D., Belousova, E. A., 2015. Transformation of an Archean craton margin during Proterozoic basin formation and magmatism: The Albany-Fraser Orogen, Western Australia. Precambrian Research 266, 440 – 466.

Venables, T., 2014. Enterprise Metals Limited, Fraser Range Project, Exploration Licence 63/1281 Final Drilling Report, Co-funded Drilling Agreement DAG 2014/00384566, 25th July, 2014. WAMEX report A103177.

Walker, A., Evans, K., Kirkland, C., Martin, L., Kiddie, O., Spaggiari, C., 2019. Tracking mineralisation with in situ multiple sulphur isotopes: a case study from the Fraser Zone, Western Australia. Precambrian Research 332.

Zhang, S.-H., Zhao, Y., Liu, X.-C., Liu, Y.-S., Hou, K.-J., Li, C.-F., Ye, H., 2012. U–Pb geochronology and geochemistry of the bedrocks and moraine sediments from the Windmill islands: implications for Proterozoic evolution of East Antarctica. Precambrian Research 206, 52–71.

Chapter 3

Tracking mineralisation with in situ multiple sulphur isotopes: a case study from the Fraser Zone, Western Australia

3.1 Abstract

Sulphur isotopes have become a widely deployed tool to address the sources of fluids in ore systems, given the widespread interaction of H_2S, HS^- and S_2^- with metals. However, the sensitivity of sulphur isotopes to magma source composition relative to other radiogenic isotopes and the nature of processes differentially affecting isotopic systems have not been extensively explored in magmatic mineral systems. In this work we present a case study of sulphide bearing magmas within the Albany-Fraser Orogen in Western Australia that seeks to evaluate the sensitivity of sulphur isotopes to track magma source composition in space and time. New δ^{34}S data from mineralised NRM, Plato and Octagonal localities of the Fraser Zone indicate variable degrees of assimilation of local sediments of the Snowys Dam Formation. Despite an Archean heritage in the Fraser Zone magmas being indicated by radiogenic isotopes, sparse xenocrystic zircon, and whole rock geochemical modelling, Δ^{33}S data from these localities reveal no evidence for Archean sulphur; implying decoupling of the sulphur component from other geochemical and isotopic systems. This is consistent with a mechanism by which Archean sulphur was removed from detrital material incorporated in the Fraser Zone. We conclude that sulphides were stripped from sediments during uplift, erosion and transport to the Fraser Zone, with these Archean-sulphur depleted sediments then assimilated by the Fraser Zone parental magmas. Our results indicate a coupling between variable assimilation of external sulphur by Fraser Zone magmas and the mineralisa-

tion present at the prospects studied. However assimilated sulphur cannot account for all of the sulphur within mineralised samples, indicating the involvement of additional processes such as tenor upgrading.

3.2 Introduction

The Albany-Fraser Orogen (AFO) is a Neoarchean to Mesoproterozoic orogenic belt extending for 1200 km along the southern and south-eastern margins of the Yilgarn Craton in Western Australia. At present there is very little published research on magmatic sulphide mineralisation in the AFO (Maier et al., 2016b,a); however the discoveries of the Tropicana Au deposit in 2005 (Doyle et al., 2015) and the Nova-Bollinger Ni-Cu deposit in 2012 (Bennett et al., 2014) suggest that the region is prospective, namely the Fraser Zone with respect to Ni. While the bulk of the metals in a magmatic sulphide deposit are of mantle origin, the majority of the sulphur required to trigger the generation of metal-rich sulphide melts is typically externally derived (Naldrett, 2004). This being the case, and with the existence of multiple terrestrial sulphur reservoirs characterised by distinct sulphur isotopic signatures, the interrogation of magmatic sulphide material via *in-situ* isotopic techniques including Secondary Ion Mass Spectrometry (SIMS) can provide critical information on the origin of sulphur in deposits, as well as insight into processes key to ore formation. With the increased interest in the magmatic sulphide potential of the Fraser Zone and at present only one study on the region that includes sulphur isotope data (Maier et al., 2016b,a), this study aims to expand the currently available sulphur isotopic data set for the Fraser Zone and place detailed *in-situ* analysis within the context of multiple prospects in the region.

3.3 Multiple sulphur isotopes and applications to magmatic sulphide deposits

It is generally accepted that the genesis of a magmatic sulphide deposit involves the emplacement of a metal-bearing (e.g. Fe, Ni, Cu, PGE) melt within the crust, most typically a mantle-derived magma. However the precipitation of an immiscible metal-bearing sulphide phase within the melt is required to concentrate the dispersed metal content within the melt, a process that itself requires sulphide saturation within a magma (Ripley and Li, 2013). Estimates for sulphur content within the upper mantle are low (approx. 400 ppm; von Gehlen, 1992). As such, the mafic mantle-derived melts involved in magmatic sulphide deposits are initially sulphide undersaturated and incapable of developing any significant quantity of sulphide liquid; the increasing solubility of sulphide in a mafic melt with decreasing pressure exacerbates this issue further (Mavrogenes and O'Neill, 1999). Aside from fractional crystallisation or magma mixing, the only other means by which sulphide saturation may be attained in a magma involves the assimilation of external sulphur-bearing country rocks to increase magmatic sulphur content (Naldrett, 2004; Ripley and Li, 2013). The addition of SiO_2 from assimilated country rock further decreases sulphide solubility and promotes formation of an immiscible sulphide phase (Irvine, 1976) in which metals may be concentrated and from which an economic deposit may develop.

Geological processes fractionate sulphur isotopes based on mass differences between isotopes; this is termed mass-dependent fractionation, with deviations from a reference ratio (0.0‰; Vienna Canyon Diablo Troilite) expressed in delta (δ) notation as parts per thousand or per mil (‰) (Seal, 2006). Studies on variations in sulphur isotope geochemistry within magmatic sulphide deposits worldwide suggest that assimilated sulphur bearing material, and by extension the magmatic sulphides themselves, can be characterised by their sulphur isotope ratios, which can indicate not only where assimilated sulphur originated from but additionally the quantity of external sulphur involved. δ^{34}S values may be used to distinguish between "modern" (post-Archean) sulphur reservoirs; primitive mantle-derived magmas initially possess a δ^{34}S value somewhere between -2‰ to 2‰ (Ripley and Li, 2003) (Fig. 3.1). Subsequent emplacement within the crust and coincident assimilation of crustal sulphur typically drives the isotopic signature of the melt towards a value somewhere between that of the mantle and that of the crustal sulphur.

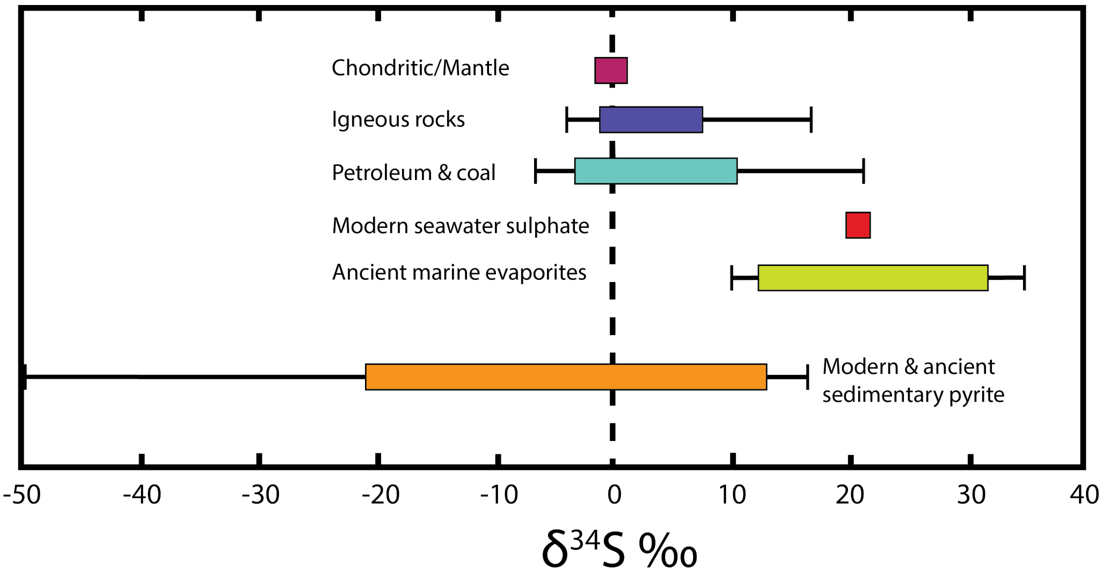

Figure 3.1: Ranges of δ^{34}S values for various geologic reservoirs (modified after Seal, 2006)

The involvement of Archean sulphur reduces the utility of δ^{34}S somewhat, as many Archean sedimentary sulphides/sulphates older than 2.45 Ga can possess δ^{34}S signatures that are similar to the mantle range (Bekker et al., 2009). In such cases, it is possible to identify Archean sulphur that has undergone mass-independent fractionation (MIF) via Δ^{33}S values; a measure of the deviation of a measured sulphur isotope ratio from a reference fractionation array (Penniston-Dorland et al., 2012). Non-zero Δ^{33}S values characterise MIF that occurred in the oxygen-free Archean atmosphere, with ultraviolent radiation induced photochemical processes leading to variable Δ^{33}S values within sulphide and sulphate minerals ranging from -2.5–8.1‰ (Farquhar et al., 2000; Ono et al., 2003; Rumble, 2005). Oxygenation of the atmosphere at c. 2.4 Ga is thought to have at least contributed to the sudden shift in Δ^{33}S from non-zero to near-zero values typically accepted to be within 0 ± 2‰ (Farquhar and Wing, 2003). Some exceptions to this remain, with Δ^{33}S values between -0.5‰ to 0.7‰ identified within modern volcanic sulphates (Savarino et al., 2003).

3.4 Regional Geology

The AFO is a component of the West Australian Craton (Fig. 3.2), extending approximately along the southern and south-eastern margins of the Yilgarn Craton. The orogen consists primarily of Palaeoproterozoic and Mesoproterozoic rocks (Spaggiari et al., 2015), covered in places by up to 150 m of regolith (Gonzalez-Alvarez et al., 2014). To the east the AFO extends to the Rodona Shear Zone, with much of the geology covered by the Eucla and Bight Basins (Spaggiari et al., 2012). The orogen has an extensive and complicated tectonic history, consisting of a sequence of metamorphic and igneous rocks derived from reworking of existing Archean crust with varying degrees of new mantle input (Kirkland et al., 2011). The AFO is divided into two main lithotectonic domains; the Northern Foreland and the Kepa Kurl Booya Province. The Northern Foreland lies immediately adjacent to the Yilgarn Craton, and is dominated by 3000–2600 Ma granites and gneisses (Spaggiari et al., 2011). The Kepa Kurl Booya Province is the major component of the orogen and includes reworked Archean crystalline rocks produced during the Proterozoic through several tectonothermal events (Spaggiari et al., 2014a, 2015; Kirkland et al., 2016). The Kepa Kurl Booya Province is subdivided into the Archean-Palaeoproterozoic Tropicana, Biranup and Nornalup Zones, and the Mesoproterozoic Fraser Zone.

The Albany-Fraser Orogeny is the principal tectonic episode that affected the Fraser Zone. The orogeny is subdivided into Stages I and II; occurring between c. 1330–1260 and 1225–1140 Ma, respectively (Clark et al., 2000; Spaggiari et al., 2014a). Stage I is attributed to collision and accretion of the Madura Province's Loongana magmatic arc onto the Nornalup Zone (Quentin de Gromard et al., 2017), while Stage II is interpreted to represent prolonged intracontinental reworking (Spaggiari et al., 2009) and voluminous magmatism, likely leading to cratonisation between the West Australian and South Australian Cratons (Kirkland et al., 2017). The orogen incorporates at least two major basin systems; the Barren (c. 1815–1600 Ma) and Arid Basins (c. 1600–1305 Ma) (Spaggiari et al., 2015).

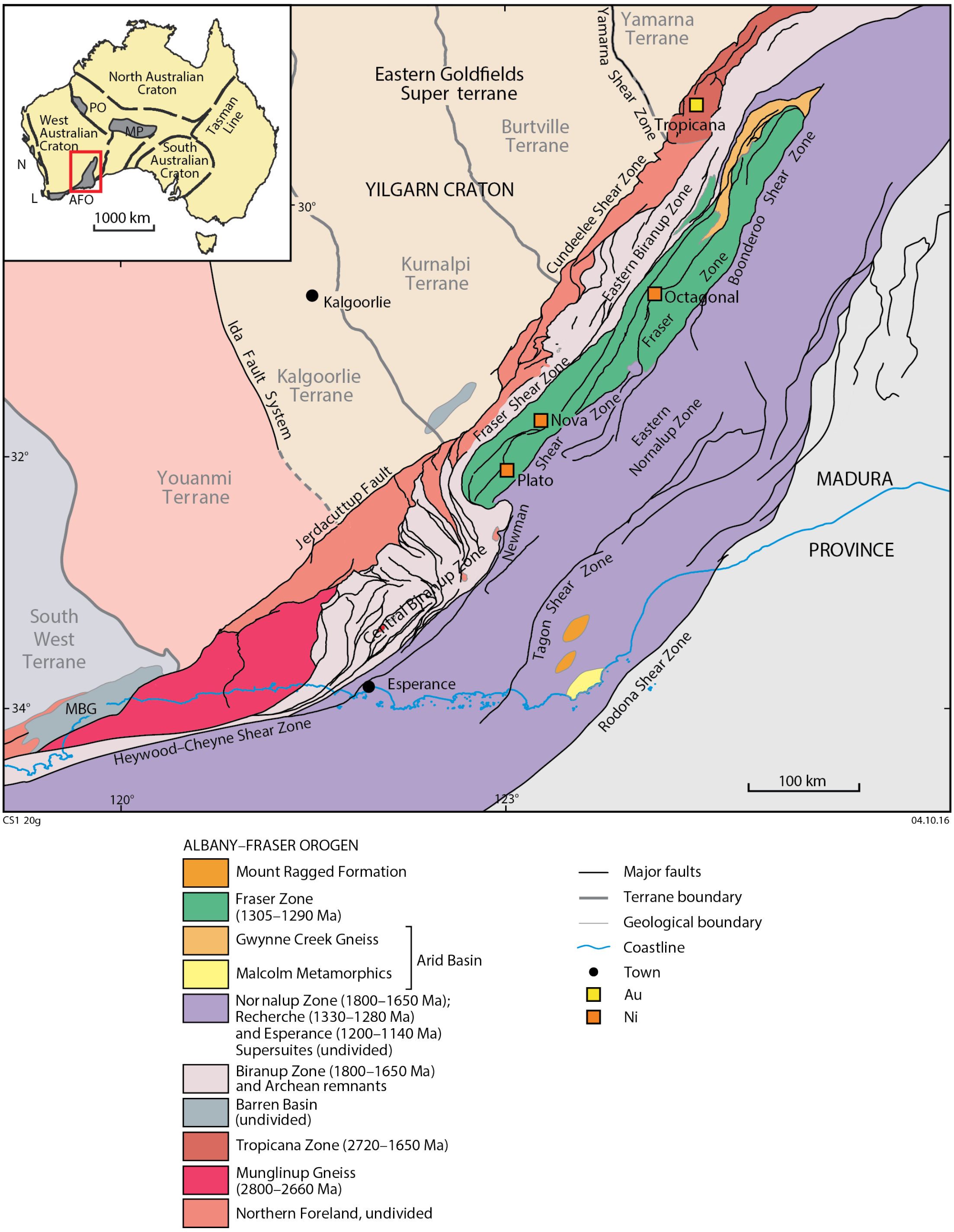

Figure 3.2: Simplified geological overview of the AFO (modified after Spaggiari et al., 2011)

3.4.1 The Fraser Zone

The Fraser Zone is an approximately 425 km long by 50 km wide, north-easterly trending belt of metagabbroic rocks intercalated with lesser granitic gneisses and paragneiss (Smithies et al., 2013; Maier et al., 2016b). It is structurally bound to the northwest by the Fraser Shear Zone and to the southeast by the Newman and Boonderoo Shear Zones, and is interpreted to have a v-shaped geometry to a maximum depth of approx. 15 km (Spaggiari et al., 2014b; Brisbout, 2015). While largely under cover with only the southern region of the zone exposed, the Fraser Zone contains significant volumes of mafic material, and possesses a strong gravity signature as a result (Maier et al., 2016b). The geology of the Fraser Zone is dominated by the 1305–1295 Ma Fraser Range Metamorphics, comprising amphibolite-granulite grade metasedimentary rocks of the Snowys Dam Formation intruded by suites of gabbroic and granitic rocks. These metasedimentary rocks are a component of the Mesoproterozoic Arid basin with a maximum depositional age of c. 1332 Ma (Spaggiari et al., 2015). The Snowys Dam Formation consists of calc-silicate and iron-rich amphibolite to granulite grade pelitic, semipelitic and psammitic rocks (Spaggiari et al., 2015). Mineral equilibria modelling for these metasediments constrains the metamorphic conditions to 800–900°C and 6.5–8.5 kbar, implying a depth of 25–30 km at peak metamorphism (Clark et al., 2014). The Fraser Zone is currently interpreted to represent a mid to deep crustal hot zone, formed by upwelling of mantle-derived gabbroic magmas into quartzofeldspathic country rock (Smithies et al., 2013; Maier et al., 2016b).

Coeval mafic and felsic magmatism was initiated between c. 1310–1283 Ma (Spaggiari et al., 2015), with zircon U-Pb geochronology indicating igneous crystallisation of mafic rocks in the Fraser Zone between 1305–1290 Ma (De Waele and Pisarevsky, 2008; Kirkland et al., 2011; Clark et al., 2014); shortly after deposition of the Snowys Dam Formation. This magmatism is part of the extensive 1330 to 1280 Ma Recherche Supersuite, itself a product of Stage I of the Albany-Fraser Orogeny (Smithies et al., 2015). High-grade metamorphism in the Fraser Zone was coeval with magmatism between 1305–1290 Ma; the short interval between magmatism and metamorphism is consistent with the thermal input from mafic magmatism driving granulite-facies metamorphism (Clark et al., 2014).

In contrast to Stage I, evidence for Stage II of the Albany-Fraser Orogeny in the Fraser Zone is very limited in the zircon record. However, recent research on the behaviour of metamorphic titanite in the Fraser Zone demonstrates that some small titanite grains from the Fraser Shear Zone record Stage II overprinting through remobilisation of radiogenic Pb, with mean reset ages of 1205±16 Ma (Kirkland et al., 2016). This is consistent with extrusion of the zone to shallower crustal levels prior to Stage II, with geological conditions being less conducive to zircon growth in the upper crust.

While c. 1300 Ma zircon ages are prevalent within the Fraser Zone, there are a number of zircon core analyses within the igneous and sedimentary zircon populations that record older ages (Fig. 3.3). Such inherited ages may be important in tracking the source components of these rocks. Inherited zircon in magmatic rocks include a single zircon extracted from the Symons Hill syenogranite with an age of 1770±13 Ma (Kirkland et al., 2010a), as well as inherited zircon cores from a Recherche Supersuite granite in the Fraser Zone dated at 1701–1604 Ma (Kirkland et al., 2012). Although sparse, these inherited components indicate the incorporation of material from magmatic rocks that are widespread throughout the adjacent Biranup and Nornalup Zones (Kirkland et al., 2011; Spaggiari et al., 2014a). The presence of Palaeoproterozoic zircons within intrusive components of the Fraser Range Metamorphics would suggest the emplacement of the Fraser Zone through a basement of comparable age.

Igneous geology of the Fraser Zone

The igneous geology of the Fraser Zone consists predominantly of metagabbroic rocks, with lesser ultramafic and granitic rocks (Smithies et al., 2015; Maier et al., 2016b). The granite can be broadly divided into two groups. Melting of local Arid Basin metasedimentary rocks formed what is typically peraluminous syenogranite, forming part of the Southern Hills Suite (Smithies et al., 2014, 2015; Maier et al., 2016b). The second group comprises metaluminous granite of the Gora Hills Suite, relatively uncommon within the Fraser Zone and limited to granodioritic compositions (Smithies et al., 2015; Maier et al., 2016b). These are considered to be the products of variable mixing between mantle-derived melts similar to parental melts of the Fraser gabbro, and more felsic partial melts of crust formed during Palaeoproterozoic events (Kirkland et al., 2014; Smithies et al., 2014, 2015; Maier et al., 2016b). The Fraser Zone metagabbro occurs as sheets that range in thickness from centimetres to several hundred metres. The prevalence of these sheets varies widely, from volumetrically dominant to smaller proportions of the stratigraphy occurring as sills within metasedimentary rocks (Smithies et al., 2013). Fraser Zone metagabbro is classified as either “main gabbro”: defined as gabbro showing no interaction with contemporaneous granite; or “hybrid gabbro”: gabbro that has interacted or mingled with felsic material during intrusion (Smithies et al., 2013; Maier et al., 2016b). Hybrid gabbro is generally distinguished from main gabbro geochemically by elevated SiO_2 concentrations and lower Mg #, and can be further subdivided into “Group 1” and “Group 2” hybrid gabbro; a division best seen in La and Th contents (Smithies et al., 2013).

Petrogenesis of Fraser Zone gabbro

The Fraser Zone is in fault contact with the Biranup Zone (Fig. 3.2), and was emplaced through a basement of Biranup and Nornalup Zone age (c. 1815–1625 Ma) (Kirkland

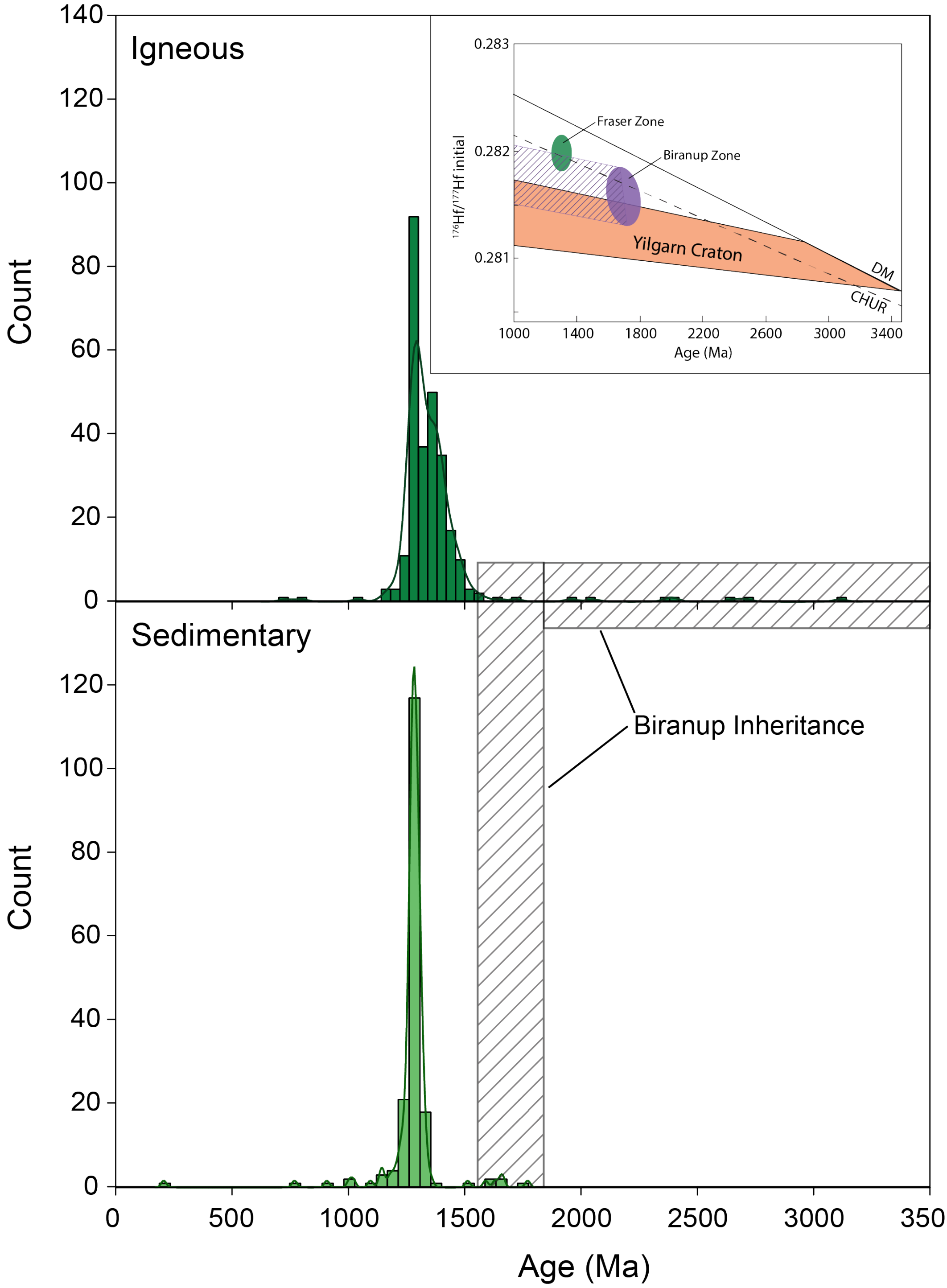

Figure 3.3: Histograms (with Kernel Distribution Estimation) illustrating U-Pb age distributions of zircons dated from metamorphosed igneous and sedimentary host rocks in the Fraser Zone. Hatched areas highlight those zircon ages considered to be of Biranup provenance or older. Inset illustrates Lu-Hf systematics of the Fraser Zone. All data extracted from Geoview.

et al., 2016; Spaggiari et al., 2014a). It was previously argued that the Fraser Zone was exotic to the AFO (Condie and Myers, 1999); primitive mantle-normalised trace elements patterns in gabbro were thought to be typical of subduction-related magmatism hence the zone was considered to comprise accreted fragments of oceanic arcs (Condie and Myers, 1999). However these patterns have since been shown to be well-explained by crustal underplating, with associated assimilation of small quantities (<10%) of crustal material by a depleted mantle sourced melt (Smithies et al., 2013). In that work the assimilated material was modelled to have been a combination of Archean granite and Munglinup Gneiss, implying an extension of the Yilgarn Craton beneath the Fraser Zone (Smithies et al., 2013). The Biranup Zone comprises reworked Archean lithologies modified by Proterozoic juvenile magma (Smithies et al., 2013). This finding is consistent with results from inherited zircons, which also indicate the presence of a component analogous to the Biranup Zone within the source of the Fraser Zone. Minor (<10%) contamination with Biranup basement material prior to emplacement in upper crustal staging chambers was likely the last step in the genesis of the Fraser Zone main gabbro before final emplacement, while the hybrid gabbro further mingled with felsic material during emplacement (Maier et al., 2016b).

Further detail on sources for the Fraser Zone is provided by Lu-Hf isotopic data from two Fraser Zone granitic samples that imply reworking of a Hf-bearing component that is isotopically comparable to the Biranup Zone, and a Biranup like source modified with additional juvenile input (Kirkland et al., 2016). The Lu-Hf character of the Biranup Zone itself extends over a range of values that include evolved Yilgarn-like values, as well as more juvenile values. Moreover, there appears to be a temporal trend to these values, interpreted to represent an older, Archean, more evolved character that was progressively diluted by the addition of more depleted juvenile input through younger stages of magmatism. A number of magmatic zircon analyses from the Fraser Zone provide Lu-Hf isotopic data that are consistent with the reworking of material with a crustal residence age of 2.0–2.5 Ga (Kirkland et al., 2011, 2014). It could be that this signature is the result of reworking of Biranup Zone material, which itself comprises a reworked Yilgarn source. Such a scenario would be compatible with the extensive magmatic reworking of the Biranup Zone occurring at c. 1300 Ma, during the emplacement of the Fraser Zone. In short, the Fraser Zone is not exotic to the AFO; Lu-Hf isotopic evidence is consistent with a reworked Biranup Zone component to the Fraser Zone, and in turn, the Biranup Zone shows clear links to the Yilgarn Craton through geochronological and isotopic data (Kirkland et al., 2011).

3.4.2 Sedimentary Basins in the AFO and their relevance to the Fraser Zone

At least two extensive metasedimentary packages are preserved in the AFO, representing changes in geodynamic setting and sedimentation through time; the Barren (1815–1600 Ma) and Arid (1600–1305 Ma) Basins.

Barren Basin

The Barren Basin overlies the Yilgarn Craton, Northern Foreland, Biranup and Nornalup Zones, and consists of Palaeoproterozoic metasedimentary rocks. It comprises sandstones, siltstones, mudstones, conglomerates and rare carbonates metamorphosed to amphibolite and granulite facies (Spaggiari et al., 2015). Basin analysis and geochronological data indicates the Barren Basin was quite extensive, implying a coverage of at least 1000 km along the southern and southeastern margins of the Yilgarn Craton (Spaggiari et al., 2015).

Three primary phases of deposition are apparent, each closely coupled to preceding magmatic events. The first and second occurred at c. 1800 Ma (Salmon Gums Event) and 1693 Ma (Zanthus Event) respectively, followed by a third event at c. 1710–1650 Ma, coincident with the latter stages of the Biranup Orogeny; the implication being a link between magmatism, uplift and erosion and the deposition of large quantities of detrital material (Spaggiari et al., 2014a, 2015).

In terms of geodynamic evolution, extension of the southern and southeastern Yilgarn Craton was ongoing by 1800 Ma, creating a source of detritus likely from a developing horst and graben architecture that exposed sections of basement geology (Spaggiari et al., 2015). The onset of magmatism at c. 1800 Ma was most likely triggered by crustal extension and the associated increased heatflow and partial melting (Spaggiari et al., 2015). Continued magmatism and thermal weakening of the crust potentially accelerated the rate of extension, and consequently the rate of expansion of the Barren Basin (Spaggiari et al., 2015). A shift in tectonic regime occurred at c. 1680 Ma during the compressional Zanthus Event, interpreted to represent potential basin inversion (Spaggiari et al., 2015). This, in conjunction with the cessation of magmatism at 1627 Ma (Kirkland et al., 2010b) likely indicates the end of basin formation tied to thermal subsidence following the end of the Biranup Orogeny. In summary, an overall extensional regime is proposed for the formation of the Barren Basin.

3.4.3 Arid Basin

The Arid Basin is similarly extensive relative to the Barren Basin, ranging from Gwynne Creek in the northeast of the orogen to Albany in the west (Spaggiari et al., 2015). It includes the Snowys Dam Formation, assumed to be the primary source of external sulphur involved in the nickel sulphide mineralisation present within the Fraser Zone (Maier et al., 2016b). In comparison to the Barren Basin, metasedimentary rocks of the Arid Basin are more variable and include metamorphosed mudstone, sandstone, calcareous rocks, iron-rich strata and probable volcanic/volcaniclastic lithologies. The first period of deposition was transitional from the Barren Basin and has been associated with the development of a marginal ocean basin from c. 1600 Ma, lasting until c. 1455 Ma; sediments were derived from the Biranup and Nornalup Zones, but also from distal exotic sources based on zircon U-Pb and Lu-Hf isotopic signatures (Spaggiari et al., 2015). A shift in tectonic regime to a convergent setting at c.1455 Ma was regarded as coincident with outboard east-dipping subduction (Spaggiari et al., 2015). This shift in tectonic forces is suggested to have led to the deposition of the Malcolm Metamorphics in the Arid Basin within a fore-arc or accretionary prism (Adams, 2012); intercalated volcanic deposits within this unit also suggest the development of the Loongana oceanic magmatic arc (Spaggiari et al., 2015). Located to the east of the AFO within the Madura Province, the arc formed at c. 1410 Ma and constitutes a source of detrital material for the upper, or second phase of Arid Basin development (Spaggiari et al., 2015). This phase of deposition continued until c. 1332 Ma after the Loongana arc had collided and accreted onto the passive margin of the ocean basin, triggering the onset of Stage I of the Albany-Fraser Orogeny (Spaggiari et al., 2015; Smithies et al., 2015). The magmatic arc is the only known source of c. 1450 and 1425–1375 Ma detrital zircons recognised in the Malcolm Metamorphics and the Snowys Dam Formation, respectively (Spaggiari et al., 2015). Deposition of the Arid Basin ceased by c. 1305 Ma, indicated by intrusion of magmas of the Recherche Supersuite and Fraser Zone.

3.5 Sample material

At present much of the Fraser Zone is considered prospective for nickel sulphide mineralisation, with a number of prospects either having been or currently being explored. Sample material for this study is derived from or in proximity to three localities in the Fraser Zone; Plato: a former prospect showing some limited mineralisation; Octagonal: a current prospect under investigation by the Creasy Group including strongly mineralised lithologies in contrast to Plato; and NRM: a locality interpreted to be representative of the mineralisation seen at Nova-Bollinger, the most significant known instance of magmatic sulphide mineralisation in the AFO (Fig. 3.2). These localities were selected in order to identify relationships between the degree of magmatic sulphide mineralisation hosted and sulphur isotopic signatures associated with mineralisation.

Thirteen samples of quarter drillcore from the Plato prospect were provided by the GSWA from Exploration Incentive Scheme (EIS) co-funded drilling, and 46 samples from Octagonal were donated by Creasy Group. Two samples of material (NRM1601/NRM1602) were acquired from the NRM locality. Petrography and mineral compositions of each sample were assessed to aid selection of material to characterise sulphur isotope signatures from magmatic sulphide mineralisation at different localities, and contrast this with nearby sulphur-bearing metasediments.

3.6 Methods

3.6.1 Thin section petrography

Polished thin sections from all samples taken for this study were studied under optical microscopy via transmitted and reflected light to identify compositions, mineral assemblages, textural relations and features of interest for further study.

3.6.2 Tescan Integrated Mineral Analysis (TIMA)

Three Octagonal samples and both NRM samples were identified as including compositions and textures indicative of key syn- and post-mineralisation processes and were selected for *in-situ* isotope analysis. These samples were analysed further via TIMA (Table 4.7.1). This technique utilises an automated Tescan Mira3 TIMA Scanning Electron Microscope to provide high resolution mineral modes and maps of sample surfaces. For samples with mineral assemblages representing more complex histories of mineralisation and subsequent remobilisation/alteration (e.g. samples GSWA 219069, 219070) TIMA images greatly aided textural interpretation, as well as identification of locations on samples optimal for *in-situ* sulphur isotope analysis.

3.6.3 Secondary Ion Mass Spectrometry (SIMS)

In-situ sulphur isotopic analysis was selected as a method over whole rock sulphur analysis, with the former preserving the textural context of isotopic information from the grains analysed. *In-situ* triple sulphur isotope (^{32}S, ^{33}S, ^{34}S) ratios were measured on a CAMECA IMS1280 ion microprobe at the Centre for Microscopy Characterisation and Analysis, within the University of Western Australia. SIMS measurements were undertaken on material from a total of 11 samples; 3 from Plato, 6 from Octagonal, and 2 NRM samples (location information for these samples may be found in Appendix 3.A). Sample pucks were made by taking 2 mm discs cut from thin sections using a drill with diamond coring bits, and embedding them within 25 mm diameter epoxy mounts. Mounts were prepared using one of two methods to include reference materials:

1. Standard materials were placed in the centre of each mount with the discs of sample material arranged radially; all sample and standard material placed no further than 6–7 mm from the centre of the mount.

2. Epoxy blocks of samples and standard materials were prepared separately, trimmed and then mounted together in a sample holder; ensuring surfaces of both blocks

were level.

Mounted samples were photographed using reflected light microscopy, providing images to aid with selection of spots for analysis. After careful cleaning in ethanol, samples were given an approx. 30 nm gold coat to prevent charging during analysis.

The sample surfaces were sputtered over a 15 x 15 µm area with a 10 kV, Gaussian Cs^+ beam with an intensity of 3.0–3.5 nA and total impact energy of 20 keV. Secondary ions were admitted in the double focusing mass spectrometer within a 60 µm entrance slit and focused in the center of a 4000 µm field aperture (x130 magnification). Secondary ions were then energy filtered using a 30 eV band pass with a 5 eV gap toward the high-energy side. All S isotopes were collected simultaneously in Faraday cup detectors fitted with 10^{10} Ω (L'2, ^{32}S) and 10^{11} Ω (L1, ^{33}S and H1, ^{34}S) resistors, operating at a mass resolution of approx. 4300. The magnetic field was regulated using NMR control. Sample surfaces were bombarded with low energy electrons from a normal incidence electron flood gun for charge compensation. Each analysis included 45 seconds of pre-sputtering over a 20 x 20 µm area and the automatic centering of the secondary ions in the field aperture, contrast aperture and entrance slit. The remainder of each analysis then consisted of a 24 second acquisition cycle. The analytical session was monitored in terms of drift using two bracketing standards every 5 sample analyses. Instrumental mass fractionation (IMF) was corrected using the matrix matched reference materials for pentlandite (VMSO), pyrrhotite (Alexo), chalcopyrite (Nifty-b) and pyrite (Sierra) (reference values can be found in LaFlamme et al. (2016). IMF correction follows the procedure described in Kita et al. (2009).

3.7 Results

3.7.1 Sample petrography

Sample GSWA 219048 (Octagonal metasediment)

Sample 219048 is a paragneiss primarily comprised of quartz (approx. 57.6%), garnet (approx. 22.7%), potassium (approx. 11%) and plagioclase feldspar (approx. 1.7%). The sample presents a strong gneissic fabric; a sub-mm grainsize groundmass of quartz and feldspar wraps around subhedral garnet porpyroblasts up to c. 4 mm in diameter (Fig. 3.4A). Apatite, zircon and monazite grains up to approx. 0.5 mm in diameter are present within the groundmass. Many of the garnet porphyroblasts have developed “tails” and more elongate morphologies attributed to deformation and metamorphism. Small (sub-mm) inclusions are present within garnets, most frequently of biotite, quartz and pyrrhotite. Sulphides in this sample (approx. 1.7%) consist of pyrrhotite and minor chalcopyrite which are almost always located in contact with garnet, or as tails within garnet strain shadows. Calcite-infilled micron-scale fractures cross-cut the groundmass, porphyroblasts and sulphides, suggesting some post-deformation fluid flow.

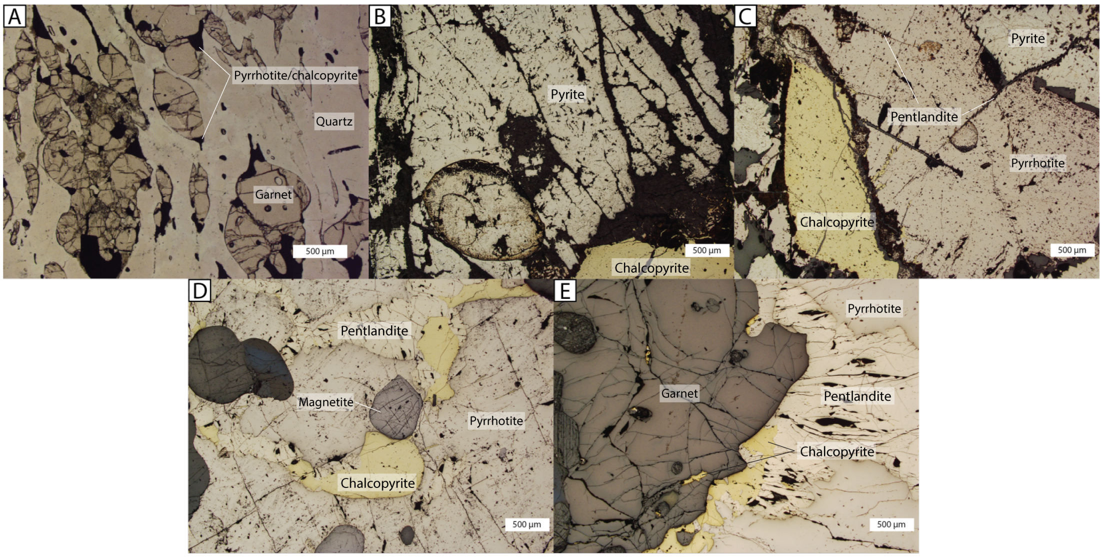

Figure 3.4: Photomicrographs illustrating primary textures and features of samples GSWA 219048 (A), GSWA 219069 (B), GSWA 219070 (C), NRM1601 (D) and NRM1602 (E).

Sample GSWA 219069 (Octagonal unaltered sulphide breccia)

219069 has been classified as a sulphide breccia. A primary assemblage of pyrite (approx. 54.3%), pentlandite (approx. 5.3%) and chalcopyrite (approx. 2.4%) is permeated by an extensive fracture network infilled with serpentine and minor magnetite (Fig. 3.4B). Clusters of micron-scale acicular carbon are present within these infilled fractures (Fig. 3.4B), indicating infiltration of carbon-rich fluids. Pentlandite and chalcopyrite have been remobilised predominantly into narrow bands or domains across the sample.

Sample GSWA 219070 (Octagonal altered sulphide breccia)

219070 is also classified as a sulphide breccia. Dominant sulphides in the assemblage are pyrrhotite (approx. 31.6%) and pyrite (approx. 22.3%), with more minor pentlandite (approx. 6.6%) and chalcopyrite (approx. 5.1%). Numerous fractures permeate the sample material (Fig. 3.4C). Where these fractures intersect pyrrhotite, pentlandite is frequently found as a halo along fracture paths; formation of pentlandite may have been tied to fluid movement along fractures, or the triggering of pentlandite exsolution from metastable Ni-rich pyrrhotite (Fig. 3.4C). Instances of pentlandite outside of fracture networks are likely remobilised, being associated with remobilised chalcopyrite. Fractures within pyrite host magnetite infill; this texture is interpreted to record that fluids within the fractures interacted with surrounding sulphide material (pyrite in this case) to produce magnetite.

Sample NRM1601 (Massive sulphide)

A sample of massive sulphide material interpreted to be representative of mineralised material at Nova, the mineral assemblage in 1601 consists almost entirely of sulphide minerals (approx. 90%), predominantly pyrrhotite (approx. 74.5%), pentlandite (approx. 15.5%) and chalcopyrite (approx. 3.1%); with very minor magnetite and plagioclase. This sample lacks a dominant fabric or the fracture networks seen in the Octagonal samples, and likely represents an accumulation of sulphides in a trap or magmatic body (Fig. 3.4D).

Sample NRM1602 (Garnet massive sulphide)

Similar to 1601, 1602 is a massive sulphide with a significant garnet component (approx. 18.7%) (Fig. 3.4E). Again, this material is likely to be representative of a sulphide accumulation within a trap or emplaced magma; the presence of garnet may indicate a proximity to garnet-bearing metasediments and assimilation of those sediments, or heterogenous distribution of partially assimilated material through the host melt.

3.7.2 TIMA results

Primary Phases	NRM1602	NRM1601	219070	219069	219048
Lithology	Garnet massive sulphide	Massive sulphide	Altered sulphide breccia	Unaltered sulphide breccia	Metasediment
Quartz	2.19	0.73	1.96	2.31	57.62
Garnet	18.74	0.28	0.10	0.00	22.73
Pyroxene	0.08	0.04	0.04	27.38	0.05
Plagioclase feldspar	4.19	1.46	10.69	0.32	1.74
Potassium feldspar	0.77	0.09	0.70	0.64	11.04
Amphibole	2.13	0.15	1.06	0.00	0.02
Magnetite	3.65	1.23	5.34	1.76	0.17
Pyrrhotite	46.80	74.54	31.63	0.40	1.68
Pentlandite	16.06	15.51	6.56	5.38	0.00
Chalcopyrite	1.34	3.08	5.11	2.39	0.03
Pyrite	0.07	0.11	22.34	54.31	0.00

Table 3.1: TIMA-derived volumetric mineral modes for the most abundant minerals within analysed samples

3.7.3 In-situ sulphur isotope measurements

δ^{34}S values

A total of 461 measurements of *in-situ* multiple sulphur isotope compositions were made from all 11 samples (Table 5.6.1). Material comprises magmatic breccias and metasediments from Octagonal, and Plato and NRM magmatic material hosting varying degrees of mineralisation. There is little variation in δ^{34}S values either within a grain, within grains of a mineral within a sample, or between the different sulphide minerals in all samples (Table 5.6.1). Annotated images of the mount material analysed can be found in Appendix 3.B.

Plato

Three samples of minimally mineralised magmatic material were selected from the Plato prospect; 216364, 216369 and 216372. Sample material from this prospect primarily comprises gabbro and norite. 90 spots on pyrrhotite, pentlandite, pyrite and chalcopyrite were analysed; the overall range of δ^{34}S Plato values lies between -0.87‰ to 3.11‰. Analysed spots returned δ^{34}S values in pyrrhotite between -0.09–2.17‰ (mean/median of 0.90/0.81‰), values in pentlandite between -0.87–2.33‰ (mean/median of 0.70/0.81‰), pyrite values between -0.85–0.54‰ (mean/median of -0.05/0.15‰) and chalcopyrite values between 1.15–3.11‰ (mean/median of 2.09/1.92‰). Mean and median values for all Plato analyses are 1.05‰ and 1.00‰ respectively, with a lack of significant outliers and a normal distribution of values. These overall mean and median values lie within the range for mantle sulphur.

NRM material

Two samples of NRM massive sulphide material were analysed (NRM1601, NRM1602). These are primarily composed of pyrrhotite, pentlandite and chalcopyrite, with variable quantities of garnet (Table 4.7.1). NRM1602 includes sulphides hosted within garnet. Analysed NRM pyrrhotite returned δ^{34}S values of 2.48–3.27‰ (with a mean/median of 2.83/2.79‰), pentlandite values of 1.55–3.19‰ (mean/median of 2.24/2.24 and chalcopyrite values of 1.37–2.45‰ (mean/median of 2.07/2.12‰). Overall, the NRM samples show δ^{34}S values between 1.37–3.27‰ with mean and median values of 2.35‰ and 2.30‰ respectively; slightly more positive than accepted values for pure mantle-derived sulphur. Again the range of values is normally distributed.

Octagonal

Five samples of variably mineralised magmatic material (GSWA 216419, 216420, 219069, 219070) and two samples of sulphide bearing metasediments (GSWA 216409, 219048) were selected for analysis from the Octagonal prospect. Analysis of both magmatic and

Locality	Sample	n	δ^{34}S	2σ	Mineral	n	δ^{34}S	2σ
Octagonal	216409	51	5.36	0.91	Po	45	5.39	0.94
					Cpt	6	5.09	0.41
	216419	31	3.62	0.46	Po	15	3.74	0.38
					Pn	4	3.28	0.42
					Cpt	12	3.58	0.27
	216420	61	4.31	0.72	Po	26	4.57	0.41
					Pn	20	3.97	0.41
					Cpt	15	4.31	0.68
	219048	41	7.07	0.59	Po	36	7.07	0.61
					Cpt	5	7.10	0.51
	219069	18	3.37	0.96	Cpt	18	3.37	0.96
	219070	48	3.98	1.18	Po	15	4.33	0.72
					Pn	5	3.41	1.18
					Pt	20	4.03	1.12
					Cpt	8	3.52	0.85
NRM	NRM1601	52	2.36	0.78	Po	15	2.87	0.51
					Pn	20	2.19	0.18
					Cpt	29	2.06	0.54
	NRM1602	69	2.34	0.83	Po	20	2.80	0.18
					Pn	20	2.29	0.75
					Cpt	29	2.06	0.54
Plato	216364	37	1.18	2.07	Po	19	0.80	1.41
					Pn	5	1.13	2.08
					Pt	3	-0.05	1.16
					Cpt	29	2.06	0.54
	216369	35	0.67	1.24	Po	15	0.60	0.55
					Pn	15	0.38	1.10
					Cpt	5	1.77	0.56
	216372	18	1.52	0.52	Po	11	1.48	0.52
					Pn	4	1.37	0.11
					Cpt	3	1.88	0.03

Table 3.2: Summary of average δ^{34}S values (‰) across all samples analysed from Plato, Octagonal and NRM material. Analyses from each sample are further subdivided by sulphide mineral

metasedimentary material produces a bimodal distribution of data.

δ^{34}S values from sulphides in the metasediments range between 4.44–7.88‰ with mean and median values of 6.12‰ and 5.85‰ respectively. Metasedimentary sulphides analysed include pyrrhotite and chalcopyrite. Analysis of Octagonal sedimentary pyrrhotite returned δ^{34}S values of 4.44–7.88‰ with mean/median values of 6.14/5.88‰, and a range of 4.68–7.40‰ in chalcopyrite, with a mean of 6.00‰ and median of 5.27‰.

Sample GSWA 216409 is from a metasedimentary rock and includes analyses of sulphide inclusions within garnet (Fig. 3.5). The analyses of these inclusions returned δ^{34}S values between 4.44–4.74‰ (mean/median of 4.55/4.53‰); these include some of the least positive analyses from the Octagonal metasedimentary sample suite, and distinctly less positive than the range of δ^{34}S values for 216409 as a whole (4.56–5.93, mean/median of 5.51/5.54‰).

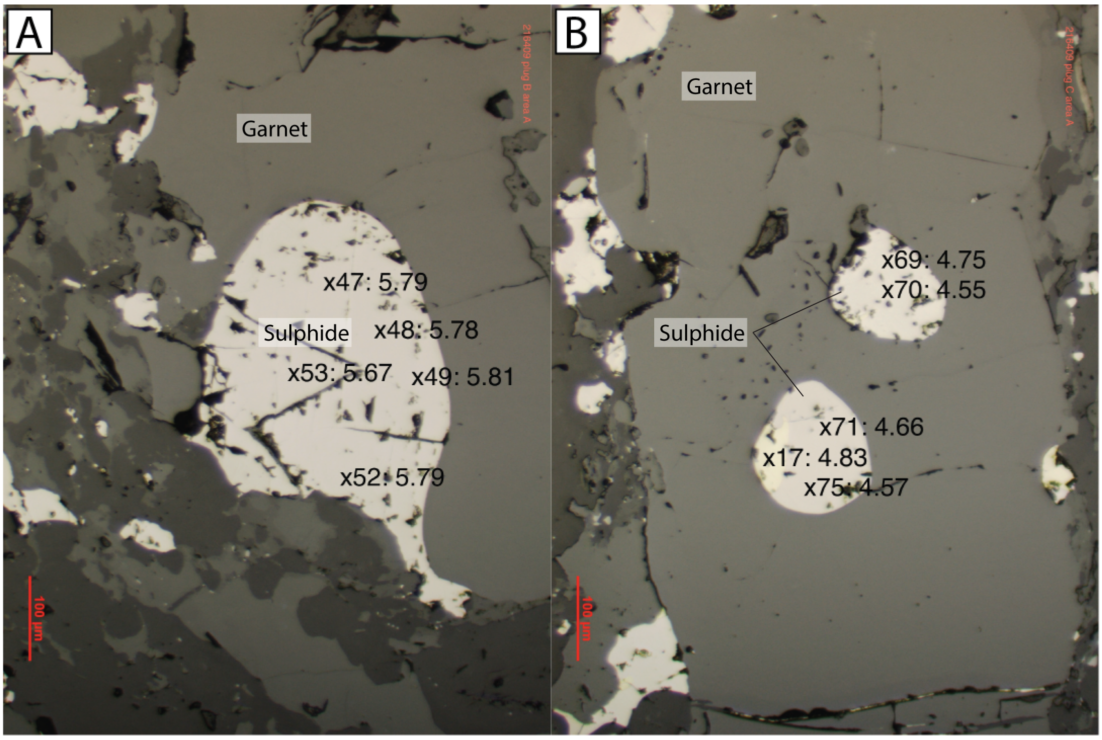

Figure 3.5: Reflected light photomicrographs of sulphides incompletely (A) and completely encompassed by garnet (B) within Octagonal sample GSWA 216409. δ^{34}S values are annotated.

Sulphides analysed from mineralised igneous Octagonal material included pyrrhotite, pentlandite, pyrite and chalcopyrite with an overall δ^{34}S range of 2.25–5.93‰, a mean of 4.31 and a median of 4.19‰. A slightly greater divergence between the mean and median values of analyses from the igneous material, relative to the data from sedimentary Octagonal sulphides, originates from a small number of less positive outliers in the igneous population, with values in the range of 2–3‰. Phase by phase, δ^{34}S values range between 3.26–5.93‰ (mean/median of 4.78/4.63‰) in igneous pyrrhotite, 2.58–4.19‰ (mean/median of 3.78/3.92‰) in pentlandite, 2.25–5.27‰ (mean/median of 3.85/3.74‰) in chalcopyrite, and 2.92–5.32‰ (mean/median of 4.03/3.97‰) in pyrite.

Δ^{33}S values

Mean Δ^{33}S values for all samples lie within the range of -0.09–0.10‰ (Table 5.6.2). These values fall within a range accepted for sulphur as indicative of a modern (post-Archean) origin.

Locality	Samples	n	Δ^{33}S (‰)	2σ
Octagonal	216409	51	-0.09	0.10
	216419	31	-0.08	0.10
	216420	61	-0.02	0.11
	219048	41	-0.01	0.09
	219069	18	-0.07	0.09
	219070	48	-0.03	0.10
NRM	NRM1601	52	-0.02	0.11
	NRM1602	69	-0.03	0.12
Plato	216364	37	-0.02	0.12
	216369	35	0.10	0.18
	216372	18	-0.05	0.25

Table 3.3: Summary of mean Δ^{33}S values (‰) from samples across Octagonal, NRM and Plato localities

3.8 Discussion

3.8.1 Implications of δ^{34}S values

The mean δ^{34}S sulphur isotopic signatures for NRM, Plato and Octagonal material are 2.35 (±0.40), 1.05 (±0.85) and 4.31±0.80) ‰ respectively (1σ) (Table 5.6.1; Fig. 6). δ^{34}S data from each locality (Octagonal data from igneous and metasedimentary samples are considered separate populations) show normal distributions, as indicated by Shapiro-Wilk testing. T-tests were used to assess whether the Plato, NRM, Octagonal magmatic and Octagonal metasedimentary δ^{34}S populations are statistically distinct from one another. These tests returned T values in excess of 20 with P values well below a 0.05 threshold, indicating each locality is characterised by a statistically distinct isotopic range. We interpret the different sulphur isotopic ratios in these magmatic rocks to principally represent a mantle source plus varying degrees of assimilation of sulphur-rich Snowys Dam Formation metasedimentary rocks at each locality. Sulphur isotopic values at each locality range between the mantle sulphur values of the parental magmas, and the higher isotopic values of the surrounding metasedimentary

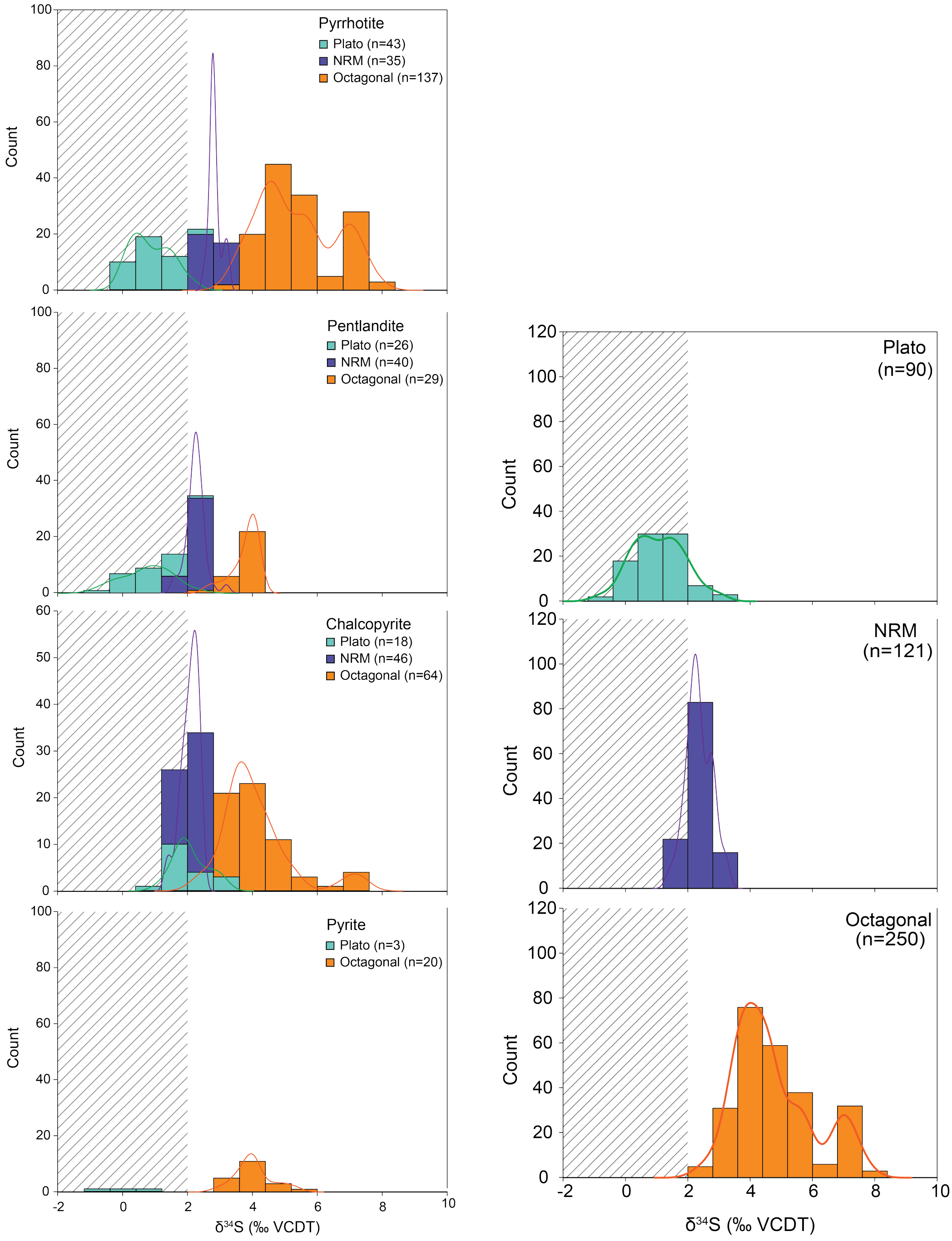

Figure 3.6: (Left) Histograms illustrating distribution of δ^{34}S values in samples analysed from Plato, NRM and Octagonal localities. (Right) Histograms illustrating distribution of δ^{34}S values across different sulphide minerals from Plato, NRM and Octagonal localities. KDEs have been overlaid. Hashed area indicates range of mantle δ^{34}S values.

rocks. The highest δ^{34}S isotope values are those from Octagonal, with a bimodal distribution due to the analysis of both magmatic and metasedimentary material. Both NRM and Octagonal magmatic material were emplaced into Snowys Dam Formation metasedimentary rocks, and show economic mineralisation; yet there is a disparity in isotopic values between the two localities. This may be due to variation in the quantity of external sulphur assimilated by the parental magmas, or due to heterogeneity in the sulphur isotopic signature within the metasedimentary rocks themselves.

The NRM material in particular can also be characterised by a narrow range of isotopic values, relative to Plato and Octagonal. The narrow range may reflect simply that only two samples of this material were analysed and/or that the samples represent only one of the several magmatic pulses recognised at Nova nearby (Maier et al., 2016b); it may also be the case that the values are indicative of a well-mixed and/or homogenous source. The latter is unlikely, given the varied analyses from Snowys Dam Formation metasedimentary rocks from Octagonal (Table 5.6.1). As such, the limited NRM sample set is likely not representative of the multiple batches of magma thought to be involved in the genesis of the Nova deposit, making it difficult to reliably interpret differences in mineralisation through variation in isotopic signatures between Octagonal and Nova via the NRM samples.

Plato, with an average δ^{34}S value of 1.05 (±0.85) ‰, lies within the accepted δ^{34}S range for mantle sulphur. This could be interpreted as reflecting little assimilation of external sulphur relative to Octagonal or NRM material, resulting in essentially no excursion of the sulphide isotopic signature from the mantle range. Exploratory work uncovered some mineralisation at Plato (Venables, 2014), albeit not to the degree seen at Octagonal or NRM/Nova. Restricted assimilation of external sulphur could have inhibited the generation and volume of an immiscible sulphide phase within Plato's parent magma and consequently have limited mineralisation potential. Alternatively, assimilation of sulphur with an isotopic signature similar to that of the mantle would produce a similar result; a magma with a δ^{34}S signature c. 1‰ assimilating sediments of c. 2‰ will see only a relatively minimal change in δ^{34}S value regardless of the quantity it assimilates. In the case of Plato however, we interpret its near mantle sulphur signature as indicating relatively minimal assimilation of crustal sulphur. This would also fit with the predominance of metagabbroic rocks in the drillcore samples from Plato, and only very sparse small inclusions of metasedimentary rock.

Intergranular δ^{34}S variations within Octagonal sample GSWA 216409

216409 is a sample of garnet-bearing metasedimentary rock from Octagonal from which in-situ analyses indicate variation in δ^{34}S values between sulphides completely encompassed within garnet and those either partially enclosed or within the matrix (Fig. 3.5). The enclosed sulphides return mean δ^{34}S values between 4.44–4.74‰ (mean/median of 4.55/4.53‰) while the range of analyses for those sulphides in the matrix lie between 4.56–5.93‰ (5.51/5.54‰). The majority of analyses from this sample were of pyrrhotite (45 of 51 analyses; Table 5.6.1), and all analyses from grains within garnet were of pyrrhotite. As such the difference in values is not due to fractionation between different sulphide phases; the difference in average δ^{34}S values of c. 1‰ must be due to a difference in the processes the different sulphide populations were exposed to. One possibility is the loss of lighter sulphur to a melt produced by sub-solidus melting of the metasedimentary rock during amphibolite grade metamorphism; growth of garnet encompassed a number of sulphide grains within the rock, shielding them from this sulphur loss and consequently leading to a less positive δ^{34}S signature within the sulphide inclusions.

3.8.2 Mixing calculations as a means of constraining assimilated sulphur

Two component mixing calculations can be used to identify the approximate contribution of external sulphur to the Octagonal parental magma (Ripley and Li, 2003):

$$\delta^{34}S_{mix} = \frac{\delta^{34}S_c f_c C_c^s + \delta^{34}S_m f_m C_m^s}{f_c C_c^s + f_m C_m^s} \tag{3.1}$$

Where $\delta^{34}S_i$ is the sulphur isotopic value of component i, f_i is the fractional abundance of i, C_i^s is the sulphur concentration within i, and $\delta^{34}S_{mix}$ is the resulting sulphur isotopic value of the Octagonal magma. Components c and m are the contaminant (Snowys Dam Formation) and the parental mantle magma respectively. We assume a homogenous sulphur content in the parental magmas equivalent to the average content within the mantle, estimated to be 400 ppm, in line with estimates for the upper mantle (von Gehlen, 1992). With a range of -2 to 2‰ (Ripley and Li, 2003), we assume an average value of 0‰ for δ^{34}S in mantle sulphur. Sulphur content in the metasedimentary rocks associated with Octagonal is equivalent to c. 1500 ppm (mean/median of 1535/1650±110 (1σ) ppm), calculated from whole rock geochemical data provided by Creasy Group (Appendix 3.C). At present, no sulphate-rich strata have been observed within the Snowys Dam Formation.

The mean isotopic value of the mineralised Octagonal material analysed is c. 4.25‰. Using the above equation to produce mixing curves (Fig. 3.7), we estimate that the fraction of metasedimentary sulphur required to produce the isotopic value seen in Octagonal magmatic material is equal to c. 30% of the sulphur in the Octagonal magmas. This in itself is not an insignificant quantity of sulphur. It is unlikely that such extensive assimilation of crustal sulphur could extend throughout the intrusion without a mechanism by which it could have been circulated and mixed within the magma body; we therefore suggest the intrusion was large enough for convective homogenisation to occur, saturating larger volumes of magma with the assimilated sulphur. It is also necessary to note that the sulphur content of mineralised material varies greatly, with end member values of c. 17500 and 165400 ppm. Such high concentrations cannot be reached solely through assimilation of the proposed quantity of metasedimentary sulphur. Thus while the Snowys Dam Formation might be the primary source of sulphur, subsequent segregation of the sulphide melts is necessary to explain the absolute sulphur contents of the mineralised rocks.

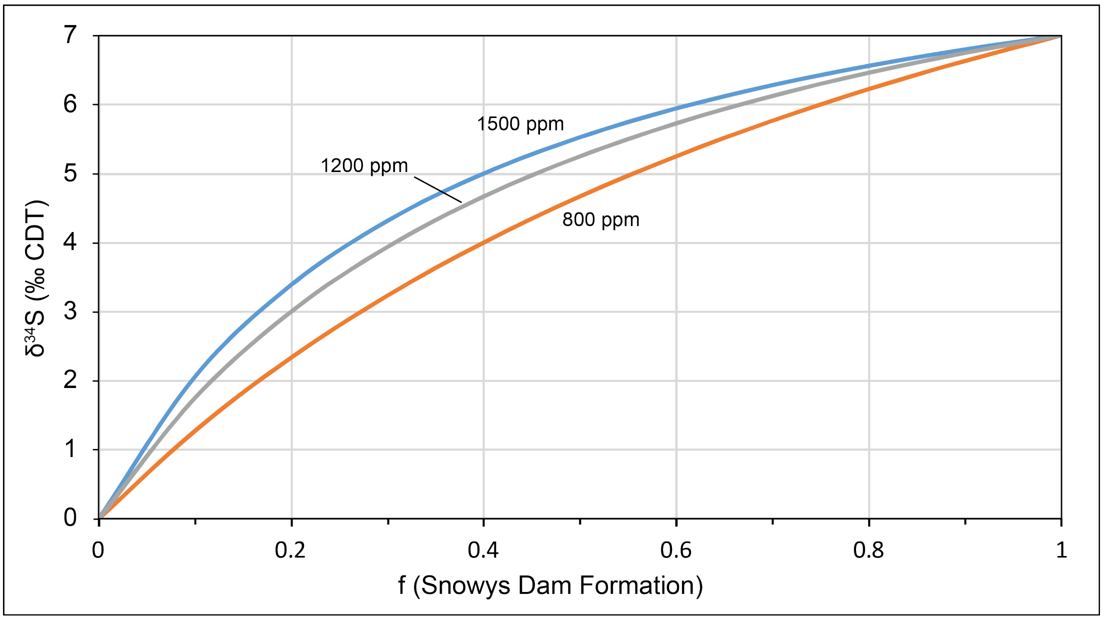

Figure 3.7: Mixing curve illustrating changes in Octagonal, Plato and NRM magma isotopic compositions due to interaction with Snowys Dam Formation metasedimentary rocks. 800, 1200 and 1500 ppm refer to the modelled metasediment sulphur concentration for each curve.

If we assume that samples NRM1601/1602 are indeed representative of Nova, and that both NRM and Plato assimilated quantities of the Snowys Dam Formation with equivalent sulphur concentrations (1500 ppm), then we can extend the model derived from the mixing equation to these localities as well. Using δ^{34}S values of 1.05 and 2.35‰ for Plato and NRM material respectively, it is estimated that a fraction of c. 5% metasedimentary sulphur was assimilated within the Plato magmas , and a fraction of c. 12% metasedimentary sulphur within NRM parental magmas. The limited mineralisation at Plato has previously been interpreted as a result of parental magmas being emplaced as relatively small scale dykes and sills and consequently having limited potential to transport a sulphide bearing slurry or assimilate sulphide-bearing country rock (Maier et al., 2016b). Assimilation of a 5% fraction of metasedimentary sulphur would be entirely compatible with this interpretation, as the emplacement of the parental magmas as smaller bodies would greatly reduce their potential to assimilate surrounding material. NRM on the other hand, much like Octagonal, is unlikely to have developed the level of mineralisation present solely through assimilation of the proposed fraction of external sulphur. It is probable that mineralisation enhancing mechanisms such as sulphide trapping or tenor upgrading concentrated the sulphides present to produce the more mineralised material seen.

When assessing the plausibility of these assimilation models, results need to be taken in context of the effects on the geochemistry of the emplaced magmas. The more limited assimilation of metasediments at Plato may not have altered the geochemistry of the magmatic volume being emplaced. The incorporation of the material hosting the estimated 30% fraction of metasedimentary sulphur at Octagonal and 12% fraction at NRM/Nova however would undoubtedly have altered magmatic geochemistry and produced more felsic compositions at each locality; what we see instead are more mafic lithologies (e.g. norite, gabbronorite, olivine cumulates, ultramafic rocks) at Nova (Maier et al., 2016b); there is minimal evidence for the felsic lithologies that would result from assimilation on this scale that would have occurred during a relatively short span of emplacement in the middle crust. The geochemical modelling of Smithies et al. (2013) also constrains the amount of felsic material involved during generation and ascent of the Fraser gabbro through the lower crust to no more than c. 5% through observed SiO_2/K_2O contents, from which we can imply that assimilation of crustal content greater than c. 5% can only have occurred during emplacement. While the modelling results are valid for the local scale of observation, it is necessary to highlight some limitations, especially where disparities exist between the degree of assimilation modelled by sulphur isotopes versus that modelled by Smithies et al from whole rock geochemistry. The isotope calculations assume a homogenous sulphur content of c. 1500 ppm within the material assimilated. If sulphur concentrations in the country rock were heterogenous (e.g. higher contents possibly confined to unobserved lithologies within the metasediments) then the degree of assimilation required to produce the δ^{34}S values at each locality would naturally deviate from that calculated; specifically, the smaller proportions of evolved felsic compositions seen could suggest that assimilated material contained more sulphur than assumed. Alternatively, this absence of felsic compositions could also be due to decoupling of the sulphur-rich and silicate fractions of the magmas; incongruent melting would result in extraction of the sulphur fraction from assimilated metasediments before much of the silicate fraction.

By the same token, there is also the possibility that the δ^{34}S values used for each locality are not truly representative. This is unlikely to be an issue for Octagonal with an average δ^{34}S value taken from a large number of data across multiple samples, while Plato as a more limited and less mineralised system (relative to Octagonal and NRM) is unlikely to show much variation from the values acquired. Assimilation estimates for NRM are the most likely to be subject to inaccuracies through deviation from the assumed δ^{34}S value, as in-situ analyses were taken from two samples possibly not representative of the entire NRM magmatic system.

3.8.3 Implications from Δ^{33}S values

The data indicate a Δ^{33}S signature (-0.03±0.08‰) (1σ) that is within the range of values (-0.5–0.7‰) characterising sulphur derived from a modern (post-Archean) source (Savarino et al., 2003; Bekker et al., 2004) (Fig. 3.8). The relative consistency of Δ^{33}S values would seem to suggest that these analyses represent sulphide compositions at crystallisation. Furthermore, high temperature processes are generally unable to induce significant fractionation of sulphur isotopes, so post-crystallisation granulite facies metamorphism (c. 850°C; Clark et al., 2014) is unlikely to have modified the sulphur signature. In essence, what we see is the genesis of magmatic sulphide phases from a two component sulphur reservoir that does not include Archean input. This lack of "old" sulphur is curious, considering the established basement of the Fraser Zone reflects material with an ancestral Yilgarn heritage (Smithies et al., 2015; Kirkland et al., 2016).

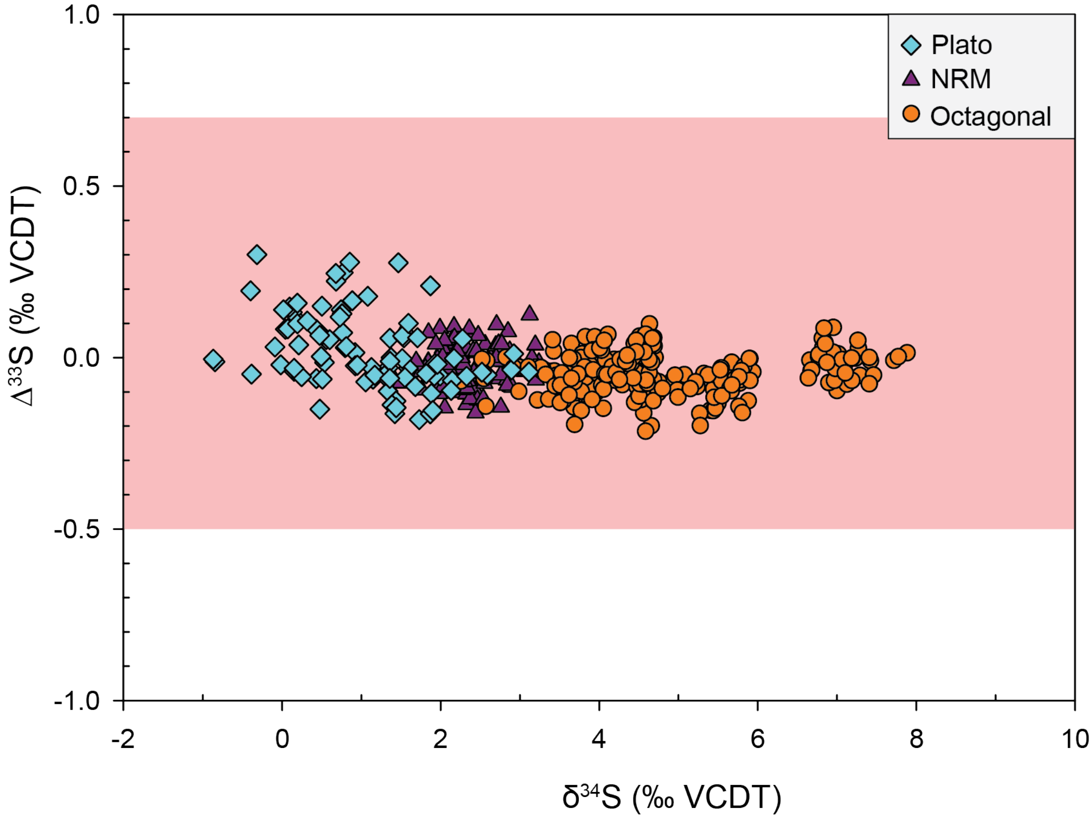

Figure 3.8: Δ^{33}S vs δ^{34}S compositions for all samples. Shaded field illustrates values considered diagnostic of modern sulphur compositions (Savarino et al., 2003; Bekker et al., 2004)

Radiogenic isotopes (e.g. Sm-Nd, Lu-Hf) imply an Archean Yilgarn crustal component (or more specifically material derived from the Proterozoic modification of Yilgarn crust) within the AFO (Kirkland et al., 2011). Indeed, Sr and Nd data presented by Maier et al. (2016b) for Fraser Zone main gabbro were interpreted to be the result of mixing between mantle derived magmas and a Biranup basement component, which itself has an established Yilgarn source component (Kirkland et al., 2011). Detrital zircon grains from the Biranup Zone have been recovered from the Fraser Zone (Kirkland et al., 2011, 2014), providing another indication that this Archean Biranup Zone material was incorporated in the Fraser Range Metamorphics, and furthermore, a number of detrital zircon crystals of Archean age have been identified within Arid Basin sediments (Spaggiari et al., 2015). Geochemical modelling of the Fraser Zone gabbro implies the assimilation of a crustal component that closely resembles a mix of Archean granite and Munglinup Gneiss (Smithies et al., 2013). Hence, it might be reasonably expected that, between the assimilation of a Biranup basement component (itself containing fragmented Yilgarn material), and metasediments bearing detrital Yilgarn zircons, a non-zero Archean sulphur component would be visible in the Δ^{33}S sulphur isotope analyses of the material studied. It is possible that Archaean material in the Fraser Zone is characterised by an absence of anomalous Δ^{33}S values and consequently a homogenous, essentially zero Δ^{33}S signature, but this is perhaps unlikely given the range of possible Δ^{33}S values Archaean sulphur retains. Assuming that this is not the case, there are two possible explanations as to why an Archaean MIF-S signature may not be seen.

Stripping of sulphides from detrital material

Within sediments, sulphur is primarily sequestered within sedimentary sulphides such as pyrite. These sulphides are reactive and susceptible to weathering when compared to mineral phases providing Nd and Hf data, such as zircon. Uplift, erosion and transport of sulphide and zircon containing sediments occurs over extended periods of time, during which it is very likely that surface processes destroy significant proportions of the less robust phases. We would not see Archean sulphur within Fraser Zone sulphides if that sulphur did not survive erosion and transport to be deposited as part of the Arid Basin sediments (Fig. 3.9).

Dilution or unfavourable distribution of Archean sulphur signature

The absence of an Archean sulphur signature need not be interpreted solely as a complete lack of an Archean input; rather it may be indicative of a relatively minimal contribution of Archean sulphur and a reflection of the sensitivity of the sulphur mixing relationship. Effective homogenisation of a minor Archean sulphur component within the Octagonal parental magmas might have diluted an Archean signature to a point where it can no longer be reliably identified. By applying the same mixing equation used previously for δ^{34}S and modelling the impact of Archean sulphur on the sulphur isotopic signature of a melt-metasediment mix, we can identify how likely this is to be

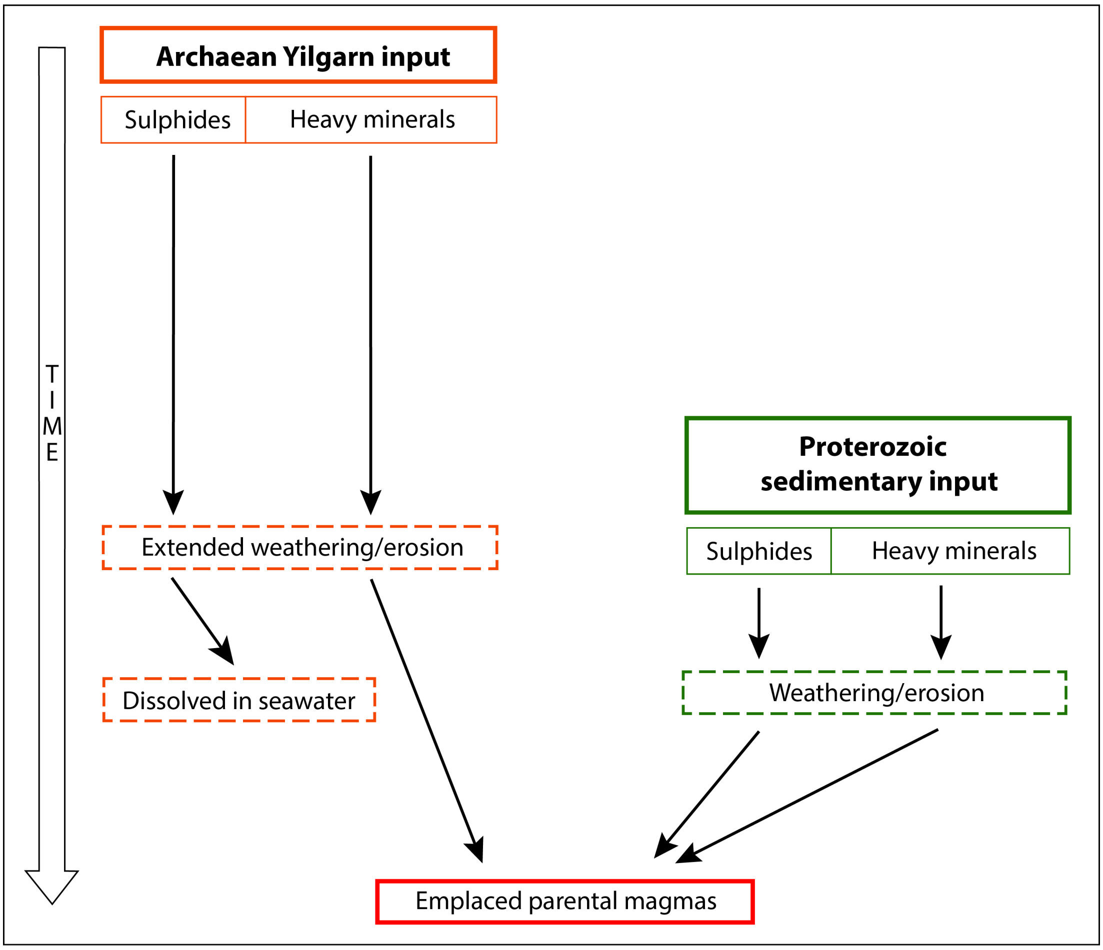

Figure 3.9: Conceptual diagram illustrating sulphide stripping from sediments as a means of removing an Archean sulphur signature from older Yilgarn material, relative to younger sedimentary input.

the case.

$$\Delta^{33}S_{mix} = \frac{\Delta^{33}S_c f_c C_c^s + \Delta^{33}S_m f_m C_m^s}{f_c C_c^s + f_m C_m^s} \tag{3.2}$$

Δ^{33}S$_i$ is the Δ^{33}S sulphur isotopic value of component $_i$, f$_i$ is the fractional abundance of $_i$, C$_i^s$ is the sulphur concentration within $_i$, and Δ^{33}S$_{mix}$ is the resulting Δ^{33}S sulphur isotopic value of the mixed magma. Components $_c$ and $_m$ are the contaminant (Snowys Dam Formation) and the mantle magma respectively. Again homogenous sulphur contents are assumed, with 400 ppm and 1500ppm in the magma and metasediments respectively. A Δ^{33}S value of 0‰ is assumed for mantle sulphur.

When modelling the resulting isotopic signature, it readily becomes apparent that assimilation of even a small metasedimentary component with a Δ^{33}S value distinct from the mantle range would still be visible within the resulting mix (Fig. 3.10). Our δ^{34}S mixing model of Octagonal suggests assimilation of external sulphur equivalent to c. 30% of the sulphur present in the emplaced magma. Assimilation of this quantity of material using a Δ^{33}S value of 1‰ results in a mix with a Δ^{33}S signature of c. 0.6‰, far outside the range of values (-0.03±0.08‰) seen in our analyses. Furthermore, we find that modelling assimilation of fractions of c. 10% or less would also produce a mix with a Δ^{33}S in excess of that seen in analysed samples.

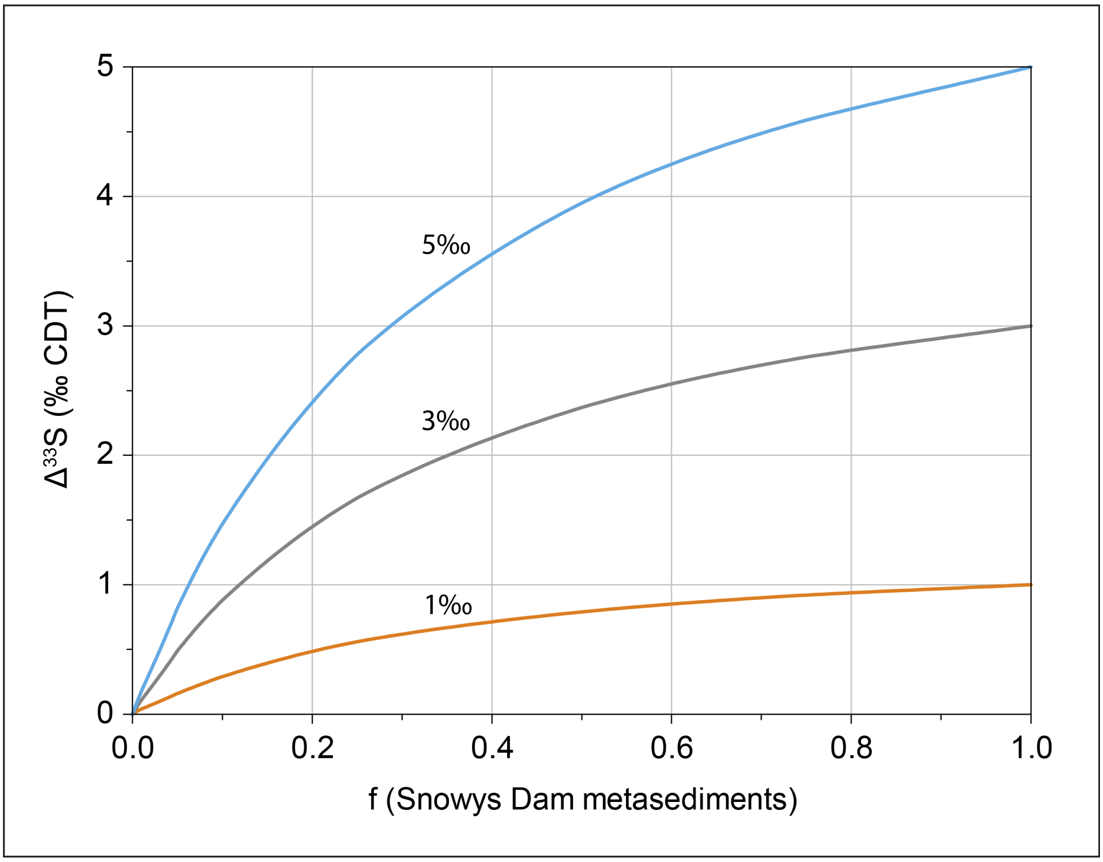

Figure 3.10: Mixing curve indicating the resulting Δ^{33}S signature of a magma-sediment mix at different values of Δ^{33}S in the assimilated component.

3.9 Conclusions

We used in-situ sulphur isotope analysis to characterise sulphur isotopic signatures and Archean sulphur contributions within the variably mineralised magmatic sulphide prospects of Plato, Octagonal and NRM in the Fraser Zone. Our findings are that:

- Unique δ^{34}S signatures characterise each locality; we interpret these signatures to represent different degrees of assimilation of Snowys Dam metasedimentary material. The more positive δ^{34}S signatures at the more strongly mineralised NRM and Octagonal localities imply greater degrees of sediment assimilation.
- Differences in δ^{34}S values from sulphides inside and outside garnets in Octago-

nal metasediments are interpreted as a consequence of loss of light sulphur to subsolidus melting from unshielded sulphides. In contrast, sulphides included in garnet were shielded from sulphur loss and consequently indicate less positive δ^{34}S.

- Mixing models indicate that approximately 30% of the sulfur at Octagonal was sourced from the host sedimentary rocks. Extension of these calculations to Plato and NRM suggests sedimentary sulphur contribution of 5 and 12% respectively. Limited sediment assimilation at Plato is consistent with a model of emplacement in which Plato magmas were emplaced as small bodies with restricted ability to incorporate surrounding material.

- Sulphur concentrations in the mineralised Octagonal material exceed a value that could be produced via mixing between melted metasediments and a mantle-derived magma in the proportion suggested by the sulphur isotope values. This observation is consistent with the involvement of multiple mechanisms promoting sulphide growth and concentration during mineralisation (e.g. upgrading and gravity-driven accumulation) rather than solely sulphide precipitation through assimilation of external sulphur.

- None of the material analysed contains Archean sulphur; an observation apparently at odds with previous geochemical and radiogenic isotopic modelling that suggests an evolved Archean crustal component in the source to Fraser Zone magmas. This could be due to characterisation of Archaean sulphur in the Fraser Zone by homogenous, essentially zero Δ^{33}S values, in which case Archaean sulphur would be indiscernible; however this would seem unlikely given the wide range of possible Δ^{33}S values characterising Archaean sulphur. We conclude that this apparent discrepancy is a consequence of weathering of Archean sulphides during the sedimentary processes that formed the Arid Basin. The weathering would have affected sulfides more than zircon, leading to decoupling of the Archean signatures for sulfur and the zircon-hosted trace elements.

- Aspects of our study have implications for the wider understanding of crustal sulphur cycling. While a MIF-S indicative Δ^{33}S isotopic signature may remain visible through dilution with a non-MIF-S-bearing sulphur reservoir, the disappearance of a MIF-indicative signature that could have been inherited from Archean sediments may be a significant impediment to the identification of Archean sulphur cycling/recycling in the crust. The loss of a MIF-S signature in the sulphur isotopic record of magmatic rocks may be indicative of weathering and transport processes in the sedimentary environment of supracrustal sulfur assimilated by magmas.

Acknowledgements

The authors acknowledge the facilities, and the scientific and technical assistance of the Australian Microscopy & Microanalysis Research Facility and the Centre for Microscopy, Characterisation & Analysis, The University of Western Australia, a facility funded by the University, State and Commonwealth Governments. Part of this research was undertaken using the TIMA instrumentation (ARC LE140100150) at the John de Laeter Centre, Curtin University. The Minerals Research Institute of Western Australia, Ponton Minerals (Creasy Group) and the Geological Survey of Western Australia are gratefully acknowledged for funding this research as a component of the MRIWA M470 project (Mineral systems on the margin of cratons: Albany-Fraser Orogen / Eucla Basement case study).

3.10 References

Adams, M., 2012. Structural and geochronological evolution of the Malcolm Gneiss, Nornalup Zone, Albany-Fraser Orogen, Western Australia. Geological Survey of Western Australia.

Bekker, A., Barley, M. E., Fiorentini, M. L., Rouxel, O. J., Rumble, D., Beresford, S. W., 2009. Atmospheric sulfur in archean komatiite-hosted nickel deposits. Science 326 (5956), 1086–1089.

Bekker, A., Holland, H., Wang, P.-L., Rumble Iii, D., Stein, H., Hannah, J., Coetzee, L., Beukes, N., 2004. Dating the rise of atmospheric oxygen. Nature 427 (6970), 117.

Bennett, M., Gollan, M., Staubmann, M., Bartlett, J., 2014. Motive, means, and opportunity: key factors in the discovery of the Nova–Bollinger magmatic nickel–copper sulfide deposits in Western Australia. Building Exploration Capability for the 21st Century. Society of Economic Geologists, Special Publications 18, 301–320.

Brisbout, L., 2015. Determining crustal architecture in the east Albany-Fraser Orogen from geological and geophysical data. Geological Survey of Western Australia.

Clark, C., Kirkland, C. L., Spaggiari, C. V., Oorschot, C., Wingate, M. T., Taylor, R. J., 2014. Proterozoic granulite formation driven by mafic magmatism: An example from the Fraser Range Metamorphics, Western Australia. Precambrian Research 240, 1–21.

Clark, D. J., Hensen, B. J., Kinny, P. D., 2000. Geochronological constraints for a two-stage history of the Albany-Fraser Orogen, Western Australia. Precambrian Research 102 (3), 155 – 183.

Condie, K. C., Myers, J. S., 1999. Mesoproterozoic Fraser Complex: geochemical evidence for multiple subduction-related sources of lower crustal rocks in the Albany-Fraser Orogen, Western Australia. Australian Journal of Earth Sciences 46 (6), 875–882.

De Waele, B., Pisarevsky, S., 2008. Geochronology, paleomagnetism and magnetic fabric of metamorphic rocks in the northeast fraser belt, western australia. Australian Journal of Earth Sciences 55 (5), 605–621.

Doyle, M. G., Fletcher, I. R., Foster, J., Large, R. R., Mathur, R., McNaughton, N. J., Meffre, S., Muhling, J. R., Phillips, D., Rasmussen, B., 2015. Geochronological Constraints on the Tropicana Gold Deposit and Albany-Fraser Orogen, Western Australia. Economic Geology 110 (2), 355.

Farquhar, J., Bao, H., Thiemens, M., 2000. Atmospheric influence of earth's earliest sulfur cycle. Science 289 (5480), 756–758.

Farquhar, J., Wing, B. A., 2003. Multiple sulfur isotopes and the evolution of the atmosphere. Earth and Planetary Science Letters 213 (1-2), 1–13.

Gonzalez-Alvarez, I., Anand, R. R., Hough, R., Salama, W., Laukamp, C., Ley-Cooper, Y., Sweetapple, M. T., Sonntag, I., Lintern, M., Abdat, T., leGras, M., Walshe, J., 2014. Greenfields exploration in the Albany-Fraser Orogen and on the southeast Yilgarn cratonic margin. GSWA extended abstracts 2014, 26–28.

Irvine, T., 1976. Crystallization sequences in the muskox intrusion and other layered intrusions—ii. origin of chromitite layers and similar deposits of other magmatic ores. In: Irvine, T. (Ed.), Chromium: its Physicochemical Behavior and Petrologic Significance. Pergamon, pp. 991 – 1020.

Kirkland, C., Smithies, R., Spaggiari, C., Wingate, M., de Gromard, R. Q., Clark, C., Gardiner, N., Belousova, E., 2017. Proterozoic crustal evolution of the Eucla basement, Australia: Implications for destruction of oceanic crust during emergence of Nuna. Lithos 278, 427–444.

Kirkland, C. L., Spaggiari, C. V., Johnson, T. E., Smithies, R. H., Danišík, M., Evans, N., Wingate, M. T. D., Clark, C., Spencer, C., Mikucki, E., McDonald, B. J., 2016. Grain size matters: Implications for element and isotopic mobility in titanite. Precambrian Research 278, 283 – 302.

Kirkland, C. L., Spaggiari, C. V., Pawley, M. J., Wingate, M. T. D., Smithies, R. H., Howard, H. M., Tyler, I. M., Belousova, E. A., Poujol, M., 2011. On the edge: U-Pb,Lu-Hf, and Sm-Nd data suggests reworking of the Yilgarn craton margin during formation of the Albany-Fraser Orogen. Precambrian Research 187 (3), 223 – 247.

Kirkland, C. L., Spaggiari, C. V., Smithies, R. H., Wingate, M. T. D., 2014. Cryptic progeny of craton margins: geochronology and isotope geology of the Albany-Fraser Orogen with implications for evolution of the Tropicana Zone. Albany-Fraser Orogen seismic and magnetotelluric (MT) workshop 2014: extended abstracts compiled by CV Spaggiari and IM Tyler, Geological Survey of Western Australia, Record 2014/6, 89–101.

Kirkland, C. L., Wingate, M. T. D., Spaggiari, C. V., 2012. 194711: metamonzogranite, Kent Dam; Geochronology Record 1044. Geological Survey of Western Australia, 4p.

Kirkland, C. L., Wingate, M. T. D., Spaggiari, C. V., Pawley, M., 2010a. 194719: metasyenogranite, Symons Hill; Geochronology Record 848. Geological Survey of Western Australia, 5p.

Kirkland, C. L., Wingate, M. T. D., Spaggiari, C. V., Pawley, M., 2010b. 194736: metasyenogranite, Bartlett Bluff; Geochronology Record 849. Geological Survey of Western Australia, 4p.

Kita, N. T., Ushikubo, T., Fu, B., Valley, J. W., 2009. High precision sims oxygen isotope analysis and the effect of sample topography. Chemical Geology 264 (1), 43 – 57.

LaFlamme, C., Martin, L., Jeon, H., Reddy, S. M., Selvaraja, V., Caruso, S., Bui, T. H., Roberts, M. P., Voute, F., Hagemann, S., et al., 2016. In situ multiple sulfur isotope analysis by sims of pyrite, chalcopyrite, pyrrhotite, and pentlandite to refine magmatic ore genetic models. Chemical Geology 444, 1–15.

Maier, W., Smithies, R., Spaggiari, C., Barnes, S., Kirkland, C., Yang, S., Lahaye, Y., Kiddie, O., MacRae, C., 2016a. Petrogenesis and Ni–Cu sulphide potential of mafic–ultramafic rocks in the Mesoproterozoic Fraser Zone within the Albany–Fraser Orogen, Western Australia. Precambrian Research 281, 27 – 46.

Maier, W. D., Smithies, R. H., Spaggiari, C. V., Barnes, S. J., Kirkland, C. L., Kiddie, O., Roberts, M. P., 2016b. The evolution of mafic and ultramafic rocks of the Mesoproterozoic Fraser Zone, Albany-Fraser Orogen, and implications for the Ni-Cu sulphide potential of the region. Geological Survey of Western Australia, Record 2016/8, 49p.

Mavrogenes, J. A., O'Neill, H. S., 1999. The relative effects of pressure, temperature and oxygen fugacity on the solubility of sulfide in mafic magmas. Geochimica et Cosmochimica Acta 63 (7), 1173 – 1180.

Naldrett, A., 2004. Magmatic sulfide deposits: Geology, geochemistry and exploration. Springer Science & Business Media.

Ono, S., Eigenbrode, J. L., Pavlov, A. A., Kharecha, P., Rumble, D., Kasting, J. F., Freeman, K. H., 2003. New insights into archean sulfur cycle from mass-independent sulfur isotope records from the hamersley basin, australia. Earth and Planetary Science Letters 213 (1), 15 – 30.

Penniston-Dorland, S. C., Mathez, E. A., Wing, B. A., Farquhar, J., Kinnaird, J. A., 2012. Multiple sulfur isotope evidence for surface-derived sulfur in the bushveld complex. Earth and Planetary Science Letters 337-338, 236 – 242.

Quentin de Gromard, R., Spaggiari, C., Munro, M., Sapkota, J., De Paoli, M., 2017. SGTSG 2017 Albany-Fraser Orogen pre-conference field trip: Transect across an Archaean craton margin to a Proterozoic ophiolite. Geological Survey of Western Australia Record 2017/14, 100p.

Ripley, E. M., Li, C., 2003. Sulfur Isotope Exchange and Metal Enrichment in the Formation of Magmatic Cu-Ni-(PGE) Deposits. Economic Geology 98 (3), 635.

Ripley, E. M., Li, C., 2013. Sulfide Saturation in Mafic Magmas: Is External Sulfur Required for Magmatic Ni-Cu-(PGE) Ore Genesis? Economic Geology, v. 108, 45–58.

Rumble, D., 2005. Presidential address to the mineralogical society of america seattle, november 4, 2003: A mineralogical and geochemical record of atmospheric photochemistry. American Mineralogist 90 (5-6), 918.

Savarino, J., Romero, A., Cole-Dai, J., Bekki, S., Thiemens, M. H., 2003. Uv induced mass-independent sulfur isotope fractionation in stratospheric volcanic sulfate. Geophysical Research Letters 30 (21).

Seal, II, R. R., 2006. Sulfur isotope geochemistry of sulfide minerals. Reviews in Mineralogy and Geochemistry 61 (1), 633.

Smithies, R. H., Spaggiari, C. V., Kirkland, C. L., 2015. Building the crust of the Albany-Fraser Orogen: constraints from granite geochemistry. Geological Survey of Western Australia, Report 150, 49p.

Smithies, R. H., Spaggiari, C. V., Kirkland, C. L., Howard, H. M., Maier, W. D., 2013. Petrogenesis of gabbros of the Mesoproterozoic Fraser Zone: constraints on the tectonic evolution of the Albany-Fraser Orogen. Geological Survey of Western Australia, Record 2013/15, 29p.

Smithies, R. H., Spaggiari, C. V., Kirkland, C. L., Maier, W. D., 2014. Geochemistry and petrogenesis of igneous rocks in the Albany-Fraser Orogen. Albany-Fraser Orogen seismic and magnetotelluric (MT) workshop 2014: extended abstracts compiled by CV Spaggiari and IM Tyler, Geological Survey of Western Australia, Record 2014/6, 69–80.

Spaggiari, C., Kirkland, C., Smithies, R., Occhipinti, S., Wingate, M., 2014a. Geological framework of the albany–fraser orogen. In: Albany–Fraser Orogen seismic and magnetotelluric (MT) workshop 2014: extended abstracts compiled by CV Spaggiari and IM Tyler: Geological Survey of Western Australia, Record. Vol. 6. pp. 12–27.

Spaggiari, C. V., Bodorkos, S., Barquero-Molina, M., Tyler, I. M., Wingate, M. T. D., 2009. Interpreted bedrock geology of the South Yilgarn and central Albany-Fraser Orogen, Western Australia. Geological Survey of Western Australia, Record 2009/10, 84p.

Spaggiari, C. V., Kirkland, C. L., Smithies, R. H., Wingate, M. T. D., 2011. The geology of the East Albany-Fraser Orogen - A Field Guide. Geological Survey of Western Australia, Record 2009/10, 84.

Spaggiari, C. V., Kirkland, C. L., Smithies, R. H., Wingate, M. T. D., 2012. What lies beneath - interpreting the Eucla basement. GSWA extended abstracts, 24–26.

Spaggiari, C. V., Kirkland, C. L., Smithies, R. H., Wingate, M. T. D., Belousova, E. A., 2015. Transformation of an Archean craton margin during Proterozoic basin formation and magmatism: The Albany-Fraser Orogen, Western Australia. Precambrian Research 266, 440 – 466.

Spaggiari, C. V., Occhipinti, S. A., Korsch, R. J., Doublier, M. P., Clark, D. J., Dentith, M. C., Gessner, K., Doyle, M. G., Tyler, I. M., Kennett, B. L. N., Costelloe, R. D., Fomin, T., Holzschuh, J., 2014b. Interpretation of Albany-Fraser seismic lines 12GA-AF1, 12GA-AF2 and 12GA-AF3: implications for crustal architecture, *in* Albany-Fraser Orogen seismic and magnetotelluric (MT) workshop 2014: extended abstracts *compiled by* CV Spaggiari and IM Tyler. Geological Survey of Western Australia, Record 2014/6.

Venables, T., 2014. Enterprise Metals Limited, Fraser Range Project, Exploration Licence 63/1281 Final Drilling Report, Co-funded Drilling Agreement DAG 2014/00384566, 25th July, 2014. WAMEX report A103177.

von Gehlen, K., 1992. Sulfur in the earth's mantle — a review. In: Schidlowski, M., Golubic, S., Kimberley, M. M., McKirdy, D. M., Trudinger, P. A. (Eds.), Early Organic Evolution: Implications for Mineral and Energy Resources. Springer Berlin Heidelberg, Berlin, Heidelberg, pp. 359–366.

Appendices

3.A Sample locations

Sample No.	Prospect	Drillhole	Depth (m)	Easting	Northing
GSWA216364	Plato	PLTD003	337.29	490454	6434150
GSWA216369	Plato	PLTD003	347.65	490454	6434150
GSWA216372	Plato	PLTD003	400.48	490454	6434150
GSWA216409	Octagonal	-	-	-	-
GSWA216419	Octagonal	DDH001	622.20	603167	6602391
GSWA216420	Octagonal	DDH001	548.00	603167	6602391
GSWA219048	Octagonal	ODH001W1	446.40	603167	6602391
GSWA219069	Octagonal	OCT0014	181.20	603079	6602944
GSWA219070	Octagonal	OCT0014	214.70	603079	6602944
NRM1601	NRM	*	*	*	*
NRM1602	NRM	*	*	*	*

Table 3.A.1: Location information for all samples analysed. *NRM1601/NRM1602 originate from within 5 km of Nova.

3.B Annotated sulphur isotope mount maps

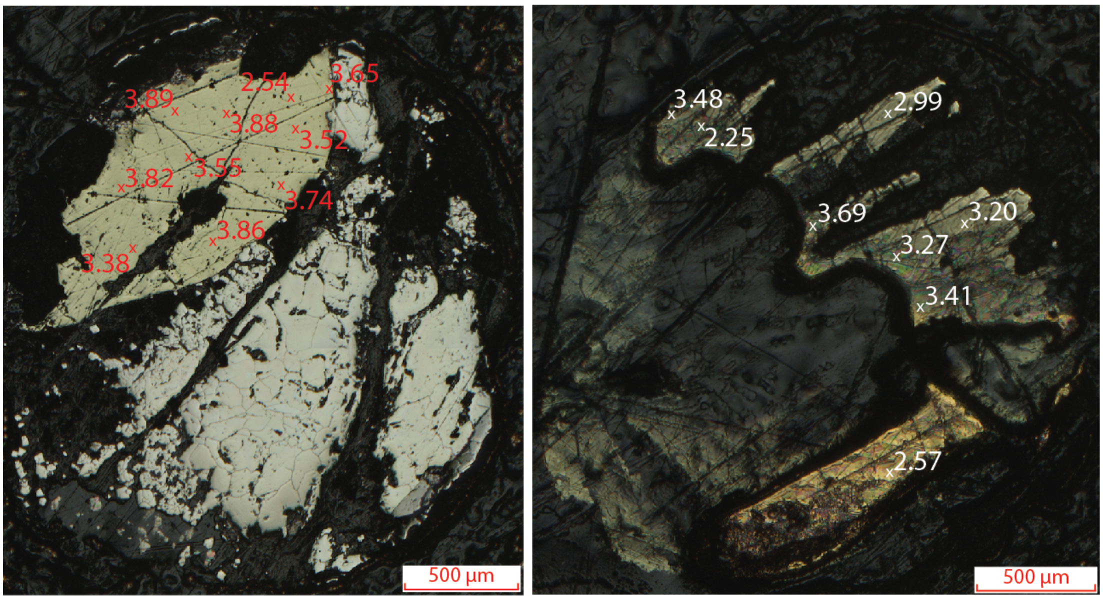

Figure 3.B.1: Annotated mount maps for sample GSWA219069 with analysed δ^{34}S sulphur values (‰).

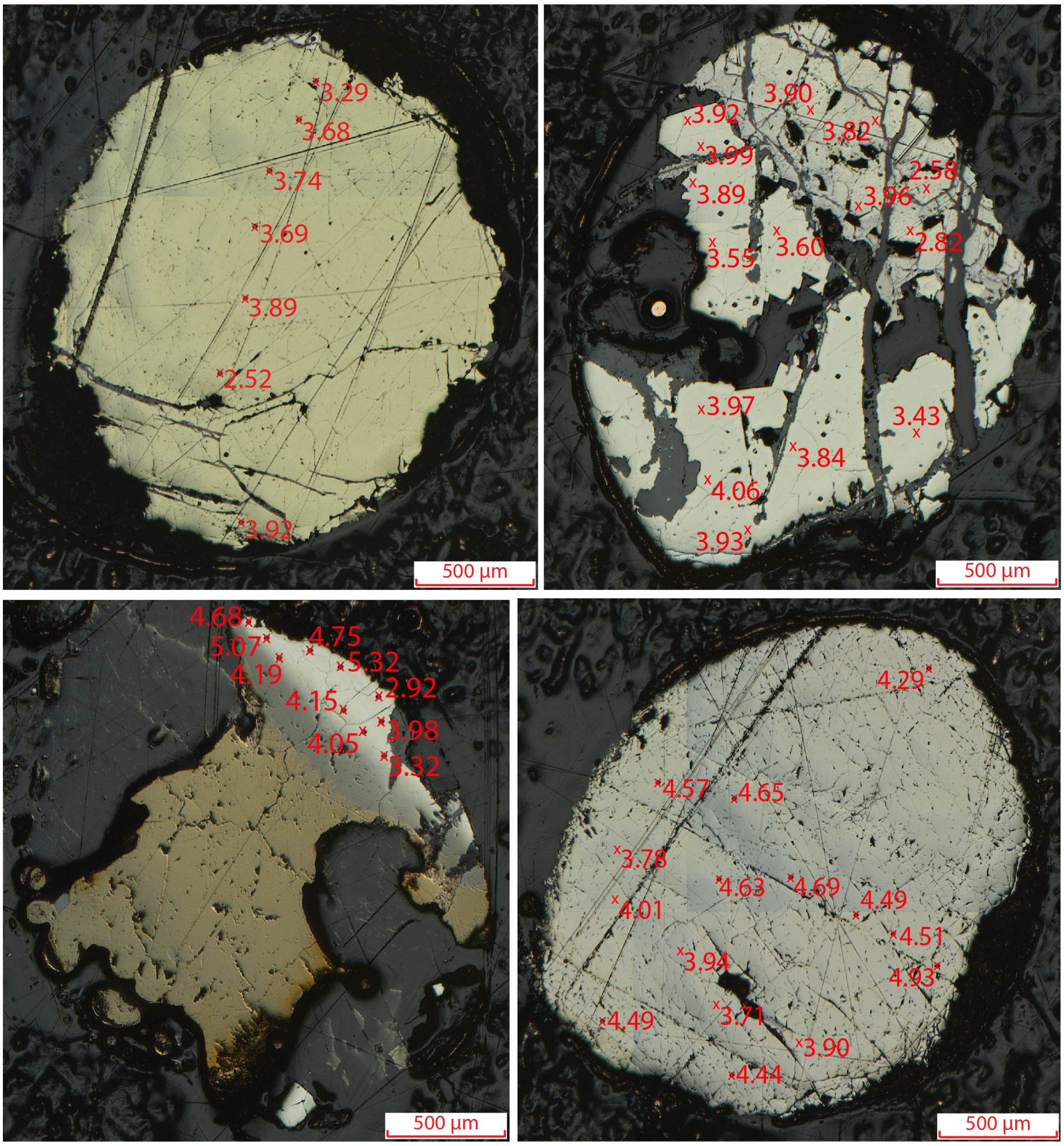

Figure 3.B.2: Annotated mount maps for sample GSWA219070 with analysed δ^{34}S sulphur values (‰).

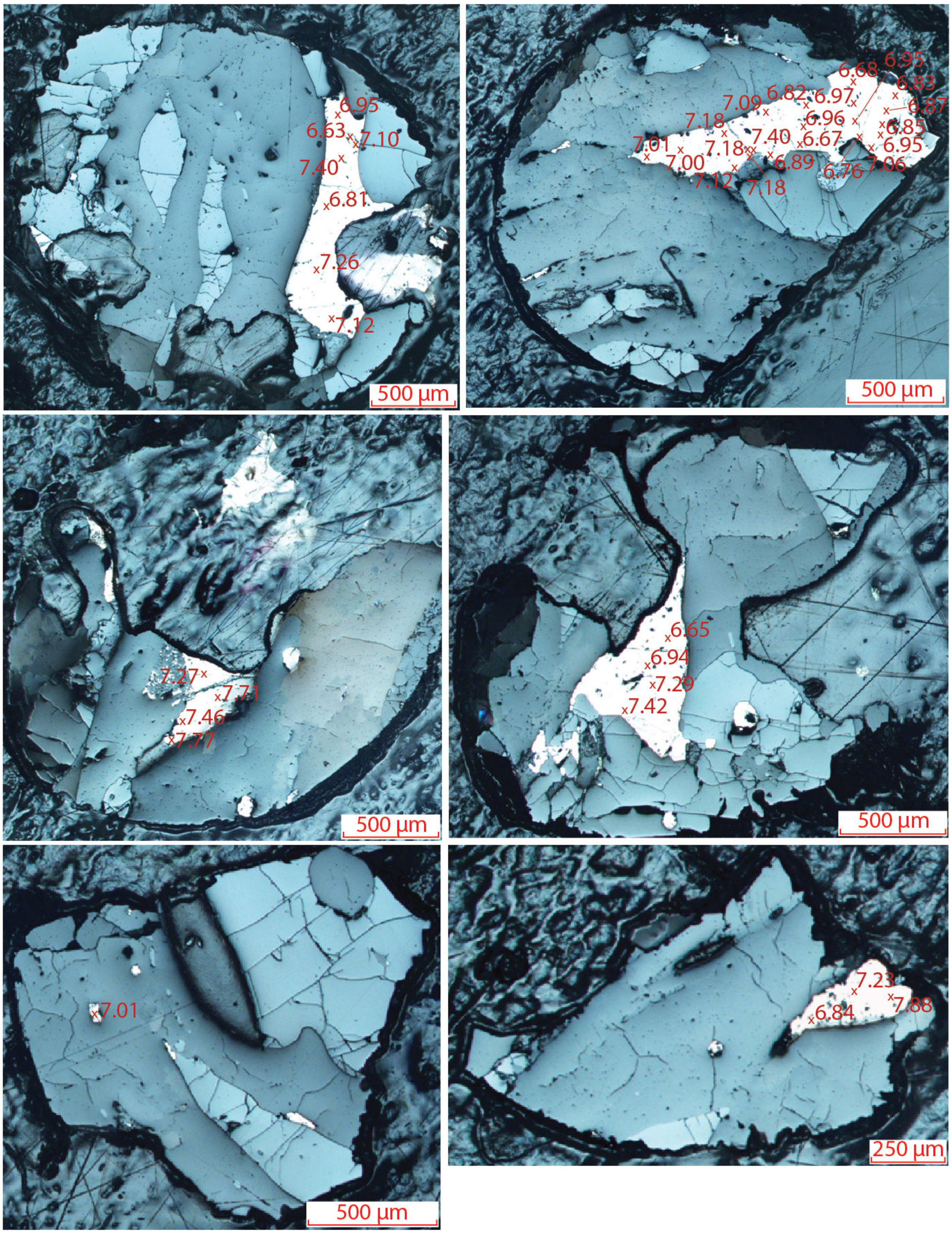

Figure 3.B.3: Annotated mount maps for sample GSWA219048 with analysed $\delta^{34}S$ sulphur values (‰).

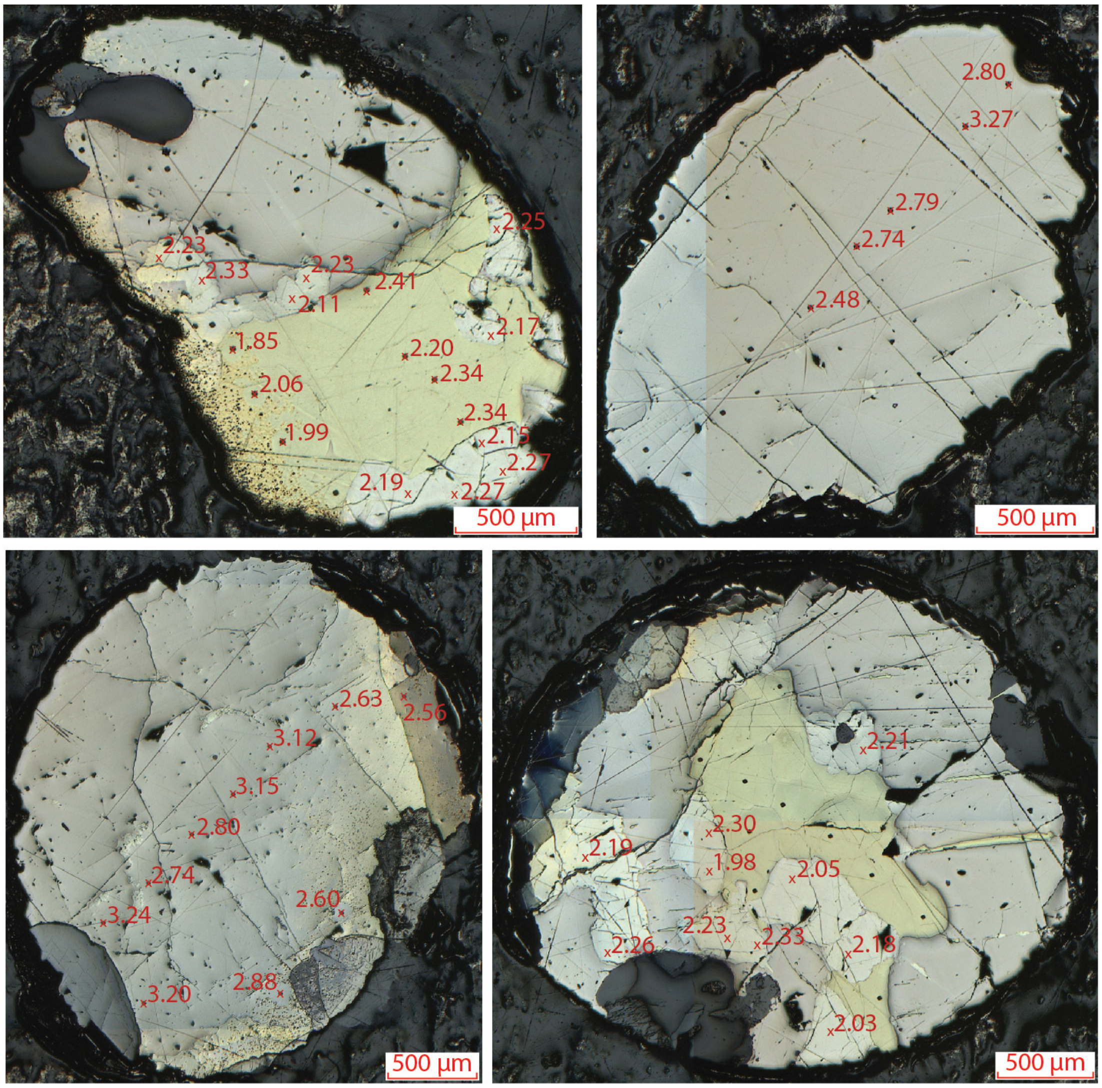

Figure 3.B.4: Annotated mount maps for sample NRM1601 with analysed δ^{34}S sulphur values (‰).

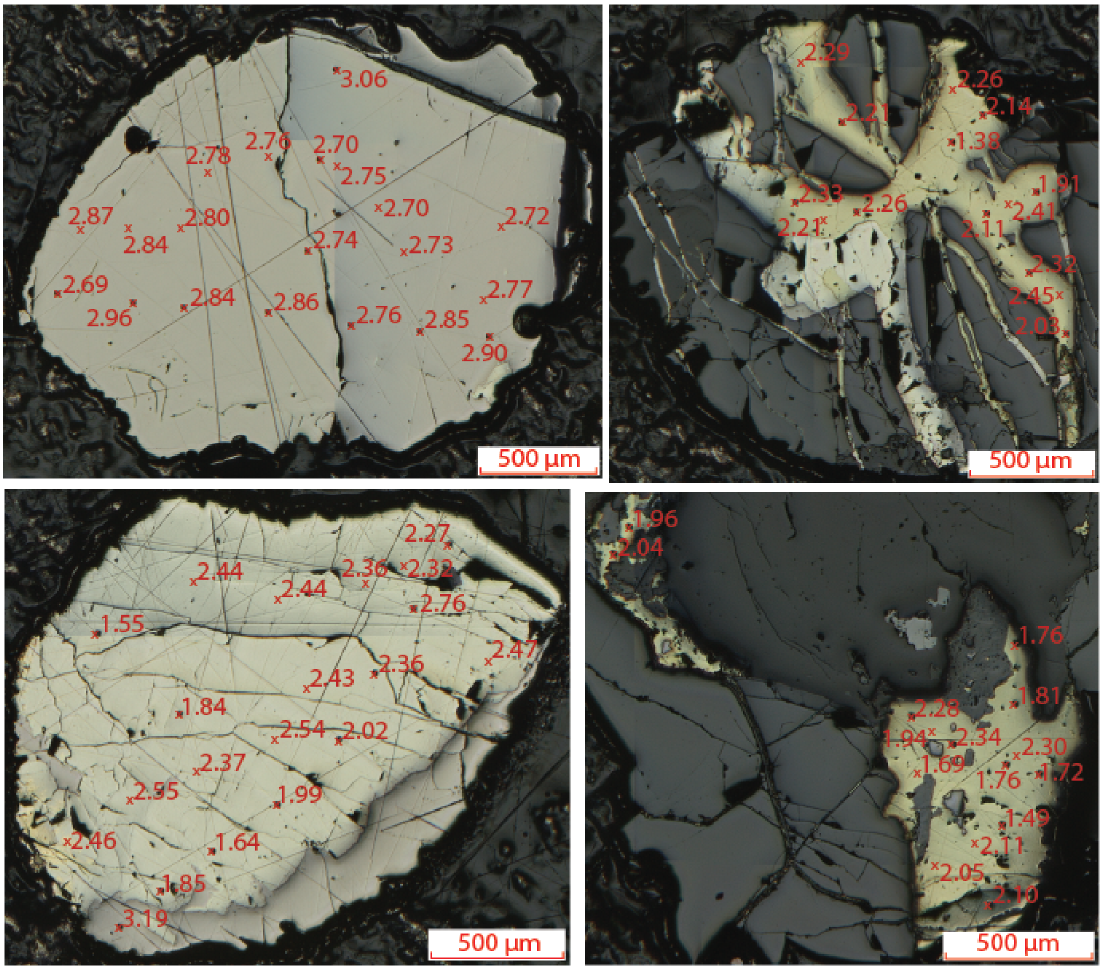

Figure 3.B.5: Annotated mount maps for sample NRM1602 with analysed δ^{34}S sulphur values (‰).

3.C Sample whole rock sulphur content

Hole ID	Interval depth	Sulphur content (%)
OCT0014	139.6	0.026
OCT0014	167.4	0.023
OCT0014	213.9	0.337
MAG0001	190	0.205
MAG0001	214	0.199
MAG0001	217	0.131

Table 3.C.1: Sulphur content of sedimentary intervals used to calculate average sedimentary sulphur content

Chapter 4

A novel application of image analysis to interpret trace element distributions in magmatic sulphides

4.1 Abstract

The Albany–Fraser Orogen in Western Australia hosts significant magmatic sulphide mineralisation but the impacts of its extensive metamorphic history on this mineralisation are poorly understood. Post-formation modification, including fluid-facilitated alteration, can upgrade or destroy mineralisation, with potentially significant consequences for economic ore deposits. We present laser ablation trace element data from samples of variably altered sulphide breccia from the mineralised Octagonal prospect located in the Fraser Zone of the Albany–Fraser Orogen. Mineral compositions are combined with laser ablation mapping and novel co-localisation analysis techniques to characterise the magmatic and post magmatic processes that modified element distributions within magmatic sulphide ore. Higher concentrations of Re, Co, Ni, Os, Ir, and lower concentrations of Cu, Zn and Ag in pyrrhotite and pentlandite relative to chalcopyrite record sulphide crystallisation from a sulphide liquid. Textural evidence and the compositions of pyrrhotite and pyrite are consistent with replacement of pyrrhotite by pyrite and associated magnetite. Element maps reveal intergranular variations in pentlandite Ag content that are systematically linked to the sulphide distribution. A novel application of co-localisation analysis reveals that the associations among Mn, Pb, Ag and the sample fracture networks are statistically significant; this association is interpreted as a consequence of fluid-assisted element remobilisation. Post-formation alteration processes at Octagonal were accompanied by variable remobilisation and de-

pletion of metal concentrations associated with mineralisation; co-localisation analysis provides an invaluable tool that has enabled quantitative assessments of relationships between metal distributions and textural features associated with post-formation sulphide modification.

4.2 Introduction

Metals are fundamental to modern life, with a plethora of uses from construction material to cancer treatments; their continued extraction and processing from the Earth's crust is essential to the maintenance and development of human society. Extraction of mineral resources is a major component of the Western Australian economy; the Ni and base metal sectors are valued at \$1.6 billion and \$514 million respectively (Department of Mines, Industry Regulation and Safety, 2018). Ni–Cu–PGE magmatic sulphide deposits are a primary source of a number of these essential metals, including Ni, Cu, and Co. The Albany-Fraser Orogen (AFO) has grown in significance to the mineral exploration industry in recent years following large finds in the region, with the Fraser Zone of this orogen prospective for magmatic sulphide mineralisation after the discovery of the Nova–Bollinger Ni–Cu deposit in 2012 (Bennett et al., 2014). Orthomagmatic deposits are predominantly composed of the base metal sulphides (pyrrhotite, pentlandite, chalcopyrite), and commonly host quantities of trace elements (e.g., Ag, As, Bi, Se, Te) including the platinum group elements (PGE). These deposits are frequently found in association with intrusive and extrusive mafic and ultramafic rocks. In these deposits, the chalcophile metals are sequestered by sulphide phases after the magma becomes sulphide-saturated (Naldrett, 2004). In the AFO it has been hypothesised that emplacement of the Fraser Zone parental magmas within locally sulphide-rich sediments of the Snowys Dam Formation triggered sulphide saturation and subsequent magmatic sulphide mineralisation (Smithies et al., 2013; Maier et al., 2016; Walker et al., 2019). Many mineralised localities, including those in the Fraser Zone, are affected by post-magmatic metamorphic and hydrothermal events, which add complexity by modifying element distributions and obscuring primary magmatic processes. For example it has been suggested that fluid assisted alteration and element remobilisation may represent a source of metals for enigmatic hydrothermal Ni deposits such as Avebury (Holwell et al., 2017) at the cost of the donor orebody.

Advances in Laser Ablation-Inductively Coupled Plasma-Mass Spectrometry (LA-ICP-MS) enable accurate analysis and assessment of sulphide trace element compositions at high spatial resolutions (Zhu et al., 2016), providing useful insights into the genesis of the host deposit. Using this technique we produced quantitative maps of the concentrations of selected minor and trace elements within mineralised sulphide breccia samples from Creasy Group's Fraser Zone Octagonal prospect. Quantitative mapping of multiple sulphides is itself a complex technique, requiring multiple iterations of data reduction using an internal standard relevant to the different compositions of the sulphides analysed, with each quantitative sulphide elemental dataset then calibrated separately against standard materials. A novel co-localisation analysis of the results was used to quantify relationships between element concentrations and textural features associated with post-magmatic processes. Co-localisation consists of co-occurrence (spatial overlap) and correlation (co-distribution), where two co-localised spatial datasets will not only overlap with one another but codistribute in proportion to one another (Dunn et al., 2011). Co-localisation is often assessed visually in the geological sciences, but this provides only a subjective and qualitative assessment. In contrast, co-localisation is typically assessed quantitatively within the life sciences; we contend this statistical approach has the potential to provide insights into geological processes. The aims of this study were to: (a) identify the distributions of elements within the sulphides; (b) apply co-localisation analysis to quantitatively assess spatial relationships between textural features and element distributions; (c) characterise post-magmatic processes that modified element distributions; and (d) ultimately understand the underlying processes that controlled these element distributions.

4.3 Regional Geology

The Palaeoproterozoic to Mesoproterozoic AFO (Fig. 4.3.1) is a component of the West Australian Craton, extending along the southern and south-eastern margins of the Yilgarn Craton (Spaggiari et al., 2015). The orogen is divided into several distinct lithotectonic domains; the Northern Foreland (which we consider to include the Tropicana Zone), Biranup Zone, Nornalup Zone and the Fraser Zone. The Northern Foreland is the portion of the AFO immediately adjacent to the Yilgarn Craton and comprises greenschist facies lithologies from the Yilgarn Craton intruded by Palaeoproterozoic and Mesoproterozoic magmatic rocks (Spaggiari et al., 2015). The Biranup, Nornalup and Fraser Zones make up the majority of the orogen and consist, in various proportions, of magmatic and metasedimentary rocks, overprinted by variable amounts of Proterozoic multistage metamorphism. Magmatic rocks include new Proterozoic juvenile material, juvenile and Archaean mixtures, and rare reworked Archaean crystalline rocks (Spaggiari et al., 2014a, 2015; Kirkland et al., 2016).

The AFO has an extensive and complex tectonic history. The Albany–Fraser Orogeny formed the predominant tectonic and metamorphic features of the belt (Kirkland et al., 2011) and is divided into Stages I and II, which occurred between 1330–1260 Ma and 1225–1140 Ma respectively. Stage I is ascribed to the accretion of the Madura Province's Loongana arc onto the Nornalup Zone (de Gromard et al., 2017), while Stage II represents intracontinental reworking and magmatism linked with widespread magmatism related to stabilisation of oceanic crust during the cratonisation that occurred between the West Australian and South Australian Cratons (Spaggiari et al., 2009; Kirkland

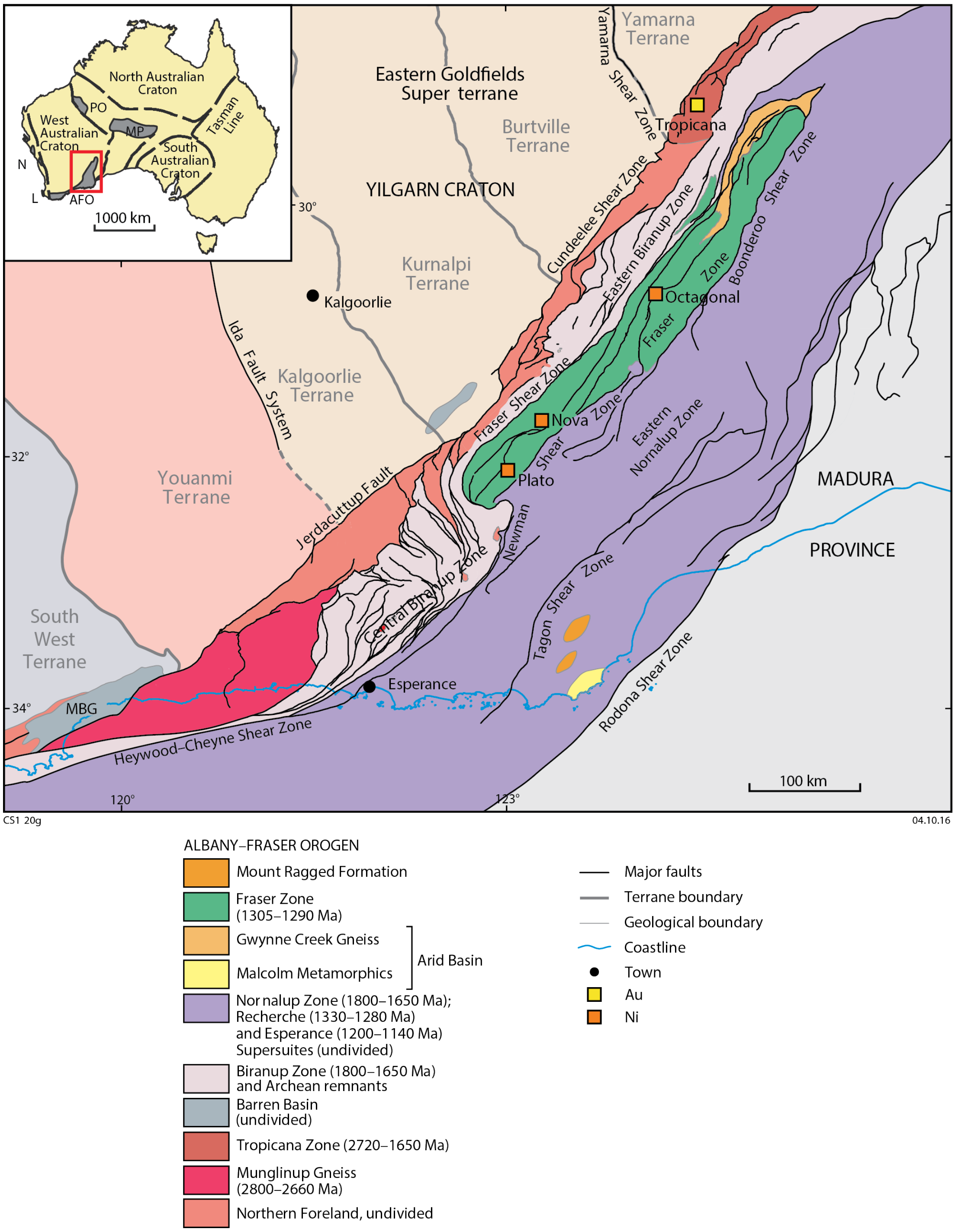

Figure 4.3.1: Simplified geological overview of the AFO (modified after Spaggiari et al., 2011)

et al., 2017).

4.3.1 Fraser Zone

The Fraser Zone is a north-easterly trending belt of metagabbroic rocks interleaved with minor ultramafic rocks, granitic gneiss and paragneiss of the Snowys Dam Formation (Smithies et al., 2013, 2015; Maier et al., 2016). Approximately 425 km long by 50 km wide, the Fraser Zone has an interpreted V-shaped geometry and a maximum depth of approximately 15 km (Spaggiari et al., 2014b; Brisbout, 2015). Most of the zone is under cover but its extent can be mapped because the mafic material has a distinctive gravity signature (Maier et al, 2016). Much of the zone comprises the 1305–1295 Ma Fraser Range Metamorphics, which includes amphibolite-granulite grade metasedimentary rocks of the Snowys Dam Formation intruded by primarily gabbroic and granitic rocks. The Snowys Dam Formation is a c. 1332 Ma component of the Mesoproterozoic Arid basin (Spaggiari et al., 2015), consisting of calc-silicate and iron-rich pelitic, semipelitic and psammitic rocks (Spaggiari et al., 2015).

The work of Clark et al. (2014) constrained the metamorphic conditions experienced by metasediments of the Snowys Dam Formation during Stage I of the Albany-Fraser Orogeny to 800–900°C and 6.5–8.5 kbar, consistent with peak metamorphism at depths of 25–30 km. Deposition of the Arid Basin sedimentary package occurred shortly before the onset of coeval mafic and felsic magmatism; U–Pb geochronology has dated igneous crystallisation of mafic material in the Fraser Zone to between 1305–1290 Ma (De Waele and Pisarevsky, 2008; Kirkland et al., 2011; Clark et al., 2014). The short time interval between the onset of magmatism and metamorphism implies that the thermal input from mafic magmatism was the driver of granulite-facies metamorphism (Clark et al., 2014). More recent work on Fraser Zone metagabbro by Glasson et al. (2019) established temperatures of 900–950°C and maximum pressures of approximately 7 kbar for the gabbroic rocks. These pressures are comparable with those estimated for the metasediments by Clark et al. (2014) and with suggested depths of burial of 20–25 km for Fraser Zone metapelitic rocks.

The higher temperatures recorded by the mafic rocks indicate that the gabbros were in closer proximity to the thermal driver of metamorphism than the sediments, consistent with the interpretation that the gabbroic rocks and associated mafic magmatism provided the metamorphic heat source (Glasson et al., 2019). The duration of magmatism has been constrained to c. 10–30 Ma, based on zircon U–Pb ages (Glasson et al., 2019). Zircons do not record Stage II of the Albany-Fraser Orogeny in the Fraser Zone, although there is abundant evidence of Stage I. However, metamorphic titanites record Stage II overprinting through remobilisation of radiogenic Pb within small titanite grains, with mean reset ages of 1205±16 Ma (Kirkland et al., 2016), consistent with extrusion of the Fraser Zone to shallower crustal levels between 1270 Ma and 1193

Ma (Kirkland et al., 2011).

Condie and Myers (1999) argued that the Fraser Zone was exotic to the AFO and represented the remnants of accreted oceanic arcs, and that the Fraser gabbro records subduction-related magmatism. More recently a Biranup Zone source for the Fraser Zone was proposed, based on zircon Lu–Hf data (Kirkland et al., 2011). This model is supported by geochemical modelling; assimilation of small (<10%) quantities of Archaean granite and Proterozoic-modified Archaean rocks into a depleted mantle source would produce the geochemical characteristics of the Fraser Zone metagabbros (Smithies et al., 2013). Currently, the Fraser Zone is interpreted as a mid- to deep-crustal hot zone formed by emplacement of mantle-derived magmas into quartzofeldspathic country rock (Smithies et al., 2013; Maier et al., 2016).

Fraser Zone metagabbro

The Fraser Zone metagabbro is formed from gabbro sheets that vary from a few centimetres to hundreds of metres thick. The gabbro is broadly divided into two categories: main gabbro that shows little geochemical indication of interaction with contemporaneous felsic material; and hybrid gabbro; gabbro that interacted or mingled with felsic material during intrusion and emplacement. Hybrid gabbro is distinguished from main gabbro by higher SiO_2 concentrations and lower Mg#. Hybrid gabbro may also be further subdivided into Group 1 and Group 2 hybrid gabbro, based on La and Th concentrations (Smithies et al., 2013). Field observations suggest that Group 2 hybrid gabbro incorporated felsic material at the level of intrusion, but that the Group 1 hybrid gabbro did not (Maier et al., 2016).

Geology of the Octagonal prospect

Octagonal comprises mafic and felsic material emplaced within the metasediments of the Snowys Dam Formation. Mafic units host weak disseminated to moderate pyrrhotite and chalcopyrite mineralisation and include norites, gabbronorites and pyroxenites, all metamorphosed to granulite facies. The sulphide breccias examined in this study are hosted within medium- to coarse-grained pyroxene and feldspar-rich mafic horizons. Metasedimentary material was found in close proximity (<2 m) to the sulphide breccia from which sample 219070 is derived. Minor fine-grained ultramafic material is present and is altered to serpentine- and magnetite-bearing mineral assemblages. Felsic material is subordinate to the mafic lithologies and consists of fine- to coarse-grained intrusive rocks and granitic gneiss. The metasediments are highly variable and include psammites, quartzites, marbles, banded iron formations and possible exhalative material.

4.4 Sample material

Two samples from the Octagonal prospect were selected for element mapping via laser ablation, based on results from thin section petrography and Tescan Integrated Mineral Analysis (TIMA). Mineralogical and textural descriptions of these samples are provided in Walker et al. (2019), and are summarised below.

4.5 Methodology

Polished thin sections of the two samples used in this study were examined via transmitted and reflected light microscopy using a petrographic microscope. This aided identification of features, mineral assemblages and textures for closer study. Two samples from the Octagonal prospect were analysed by TIMA to provide high resolution mineral modes and maps of sample surfaces. For TIMA analysis a 15 mm working distance, a beam energy of 25 keV and a spot size of 52.29 nm were used. Mapping was performed in a spot-mapping acquisition mode was used with a pixel spacing of 3 µm and a spot spacing of 33 µm.

Element analysis was undertaken using LA-ICP-MS facilities at the Department of Applied Geology in Curtin University using a Resonetics RESOlution M-50A-LR system incorporating a COMPex 102-193 nm excimer UV laser, with ablated material measured using an Agilent 7700s quadrupole ICP-MS. A spot size of 60 µm was used with a laser energy of 2.1 J/cm^2 and an ablation time of 35s. Spot grids were used to map sample surfaces. The sample cell was flushed with He (300mL.min^{-1}) and N^2 (1.0mL.min^{-1}) after each ablation. Ablated material was carried to the mass spectrometer by an Ar carrier gas (1.0L.min^{-1}). Counts of the following isotopes were monitored: ^{106}Ag, ^{75}As, ^{197}Au, ^{209}Bi, ^{59}Co, ^{65}Cu, ^{56}Fe, ^{193}Ir, ^{55}Mn, ^{60}Ni, ^{192}Os, ^{208}Pb, ^{105}Pd, ^{195}Pt, ^{187}Re, ^{103}Rh, ^{121}Sb, ^{82}Se, ^{130}Te, ^{51}V, ^{182}W, ^{66}Zn. Six reference materials were used to calibrate ablation data: GSD-1g, BCR2G, BHVO2G, BONN, IMER and PO726; details of these materials is provided in Appendix 4.A. The data were reduced using the trace element scheme within the Iolite package provided with the Igor Pro software. Internal standardisation was based on Fe^{57}. Maps of multiple sulphides require that the data reduction is based on the specific sulphide present in each pixel, so a series of data reductions was performed using the Fe contents of pyrrhotite, pentlandite, chalcopyrite and magnetite. The trace element concentrations were assigned to each laser spot in each map based on the data reduction appropriate for the dominant sulphide phase present, which was identified from the TIMA data. Rh^{103} and Pd^{105} concentrations in chalcopyrite are not reported in this study because of interferences by Cu^{63}Ar^{40} and Cu^{65}Ar^{40} respectively.

4.6 Co-localisation analysis

4.6.1 Development of methods to assess co-localisation

Co-localisation is comprised of two separate components: co-occurrence and correlation. Co-occurrence is the spatial overlap of two datasets, while correlation describes the extent to which the datasets are in proportion to one another within the mapped area (Dunn et al., 2011). Qualitative assessments may be made by merging two single channel images (e.g. green and red) so that areas of overlap appear yellow. Quantitative assessments of overlap require simultaneous evaluation of spatial and signal intensity in a combined dual channel image; co-localisation is considered to occur when the locations and intensities of pixels are within a specified range (Penarrubia et al., 2005). A number of software packages have been developed to perform quantitative image-based co-localisation analysis and measure the co-localisation through one or more statistical parameters.

A variety of parameters are used to quantify co-localisation, summarised by Bolte and Cordelieres (2006) (and references therein). Most of these methods are based on the Pearson Correlation Coefficient (PCC), as summarised below. If the spatial distribution of two populations are independent then no co-localisation exists, other than random overlap. When two populations are co-localised, correlations exist that exceed those expected for random overlap.

4.6.2 Pearson Correlation Coefficient

The Pearson Correlation Coefficient (PCC) is a measure of the linear correlation between two variables (Equation 4.1). Correlations may be positive or negative, with a perfect positive correlation manifesting as a set of data points that lie on a line. The value of the PCC is commonly expressed as r and ranges from -1 to 1; 1 indicates a perfect positive correlation and -1 indicates a negative correlation. For the purposes of this study, dual channel images (e.g., maps of two elements) were split into two images, one for each channel, and the greyscale values of the pixels plotted against each other. Typically, dual channel images are split into red and green pixels, and the intensities of each pixel in the green and red images are used as the x- and y-coordinates respectively on a scatter plot (Bolte and Cordelieres, 2006).

There are limitations to the use of PCC to quantify co-localisation as described by Bolte and Cordelieres (2006). The PCC is sensitive to variations in pixel intensity, with differences in intensity between the colour channels changing the pixel distribution and consequently changing the calculated PCC. Furthermore PCC is also influenced by random noise, tending towards 0 with increasing noise (Bolte and Cordelieres, 2006). We managed these limitations by setting the brightness of the background pixels to zero to restrict noise interference, and editing the red and green channels to ensure intensities are in proportion.

$$r = \frac{\sum_i (R_i - R_{\text{av}}.(G_i - G_{\text{av}})}{\sqrt{\sum_i (R_i - R_{\text{av}})^2 . \sum_i (G_i - G_{\text{av}})^2}} \tag{4.1}$$

Where R_i is the intensity of the first colour (red) in pixel i, R_{av} the arithmetic mean of the intensity of the red pixels; G_i and G_{av} are intensities of the second colour (green) in the pixel i and the arithmetic mean of the intensity of the green pixels, respectively.

Manders Overlap and Co-localisation Coefficients

The Manders Overlap Coefficient (MOC) is based on the PCC and omits the subtraction of average pixel intensities to avoid negative values that can be hard to interpret (Equation 4.2) (Manders et al., 1993). As a consequence, the MOC is effectively independent of signal proportionality (differences in signal intensity between the two colour channels or distributions being analysed) and is a better measure of co-occurrence (the proportion of pixels in both channels with positive values) than co-localisation (Dunn et al., 2011).

$$MOC = \frac{\sum_i (R_i . G_i)}{\sqrt{\sum_i R_i^2 . \sum_i G_i^2}} \tag{4.2}$$

The MOC ranges between 0 to 1, with 0 indicating non-overlapping images and 1 representing complete co-localisation, the numerator in Equation 4.2 contributes a significant value when R_i and G_i belong to a voxel (a point on a regular grid in three-dimensional space) of one of the co-localising objects (where both R_i and $G_i > 0$) (Manders et al., 1993). The numerator is proportional to the number of co-localising objects while the denominator is proportional to the number of co-localising and non co-localising objects. The result of this calculation is strongly influenced by the ratio of the number of objects in both components analysed. Consequently, Manders et al. (1993) advised division of the MOC into two separate coefficients, M_1 and M_2 one for each component/channel as defined by equations

$$M_1 = \frac{\sum_i R_{i,coloc}}{\sum_i R_i} \tag{4.3}$$

and

$$M_2 = \frac{\sum_i G_{i,coloc}}{\sum_i G_i} \tag{4.4}$$

Where $R_{i,coloc} = G_i$ if $R_i > 0$ and $G_{i,coloc} = 0$ if $R_i = 0$. The Manders Co-localisation

Coefficients (MCC) M_1 and M_2 are defined as the co-localisation coefficients and are proportional to the intensity of co-localising objects in each colour channel of the image relative to the total intensity in that component (Manders et al., 1993). Each coefficient provides a measure of the fraction of the specified component that is co-localised with the second component. Again, this is a measure sensitive to noise; noise is managed by setting a threshold to the estimated background.

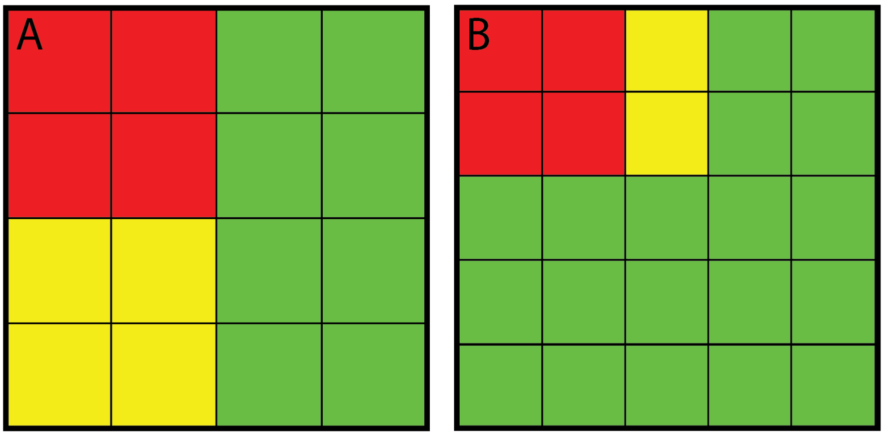

Figure 4.6.1: Grids illustrating distributions of red and green coloured pixels. Yellow indicates where the red and green distributions co-occur; 4.6.1A: 8 red pixels and 12 green pixels co-occur in 4 pixels; 4.6.1B: 6 red pixels and 21 green pixels co-occur in 2 pixels. See text for application to MOC/MCC.

The extent to which the M_1 and M_2 coefficients are independent of the object ratio bias intrinsic to the MOC calculation can be investigated by calculating co-occurrence for the pixel grids in Fig. 4.6.1. In these calculations M_1 indicates the proportion of the red pixel population co-occurring with green pixels, and M_2 indicates the proportion of the green pixel population co-occurring with red pixels. For the 16 pixels in Fig. 4.6.1A an MOC value of 0.41 is calculated, with M_1 and M_2 values of 0.50 and 0.33 respectively. For Fig. 4.6.1B a grid of 25 pixels give rise to an MOC value of 0.18, an M_1 value of 0.33 and an M_2 value of 0.10. With increasing numbers of green pixels relative to red, the MOC value tends towards the M2 value and becomes less representative of overall co-occurrence in both pixel populations.

Costes method

To resolve issues related to quantification of co-localisation for populations with intermediate r values (i.e., values indicating that co-localisation is neither strongly positive or negative), Costes et al. (2004) developed a two-part automatic method to measure co-localisation within images. This method uses first a statistical significance test to evaluate the probability that significant co-localisation exists in the region of interest, based on the use of the null hypothesis of a false positive co-localisation generated by the coincidental arrangement of random pixels. This is accomplished using an algorithm to automatically threshold images and calculate an r value, sidestepping the operator bias inherent in an operator-set threshold. The objective of the significance test is to determine whether a measured r value is significantly greater than an r value calculated from components with random overlap and comprises scrambling the pixels in one image so that only correlation from random overlap is measured. This randomisation and measurement process is repeated a number of times, producing a probability distribution for random overlap that can be compared to the overlap measured using the unscrambled image. The result is the probability (P-value) of genuine co-localisation; Costes et al considered that a P-value of > 0.95 indicated statistically significant co-localisation. In that study this approach was able to identify significant co-localisation in computer generated images that included as little as 3% predetermined co-localisation with P-values > 0.95.

Applying co-localisation analysis to geological questions

The viability of co-localisation analysis for our geological case study was tested using simple images to confirm that the calculated parameters were as expected. In the first test, grids of red and green spots that were perfectly co-located were tested (Fig. 4.6.2A, 4.6.2B). The coloured spots were placed against a zero-intensity background to facilitate easy thresholding. The pixel dimensions are identical for both images.

Analysis of images Fig. 4.6.2A and Fig. 4.6.2B returns an r value of 1.0, an M_1 value of 1 and an M_2 value of 1; indicating perfect positive correlation, and that the entirety of both grids overlap each other. The significance test from the Costes method returns a value of 1, indicating the presence of significant co-localisation.

For the second test Fig. 4.6.2C was used. In this test, the grids of coloured spots are completely non-overlapping. Analysis of the channels in this image returns an r value of 0, an M_1 value of 0 and an M_2 value of 0; there is no detectable co-localisation, and the grids do not overlap. This is supported by a P-value of 0 indicating no significant co-localisation. In Fig. 4.6.2D a portion of the green grid is overlapped by a smaller red grid, with the overlapped green and red shown in yellow. Splitting Fig. 4.6.2D into red and green channels and performing the analysis returns an r value of 0.45, an M_1 value of 1, an M_2 value of 0.25 and a P-value of 1. The MCC values correctly identify the proportions of the grids that overlap, the r value of 0.45 signifies a positive correlation and the P-value indicates significant co-localisation.

With these basic principles established and the operation of the test validated, we apply the tests to a more geological, albeit still synthetic, test dataset. We used the red channel to represent a fracture within a rock (Fig. 4.6.3A) and a green channel to illustrate the distribution of an element in the same area (Fig. 4.6.3B). Analysis of these images returns an r value of 0.45, an M_1 value of c. 0.95 and an M_1 value of 0.27. The implication of these results is that 95% of the fracture co-occurs with the

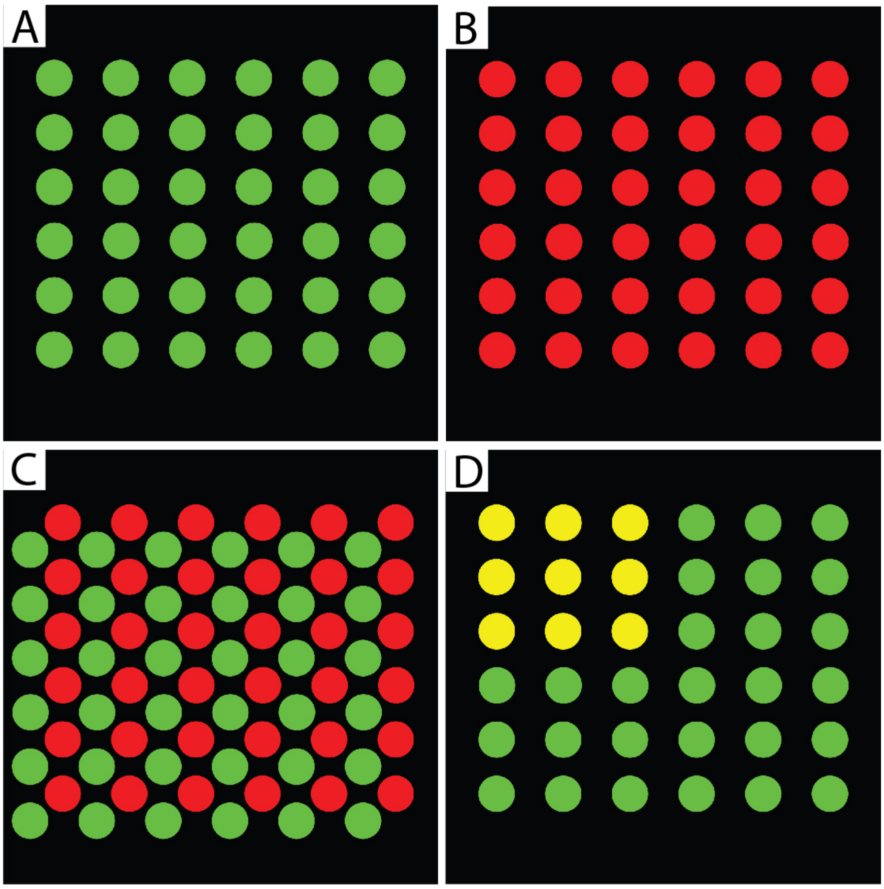

Figure 4.6.2: A, B: Image set used to demonstrate perfect positive co-localisation. The coloured dots in both images overlap completely; C, D: Second image set used to further test simple co-localisation scenarios. 4.6.2C depicts coloured grids illustrating perfect negative co-localisation. 4.6.2D depicts coloured grids showing partial co-localisation.

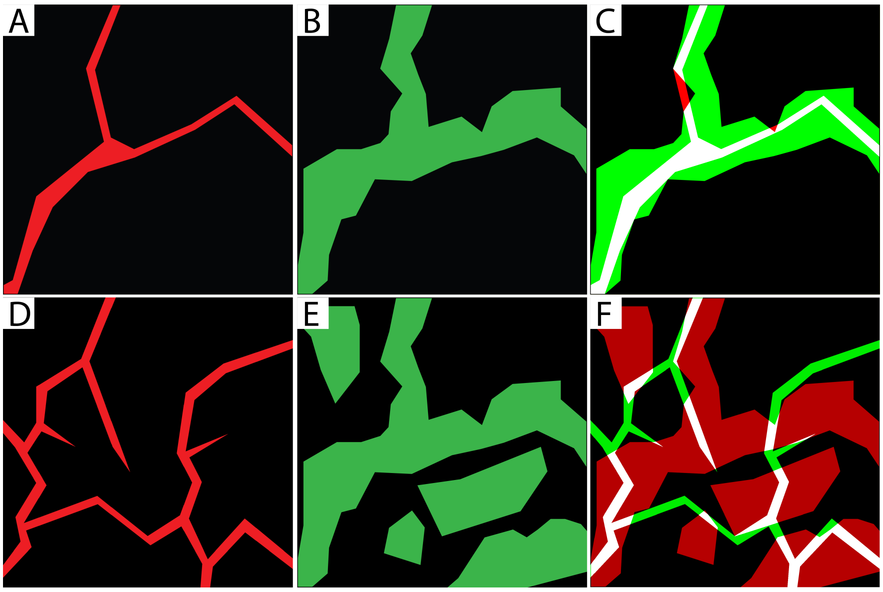

Figure 4.6.3: Third image set used to apply co-localisation analysis to more geologically relevant synthetic datasets. 4.6.3A: Red channel representative of an imagined fracture; 4.6.3B: green channel representative of an imagined element distribution related to fracture in 4.6.3A; 4.6.3C: composite image of red and green channels, illustrating overlap; 4.6.3D: more complex representative fracture network; 4.6.3E: channel representing distribution of an element not colocalised with fracture network in 4.6.3D; 4.6.3F: Composite image of channels in 4.6.3D, 4.6.3E.

element dataset while 27% of the element dataset overlaps the fracture (Fig. 4.6.3C). An r value of 0.45 in tandem with a P-value of 1 indicates significant and positive co-localisation between coloured pixels in both channels. Geologically these values are indicative of co-localisation between the fracture and the element in question, consistent with a standard visual geological interpretation.

The next test involved a different, more complex, fracture network (Fig. 4.6.3D) and element distribution (Fig. 4.6.3E). The composite image shows that the two datasets are not co-localised (Fig. 4.6.3F). These images return an r value of 0.07, M_1 value of 0.55 and M_2 value of 0.14; that is, 55% of the fracture network co-occurs with the element dataset, while only 14% of the distributed element co-occurs with fractures. These figures, in conjunction with an r value close to zero (no linear correlation), should be interpreted as an indication that there is no co-localisation between the two datasets. A P-value of 0 supports this and suggests no evidence of non-random co-localisation. We conclude that co-localisation analysis is a powerful tool that can be applied to geological case studies to further quantify relationships.

Application of co-localisation analysis to the Fraser Zone samples

Co-localisation analysis was applied to assess the extent of co-localisation between fracture maps constructed from the TIMA analysis and element datasets derived from the laser ablation analysis. The objective of the analysis was to recognise the elements that show a statistically significant co-location with the fractures, and to use this information to help to differentiate between element distributions controlled by primary magmatic processes and those controlled by processes related to subsequent metamorphism.

The TIMA maps were used to locate suitable areas for laser mapping and to input the laser spot co-ordinates. This simplified the task of matching the spatial co-ordinates of TIMA and laser data. The TIMA maps were processed to produce images in which the fractures are shown in red of a uniform intensity. The element maps were processed using the Surfer software with black-green intensity scales; black indicates areas with zero or near-zero element concentrations (ppm), and green areas show the concentration of the element of interest, with pixel brightness proportional to element concentration. The element maps were gridded using nearest neighbour values so that the number of grid nodes matched the number of laser spots. The images were checked carefully and edited as necessary to ensure that areas of zero element concentration were also areas of zero pixel intensity. The resolution of the fracture maps was adjusted using Adobe Photoshop so that the processed fracture and element maps had identical resolutions, which is essential for co-localisation analysis. Co-localisation analysis was performed using the Fiji (ImageJ) software. The Costes P-values were calculated based on 100 image randomisations and compared to the corresponding r values.

4.7 Results

4.7.1 Petrography

GSWA219069 (Sulphide breccia)

This sample comprises pyrite (approx. 58.6%), pentlandite (approx. 5.8%), and 1–2 mm granular chalcopyrite (approx. 2.6%) (Fig. 4.7.1A). Pyrite is texturally massive and present as approx. 1–3 mm subhedral grains. Minor (<1%) fine grained (<100 µm) marcasite is present within pyrite but cannot be distinguished in the TIMA analysis. Fine grained (<1 mm) pentlandite occurs as ribbons and loops through pyrite and around chalcopyrite, or as flames within pyrite (Fig. 4.7.1B). Chalcopyrite and pentlandite are predominantly confined to narrow bands or domains across the samples, consistent with remobilisation. The substantial pyrite component is atypical of a primary magmatic sulphide assemblage. An extensive network of fractures filled with serpentine (approx. 21.7%) and magnetite (approx. 1.9%) cut the sulphides, and some of the fractures host clusters of acicular carbon (Fig. 4.7.1C). These clusters of micron scale carbon needles are found exclusively within voids and fractures.

GSWA219070 (Sulphide breccia)

The sulphide assemblage of GSWA219070 is primarily massive anhedral pyrrhotite (approx. 31.6%), pyrite (approx. 22.3%), pentlandite (approx. 6.6%), and chalcopyrite (approx. 5.1%) (Fig. 4.7.1D–F). Pyrite forms approx. 1–3 mm subhedral to anhedral grains. Fractures cross-cutting pyrite are infilled with magnetite. Minor (<1%) marcasite is present as clusters of small (50–100 µm) anisotropic grains within isotropic pyrite.

Pentlandite radiates in haloes from fractures where they intersect pyrrhotite and forms rims on chalcopyrite (Fig. 4.7.1F). Chalcopyrite occurs as anhedral approx. 0.5–4 mm grains and shows morphological indications of remobilisation including grain rounding and elongation. This sample includes a larger fraction of silicate material than GSWA219069; it includes plagioclase (approx. 9.2%) and actinolite (approx. 1.1%), and shows fracturing comparable to that seen in 219070. The fractures show a common orientation.

4.7.2 TIMA results

The mineral modes were quantified by TIMA and the modes of the most abundant minerals are summarised in Table 4.7.1.

Primary Phases Lithology	219069 Sulphide breccia	219070 Sulphide breccia
Pyrite	58.6	22.3
Pyrrhotite	0.4	31.6
Pentlandite	5.8	6.6
Chalcopyrite	2.6	5.1
Magnetite	1.9	5.3
Serpentine	21.7	-
Plagioclase	-	9.2
Quartz	2.5	2.0
Actinolite	-	1.1
Potassium feldspar	0.7	0.7

Table 4.7.1: TIMA-derived mineral modes for samples 219069, 219070.

4.7.3 Element concentrations

Manganese

Concentrations are, unless otherwise stated, the median concentrations for the specified sulphide phase. Concentrations of Mn in analysed sulphides in samples 219069

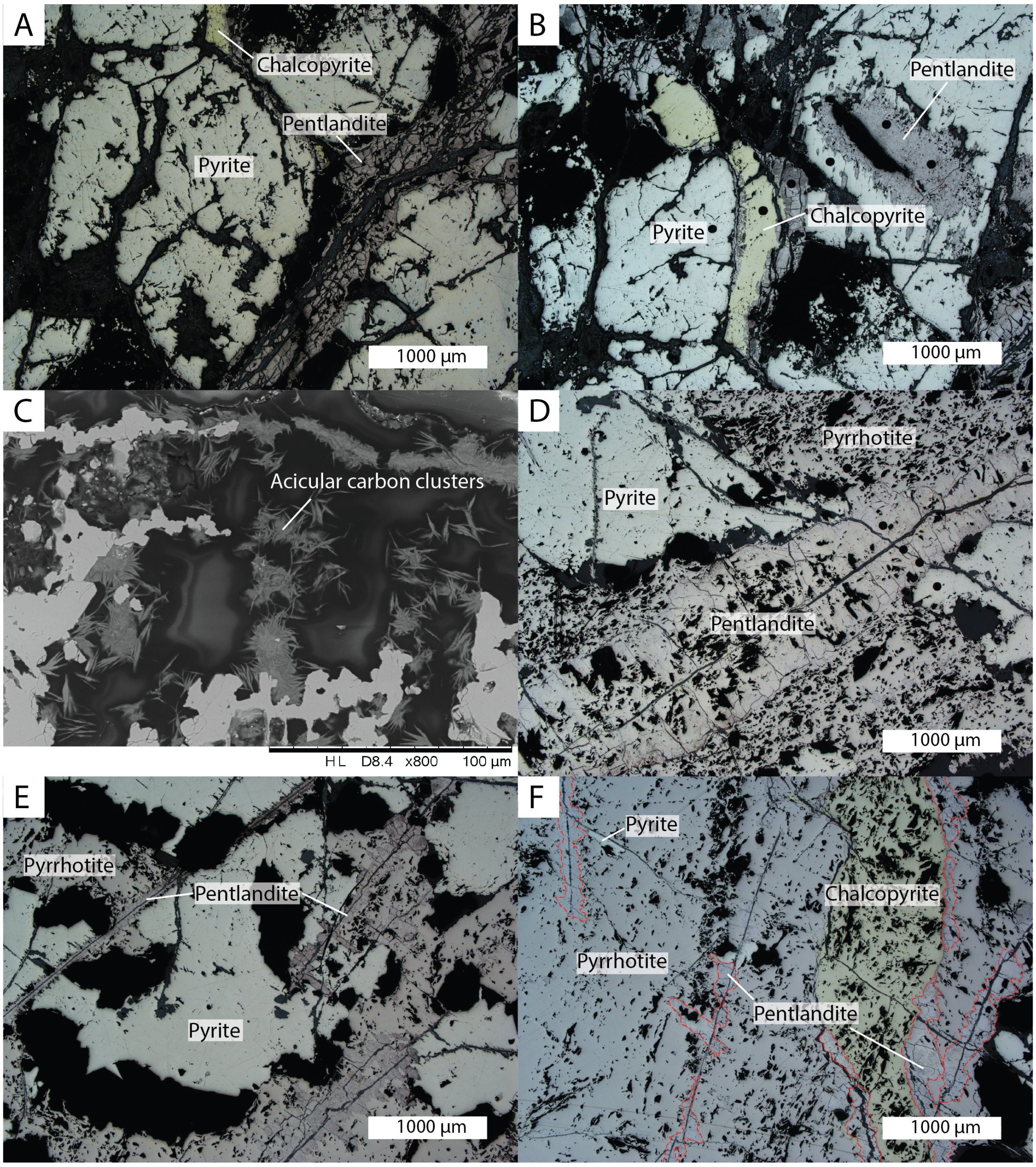

Figure 4.7.1: A: 219069, reflected light, anhedral pyrite and ribbon-like pentlandite; B: 219069, reflected light, pentlandite flames within pyrite; C: 219069, SEM image of clusters of acicular carbon within voids; D: 219070, reflected light, massive pyrrhotite, and pentlandite radiating from fractures; E: 219070, reflected light, radiating haloes of pentlandite where fine fractures intersect pyrrhotite; F: 219070, reflected light, granular chalcopyrite with a pentlandite rim. Pentlandite is outlined in red.

Element	Pyrrhotite			Pentlandite			Chalcopyrite			Pyrite		
	n=6			n=126			n=93			n=112		
	Median	Min	Max	Median	Min	Max	Median	Min	Max	Median	Min	Max
^{51}V	0.414	0.095	1.67	0.709	0.046	9.37	0.048	0.023	6.11	0.135	0.018	15.81
^{55}Mn	296	146.2	397	120.75	29.5	533	46.3	1.2	842	97.95	4	1217
^{59}Co	1044	358	7250	26400	520	32140	13.9	0.52	828	195	20.3	1810
^{60}Ni	250050	97800	503300	312500	127900	384000	139	3.03	9200	25600	639	156000
^{65}Cu	181.85	113	389	208.5	60.5	37700	371000	6500	439000	22.25	0.55	310
^{66}Zn	35.6	14.2	56	7.45	0.8	26200	259	43.9	2490	3.4	0.2	90
^{75}As	0.445	0.22^1	1.30	0.36	0.072	1.66	0.25	0.17	32	0.19	0.081	1.22
^{82}Se	40.1	32.2	50.1	28.7	18	57.6	22.4	0.55	42.4	17.3	0.62	34.2
^{103}Rh	0.027	0.008	0.054	0.01795	0.0055	1.344	-	-	-	0.0072	0.0019	0.042
^{105}Pd	0.169	0.069	0.56	0.3985	0.0052	3.22	-	-	-	0.03	0.0044	1.4
^{106}Ag	13.815	7.15	33	107.1	6.18	289	18.57	3.5	59.6	2.835	0.54	58.83
^{121}Sb	0.105	0.074^1	0.22^1	0.1775	0.035	5.1	0.475	0.071	7.83	0.11	0.03	0.877
^{130}Te	4.645	3.19	7.6	1.995	0.34	17	1.97	0.46	142	2.128	0.16	21
^{182}W	0.605	0.34	1.95	0.015	0.0012	1.81	0.015	0.002^1	0.39	0.018	0.0024	1.95
^{187}Re	1.176	0.178	2.37	0.173	0.068	1.62	0.152	0.001	1.51	0.2075	0.0197	2.55
^{192}Os	0.06	0.023^1	0.146	0.0131	0.0032	0.051	0.008	0.003	0.78	0.01265	0.0031	0.31
^{193}Ir	0.012	0.007^1	0.019	0.0047	0.0006	0.036	0.005	0.002	0.034	0.00485	0.0015	0.016
^{195}Pt	1.405	0.021^1	6.4	0.018	0.0017	2.15	0.029	0.005	2.8	0.0135	0.0036	11.2
^{197}Au	0.025	0.008^1	0.37	0.0104	0.00222	0.19	0.02	0.003	0.139	0.0065	0.0007	0.09
^{208}Pb	16.775	9.6	87.1	83.85	9.27	430	58.6	0.83	640	3.535	0.062	82
^{209}Bi	3.845	1.84	6.5	4.49	0.472	23.8	4.77	0.051	15.49	0.679	0.101	12.6

Table 4.7.2: Minimum, median and maximum concentrations (ppm) for all elements analysed in 219069. ^{1}Indicates limit of detection value used.

Element	Pyrrhotite			Pentlandite			Chalcopyrite			Pyrite		
	n=75			n=187			n=82			n=61		
	Median	Min	Max	Median	Min	Max	Median	Min	Max	Median	Min	Max
^{51}V	0.06	0.036	38	0.05	0.018	0.37	0.0395	0.028	0.85	0.029	0.017	7.1
^{55}Mn	25	1.4	18500	1280	2.09	11570	12.35	2.1	8080	3.39	0.58	7100
^{59}Co	115	58.6	8100	32200	3200	42000	11.55	0.625	6810	141	76.8	1230
^{60}Ni	6350	2310	253000	351000	104300	445000	203	24.3	75700	8770	4600	37700
^{65}Cu	28	7.2	31500	62	5.8	41600	407000	173500	446000	37.9	4	41500
^{66}Zn	1.38	0.097	218	0.95	0.17	630	470	115.8	890	1.58	0.2	87
^{75}As	0.45	0.28	2400	0.46	0.13	4.4	0.325	0.17	3.6	0.24	0.16	52
^{82}Se	31.9	17.6	900	29.3	16.28	44.2	24.45	11.6	39.4	31.7	21.9	218.3
^{103}Rh	0.007	0.002	3.7	0.0055	0.0011	1.28	-	-	-	0.0053	0.00089	1.21
^{105}Pd	0.037	0.008	17	0.5	0.042	2.81	-	-	-	0.016	0.0023	2.44
^{106}Ag	1.19	0.341	53.7	8.8	0.432	110.1	10.785	1.63	28.5	2.14	0.568	20.08
^{121}Sb	0.11	0.063	2300	0.13	0.059	660	0.082	0.039	410	0.052	0.033	270
^{130}Te	6.17	2.48	930	3.81	0.58	38	8.685	0.6	54	4.21	1.25	780
^{182}W	0.015	0.002	6.9	0.0099	0.0018	0.026	0.011	0.0035	0.018	0.0172	0.0029	2.5
^{187}Re	0.259	0.061	30	0.201	0.0039	1.68	0.0055	0.0009	0.51	0.248	0.0593	1050
^{192}Os	0.016	0.004	9.7	0.0101	0.0018	0.84	0.00965	0.0032	0.102	0.0085	0.0014	4.9
^{193}Ir	0.008	0.001	11	0.006	0.0012	0.036	0.00505	0.001	0.014	0.00415	0.0018	0.31
^{195}Pt	0.096	0.01	125	0.024	0.0052	10	0.042	0.0048	28	0.019	0.0038	109
^{197}Au	0.015	0.004	11	0.014	0.0019	0.149	0.0255	0.0033	5.4	0.0069	0.002	0.32
^{208}Pb	0.67	0.016	7600	11.4	0.127	74.8	5.09	0.69	78.8	0.6	0.019	520
^{209}Bi	0.243	0.063	37	3.79	0.26	63	4.025	0.899	24.4	0.146	0.0074	14.4

Table 4.7.3: Minimum, median and maximum concentraions (ppm) for all elements analysed in 219070. ^{1}Indicates limit of detection value used.

and 219070 are less than 296 ppm and 1280 ppm, respectively. There is a significant difference in the maximum concentrations between these samples, with a maximum Mn content of 1217 ppm in 219069 and 18500 ppm in 219070. The highest average Mn contents in 219070 are in pentlandite grains; Mn-rich pentlandite is common adjacent to fractures. Higher manganese concentrations occur within the fracture infill (Fig. 4.7.2).

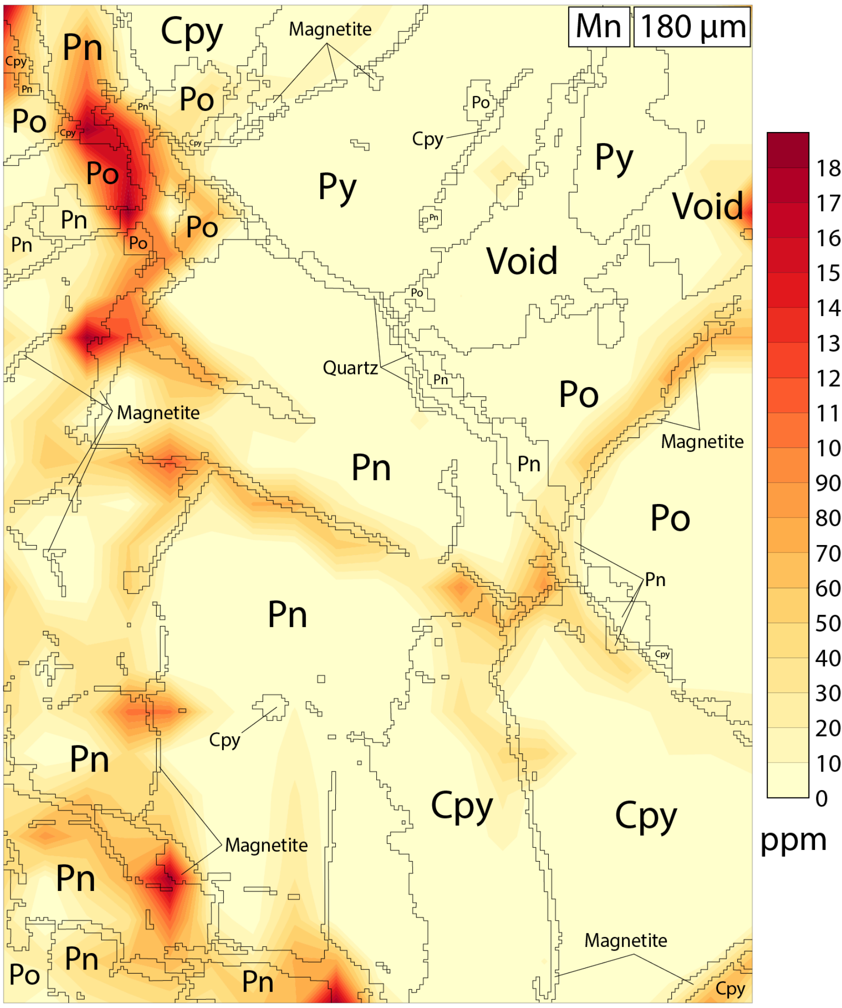

Figure 4.7.2: Element map illustrating Mn distribution across analysed area of 219070, with apparent concentration of Mn in and adjacent to fracture material. Scale is indicated in the inset figure in the upper right.

Cobalt, zinc, silver and lead

Cobalt is strongly partitioned into pentlandite (26400 and 32200 ppm in 219069 and 219070 respectively). Zinc is strongly associated with chalcopyrite with concentrations up to 470 ppm in GSWA219070. Zn concentrations in 219069 chalcopyrite are lower and more variable than those in 219070 chalcopyrite, with lower minimum (259 ppm) and higher maximum (2490 ppm) concentrations.

Chalcopyrite and pentlandite are the primary Ag-hosting sulphides with concentrations of 107.1 ppm and approx. 10.8 ppm in 219069 (pentlandite) and 219070 (chalcopyrite) respectively. Zonation is apparent in the distribution of Ag within pentlandite grains in 219069, with higher concentrations towards pentlandite grain cores (Fig. 4.7.3). Element mapping of 219070 illustrates elevated Ag concentrations close to grain boundaries, particularly towards boundaries adjacent to fractures (Fig. 4.7.4).

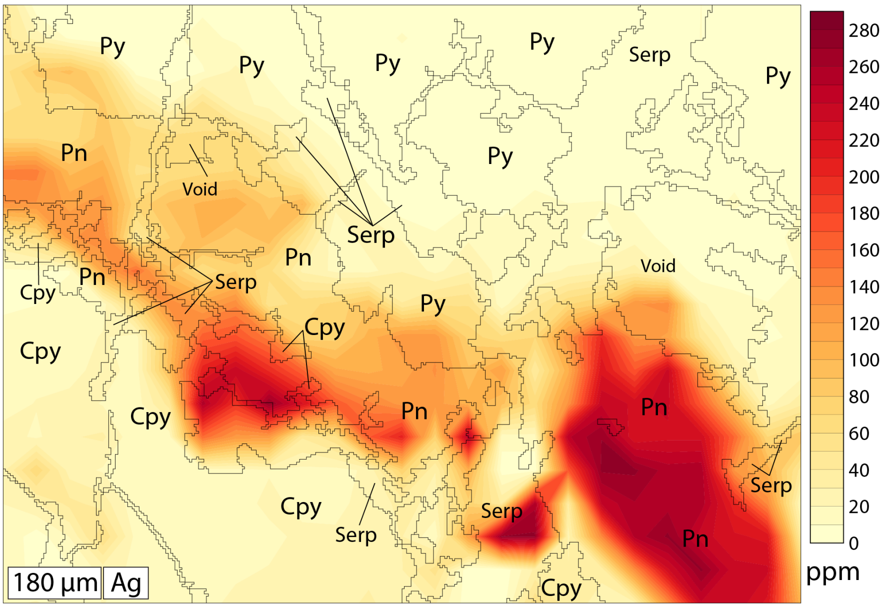

Figure 4.7.3: Element map of Ag distribution in 219069; note the high concentrations and Ag zonation within pentlandite grains.

The highest lead concentrations occur within pentlandite (83.85 and 11.4 ppm in 219069 and 219070 respectively) and chalcopyrite (58.6 and 5.09 ppm in 219069 and 219070 respectively). Lead concentrations are higher in all sulphides in 219069 than in the corresponding sulphide in 219070. Lead is not preferentially associated with a specific sulphide phase (Fig. 4.7.5).

Platinum group elements

Partitioning of the PGE between the sulphides is consistent with literature data. The highest concentrations of the IPGE analysed in this study (Os, Ir) were found in sulphide phases interpreted to have exsolved from MSS, though both were close to, or below, the limits of detection in most analyses. The highest concentrations of Os and Ir are within pyrrhotite (median values up to 0.06 and 0.012 ppm respectively in 219069 pyrrhotite). Palladium was sequestered mainly by pentlandite in both samples at approximately equal concentrations (median concentrations of approx. 0.4 ppm and 0.5 ppm, respectively). Platinum was below the limits of detection in most analyses. Where above the limits of detection, Pt concentrations are typically below 0.1 ppm, with an exception of the Pt concentration in 219069 pyrrhotite, which is approx. 1.4

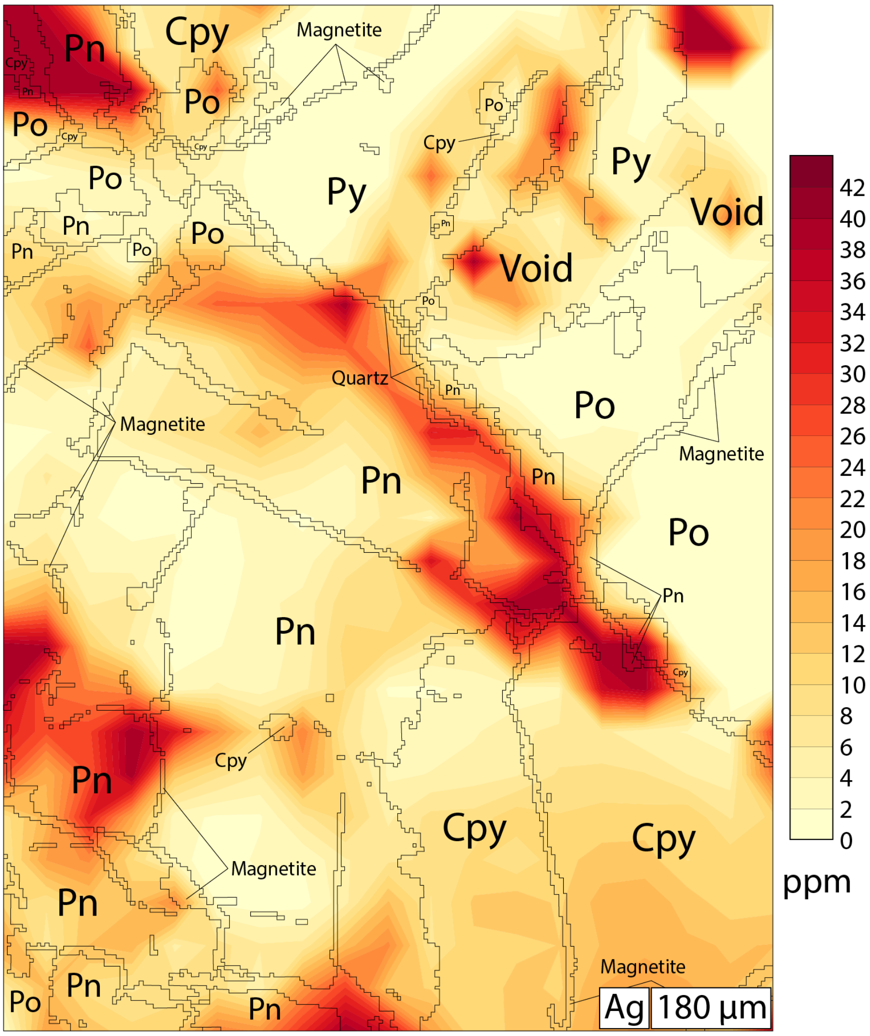

Figure 4.7.4: Element map of Ag distribution in 219070, Ag is concentrated within pentlandite grains and adjacent to fractures.

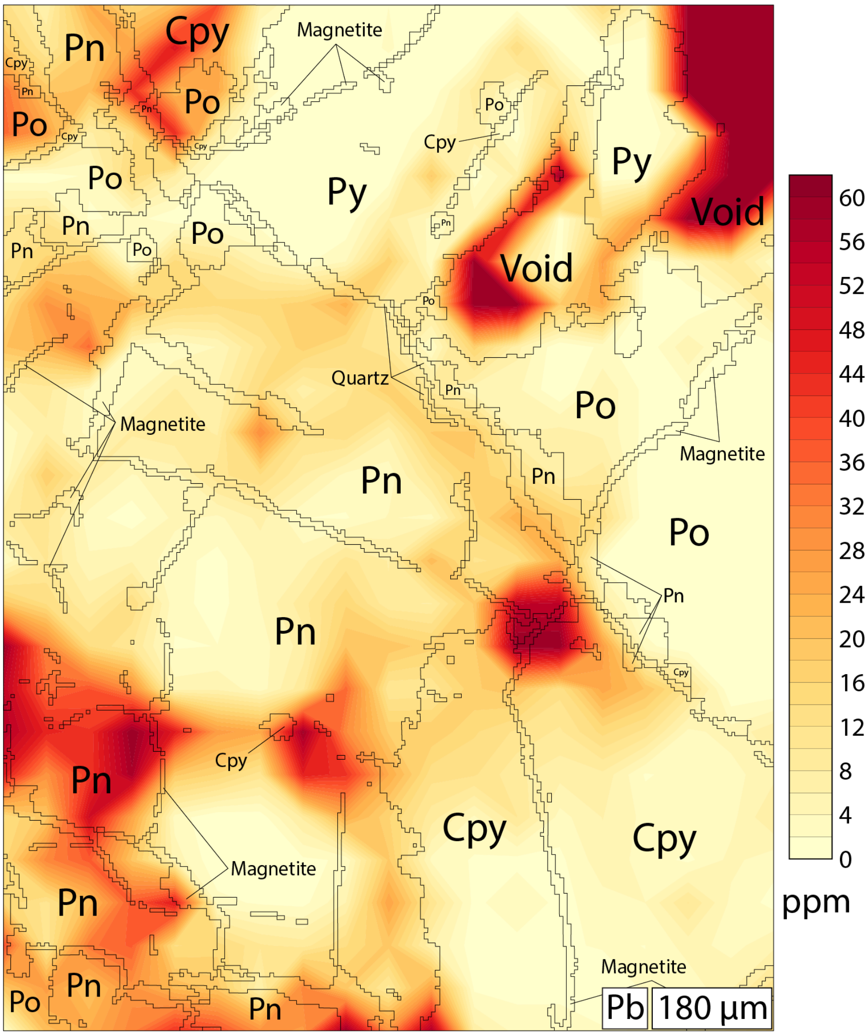

Figure 4.7.5: Element map of Pb distribution across analysed area of 219070. Note Pb concentrations within void areas are not reliable.

ppm.

Chalcogens and semi-metals

The chalcogens and semi-metals (Se, Te, As, Bi, Sb) show a variety of partitioning behaviours. Selenium is approximately equally distributed among the sulphide phases, with median concentrations between 22.4 ppm (219069 chalcopyrite) and approx. 40 ppm (219069 pyrrhotite). Partitioning of Te differs between samples; pyrrhotite is the dominant host of Te (approx. 4.6 ppm) in 219069, with pentlandite, chalcopyrite and pyrite each containing approx. 2 ppm. In 219070, the Te distribution is more variable and slightly higher median concentrations for pyrrhotite (6.17 ppm); pentlandite (3.81 ppm), chalcopyrite (8.69 ppm) and pyrite (4.21 ppm). Bismuth is equally distributed among pyrrhotite, pentlandite and chalcopyrite in 219069 (3.845, 4.49 and 4.77 ppm respectively) and pentlandite and chalcopyrite in 219070 (3.79 and 4.025 ppm respectively); Bi concentrations within the other sulphides are typically less than 0.7 ppm. Most arsenic analyses were close to, or below, detection limits in all analysed material analysed. Median As concentrations are no higher than 0.46 ppm (219070 pentlandite). A small number of analyses with significantly higher (>10 ppm) concentrations indicate local concentration of As within small regions of sulphide material, but no discrete As rich phases (e.g., arsenides) were observed. The concentration of Sb is close to or below detection limits, with most median concentrations less than approx. 0.18 ppm, with the exception of 219069 chalcopyrite (0.475 ppm).

Other elements

Gold concentrations are close to or below detection limits in sulphide phases other than chalcopyrite in both samples with chalcopyrite hosting less than 0.03 ppm Au (median). Most analyses of W in 219069 chalcopyrite and 219070 pyrrhotite, chalcopyrite and pentlandite are close to or below the detection limits. The highest W concentration is approx. 0.6 ppm in 219069 pyrrhotite.

4.8 Discussion

Characterisation of post-crystallisation modification of the sulphides requires that we identify whether element distributions are solely magmatic or show evidence of modification by secondary processes. The distribution of many elements is consistent with sulphide crystallisation as the dominant control, but others do not conform to previously established partitioning behaviour, or are associated with features attributed to secondary processes such as fractures. Textural and geochemical evidence was combined with the co-localisation analysis to recognise element distributions that were predominantly proximal to fracture networks and, by extension, transport by an aqueous phase through these fracture networks.

4.8.1 Primary magmatic controls on sulphide compositions

Chalcophile element data are typically normalised to mantle values and presented on spider-type diagrams with the elements arranged from left to right in increasing order of incompatibility (e.g., Barnes and Lightfoot, 2005). This facilitates interpretation of the processes that control element distributions within sulphides (e.g., PGE contents). Improvements in analytical techniques, especially laser ablation, and further experimental investigations of the partitioning behaviour of trace elements have enabled analyses of a much wider range of elements than those used in earlier works.

To better utilise these data, Duran et al. (2016) presented alternative versions of the conventional spider-type diagrams that include a wider range of elements plotted left to right in decreasing order of compatibility in the first phase crystallising from magmatic sulphide liquids. An exception are the PGE, which are plotted together in order of increasing melting point to retain PGE patterns, rather than plotted in order of the MSS compatibility. In the present study, we use the diagram of Duran et al. (2016) to show more of the elements analysed.

Fractional crystallisation is one of the main processes that controls element partitioning among magmatic sulphides. After sulphide saturation, sulphide liquid separates from silicate magmas at approx. 1200°C (Naldrett, 2004), and chalcophile elements, including the PGE and base metals, partition preferentially into the sulphide liquid. The first phase to crystallise is Fe-rich monosulphide solid solution (MSS) at approx. 1180–950°C (Naldrett, 2004); Cu is concentrated in the remaining sulphide liquid (Kullerud, 1969; Dutrizac, 1976; Ebel and Naldrett, 1997; Sinyakova and Kosyakov, 2009). Nickel is initially incompatible within MSS — the partition coefficient of Ni between MSS and sulphide liquid is dependent on temperature and fS_2, increasing from approx. 0.2 to c. 1 between 1100°C and 900°C (Li et al., 1996; Barnes et al., 1997; Makovicky, 2002; Liu and Brenan, 2015; Barnes and Ripley, 2016). Crystallisation of MSS can be followed by crystallisation of iron oxides from the sulphide liquid. The iron oxides typically consist of magnetite ± exsolved ilmenite (Buddington and Lindsley, 1964; Naldrett, 1969). Below 900°C the Cu-rich sulphide liquid crystallises to form an intermediate solid solution (ISS) phase (Barnes and Ripley, 2016). As temperatures continue to decrease below 600°C, the MSS and ISS become unstable and precipitate pyrrhotite + pentlandite ± pyrite and chalcopyrite ± cubanite ± pyrite ± pentlandite respectively (Barnes and Ripley, 2016; Mansur et al., 2019). The partition coefficients between sulphide liquid and MSS, and MSS and ISS, dictate the distribution of the trace elements among the sulphide phases derived from MSS and ISS, and can be predicted if the precipitated sulphides and the residual sulphide and silicate liquids are assumed to have been at equilibrium.

Nickel initially partitions into Cu-rich liquids but decreasing temperature leads to increasing compatibility within the MSS. Consequently, Ni is distributed between pentlandite (Fe, Ni)$_9$S$_8$ and to an extent pyrrhotite (Fe$_{1-x}$S) in solid solution, where Ni-rich domains within pyrrhotite can exsolve to form pentlandite flame structures. Cobalt substitutes for Ni in the structure of pentlandite (Barnes and Lightfoot, 2005) so pentlandite is expected to contain the highest concentrations of Co.

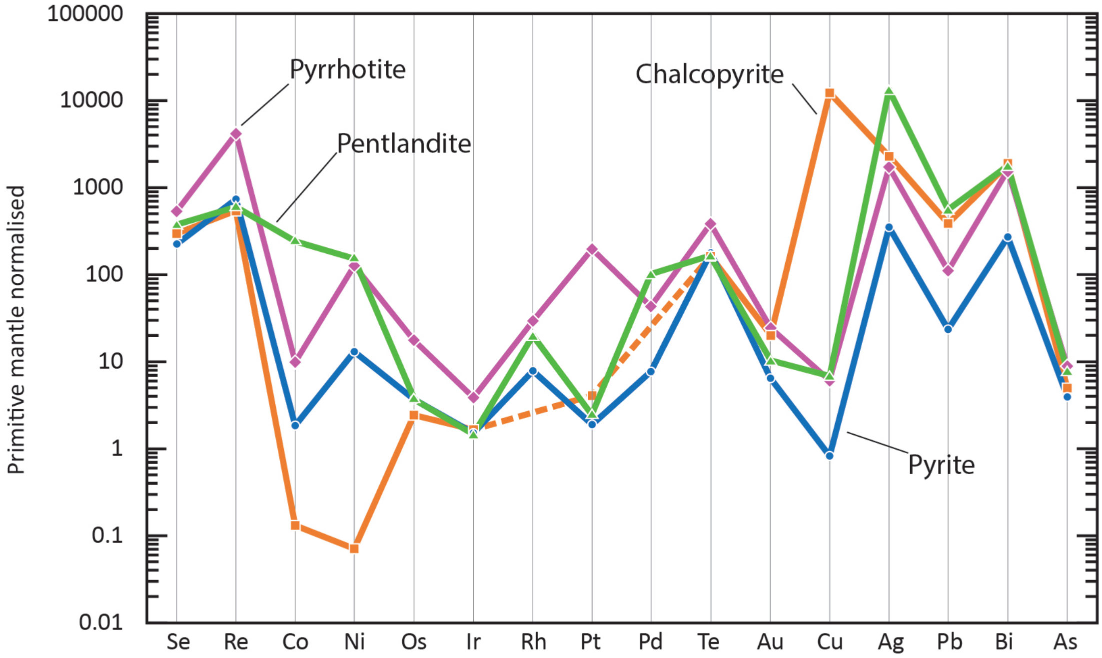

Figure 4.8.1: Primitive mantle normalised multi-element variation diagram of pyrrhotite, pentlandite, chalcopyrite and pyrite for sample 219069

The concentrations of mantle-normalised chalcophile elements within samples 219069 and 219070 were compared to chalcophile element distributions established as characteristic of fractional crystallisation (Figures 4.8.1, 4.8.2). This allowed recognition of elements that do and do not conform with established fractionation trends to be recognised.

Rhenium, Ir and Os are generally enriched in pyrrhotite and/or pentlandite relative to chalcopyrite in 219069 and 219070 (Figures 4.8.1, 4.8.2). Re, Ir, Os, Ru and Rh typically partition into MSS and end up sequestered by the pyrrhotite and pentlandite that exsolve from MSS (Barnes et al., 1994; Mungall et al., 2005; Godel and Barnes, 2008; Barnes et al., 2008). Platinum, Pd, Au and Ag are incompatible within MSS (Barnes and Ripley, 2016), and experimental work by Peregoedova (1998) showed that Pt, Pd (and by extension Au) are also incompatible in ISS. These elements typically concentrate into late stage melts that become enriched in Te, Bi, As and Sb and form PGM (Helmy et al., 2007). Platinum group minerals (PGM) were not found within 219069 or 21970. This might be a consequence of the low concentrations of the relevant elements (Pt, Pd, Au, Ag, Te, Bi, As, Sb) (Tables 4.7.2, 4.7.3) as a result of low R

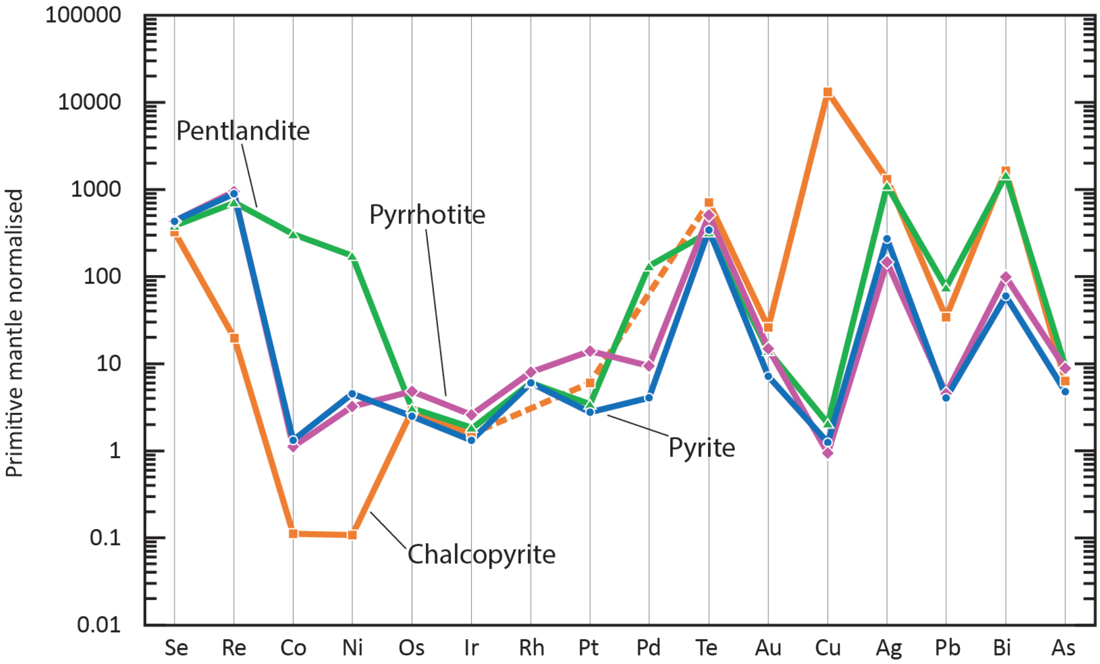

Figure 4.8.2: Primitive mantle normalised multi-element variation diagram of pyrrhotite, pentlandite, chalcopyrite and pyrite for sample 219070

factors or an early PGE-removing sulphide saturation event. Alternatively, the PGM might be present but not observed; tiny PGM grains (<3 microns) could have been missed by the TIMA and petrographic analysis. A single PGM grain can account for the bulk of Pt within analysed material (Duran et al., 2017), and such grains can be excluded during sampling, if the sample sizes are insufficiently large. We performed mass-balance calculations using the whole rock geochemistry data to assess the possibility that PGMs were present but overlooked (Tables 4.8.1, 4.8.2). Full details of the calculations are provided in Appendix 4.B. The results indicate that the measured Pt concentrations are more than accounted for by the Pt in pyrrhotite alone in both rocks. In contrast, the calculated budgets of Re and Au account for only 2%–70% of the whole rock concentrations. It was not possible to assess the possibility of Pd-bearing PGMs, because of the lack of robust Pd concentration data for chalcopyrite. One interpretation of these results is that Re- and Au-bearing PGM are likely to be present. However, the sample used for geochemical analysis is on a different scale to that used for the thin-section, and is likely to have contained different modes and relative proportions of the sulphides, so there is a high degree of uncertainty on the calculations.

Partitioning coefficients determined by Liu and Brenan (2015) indicate that Se is compatible within products of both MSS and ISS, while As, Te, Bi and Sb are incompatible in products of both MSS and ISS; As, Te, Bi and Sb may be present in small concentrations within MSS and ISS, but generally concentrate within a late stage melt (Holwell and McDonald, 2010). Here, the chalcogens and semi-metals broadly conform with

Sample	Phase	Weight fraction	Percentage (%)
219069	Pyr	0.1841	75.6
	Pn	0.0261	10.7
	Cpt	0.0333	13.7
219070	Po	0.0195	47.0
	Pyr	0.0138	33.2
	Pn	0.0058	14.0
	Cpt	0.0024	5.7

Table 4.8.1: Calculated weight fractions and proportions of BMS in whole rock. Po=pyrrhotite, Pyr=pyrite, Pn=pentlandite, Cpt=chalcopyrite.

Sample	Phase	Pt	Pd	Re	Au	As	Sb	Bi
219069	Pyr	135.7	24.1	35.5	1.3	1.5	12.7	7.1
	Pn	24.7	45.5	4.2	0.3	0.4	2.9	6.7
	Cpt	50.8	-	4.7	0.7	0.4	9.9	9.0
	All	211.2	69.6	44.3	2.2	2.3	25.4	22.8
219070	Po	124.8	11.3	31.6	2.3	0.9	1.5	1.1
	Pyr	17.5	3.4	21.4	0.7	0.3	0.5	0.5
	Pn	9.3	45.3	7.3	0.6	0.3	0.5	5.0
	Cpt	6.7	-	0.1	0.5	0.1	0.1	2.2
	All	158.2	60.0	60.3	4.1	1.6	2.7	8.7

Table 4.8.2: Calculated proportions (%) of PGE and chalcogens hosted within BMS. Po=pyrrhotite, Pyr=pyrite, Pn=pentlandite, Cpt=chalcopyrite. Pd excluded in chalcopyrite. Proportions not calculated for po in 219069 as minimal ($< 1\%$).

these established partioning behaviours. Se is the most compatible of these elements and substitutes for S; this is consistent with the similar Se concentrations in all sulphides and with similar Se distribution documented in other localities (Paktunc et al., 1990; Czamanske et al., 1992). Tellurium is also distributed relatively evenly among the different sulphides; Te, much like Se albeit more incompatible, can substitute for S in sulphides and has no particular affinity for specific sulphide phases (Helmy et al., 2007). The mass balance calculations indicate that the sulphides might not contain all of the As, Sb and Bi in the whole rock. It is possible that the PGM contain these elements, but, as for the sulphides, the uncertainties on the calculations are large.

4.8.2 Co-localisation between element distributions and the fracture networks

Both samples contain extensive fracture networks associated with minerals that are products of post-mineralisation deformation and metamorphism (e.g., serpentine). There are subjective and qualitative spatial relationships between the distributions of elements such as Mn and these fracture networks.

Sample	Element	r	M_1	M_2	P
219069	Ag	-0.10	0.49	0.20	0
	Mn	0.40	0.82	0.43	1
	Pb	-0.18	0.40	0.16	0
219070	Ag	0.12	0.77	0.14	1
	Mn	0.30	0.78	0.24	1
	Pb	0.04	0.78	0.12	1

Table 4.8.3: Compiled results of the co-localisation analysis comparing the fracture network with maps of selected elements.

Elements that showed varying degrees of apparent co-localisation, based on a qualitative assessment, were selected for the co-localisation analysis (Table 4.8.3). The r value is the PCC, M_1 and M_2 are the MCC values: M_1 shows the fraction of the fracture map that co-occurs with the element distribution, and M_2 shows the fraction of the element map that co-occurs with the fracture map.

In sample 219069, only Mn showed a statistically signficant relationship between the element distribution and fracture network, with 82% of the fracture network coincident with high Mn concentrations (Table 4.8.3). In sample 219070, Ag, Mn, and Pb showed statistically significant relationships with the fracture networks, with 77%–78% of the high-concentration pixels for each element co-located with the fracture network. The mechanisms underlying these relationships are discussed below.

Intragranular variations in silver and modification of silver content by post-sulphide exsolution processes

Silver is concentrated in pentlandite and chalcopyrite, which is consistent with known partitioning behaviour of Ag during sulphide exsolution. The concentration of Ag decreases from the core to the rim of pentlandite grains in 219069 (Fig. 4.7.3). This is interpreted as a record of Ag depletion within the melt as MSS crystallised within a closed system, and transfer of the zoning to MSS-derived pentlandite. In 219070, Ag is also concentrated within the pentlandite but the zoning is different. Instead of a core–rim decrease, the highest Ag concentrations occur on grain margins, including those adjacent to fractures (Fig. 4.7.4).

These observations are consistent with the results of the co-localisation analysis. The r values for Ag in samples 219069 and 219070 are -0.10 (P = 0) and 0.12 (P = 1), respectively, with M_1 and M_2 values of 0.49 and 0.20, and 0.77 and 0.14 respectively (Table 4.8.3). These results show a weak but positive co-localisation of Ag within fractures in 219070. Our preferred explanation for this pattern is that Ag was remobilised by alteration and fluid flow. An alternative possibility is deformation-induced element redistribution; Duran et al. (2016) suggested that heterogenous distributions of Ag, Bi and Pb within pentlandite and some pyrrhotite recorded deformation. However, if deformation was the cause of the heterogenous Ag distributions within 219070 then similar characteristics would be expected within the Ag within nearby 219069, which has undergone similar deformation, based on the brecciation textures.

4.8.3 Formation of sulphide breccia material and the operation of post formation processes

Both samples are described as magmatic sulphide breccias, which are thought to form in magmatic sulphide environments. The nomenclature and classification of sulphide ores are relatively loosely defined; recent work by Barnes et al. (2018) attempted to remedy this by defining 5 gradational textural types of massive and semi-massive ores: inclusion-free massive sulphide ores, sulphide matrix ore breccias, emulsion textured ores, vein-hosted sulphides and tectonic breccias. Brecciation and remobilised sulphides within a sample are strong indicators of formation within a dynamic environment. Breccias can represent material crystallised from sulphide slurries accumulated within a sulphide trap, with jumbled disrupted textures created by dislodgement, transportation and emplacement subsequent to accumulation. Disruption during post-crystallisation metamorphism is also possible; pentlandite and chalcopyrite are relatively ductile and easy to remobilise relative to the more brittle pyrrhotite and pyrite (Craig and Vokes, 1993). Tectonic breccias are common in the Thompson and Pechenga deposits, where massive sulphides interleaved between country rock and a magmatic body form an incompetent layer that focused deformation and formed a matrix to the brecciated silicate rocks (Barnes and Lightfoot, 2005).

The characteristics of samples 219069 and 219070 indicate that their formation processes were different.

Sample 219069 comprises approx. 67% sulphide minerals (approx. 87% of which is pyrite), approx. 22% serpentine and approx. 2% magnetite (Table 4.7.1). The extensive fracture network filled with serpentine records pervasive fluid flow, possibly associated with metamorphism.

In explaining the formation of 219069, it is necessary to understand the abundance of pyrite rather than pyrrhotite, the latter typically being a dominant sulphide phase in magmatic sulphide deposits, and the presence of mafic silicate material. Loop-textures and lamellar pentlandite form during the exsolution of pyrrhotite and pentlandite from MSS (Kelly and Vaughan, 1983) so their presence is consistent with the previous presence of pyrrhotite. Furthermore, the normalised chalcophile element pattern of 219069 pyrite mirrors the chalcophile element pattern of 219069 pyrrhotite, albeit with lower concentrations of Pt and Pd (Fig. 4.8.3). Small quantities of pyrite can exsolve from S-rich MSS below 700°C (Kullerud and Yoder, 1959; Naldrett et al., 1967) but this process is unlikely to produce a primary sulphide assemblage in which pyrite is the predominant phase. It is more likely that the mineralogy and textures record the replacement of pyrrhotite by pyrite, potentially facilitated by fluid flow. This conclusion is similar to that of Duran et al. (2015), based on studies of pyrite-rich (>10%) samples from the Lac des Iles deposit, the work of Piña et al. (2013) on pyrite from Aguablanca and the work of Smith et al. (2014) in the Bushveld Complex. Our samples also contain trace quantities of marcasite. The presence of marcasite is indicative of relatively acidic (<pH 5), low temperature (<240°C) conditions (Murowchick and Barnes, 1986; Schoonen and Barnes, 1991) during formation. The fact that marcasite is present only within pyrite in samples 219069 and 219070 suggests almost complete inversion of marcasite to pyrite following increases in pH and/or temperature.

The depletion of Pt and Pd in in pyrite relative to the inferred precursor pyrrhotite is interpreted as a consequence of element remobilisation by fluid flow during replacement. Most elements were effectively conserved in pyrite but small amounts of Pt and Pd were lost or redistributed locally. There is some textural evidence of post-brecciation deformation within 219069. For example, pentlandite lamellae and many of the fractures share common orientations, which indicates formation under non-hydrostatic stress. However, durchbewegung textures or a strong foliation were not identified. To summarise, sample 219069 is interpreted as a massive magmatic sulphide modified by post-crystallisation brecciation, with coeval fluid flow and associated element remobilisation.

Sample 219070 is comprised of approx. 66% sulphide material (22.3% of which is pyrite), approx. 5.3% magnetite and approx. 9% mafic material (plagioclase feldspar) (Table 4.7.1). This sample is different to sample 219069 in that there is less pyrite, and the pyrite that is present shows euhedral to subhedral morphologies and coexists with pyrrhotite, as well as the pentlandite and chalcopyrite which are also present in sample 219069. The pyrite is interpreted as a replacement of pyrrhotite, as in the case of sample 219069, based on the proximity of the two samples, and the similar chalcophile element patterns in pyrite and pyrrhotite (Fig. 4.8.3). We suggest differences between the pyrrhotite and pyrite chalcophile element patterns reflect local differences in the intensity of the same fluid-assisted alteration and replacement event.

Pentlandite in 219070 is predominantly confined to domains associated with fractures, implying that pentlandite exsolution might have been associated with fluid activity.

Co-localisation analysis indicates that Mn is co-localised with serpentine and magnetite fracture infill in both samples (Fig. 4.8.4, Fig. 4.7.2, Table 4.8.3). 82% and 78% of the fracture networks coincide with high Mn concentrations in samples 219069 and 219070, respectively. The Mn concentrations of the sulphides vary, but the highest concentration occurs in the pentlandite of sample 219070 (1280 ppm; Table 4.7.3). The most likely explanation for the observed co-localisation of fracture infill and Mn

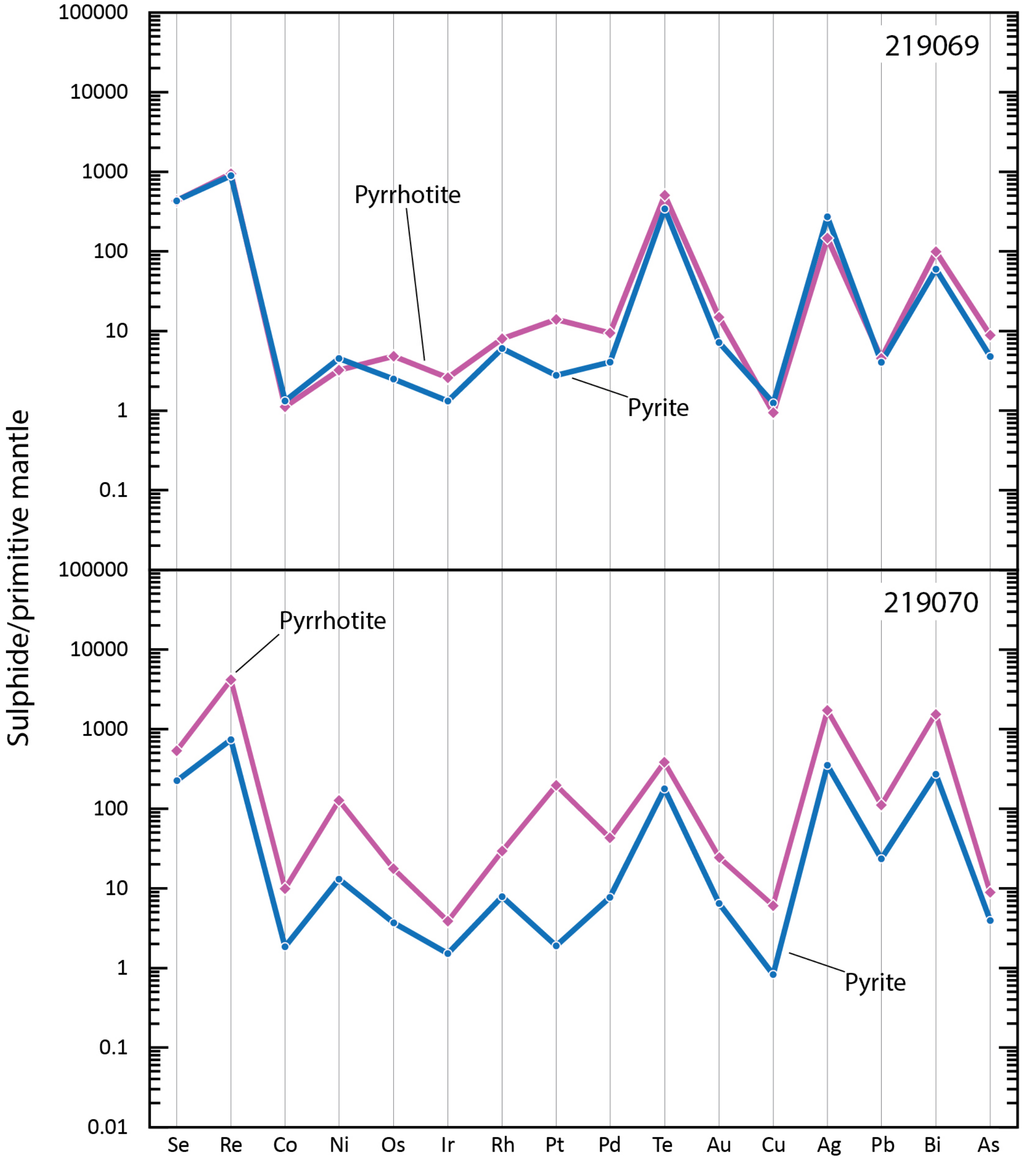

Figure 4.8.3: Primitive mantle normalised element diagrams of pyrrhotite and pyrite from 219069 and 219070.

is that Mn was introduced by fluids, based on the presence of serpentine, a hydrous mineral that records the introduction of an aqueous fluid phase. The fluid-derived Mn would have been captured by serpentine and magnetite filling the fractures, and by those sulphides adjacent to fractures. Magnetite is present within fractures where they intersect pyrite, which indicates that pyrite was replaced by magnetite in processes associated with the fracturing. Magnetite might have formed from Fe liberated by pyrrhotite replacement as the Fe:S ratio of the sulphide phase decreased.

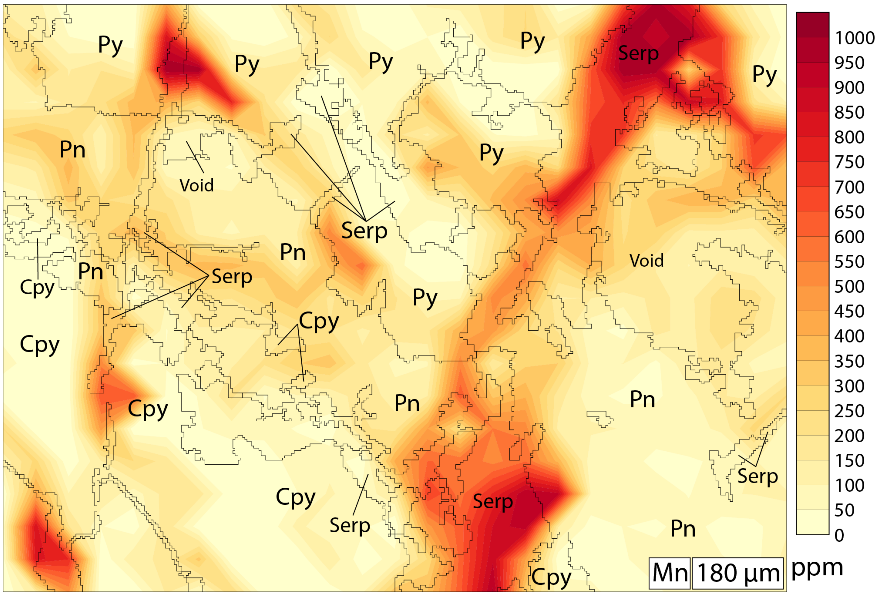

Figure 4.8.4: element map of Mn distribution across analysed area of 219069. Note the concentration of Mn within fracture infill material (predominantly serpentine) and adjacent sulphides.

In sample 219070, the distributions of Ag and Pb also show statistically significant relationships with the fracture network (Table 4.8.3). The extent and nature of the co-localisation shown by these elements differs significantly. However, each element is co-localised with a different portion of the fracture network (Figs. 4.7.2, 4.7.4, 4.7.5). These results might indicate that these elements were remobilised at different times or in different fluids. For example, Ag, Pb and Mn might have been remobilised by different fluids, or remobilised from different locations, with some elements from distal sources and others from sulphides adjacent to the veins.

Differences between the two samples are attributed to a more extensive fluid facilitated alteration and replacement in 219069, which produced a larger proportion of pyrite in the sample and a more significant element depletion.

4.9 Conclusions

Two samples of sulphide breccia from Octagonal prospect showing varying degrees of alteration were analysed via laser ablation. Element maps of multiple sulphides facilitated assessment of element partitioning behaviours. These spatial datasets allowed co-localisation analysis to be applied to assess the relationships between the element distributions and geological features.

The pyrite is likely to have formed during pyrrhotite replacement, based on similar chalcophile element patterns for the two phases. However, pyrite is depleted in most of the chalcophile elements relative to pyrrhotite, which, in conjunction with pervasive serpentine in GSWA219069, in interpreted as a record of fluid flow and element remobilisation. Elevated levels of Mn within sample fracture networks indicate that Mn was introduced during this fluid flow.

Element mapping revealed Ag-zoning within pentlandite, and the co-localisation analysis confirmed that Ag is preferentially located proximal to fractures. The zoning is interpreted as a record of progressive Ag depletion within MSS during pentlandite crystallisation. The Ag–fracture co-location is intepreted to be a product of Ag remobilisation by fluid flow and associated alteration. Element mapping and co-localisation analysis shows that Pb is also co-located with the fractures. Differences in the style of co-localisation exhibited by Mn, Pb and Ag indicate they were remobilised in different ways. This might record remobilisation at different times, differences in remobilising fluid compositions, or different element sources.

The investigated samples preserve evidence of metal remobilisation between sulphide minerals. This redistribution process was also related to sulphide alteration, and created varying degrees of element depletion in pyrite, which was a product of pyrrhotite alteration. More extensive or prolonged redistribution, driven perhaps by post-crystallisation fluid movement, could have profound effects on ore deposits, with upgrading or downgrading of ores via element remobilisation. Such redistribution processes might also progress to the point of destruction of a once economic horizon. The quantification of the relationship between mineral chemistry and petrographic textures provides a powerful tool that can track the redistribution of elements of economic interest. Co-localisation analysis also has applications beyond those described in this study, including quantification of open system processes such as serpentinisation, formation of metasomatic zoning, and retrograde metamorphic overprinting.

4.10 Acknowledgements

The Minerals Research Institute of Western Australia, Ponton Minerals (Creasy Group) and the Geological Survey of Western Australia are gratefully acknowledged for funding this research as a component of the M470 project (Mineral systems on the margin of cratons: Albany-Fraser Orogen / Eucla Basement case study). Part of this research was undertaken using LA-ICP-MS and TIMA instrumentation at the John de Laeter Centre, Curtin University with the financial support of the Australian Research Council (LE140100150 and LE150100013). Noreen Evans and Bradley McDonald are thanked for their invaluable assistance with LA-ICP-MS analysis. The authors thank an anonymous reviewer for their constructive comments, and Charley Duran for a comprehensive review that substantially improved the quality of this work.

4.11 References

Barnes, S.J., Lightfoot, P.C., 2005. Formation of magmatic nickel-sulfide ore deposits and processses affecting their copper and platinum-group element contents. Economic Geology 100th Anniversary , 179–213.

Barnes, S.J., Makovicky, E., Karup-Moller, S., Makovicky, M., Rose-Hansen, J., 1994. Partition coefficients for Ni, Cu, Pd, Pt, Rh, and Ir between monosulphide solid solution and sulphide liquid and the implications for the formation of compositionally zoned Ni-Cu sulphide bodies by fractional crystallization of sulphide liquid. Mineralogical Magazine 58, 51–52.

Barnes, S.J., Makovicky, E., Makovicky, M., Rose-Hansen, J., Karup-Moller, S., 1997. Partition coefficients for Ni, Cu, Pd, Pt, Rh, and Ir between monosulfide solid solution and sulfide liquid and the formation of compositionally zoned Ni–Cu sulfide bodies by fractional crystallization of sulfide liquid. Canadian Journal of Earth Sciences 34, 366–374.

Barnes, S.J., Prichard, H.M., Cox, R.A., Fisher, P.C., Godel, B., 2008. The location of the chalcophile and siderophile elements in platinum-group element ore deposits (a textural, microbeam and whole rock geochemical study): Implications for the formation of the deposits. Chemical Geology 248, 295–317.

Barnes, S.J., Ripley, E.M., 2016. Highly siderophile and strongly chalcophile elements in magmatic ore deposits. Reviews in Mineralogy and Geochemistry 81, 725–774.

Barnes, S.J., Staude, S., Le Vaillant, M., Piña, R., Lightfoot, P.C., 2018. Sulfide-silicate textures in magmatic Ni-Cu-PGE sulfide ore deposits: Massive, semi-massive and sulfide-matrix breccia ores. Ore Geology Reviews .

Bennett, M., Gollan, M., Staubmann, M., Bartlett, J., 2014. Motive, means, and opportunity: key factors in the discovery of the Nova–Bollinger magmatic nickel–copper sulfide deposits in Western Australia. Building Exploration Capability for the 21st Century. Society of Economic Geologists, Special Publications 18, 301–320.

Bolte, S., Cordelieres, F., 2006. A guided tour into subcellular colocalization analysis in light microscopy. Journal of microscopy 224, 213–232.

Brisbout, L., 2015. Determining crustal architecture in the east Albany-Fraser Orogen from geological and geophysical data. Geological Survey of Western Australia.

Buddington, A., Lindsley, D., 1964. Iron-titanium oxide minerals and synthetic equivalents. Journal of petrology 5, 310–357.

Clark, C., Kirkland, C.L., Spaggiari, C.V., Oorschot, C., Wingate, M.T., Taylor, R.J., 2014. Proterozoic granulite formation driven by mafic magmatism: An example from the Fraser Range Metamorphics, Western Australia. Precambrian Research 240, 1–21.

Condie, K.C., Myers, J.S., 1999. Mesoproterozoic Fraser Complex: geochemical evidence for multiple subduction-related sources of lower crustal rocks in the Albany-Fraser Orogen, Western Australia. Australian Journal of Earth Sciences 46, 875–882.

Costes, S.V., Daelemans, D., Cho, E.H., Dobbin, Z., Pavlakis, G., Lockett, S., 2004. Automatic and quantitative measurement of protein-protein colocalization in live cells. Biophysical journal 86, 3993–4003.

Craig, J.R., Vokes, F.M., 1993. The metamorphism of pyrite and pyritic ores: an overview. Mineralogical Magazine 57, 3–18.

Czamanske, G.K., Kunilov, V.E., Zientek, M.L., Cabri, L.J., Likhachev, A.P., Calk, L.C., Oscarson, R.L., 1992. A proton microprobe study of magmatic sulfide ores from the Noril'sk-Talnakh District, Siberia. The Canadian Mineralogist 30, 249–287.

De Waele, B., Pisarevsky, S., 2008. Geochronology, paleomagnetism and magnetic fabric of metamorphic rocks in the northeast fraser belt, western australia. Australian Journal of Earth Sciences 55, 605–621.

Department of Mines, Industry Regulation and Safety, 2018. Latest statistics release. `http://dmp.wa.gov.au/About-Us-Careers/Latest-Statistics-Release-4081.aspxm`, [Online; accessed 25-July-2019].

Ding, L., Yang, G., Xia, F., Lenehan, C.E., Qian, G., McFadden, A., Brugger, J.L., Zhang, X., Chen, G., Pring, A., 2011. A LA-ICP-MS sulphide calibration standard based on a chalcogenide glass. Mineralogical Magazine 75, 279–287.

Dunn, K.W., Kamocka, M.M., McDonald, J.H., 2011. A practical guide to evaluating colocalization in biological microscopy. American Journal of Physiology-Cell Physiology 300, C723–C742.

Duran, C.J., Barnes, S.J., Corkery, J.T., 2015. Chalcophile and platinum-group element distribution in pyrites from the sulfide-rich pods of the Lac des Iles Pd deposits, Western Ontario, Canada: Implications for post-cumulus re-equilibration of the ore and the use of pyrite compositions in exploration. Journal of Geochemical Exploration 158, 223–242.

Duran, C.J., Barnes, S.J., Corkery, J.T., 2016. Trace element distribution in primary sulfides and Fe–Ti oxides from the sulfide-rich pods of the Lac des Iles Pd deposits, Western Ontario, Canada: constraints on processes controlling the composition of the ore and the use of pentlandite compositions in exploration. Journal of Geochemical Exploration 166, 45–63.

Duran, C.J., Barnes, S.J., Pleše, P., Prašek, M.K., Zientek, M.L., Pagé, P., 2017. Fractional crystallization-induced variations in sulfides from the Noril'sk-Talnakh mining district (polar Siberia, Russia). Ore Geology Reviews 90, 326–351.

Dutrizac, J., 1976. Reactions in cubanite and chalcopyrite. The Canadian Mineralogist 14, 172–181.

Ebel, D., Naldrett, A., 1997. Crystallization of sulfide liquids and the interpretation of ore composition. Canadian Journal of Earth Sciences 34, 352–365.

Glasson, K.J., Johnson, T.E., Kirkland, C.L., Gardiner, N.J., Clark, C., Blereau, E., Hartnady, M.I., Spaggiari, C., Smithies, H., 2019. A window into an ancient backarc? The magmatic and metamorphic history of the Fraser Zone, Western Australia. Precambrian Research 323, 55–69.

Godel, B., Barnes, S.J., 2008. Platinum-group elements in sulfide minerals and the whole rocks of the JM Reef (Stillwater Complex): Implication for the formation of the reef. Chemical Geology 248, 272–294.

de Gromard, R., Spaggiari, C., Munro, M., Sapkota, J., De Paoli, M., 2017. SGTSG 2017 Albany-Fraser Orogen pre-conference field trip: Transect across an Archaean craton margin to a Proterozoic ophiolite. Geological Survey of Western Australia Record 2017/14, 100p.

Helmy, H.M., Ballhaus, C., Berndt, J., Bockrath, C., Wohlgemuth-Ueberwasser, C., 2007. Formation of Pt, Pd and Ni tellurides: experiments in sulfide–telluride systems. Contributions to Mineralogy and Petrology 153, 577–591.

Holwell, B.D., McDonald, I., 2010. A review of the behaviour of platinum group elements within natural magmatic sulfide ore systems. Platinum Metals Review 54, 26–36.

Holwell, D.A., Adeyemi, Z., Ward, L.A., Smith, D.J., Graham, S.D., McDonald, I., Smith, J.W., 2017. Low temperature alteration of magmatic Ni-Cu-PGE sulfides as a source for hydrothermal Ni and PGE ores: A quantitative approach using automated mineralogy. Ore Geology Reviews 91, 718–740.

Jochum, K.P., Nohl, U., Herwig, K., Lammel, E., Stoll, B., Hofmann, A.W., 2005. Georem: A new geochemical database for reference materials and isotopic standards. Geostandards and Geoanalytical Research 29, 333–338.

Kelly, D., Vaughan, D., 1983. Pyrrhotine-pentlandite ore textures: a mechanistic approach. Mineralogical Magazine 47, 453–463.

Kirkland, C., Smithies, R., Spaggiari, C., Wingate, M., de Gromard, R.Q., Clark, C., Gardiner, N., Belousova, E., 2017. Proterozoic crustal evolution of the Eucla basement, Australia: Implications for destruction of oceanic crust during emergence of Nuna. Lithos 278, 427–444.

Kirkland, C.L., Spaggiari, C.V., Johnson, T.E., Smithies, R.H., Danišík, M., Evans, N., Wingate, M.T.D., Clark, C., Spencer, C., Mikucki, E., McDonald, B.J., 2016. Grain size matters: Implications for element and isotopic mobility in titanite. Precambrian Research 278, 283 – 302.

Kirkland, C.L., Spaggiari, C.V., Pawley, M.J., Wingate, M.T.D., Smithies, R.H., Howard, H.M., Tyler, I.M., Belousova, E.A., Poujol, M., 2011. On the edge: U-Pb,Lu-Hf, and Sm-Nd data suggests reworking of the Yilgarn craton margin during formation of the Albany-Fraser Orogen. Precambrian Research 187, 223 – 247.

Kullerud, G., 1969. Phase relations in the Cu-Fe-S, Cu-Ni-S and Fe-Ni-S system. Magmatic ore deposits , 323–343.

Kullerud, G., Yoder, H.S., 1959. Pyrite stability relations in the Fe-S system. Economic Geology 54, 533–572.

Li, C., Barnes, S.J., Makovicky, E., Rose-Hansen, J., Makovicky, M., 1996. Partitioning of nickel, copper, iridium, rhenium, platinum, and palladium between monosulfide solid solution and sulfide liquid: effects of composition and temperature. Geochimica et Cosmochimica Acta 60, 1231–1238.

Liu, Y., Brenan, J., 2015. Partitioning of platinum-group elements (PGE) and chalcogens (Se, Te, As, Sb, Bi) between monosulfide-solid solution (MSS), intermediate solid solution (ISS) and sulfide liquid at controlled fO_2–fS_2 conditions. Geochimica et Cosmochimica Acta 159, 139–161.

Maier, W.D., Smithies, R.H., Spaggiari, C.V., Barnes, S.J., Kirkland, C.L., Kiddie, O., Roberts, M.P., 2016. The evolution of mafic and ultramafic rocks of the Mesoproterozoic Fraser Zone, Albany-Fraser Orogen, and implications for the Ni-Cu sulphide potential of the region. Geological Survey of Western Australia, Record 2016/8 , 49p.

Makovicky, E., 2002. Ternary and quaternary phase systems with PGE, in: Geology, Geochemistry, Mineralogy and Mineral Beneficiation of Platinum-group Elements. Canadian Institute of Mining, Metallurgy and Petroleum, pp. 131–175.

Manders, E., Verbeek, F., Aten, J., 1993. Measurement of co-localization of objects in dual-colour confocal images. Journal of microscopy 169, 375–382.

Mansur, E.T., Barnes, S.J., Duran, C.J., Sluzhenikin, S.F., 2019. Distribution of chalcophile and platinum-group elements among pyrrhotite, pentlandite, chalcopyrite and cubanite from the Noril'sk-Talnakh ores: implications for the formation of platinum-group minerals. Mineralium Deposita , 1–18.

Mungall, J.E., Andrews, D.R., Cabri, L.J., Sylvester, P.J., Tubrett, M., 2005. Partitioning of Cu, Ni, Au, and platinum-group elements between monosulfide solid solution and sulfide melt under controlled oxygen and sulfur fugacities. Geochimica et Cosmochimica Acta 69, 4349–4360.

Murowchick, J.B., Barnes, H., 1986. Marcasite precipitation from hydrothermal solutions. Geochimica et Cosmochimica Acta 50, 2615 – 2629.

Naldrett, A., 1969. A portion of the system Fe–S–O between 900 and 1080°c and its application to sulfide ore magmas. Journal of Petrology 10, 171–201.

Naldrett, A., 2004. Magmatic sulfide deposits: Geology, geochemistry and exploration. Springer Science & Business Media.

Naldrett, A., Craig, J., Kullerud, G., 1967. The central portion of the Fe-Ni-S system and its bearing on pentlandite exsolution in iron-nickel sulfide ores. Economic Geology 62, 826–847.

Paktunc, A.D., Hulbert, L.J., Harris, D.C., 1990. Partitioning of the platinum-group and other trace elements in sulfides from the Bushveld Complex and Canadian occurrences of nickel-copper sulfides. The Canadian Mineralogist 28, 475–488.

Penarrubia, P.G., Ruiz, X.F., Gálvez, J., 2005. Quantitative analysis of the factors that affect the determination of colocalization coefficients in dual-color confocal images. IEEE transactions on image processing 14, 1151–1158.

Peregoedova, A., 1998. The experimental study of the Pt–Pd–partitioning between monosulfide solid solution and Cu–Ni–sulfide melt at 900–840°c, in: The 8th International Platinum Symposium, pp. 325–373.

Piña, R., Gervilla, F., Barnes, S.J., Ortega, L., Lunar, R., 2013. Platinum-group elements-bearing pyrite from the Aguablanca Ni-Cu sulphide deposit (SW Spain): a LA-ICP-MS study. European Journal of Mineralogy 25, 241–252.

Schoonen, M., Barnes, H., 1991. Mechanisms of pyrite and marcasite formation from solution: III. Hydrothermal processes. Geochimica et Cosmochimica Acta 55, 3491–3504.

Sinyakova, E., Kosyakov, V., 2009. Experimental modeling of zonality of copper-rich sulfide ores in copper-nickel deposits, in: Doklady Earth Sciences, Springer. pp. 787–792.

Smith, J., Holwell, D.A., McDonald, I., 2014. Precious and base metal geochemistry and mineralogy of the Grasvally Norite–Pyroxenite–Anorthosite (GNPA) member, northern Bushveld Complex, South Africa: implications for a multistage emplacement. Mineralium Deposita 49, 667–692.

Smithies, R.H., Spaggiari, C.V., Kirkland, C.L., 2015. Building the crust of the Albany-Fraser Orogen: constraints from granite geochemistry. Geological Survey of Western Australia, Report 150 , 49p.

Smithies, R.H., Spaggiari, C.V., Kirkland, C.L., Howard, H.M., Maier, W.D., 2013. Petrogenesis of gabbros of the Mesoproterozoic Fraser Zone: constraints on the tectonic evolution of the Albany-Fraser Orogen. Geological Survey of Western Australia, Record 2013/15 , 29p.

Spaggiari, C., Kirkland, C., Smithies, R., Occhipinti, S., Wingate, M., 2014a. Geological framework of the albany–fraser orogen, in: Albany–Fraser Orogen seismic and magnetotelluric (MT) workshop 2014: extended abstracts compiled by CV Spaggiari and IM Tyler: Geological Survey of Western Australia, Record, pp. 12–27.

Spaggiari, C.V., Bodorkos, S., Barquero-Molina, M., Tyler, I.M., Wingate, M.T.D., 2009. Interpreted bedrock geology of the South Yilgarn and central Albany-Fraser Orogen, Western Australia. Geological Survey of Western Australia, Record 2009/10 , 84p.

Spaggiari, C.V., Kirkland, C.L., Smithies, R.H., Wingate, M.T.D., 2011. The geology of the East Albany-Fraser Orogen - A Field Guide. Geological Survey of Western Australia, Record 2009/10 , 84.

Spaggiari, C.V., Kirkland, C.L., Smithies, R.H., Wingate, M.T.D., Belousova, E.A., 2015. Transformation of an Archean craton margin during Proterozoic basin formation and magmatism: The Albany-Fraser Orogen, Western Australia. Precambrian Research 266, 440 – 466.

Spaggiari, C.V., Occhipinti, S.A., Korsch, R.J., Doublier, M.P., Clark, D.J., Dentith, M.C., Gessner, K., Doyle, M.G., Tyler, I.M., Kennett, B.L.N., Costelloe, R.D., Fomin, T., Holzschuh, J., 2014b. Interpretation of Albany-Fraser seismic lines 12GA-AF1, 12GA-AF2 and 12GA-AF3: implications for crustal architecture, *in* Albany-Fraser Orogen seismic and magnetotelluric (MT) workshop 2014: extended abstracts *compiled by* CV Spaggiari and IM Tyler. Geological Survey of Western Australia, Record 2014/6.

Sylvester, P., Cabri, L., Tubrett, M., McMahon, G., Laflamme, J., Peregoedova, A., et al., 2005. Synthesis and evaluation of a fused pyrrhotite standard reference material for platinum group element and gold analysis by laser ablation-ICPMS, in: 10th International Platinum Symposium: Oulu, Geological Survey of Finland, Extended Abstracts, pp. 16–20.

Walker, A., Evans, K., Kirkland, C., Martin, L., Kiddie, O., Spaggiari, C., 2019. Tracking mineralisation with in situ multiple sulphur isotopes: a case study from the Fraser Zone, Western Australia. Precambrian Research 332.

Wohlgemuth-Ueberwasser, C.C., Ballhaus, C., Berndt, J., Stotter née Paliulionyte, V., Meisel, T., 2007. Synthesis of pge sulfide standards for laser ablation inductively coupled plasma mass spectrometry (la-icp-ms). Contributions to Mineralogy and Petrology 154, 607–617.

Zhu, Z.Y., Cook, N., Yang, T., Ciobanu, C., Zhao, K.D., Jiang, S.Y., 2016. Mapping of sulfur isotopes and trace elements in sulfides by la-(mc)-icp-ms: potential analytical problems, improvements and implications. Minerals 6, 110.

Appendices

4.A Laser ablation standard materials and calibration details

Six reference materials were used to calibrate ablation data: GSD-1g, BCR2G, BHVO2G, BONN, IMER and PO726. Details for glass standards GSD-1g, BCR2G and BHVO2G may be found on GeoRem (http://georem.mpch-mainz.gwdg.de/) (Jochum et al., 2005). GSD-1G was used as a primary standard for elements other than Te, Rh, Pd, Os, Ir, Pt, Au, S, Ni, Re and Ag, with BHVO2G and BCR2G used as secondary standards. IMER is a chalcogenide glass matrix standard containing 4 minor and 33 trace elements (Ding et al., 2011) and was used to calibrate Te. PO726 is a synthetic pyrrhotite doped with Au and PGE (Sylvester et al., 2005) and was used to calibrate Rh, Pd, Os, Ir, Pt and Au. BONN is a synthetic sulphide standard doped with PGE made using methods similar to those described by Wohlgemuth-Ueberwasser et al. (2007), and used to calibrate S, Ni, Re and Ag in this study.

4.B Mass balance calculations

The reasoning and calculations used for the mass balance component of this work follow those laid out by Godel and Barnes (2008). Percentages of each PGE and chalcogen associated with each BMS were calculated using average concentrations from in-situ analysis of the BMS and the limited whole rock geochemical data available. Whole rock geochemistry was provided by Creasy Group.

Weight fractions of chalcopyrite in each sample were calculated by assuming all Cu present in whole rock geochemistry is sequestered within chalcopyrite:

$$F_{cpt} = Cu_{WR}/Cu_{cpt} \tag{4.5}$$

Where F_{cpt} is the weight fraction of chalcopyrite, Cu_{WR} is the concentration of Cu in whole rock, and Cu_{cpt} is the average concentration of Cu in chalcopyrite.

In the absence of any olivine within the samples considered, the weight fraction of pentlandite was calculated by assuming all Ni in the whole rock is hosted within pentlandite:

$$F_{pn} = Ni_{WR}/Ni_{pn} \tag{4.6}$$

Where F_{pn} is the weight fraction of pentlandite, Ni_{WR} is the concentration of Ni in the whole rock, and Ni_{pn} is the average concentration of Ni in pentlandite.

To calculate weight fractions of pyrrhotite and pyrite, we assume the remainder of the sulphur in whole rock not within pentlandite and chalcopyrite is hosted within pyrrhotite and pyrite. TIMA analysis indicates a mineral composition of 0.4% pyrrhotite and 54.31% pyrite in sample 219069. Therefore we assume that minimal sulphur is sequestered within the negligible pyrrhotite present and therefore that the remainder of whole rock S for 219069 is hosted within pyrite:

$$F_{pt} = (S_{WR} - F_{pn} \cdot S_{pn} - F_{cpt} \cdot S_{cpt})/S_{pt} \tag{4.7}$$

Where F_{pt} is the weight fraction of pyrite, S_{WR} is the concentration of S in the whole rock, S_{pn} is the average sulphur content in pentlandite, S_{cpt} is the average sulphur content in chalcopyrite and S_{pt} is the average sulphur content in pyrite. TIMA analysis of 219070 indicates proportions of pyrrhotite and pyrite of 31.63% and 22.34% respectively. In this case Equation 4.7 was used but F_{pt} and S_{pt} are replaced with F_{pt+po} and S_{pt+po} respectively. S_{pt+po} is equal to the sum of the average sulphur contents in pyrite and pyrrhotite multiplied by the relative TIMA identified proportons of pyrite and pyrrhotite. The weight fraction of pyrrhotite and pyrite can then be calculated by multiplying F_{pt+po} by the relative TIMA identified proportions of pyrrhotite and pyrite respectively (i.e. $F_{pt} = F_{pt+po} \times 0.414$).

Using calculated weight fractions of the BMS minerals, the percentage of each PGE and chalcogen (P^i_{sul}) in a given BMS mineral is given by the equation:

$$(P^i_{sul}) = (F_{sul} \times C^i_{sul}/C^i_{WR}) \times 100 \tag{4.8}$$

where F_{sul} is the weight fraction of the BMS mineral in question, C^i_{sul} is the concentration of the element in question in this mineral, and C^i_{WR} is the whole rock concentration of element i (Godel and Barnes, 2008).

Chapter 5

An Archaean sulphur source for Proterozoic VMS-style mineralisation: a case study from the Fraser Zone, Western Australia

5.1 Abstract

Sulphur isotope analysis is a powerful tool in fingerprinting sulphur sources within mineral systems and tracing sulphur cycling through time. In this work we present results from petrographic and *in-situ* sulphur isotope analysis of sulphide material from the mineralised Andromeda locality in the Fraser Zone of the Albany-Fraser Orogen, with the aim of characterising incorporated sulphur and placing it in the wider context of sulphur cycling within the Fraser Zone. Sulphide assemblages include sphalerite which is atypical of magmatic sulphide mineralisation previously identified in the Fraser Zone. δ^{34}S data falls between 4.50‰ to 6.70‰, a range that is characteristic of Archaean and Proterozoic VMS-style deposits worldwide. Δ^{33}S data indicate Archaean sulphur has been incorporated within Andromeda sulphides in close proximity to the Fraser Shear Zone. This contrasts with the findings of previous sulphur isotope analysis of Fraser Zone magmatic sulphides that are distal to major shear zones, and in which Archaean sulphur was absent, interpreted as a consequence of cycling through ocean basins. The presence of Archaean sulphur in Andromeda is attributed to a preserved MIF-S-bearing sulphur reservoir within the Biranup Zone in close proximity to the Fraser Shear Zone. Fluid movement across the Fraser Shear Zone, a lithospheric-scale

structure, is a viable mechanism by which MIF-S sulphur signatures were incorporated from preserved Archaean sulphur-bearing pyrite in the Biranup Zone and passed on to sulphides at Andromeda. These findings support multiple modes of sulphur cycling within a single Proterozoic mineralised system, with implications for sulfur cycling in other localities and settings worldwide.

5.2 Introduction

Sulphur is an important ligand within mineral systems and critical for the sequestration of chalcophile elements (e.g. Ni, Cu, Co, PGEs). Sulphur isotopes can be used to track sulphur sources and speciation through various earth system processes (Seal, 2006; Johnston, 2011; LaFlamme et al., 2018a). Four stable isotopes of sulphur exist on Earth today; ^{32}S, ^{33}S, ^{34}S and ^{36}S, with approximate abundances of 95%, 0.75%, 4.20% and 0.017%, respectively (MacNamara and Thode, 1950). Fractionation occurs during reaction between different sulphur-bearing compounds, which alters the isotope abundances present in each species. Sulphur isotopic fractionation is commonly expressed via ratios of ^{34}S/^{32}S and ^{33}S/^{32}S in a sample. For ^{34}S/^{32}S fractionation is commonly represented by:

$$\delta^{34}S(‰) = \left[\frac{(^{34}S/^{32}S)_{sample} - (^{34}S/^{32}S)_{reference}}{(^{34}S/^{32}S)_{reference}}\right] \times 1000 \tag{5.1}$$

where the reference material used is the Vienna Canyon Diablo Troilite (VCDT) with δ^{34}S = 0‰. Positive δ^{34}S values indicate an enrichment in the heavier ^{34}S isotope relative to the reference isotopic ratio, and negative δ^{34}S values a depletion in ^{34}S.

At thermodynamic equilibrium (Urey, 1947) and in many non-equilibrium processes, the extent of fractionation of the different sulphur isotopes between compounds is proportional to the relative differences in mass between each isotope, a process known as mass dependent fractionation (MDF). This produces near linear relationships between isotopic ratios; for example, $\delta^{33}S_{MDF} = 0.515 \times \delta^{34}S$. That is, the isotopic fractionation measured by ^{33}S will be approximately half that measured by ^{34}S, based on the difference of one atomic mass unit between ^{32}S and ^{33}S versus the two atomic mass unit difference between ^{32}S and ^{34}S (Hulston and Thode, 1965).

Sulphur isotopes may also undergo mass independent fractionation (MIF), by which anomalous deviations from mass-dependent relationships may be imparted to sulphur isotopes. Deviations in the value of ^{34}S/^{32}S from the established mass dependent fractionation relationship is represented by the variable Δ^{33}S. The most significant example of MIF is seen in the sulphur record prior to the Great Oxygenation Event at c. 2.4 Ga (Farquhar et al., 2000). In the Archaean, atmospheric SO$_2$ experienced ultraviolet radiation-facilitated photodissociation which generated Δ^{33}S values ranging from

c. -5‰ to 15‰ (Selvaraja et al., 2017) The Archaean Δ^{33}S record is temporally and spatially heterogeneous and shows positive and negative Δ^{33}S anomalies of different magnitudes (Farquhar and Wing, 2003). Elemental sulphur with positive Δ^{33}S anomalies is produced by photolysis of SO_2 (Farquhar and Wing, 2003) (Fig. 5.2.1) and this sulphur was reduced and preserved in sedimentary sulphides within supracrustal material. In contrast, negative Δ^{33}S anomalies are recorded by the seawater sulphate reservoir, which incorporated soluble atmospheric sulphate (Farquhar and Wing, 2003) (Fig. 5.2.1). The MIF anomalies that formed in the Archaean are denoted by $\Delta^{33}S_0$, and are thought to be preserved during cycling through sulphur reservoirs (Farquhar and Wing, 2003); $\Delta^{33}S_0$ anomalies that have been recycled and inherited by younger material are denoted by $\Delta^{33}S_1$. Small Δ^{33}S anomalies can be generated by MDF; these anomalies are denoted by $\Delta^{33}S_B$ and were previously thought to be limited to values of 0 ± 0.2‰ (Farquhar and Wing, 2003). However, more recent work has redefined the limits of MDF-generated Δ^{33}S values (LaFlamme et al., 2018b) as:

$$\Delta^{33}S_B = 1000 \times \left(\left(\frac{\delta^{34}S}{1000} + 1 \right)^{\lambda} - 1 \right) - 1000 \times \left(\left(\frac{\delta^{34}S}{1000} + 1 \right)^{0.515} - 1 \right) \tag{5.2}$$

Where λ equals the slope of the observed mass dependent relationship (LaFlamme et al., 2018b). While reactions that occur at, or close to, equilibrium generally produce mass-dependent sulphur fractionation with a $\lambda^{33} = 0.515$ (Hulston and Thode, 1965), kinetically-controlled reactions may generate deviations in δ^{33}S-δ^{34}S mass dependent relationships with λ^{33} values of 0.508–0.519 (e.g. Ono et al., 2006; Leavitt et al., 2014). For example, if a process induces mass-dependent fractionation where $\lambda^{33} = 0.508$ rather than 0.515 then each 1.0‰ variation in δ^{34}S is associated with a maximum $\Delta^{33}S_B$ of c. 0.007‰ (LaFlamme et al., 2018b).

Sulphur contributions within Volcanogenic Massive Sulphide (VMS) deposits are variable and often from multiple sources including reduction of seawater sulphate, magmatic fluids and wall rock (Brueckner et al., 2015 and references therein). VMS deposits are mineralised occurrences formed by interactions between mineralised hydrothermal fluids and wall rock at or near the seafloor in submarine volcanic environments (Galley et al., 2007; Piercey, 2011). VMS deposits contain Zn, Cu, Pb, Ag, Co, Sn, Se, Mn, Cd, In, Bi, Te, Ga, Ge and are found within high temperature, extensional geodynamic environments (Piercey, 2011). Deposits generally share a two-component structure comprising a tabular stratabound lens of massive sulphide, quartz, phyllosilicates, iron oxide and altered rock above a discordant to semi discordant stockwork of veins and disseminated sulphide (Galley et al., 2007). A widely accepted classification of VMS deposits exists, with five subcategories dependent on host lithostratigraphy (Barrie et al., 1999; Franklin et al., 2005; Galley et al., 2007): mafic (Cyprus-type), mafic-siliciclastic

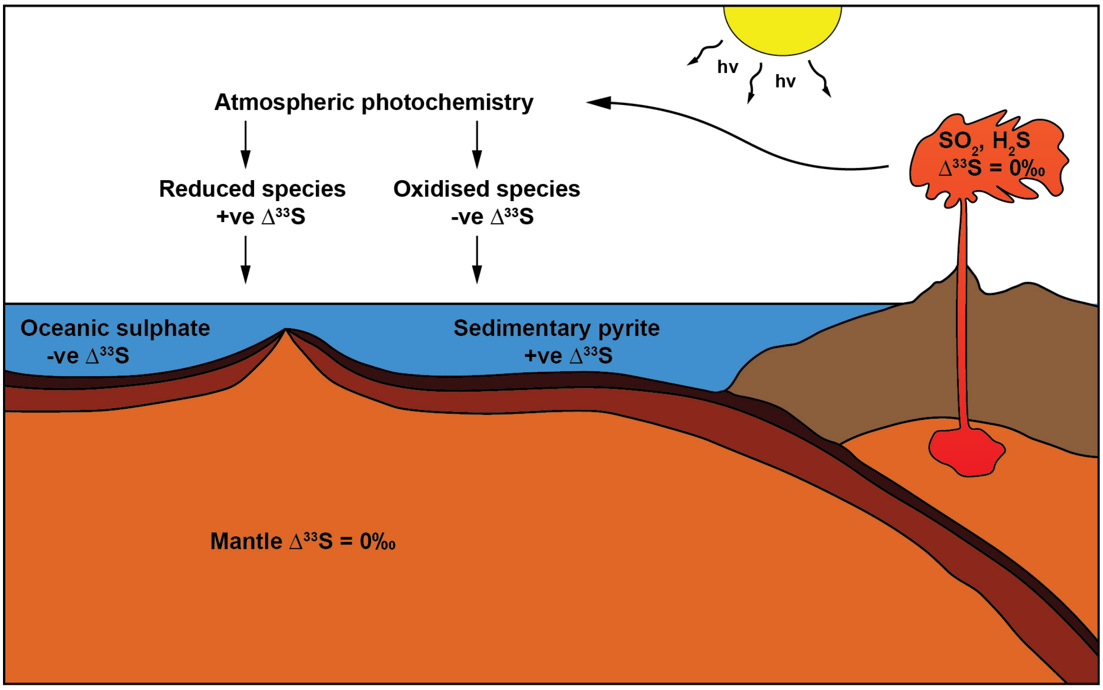

Figure 5.2.1: Simplified illustration of the Archaean sulphur cycle and paths by which Δ^{33}S anomalies may be imparted (after Farquhar and Wing, 2003).

(Besshi-type), bimodal-mafic (Noranda-type), bimodal-felsic (Kuroko-type) and felsic-siliciclastic (Bathurst-type) (Piercey, 2011).

In this study, *in-situ* sulphur isotope measurements were used to characterise the sulphur isotope compositions of sulphides from Andromeda, a Zn–Cu prospect in the Fraser Zone of the Albany-Fraser Orogen, Western Australia. The Fraser Zone is known to be prospective for nickel sulphide mineralisation. Previous sulphur isotope analyses of magmatic sulphides from the Fraser Zone by Walker et al. (2019) indicated that mineralisation was linked to assimilation of local sedimentary material, and that Archaean sulphur was not preserved in the sulphides analysed. The lack of Archaean sulphur is, at first sight, inconsistent with the Fraser Zone's Archaean heritage. The absence was attributed to recycling of sulphur-bearing material through sedimentary processes (Walker et al., 2019). In the present study we focus on Andromeda, which preserves a different style of mineralisation to that previously studied. We analysed material from the predominant mafic granulite host lithology, sulphide breccia and remobilised sulphides from the main orebody, and sulphides spatially associated with fluid pathways. The proximity of Andromeda to the Fraser Shear Zone, a major lithotectonic-zone-bounding structure within the orogen, is important to note as the shear zone may have influenced the formation of Andromeda. The objectives of this study are a) to characterise the sources of sulphur at Andromeda, a possible Proterozoic VMS deposit; b) compare Andromeda sulphur isotopic signatures to those of Fraser Zone magmatic sulphide deposits; and c) use these results to constrain fluid sources and place Andromeda within the context of the regional geodynamic setting.

5.3 Regional Geology

The Palaeoproterozoic and Mesoproterozoic Albany-Fraser Orogen (AFO) extends from the southern and south-eastern margins of the Yilgarn Craton in the east to the Rodona Shear Zone in the west (Fig. 5.3.1) (Spaggiari et al., 2012, 2015b). The Northern Foreland includes the region of the AFO adjacent to the Yilgarn Craton and comprises greenschist facies rocks of Yilgarn affinity that have been modified by Palaeoproterozoic and Mesoproterozoic magmatism (Spaggiari et al., 2015b). South of the Northern Foreland are, from north to south, the Biranup, Fraser and Nornalup Zones (Fig. 5.3.1). These consist of varying proportions of igneous and metasedimentary rocks that have been variably overprinted Proterozoic metamorphism. Magmatism and deformation during the Albany–Fraser Orogeny produced new Proterozoic juvenile igneous rocks, mixtures of juvenile and Archaean provenance, and, less commonly, reworked Archaean crystalline rocks (Spaggiari et al., 2014a; Kirkland et al., 2016).

The orogen includes two substantial basins. The Barren Basin (1815–1600 Ma) formed during extension of the southern Yilgarn Craton and preserves Proterozoic detritus from a developing horst and graben architecture (Spaggiari et al., 2015b). The Arid Basin (1600–1305 Ma) formed during the development of a marginal ocean basin (c. 1600–1455 Ma) and records a tectonic switch to a convergent regime (c. 1455 Ma) with subsequent accretion of the c. 1410 Ma Loongana magmatic arc onto the basin margin at c. 1332 Ma (Spaggiari et al., 2015b). The Arid Basin includes material shed by the Loongana arc during accretion (Spaggiari et al., 2015b). Much of the eastern AFO is concealed by the Bight and Eucla Basins, which extend eastward over the Rodona Shear Zone, where the AFO is juxtaposed against the Madura Province, which comprises igneous material derived from parental magmas of the Loongana arc (Spaggiari et al., 2015b).

The AFO has a complex tectonic history and Archaean and Palaeoproterozoic events are reflected by the structural and geochemical characteristics of the rocks. However, the Albany-Fraser Orogeny is the tectonic episode most pertinent to this study, because it produced most of the existing tectonic and metamorphic features of the orogen (Kirkland et al., 2011a). The Orogeny is divided into Stages I (1330–1260 Ma) and II (1225–1140 Ma). Stage I has been linked to the accretion of the Loongana magmatic arc onto the Nornalup Zone (Spaggiari et al., 2015b), while Stage II is interpreted as a period of intracontinental reworking and magmatism during cratonisation of material that lies between the West Australian and South Australian Cratons (Spaggiari et al., 2009; Kirkland et al., 2017).

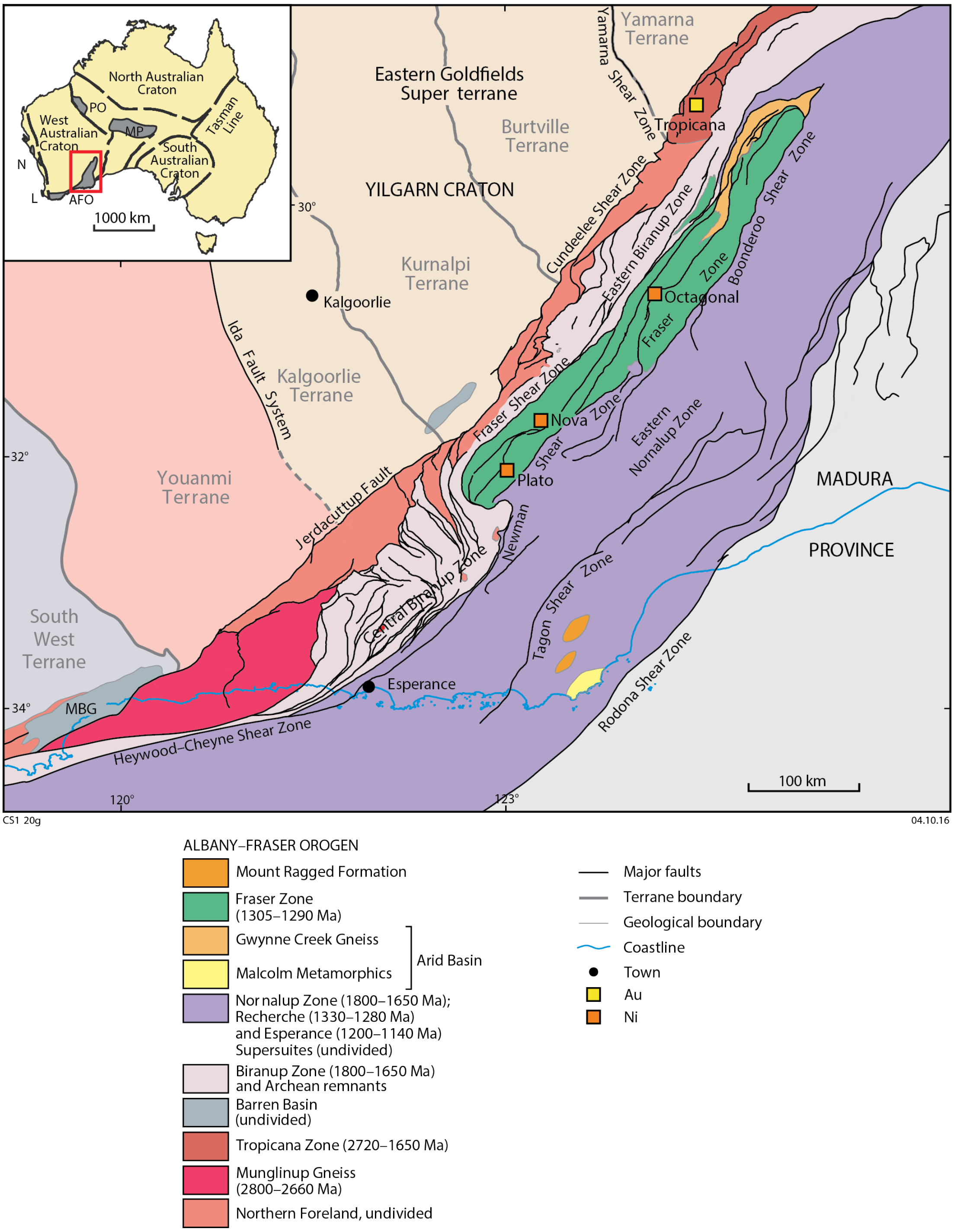

Figure 5.3.1: Simplified geological overview of the AFO (modified after Spaggiari et al., 2011)

5.3.1 Fraser Zone

The Fraser Zone is characterised by a strong NE–SW trending gravity signature, and is approximately 425 km long and 50km wide (Maier et al., 2016), with a v-shaped geometry and a depth of approximately 15 km. It is bounded by the Fraser Shear Zone, Newman Shear Zone, and the Boonderoo Shear Zone (Fig. 5.3.1) (Spaggiari et al., 2014b; Brisbout, 2015). The 1305–1295 Ma Fraser Range Metamorphics, which comprise sheeted metagabbro and metagranite, are the dominant lithology in the Fraser Zone (Spaggiari et al., 2015b). This unit is intercalated with amphibolite–granulite grade metasedimentary sandstones and mudstones of the Snowys Dam Formation. The metasediments of the Snowys Dam Formation from part of the Arid Basin, and also include calcareous rocks, iron rich strata and possible volcaniclastics (Spaggiari et al., 2015b). The Snowys Dam Formation has a maximum depositional age of 1332 ± 21 Ma, and detrital zircons provide evidence that sediments were derived from the Loongana Arc and the oceanic crust of the Madura Province (Spaggiari et al., 2014b, 2015a). Metamorphic zircon rims indicate that the minimum depositional age is 1298 ± 12 Ma (Spaggiari et al., 2015b). The Arid Basin sediments were deposited shortly before the onset of coeval mafic and felsic magmatism.

The onset of mafic and felsic magmatism in the Fraser Zone was approximately contemporaneous at c. 1310–1284 Ma (Spaggiari et al., 2015b; Waddell et al., 2015), with crystallisation of mafic material dated by U-Pb geochronology at 1305–1290 Ma (De Waele and Pisarevsky, 2008; Kirkland et al., 2011a; Clark et al., 2014); shortly before deposition of the Arid Basin. The voluminous metagabbros and less common metagranites have been deformed and metamorphosed to granulite facies, which produced complex layering in the rocks (Spaggiari et al., 2009, 2011; Clark et al., 2014). Minor ultramafic material has been recorded in the central portions of some gabbroic sills and in some larger cumulate bodies, such as the rocks that host the Nova-Bollinger nickel sulphide deposit (Maier et al., 2016).

Upper amphibolite to granulite facies metamorphism occurred coevally with magmatism, with the brief interval between initiation of magmatism and metamorphism implying mafic magmatism was a thermal driver for metamorphism (Clark et al., 2014). Thermodynamic modelling conducted by Clark et al. (2014) constrained metamorphic conditions imposed on metasedimentary pelitic material to 800–900°C and 6.5–8.5 kbar, consistent with peak metamorphism at depths of 25–30 km. Further modelling by Glasson et al. (2019) on metagabbroic material estimated temperatures of 900–950°C and pressures of approximately 7 kbar. The higher temperatures in Fraser Zone metagabbro (900–950°C) relative to metapelitic material (approx. 830–860°C) is consistent with mafic magmatism operating as the thermal driver for metamorphism (Clark et al., 2014; Glasson et al., 2019). Zircons in the Fraser Zone commonly record Stage I metamorphism, but do not record overprinting related to Stage II of the orogeny. The lack of a zircon record of Stage II has been attributed to crustal dehydration and a dearth of zircon precipitating fluids (Kirkland et al., 2016). However, metamorphic titanite preserves some evidence of AFO Stage II within the Fraser Zone. Remobilisation of radiogenic Pb within small titanite grains yields reset ages of 1205 ± 16 Ma (Kirkland et al., 2016). These titanite data are consistent with a tectonic model in which the Fraser Zone was extruded or otherwise exhumed to shallower crustal levels between 1270–1193 Ma (Kirkland et al., 2011a).

Multiple models of formation have been postulated for the initial development of the Fraser Zone. Initially an exotic origin was proposed, based on trace element characteristics, in which the Fraser Zone consisted of remnants of accreted oceanic arcs (Condie and Myers, 1999). Furthermore, the geochemistry of the Fraser Zone metagabbros was interpreted as characteristic of subduction-related magmatism (Condie and Myers, 1999). Lutetium–Hf data are used as the basis for an alternative interpretation, in which the Fraser Zone is related to extensional processes and rooted on the Biranup Zone, and hence the Fraser Zone is regarded as forming an autochthonous component of the AFO (Kirkland et al., 2011a). The Lu-Hf data show via a stair-stepping evolutionary trajectory that the Fraser Zone contains a Hf component isotopically comparable to that of the Biranup Zone, but modified by juvenile input, and that the Biranup Zone itself incorporates reworked Archaean material (Kirkland et al., 2011a). Furthermore, geochemical modelling indicates that the geochemistry of Fraser Zone gabbro is consistent with the assimilation of minor (<10%) quantities of Archaean granite and Munglinup Gneiss by a depleted mantle source, and that the assimilated material is comparable to material known from the Biranup Zone (Smithies et al., 2013). Both these datasets support an interpretation in which the Fraser Zone reflects an extension of the highly modified Yilgarn Craton. The igneous component of the Fraser Zone is thus interpreted as a mid to deep-crustal hot zone formed by intrusion of mantle-derived magmas into heavily modified (para)autochthonous quartzofeldspathic country rock (Smithies et al., 2013). Within the interpreted regional geodynamic setting, the Fraser Zone is a component of a hyperextended continental margin (Kirkland et al., 2017) with the Madura Province to the east reflecting remnants of oceanic crust (Kirkland et al., 2017; Spaggiari et al., 2018). Emplacement of magmatic rocks of the Fraser Zone is suggested to have occurred within an intracontinental rift or back-arc setting (Kirkland et al., 2011a; Spaggiari et al., 2011);); the currently available datasets are consistent with either interpretation (Glasson et al., 2019).

5.4 Sample material

Andromeda is located within 4 km of the Fraser Shear Zone, a zone of upper amphibolite mylonitic to ultramylonitic rocks that lie on the contact between the Palaeoproterozoic Biranup Zone and the Mesoproterozoic Fraser Zone (Fig. 5.3.1) (de Gromard et al., 2017; Munro et al., 2017). Fraser Zone rocks within the Fraser Shear Zone are isoclinally folded, strongly boudinaged, migmatitic and intruded by pegmatite veins (de Gromard et al., 2017). The shear zone itself has a prolonged history of dextral strike-slip kinematics although low strain areas appear record an earlier sinistral shearing history (Munro et al., 2017).

Andromeda was discovered in 2018; four drill holes, approximately 650–750 m deep, intersected a mineralised horizon approximately 400 x 150 x 15m (Fig. 5.4.1) which is hosted by rocks dominated by amphibole-garnet- feldspar granulites (Fig. 5.4.2).

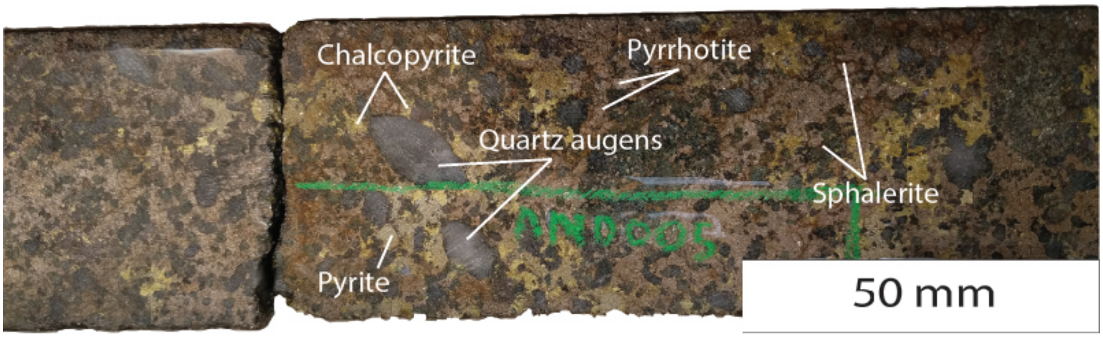

Figure 5.4.1: Example of sulphide breccia material comprising Andromeda orebody

Limited retrogression is evidenced by variable quantities of amphibole, and some granulite material has retrogressed sufficiently to be classified as amphibolite (see sample 227317). The Andromeda host rocks also include minor granitic, doleritic and pegmatitic units, and multiple cross-cutting generations of pegmatites record multiple episodes of fluid flow (Fig. 5.4.3).

Figure 5.4.2: Example of mafic granulite lithology hosting the Andromeda orebody

5.5 Methods

Thirty-one samples of quarter core material from the Andromeda prospect were provided by Creasy Group and IGO. Petrographic analysis was used to characterise the samples and as a basis for the selection of material for *in-situ* sulphur isotope analysis.

Figure 5.4.3: Example of brecciated and recemented pegmatite vein

5.5.1 Thin section petrography

Polished thin sections were made from all 31 samples and these were examined using transmitted and reflected light optical microscopy to identify mineral assemblages, textural relations and features of interest for further study. Representative samples of mafic granulite, sulphide breccia, sulphide-bearing pegmatite and mafic amphibolite hosting remobilised sulphides were selected for *in-situ* sulphur isotope analysis.

5.5.2 Secondary Ion Mass Spectrometry (SIMS)

The SIMS methodology follows the methodology discussed in Walker et al. (2019). *In-situ* triple sulphur isotopic ratios (^{32}S, ^{33}S, ^{34}S) were measured on a CAMECA IMS1280 ion microprobe at the Centre for Microscopy Characterisation and Analysis within the University of Western Australia. Measurements were undertaken on 25 mm diameter mounts containing sample material, made by taking 2 mm discs or larger saw-cut pieces from thin sections and embedding them within epoxy. Epoxy blocks of samples and standard materials were prepared separately, trimmed and then mounted with the unknown samples in sample holders. All sample and standard material was placed no further than 6–7 mm from the centre of each mount. Mounted sample material was photographed using reflected light microscopy to assist with selection of spots for analysis. Following imaging, and prior to analysis, samples were cleaned with ethanol and coated with approx. 30 nm of gold to prevent charging during analysis.

Sample surfaces were sputtered over a 15 x 15 µm area with a 10 kV, Gaussian Cs^+ beam with an intensity of 3.0–3.5 nA and total impact energy of 20 keV. Secondary ions were admitted in a double focusing mass spectrometer via a 60 µm entrance slit and focused in the centre of a 4000 µm field aperture (x130 magnification). Secondary ions were then energy filtered using a 30 eV band pass with a 5 eV gap toward the high energy side. All S isotopes were collected simultaneously in Faraday cup detectors fitted with 10^{10} Ω (L'2, ^{32}S) and 10^{11} Ω (L1, ^{33}S and H1, ^{34}S) resistors, operating at a mass resolution of approx. 4300. The magnetic field was regulated using NMR control. Sample surfaces were bombarded with low energy electrons from a normal incidence electron flood gun for charge compensation. Each analysis included 45 seconds of pre-sputtering over a 20 x 20 µm area and automatic centring of the secondary ions in the field aperture, contrast aperture and entrance slit. The remainder of each analysis comprised a 24 second acquisition cycle. Drift in each analytical session was monitored using two bracketing standards every 5 sample analyses. Instrumental mass fractionation (IMF) was corrected using matrix matched reference materials for pentlandite (VMSO), pyrrhotite (Alexo), chalcopyrite (Nifty-b) and pyrite (Sierra) (reference values found in LaFlamme et al., 2016). The IMF correction follows the procedure described in Kita et al. (2009).

5.6 Results

5.6.1 Petrography

227303 (Mafic granulite with disseminated sulphides)

Sample 227303 is a fine to medium grained weakly foliated garnet bearing mafic granulite (Fig. 5.6.1A). The groundmass consists of quartz (15 vol%) and plagioclase feldspar (55 vol%), with fine to medium grained (<1500 µm) fractured pink garnet porphyroblasts (10 vol%) (Fig. 5.6.1B). The plagioclase feldspar is fine to medium grained and subhedral to anhedral. Fine grained (<500 µm) anhedral quartz is subordinate to plagioclase feldspar within the groundmass and occurs as inclusions within garnet. Minor (5 vol%) fine grained subhedral to anhedral deep green to khaki-green pleochroic hornblende is frequently found in contact with sulphides, with minor (2 vol%) fine brown laths of biotite. Fine-grained (<500 µm) anhedral clinopyroxene (2 vol%) is associated with domains of quartz and feldspar and has partially altered to hornblende. Fine euhedral to subhedral lathes of muscovite are present in trace (<1 vol%) quantities. Opaque minerals form 10% of the sample and include fine (<500 µm) disseminated globular/blebby grains of magnetite, pyrrhotite and chalcopyrite hosted by pyrrhotite (Fig. 5.6.1C). The sulphides are net textured in places (Fig. 5.6.1B), particularly where they are associated with garnet porphyroblasts, crystal margins and garnet fractures.

227307 (Sulphide breccia)

Sample 227307 is a sulphide breccia and comprises approx. 40 vol% silicate material and c. 60 vol% sulphide material. Fine to coarse (approx. 100–3000 µm, frequently approx. 100 µm) anhedral quartz (15 vol%) occurs as clusters of grains several mm across, with undulose extinction and triple grain junctions. Green-brown pleochroic hornblende (25 vol%) is the predominant silicate mineral. Hornblende grains are anhedral to subhedral and approx. 250–2400 µm across, with many grains are up to approx. 1500 µm across. Quartz inclusions occur in several hornblende grains and are more frequent in hornblende grains in contact with quartz.

Sulphides and oxides include sphalerite (6 vol%), pyrrhotite (25 vol%), pyrite (20 vol%), chalcopyrite (3 vol%) and magnetite (6 vol%). The sphalerite is red in plane polarised light, and isotropic in reflected light. Sphalerite grains are between approx. 400–1800 µm across and most are blebby and anhedral. Inclusions of pyrrhotite and chalcopyrite are common (Fig. 5.6.1D). Pyrrhotite is pink-brown and strongly anisotropic, and occurs as anhedral grains approx. 350–1650 µm across with occasional inclusions of magnetite that in some instances appear pseudomorphic (Fig. 5.6.1E). Pyrite grains are commonly coarser than the other sulphides and oxides present, with grains 400–3000 µm in size. These grains are subhedral to anhedral and commonly include pyrrhotite, chalcopyrite, magnetite and, rarely, sphalerite (Fig. 5.6.1F). Chalcopyrite forms mostly anhedral grains 200–1200 µm across that include magnetite, pyrrhotite and sphalerite. Magnetite occurs as approx. 450–1200 µm anhedral grains that include pyrrhotite and chalcopyrite.

227306 (Sulphide-bearing pegmatite)

The primary silicate minerals in 227306 are alkali feldspar, biotite and muscovite. Colourless alkali feldspar clouded by sericitic alteration makes up the majority of 227306 (approx. 60 vol%) and comprises a small number of very coarse grains (approx. 3500–7000 µm). This sample contains a single grain of coarse subhedral platy (approx. 5000 µm) brown-dark brown pleochroic biotite (10 vol%). Muscovite mica makes up approx. 8 vol% of observed material in the form of colourless, platy, euhedral-subhedral crystals between approx. 300–2000 µm across. Several crystals show myrmekitic textures with apparent intergrowths of quartz.

Sulphides and oxides comprise approx. 22 vol% of 227306 and include pyrrhotite, pyrite, chalcopyrite and magnetite. These minerals mainly occur in a vein-hosted aggregate, and there is very little sulphide material outside the vein. Pyrrhotite (8 vol%) is present as approx. 200–1100 µm pink–cream-coloured strongly anisotropic anhedral grains and contains occasional inclusions of pyrite and chalcopyrite. Pyrite (5 vol%) forms approx. 40–1800 µm euhedral–subhedral isotropic grains. These often contain inclusions of pyrrhotite and chalcopyrite, and fine (<100 µm) pyrite grains are commonly seen intergrown with pyrrhotite (Fig. 5.6.2A–B). Chalcopyrite is a minor component of the rock (approx. 1 vol%) and occurs as approx. <100–1000 µm anhedral grains that are disseminated in small quantities across the sample or spatially associated with pyrrhotite. Isotropic brown-grey magnetite (8 vol%) forms masses of fine (approx. 150–200 µm) grains, that are interspersed with, and envelope, sulphide grains, forming caries textures (Fig. 5.6.2A,C).

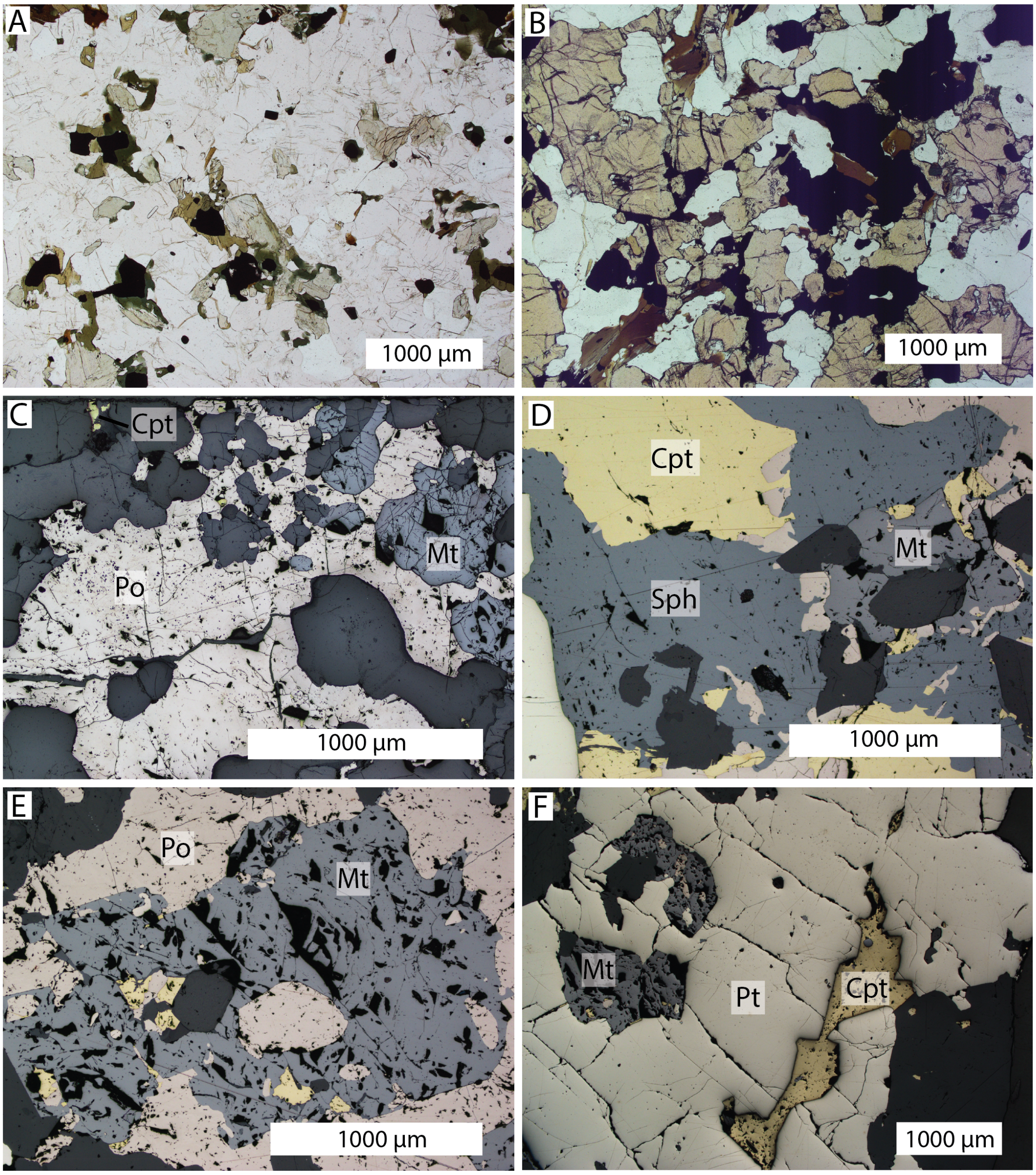

Figure 5.6.1: A-C: Photomicrographs of 227303. A: representative image of quartz, feldspar, hornblende groundmass; B: fractured garnet porphyroblasts with associated net-textured sulphides; C: predominant pyrrhotite with minor associated chalcopyrite and associated magnetite. D-F: Photomicrographs of 227307. D: Massive textured sulphides, with enclaves of pyrrhotite and chalcopyrite within sphalerite; E: Grey pseudomorphic magnetite, with inclusions of pyrrhotite and chalcopyrite; F: Enclaves of magnetite and chalcopyrite within pyrite

227317 (Mafic amphibolite with remobilised sulphides)

Sample 227317 is a fine- to medium-grained mafic amphibolite. Fine to medium grained (approx. 500–1700 µm) subhedral to anhedral, fractured, pink garnet porphyroblasts (5 vol%) are set within a groundmass of hornblende (80 vol%). These garnets contain fine (<500 µm), rounded inclusions of pyrrhotite, chalcopyrite and, very rarely, sphalerite. Hornblende is medium to coarse grained (approx. 1000–3000 µm), euhedral to anhedral and forms mats of overlapping laths. Minor and trace phases within the groundmass include fine to medium grained anhedral feldspar (<1 vol%), fine brown euhedral to subhedral laths of biotite (<1 vol%) and fine (<1000 µm) anhedral quartz (<1 vol%). Trace amounts (<1 vol%) of calcite infill a cavity, and are associated with an area of the sample comprising sericite and pale green actinolite.

Opaques/sulphides comprise approx. 15 vol% of the sample and include chalcopyrite (30 vol%), pyrrhotite (50 vol%), pyrite (<1 vol%), sphalerite (13 vol%), ilmenite (5 vol%) and magnetite (<1 vol%). Chalcopyrite forms fine to coarse stringers and blebby grains and is almost always associated with pyrrhotite (Fig. 5.6.2D). Pyrite forms rare fine (approx. 600 µm) euhedral grains (Fig. 5.6.2E). Pyrrhotite is present as fine to coarse blebby/globular grains and as net-textured pyrrhotite adjacent to garnet. Pyrrhotite is also present as fine laths in the vicinity of the area of the sample that consists of calcite, actinolite and sericite (Fig. 5.6.2F). Fine to coarse stringer and blebby grains of red sphalerite are associated with chalcopyrite and pyrrhotite. Fine-grained, rounded and blebby ilmenite grains occur in aggregates with the other sulphides and on hornblende cleavage planes. One ilmenite grain includes pyrrhotite, chalcopyrite and sphalerite lamellae. Trace magnetite occurs as fine rounded grains associated with the other opaque minerals.

5.6.2 In-situ sulphur isotope measurements

A total of 138 *in-situ* measurements of multiple sulphur isotope compositions were made on the four selected samples (Tables 5.6.1 and 5.6.2). Shapiro-Wilk statistical tests were used to assess the normality of the data distributions.

δ^{34}S measurements

Pyrrhotite within mafic granulite sample 227303 has δ^{34}S values between 3.84‰–5.37‰ with mean and median values of 4.51‰ and 4.52‰ respectively (n = 24, $2\sigma = 0.77$‰) (Fig. 5.6.3). These values are normally distributed ($P = 0.785$).

Chalcopyrite from pegmatite sample 227306 has δ^{34}S values of 4.06‰–6.03‰ (n = 8, mean/median of 5.43/5.57‰, $2\sigma = 1.15$‰). The δ^{34}S values of pyrite in this sample are 5.44‰–6.93‰ (n = 8, mean/median of 5.87‰/5.72‰, $2\sigma = 0.90$‰). Overall δ^{34}S values for 227306 show a range of 4.06‰–6.93‰ with mean and median values of

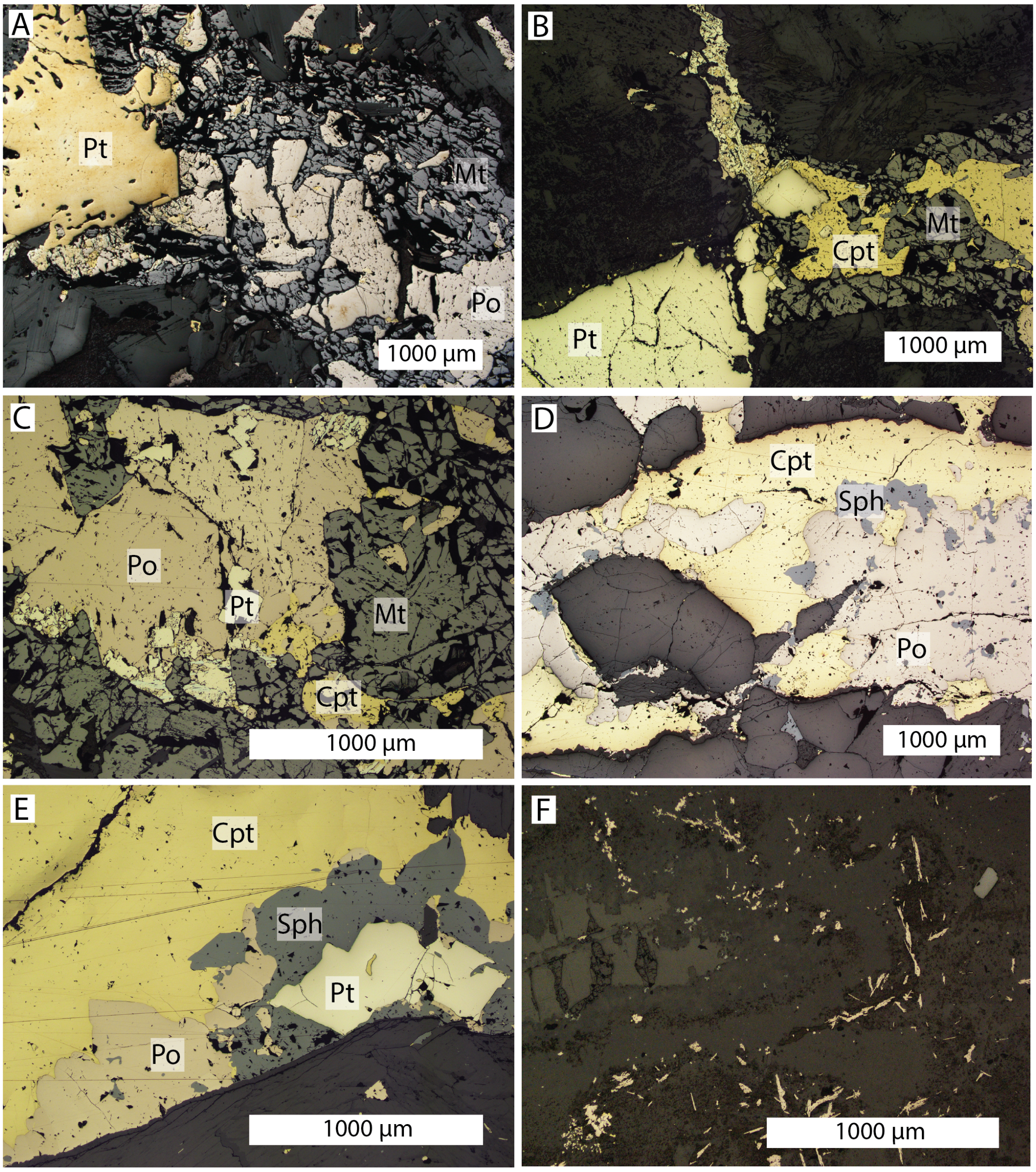

Figure 5.6.2: Photomicrographs of 227306. A: Caries-texture pyrrhotite within magnetite; B: Inclusion of euhedral pyrite within chalcopyrite; C: Inclusion of pyrite within pyrrhotite, surrounded by magnetite. D-F: Photomicrographs of 227317. D: Massive-textured chalcopyrite, sphalerite and pyrrhotite; E: Euhedral pyrite enveloped by sphalerite, with associated chalcopyrite and pyrrhotite; F: laths of pyrrhotite associated with calcite, actinolite and sericite

Sample	n	δ^{34}S	2σ	Mineral	n	δ^{34}S	2σ
227303	24	4.51	0.77	Po	24	4.51	0.77
227306	16	5.65	1.16	Cpt	8	5.43	1.15
				Pt	8	5.87	0.90
227307	38	5.99	0.53	Po	17	5.87	0.54
				Cpt	15	5.99	0.40
				Pt	6	6.30	0.12
227317	60	6.23	1.17	Po	24	6.08	0.89
				Cpt	22	6.08	1.47
				Pt	14	6.67	0.46

Table 5.6.1: Summary of average δ^{34}S values (‰) of Andromeda samples. Po = pyrrhotite, Cpt = chalcopyrite, Pt = pyrite

5.65‰ and 5.66‰ respectively (n = 16, $2\sigma = 1.16$‰). These values are not normally distributed ($P = 0.027$).

In sample 227307, the sulphide breccia, we analysed pyrrhotite, chalcopyrite and pyrite. The pyrrhotite has δ^{34}S compositions of 5.60‰–6.72‰ (n = 17, mean/median values of 5.87‰/5.77‰, $2\sigma = 0.54$‰); the chalcopyrite δ^{34}S values are 5.56‰–6.33‰ (n = 15, mean/median values of 5.99‰/6.01‰, $2\sigma = 0.40$‰) and the pyrite δ^{34}S values are 6.20‰–6.40‰ (n = 6, mean/median values of 6.30‰/6.29‰, $2\sigma = 0.12$‰). These δ^{34}S values are normally distributed (P = 0.313).

Sample 227317 comprises mafic amphibolite material hosting remobilised sulphides. We analysed pyrrhotite, chalcopyrite and pyrite. The δ^{34}S value of pyrrhotite is 5.26‰–6.79‰ (n = 24, mean/median values of 6.08‰/6.16‰, $2\sigma = 0.89$‰), chalcopyrite has δ^{34}S values of 3.66‰–6.94‰ (n = 22, mean/median values of 6.08‰/6.30‰, $2\sigma = 1.47$‰) and pyrite has δ^{34}S values of 6.19‰–7.04‰ (n = 14, mean/median values of 6.67‰/6.74‰, $2\sigma = 0.46$‰). The data from 227317 are not normally distributed (P <0.001).

Δ^{33}S measurements

The Δ^{33}S values of pyrrhotite in sample 227303 are -0.12‰–0.2‰. The Δ^{33}S values of 227306 are -0.25‰ to -0.03‰; the Δ^{33}S of 227306 chalcopyrite and pyrite is -0.25‰ to -0.05‰ and -0.19‰ to -0.03‰ respectively. The Δ^{33}S of 227307 are -0.14‰ to 0.10‰. The pyrrhotite in 227307 has Δ^{33}S values of -0.13–0.10‰, chalcopyrite has values of -0.14‰ to -0.01‰, and pyrite has Δ^{33}S values of -0.13‰ to 0.03‰. The Δ^{33}S values of 227317 are -0.38‰ to -0.03‰; pyrrhotite Δ^{33}S values are -0.36‰ to -0.04‰, chalcopyrite Δ^{33}S values are -0.35‰ to -0.03‰ and pyrite Δ^{33}S values are -0.30‰ to -0.10‰.

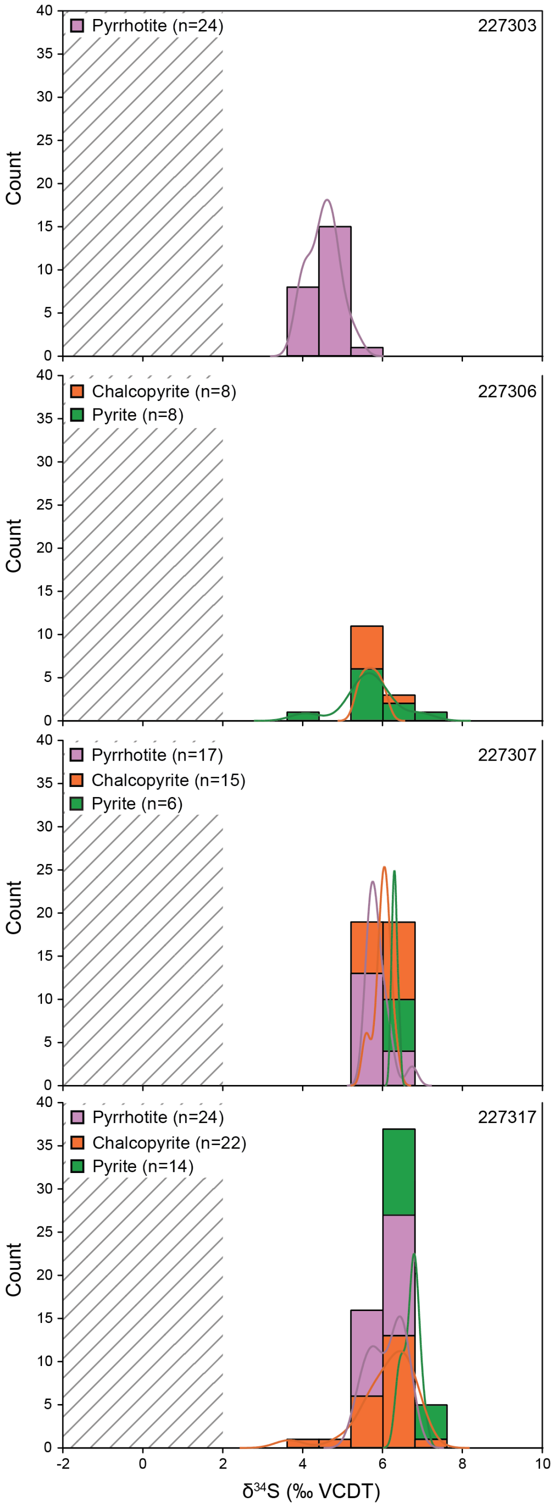

Figure 5.6.3: Histograms illustrating distributions of δ^{34}S in samples from Andromeda. Kernel Density Estimations have been overlaid. Hashed area indicates range of values indicative of mantle sulphur.

Sample	n	Δ^{33}S	2σ	Mineral	n	Δ^{33}S	2σ
227303	24	0.05	0.17	Po	24	0.05	0.17
227306	16	-0.13	-0.05	Cpt	8	-0.14	0.12
				Pt	8	-0.12	0.09
227307	38	-0.05	0.10	Po	17	-0.03	0.13
				Cpt	15	-0.12	0.06
				Pt	6	-0.08	0.03
227317	60	-0.22	0.08	Po	24	-0.21	0.19
				Cpt	22	-0.23	0.17
				Pt	14	-0.21	0.09

Table 5.6.2: Summary of average Δ^{33}S values (‰) of Andromeda samples. Po = pyrrhotite, Cpt = chalcopyrite, Pt = pyrite.

5.7 Discussion

5.7.1 Mineralisation at Andromeda

The δ^{34}S values of Andromeda sulphides are 3.84‰–7.04‰ (Table 1). The sample with the most positive average δ^{34}S is the mineralised breccia horizon (227307, mean δ^{34}S of 5.99‰ ± 0.53‰ (2σ) and the one with the least positive δ^{34}S is the representative sample of the host rock (227303, mean δ^{34}S of 4.51‰ ± 0.77‰ (2σ) (Fig. 5.7.1). The δ^{34}S sulphur isotope values from mineralised Andromeda sulphides are more positive than the sulphur isotope values from the Andromeda host granulite sulphides. This indicates that mineralised Andromeda sulphide sulphur isotope values are not the result of mixing between mantle derived sulphur (δ^{34}S = 0‰ ± 2‰) and assimilated host rock sulphides, as proposed for the Fraser Zone magmatic sulphide examples described by Walker et al. (2019).

The range of δ^{34}S isotopic values observed at Andromeda is similar to that observed in VMS deposits worldwide (Huston et al., 2010), where sulphur sources include thermal reduction of seawater sulphate, magmatic fluids, wall rock, and bacterial sulphate reduction of seawater sulphate (Brueckner et al., 2015 and references therein).

Archaean and Proterozoic VMS deposits are characterised by δ^{34}S compositions within the range of 0‰ ± 10‰ with limited intradeposit variability. Phanerozoic VMS deposits show much greater variability with δ^{34}S values up to > 20‰ (Huston et al., 2010). The δ^{34}S compositions of sulphides from Andromeda fall within the range of sulphur isotopic compositions of Proterozoic VMS deposits.

The presence of sphalerite as a component of the sulphide assemblages at Andromeda is inconsistent with the typical magmatic sulphide assemblage of pyrrhotite, pentlandite and chalcopyrite ± pyrite (Naldrett, 2004 and references therein). Sphalerite is, however, typical of VMS sulphide assemblages. Bimodal-mafic and pelitic-mafic type VMS

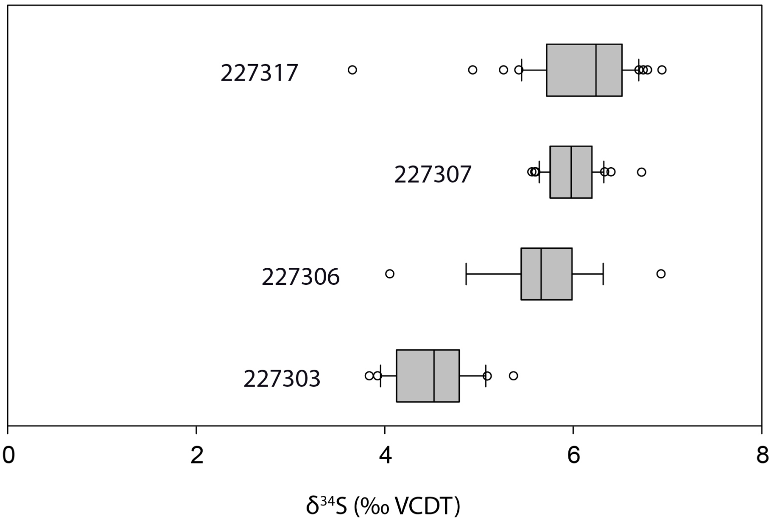

Figure 5.7.1: Box plots showing the distribution of δ^{34}S values for the analysed Andromeda samples. Median values, 10th, 25th, 75th and 90th percentiles are marked. Outliers are represented by circles.

deposits are characterised by assemblages comprising pyrrhotite, pyrite, chalcopyrite and sphalerite with generally low to no Pb (galena) content (Galley et al., 2007).

The mineralisation is hosted within a sequence of mafic granulites that contain significant late amphibole, intercalated with minor fine-grained doleritic units and intruded by coarse-grained granitic units. The prevalence of garnet within the host lithologies is consistent with variable assimilation of sedimentary material by mafic magmas during emplacement, or the presence of intercalated sedimentary lithologies within the host sequence. No discrete sedimentary units were recognised within the Andromeda wallrock sequence so we attribute the garnet content to assimilated sedimentary material.

5.7.2 The role of an Archaean sulphur component

Samples 227303, 227306, 227307 and 227317 show mean Δ^{33}S values of 0.05‰ (± 0.21‰), -0.13‰ (± 0.11‰), -0.05‰ (± 0.10‰) and -0.22‰ (± 0.08‰) respectively (2σ) (Table 5.6.2). The majority of these values fall into the range of 0‰ ± 0.2‰ that is commonly considered to define the limits of Δ^{33}S values that could be generated by MDF processes (Farquhar and Wing, 2003). However if the narrower definition proposed by LaFlamme et al. (2018b) is adopted then many of the Δ^{33}S values in the Andromeda samples are consistent with the presence of Archaean sulphur (Fig. 5.7.2).

The inference of Archaean sulphur at Andromeda contrasts with the conclusions drawn from *in-situ* sulphur isotope analyses of Fraser Zone magmatic sulphides and sedimentary rocks described by Walker et al. (2019). In that work, three variably mineralised Fraser Zone magmatic sulphide localities and sedimentary sulphides from the Snowys Dam Formation were analysed. The sedimentary sulphides have a mean Δ^{33}S value of

-0.01‰ ± 0.09‰ (2σ); as this value is within error of zero and within the narrower definition of MDF-generated MIF-S values proposed by LaFlamme et al. (2018b), it is interpreted to indicate an absence of MIF-S sulphur within sedimentary rocks of the Snowys Dam Formation.

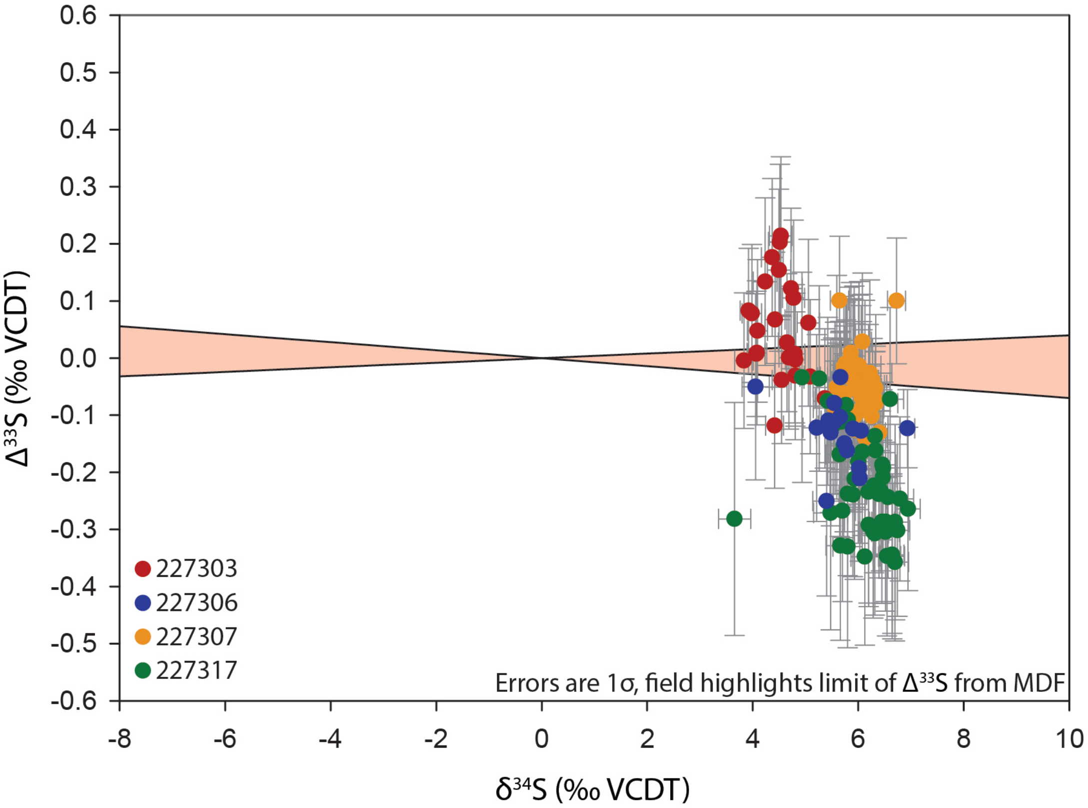

Figure 5.7.2: Sulphur isotope data from Andromeda samples plotted on a δ^{34}S versus Δ^{33}S diagram. The shaded field shows the limits of MDF-derived MIF proposed by LaFlamme et al. (2018b)

The absence of a MIF-signal in the magmatic sulphides contrasts with the evidence of an Archaean component in the host rocks provided by geochemical modelling, detrital zircon geochronology and Lu-Hf isotope data (Kirkland et al., 2011a; Spaggiari et al., 2014b; Smithies et al., 2015). To resolve this apparent contradiction, Walker et al. (2019) suggested that sulphur was decoupled from the isotopes that record an Archaean heritage for the Fraser Zone by sedimentary processes. Sulphur is hosted by sulphide minerals which are easily weathered and dissolved by a sedimentary cycle, so the sediments of the Snowys Dam Formation and the Arid Basin are likely to contain sulphur that was incorporated by precipitation from seawater, rather than as detrital grains. Zircon, on the other hand, is one of the most resistant minerals (Corfu et al., 2003), and as documented by the preservation of the Archaean signature, can survive a sedimentary cycle intact. Based on this argument, Walker et al. (2019) proposed that weathering and erosion over an extended period of time stripped Archaean sulphides from the sediments that formed the Arid Basin while leaving more robust phases like zircon intact. In this scenario sulphides within the Snowys Dam Formation were derived from seawater, so any Archaean component would have been massively diluted and the MIF-signature effectively removed.

If Andromeda is an example of VMS mineralisation within the Mesoproterozoic Fraser Zone, then the MIF-signature places useful constraints on the sulphur source. It has been suggested that hydrothermal fluids can mobilise and transport Archaean sulphur without loss of the MIF-signature, and this mechanism has been used to explain MIF-signals within orogenic gold deposits (e.g. the Archaean Lady Bountiful deposit, LaFlamme et al., 2018b). Successful genetic models for Andromeda must: (1) explain the positive and negative MIF values; (2) include a sulphur source accessible to the fluids that formed Andromeda but not to the magmas that formed the magmatic sulphide deposits.

The MIF anomalies must have been generated prior to 2.4 Ga, so the Archaean sulphur must have existed in some other reservoir for a significant period before being incorporated within Andromeda in the c. 1300 Ma Fraser Zone. Discrete fragments of Archaean material are preserved within the Biranup Zone, which lies on the south-eastern margin of the Yilgarn Craton, adjacent to the Fraser Zone (Kirkland et al., 2011a,b; Smithies et al., 2015). The Biranup Zone consists of Archaean Yilgarn crustal material that has been modified by the addition of juvenile mantle-derived material over the course of several tectonothermal episodes (Kirkland et al., 2011a; Smithies et al., 2015). If the parts of the Yilgarn Craton that were reworked to form the Biranup Zone consisted of stratigraphy broadly similar to that of the present south-eastern Yilgarn Craton (i.e. the Eastern Goldfields), then Archaean MIF-bearing sulphur-rich lithologies would have been incorporated into the Biranup Zone. The 2.8–2.6 Ga Eastern Goldfields Superterrane comprises belts of deformed and metamorphosed volcanic and sedimentary lithologies intruded by granitic rocks. These include the Kurnalpi and Gindalbie Terranes, which are interpreted as Archaean volcanic arcs (Barley et al., 2008). Associated volcanic–sedimentary stratigraphy includes the c. 2692 Ma Kapai Slate; a regionally extensive metasedimentary unit noted for minor Au mineralisation near Kambalda (Steadman et al., 2015), and the c. 2680 Ma Black Flag Group; a thick (>2 km) volcanic-sedimentary succession overlying many other units in the Eastern Goldfields (Squire et al., 2010; Tripp, 2013; Steadman et al., 2015). The Kapai Slate and the Black Flag Group are sulphidic and contain pyrite bearing Δ^{33}S values between approximately -3‰ to +3‰ (Steadman et al., 2015; Gregory et al., 2016; Godefroy-Rodríguez et al., 2018). Recycled pyrite-bearing Kapai Slate or Black Flag Group material within the Biranup Zone is a plausible source of the sulphur MIF-signature we identified at Andromeda.

The Fraser Shear Zone (FSZ) is a significant lithospheric scale structure that is within

4 km of Andromeda's current position. It separates the Fraser Zone from the Biranup Zone. We suggest that the FSZ was a fluid pathway, and that fluids moving on the FSZ mobilised Archaean sulphur with a MIF-signature from a reservoir in the Biranup Zone to the mineralising system that formed Andromeda (Fig. 5.7.3). This process formed $\Delta^{33}S_1$ anomalies within the mineralised and wallrock sulphides at Andromeda. The presence of positive and negative Δ^{33}S values indicate that the reservoir sampled by the FSZ is heterogenous and includes material derived from Archaean sulphate and sulphide (Farquhar and Wing, 2003). Furthermore, the more negative $\Delta^{33}S_1$ values in the more altered rocks (227307: breccia, 227306: pegmatite, and 227317: retrogressed granulite) indicate that at least two sources of sulphur contributed to mineralisation. The most likely sources are: Proterozoic seawater, incorporated into the rocks by bacterial sulphate reduction, thermal sulphate reduction, or other processes and Archaean sulphur transported by fluids moving on the FSZ. A contribution from mantle-derived sulphur cannot be excluded. The most negative $\Delta^{33}S_1$ are found in the most retrogressed sample, indicating that the MIF-source continued to contribute to the sulphur budget of the rocks after peak metamorphism, which implies that the FSZ is a long-lived fluid-bearing structure.

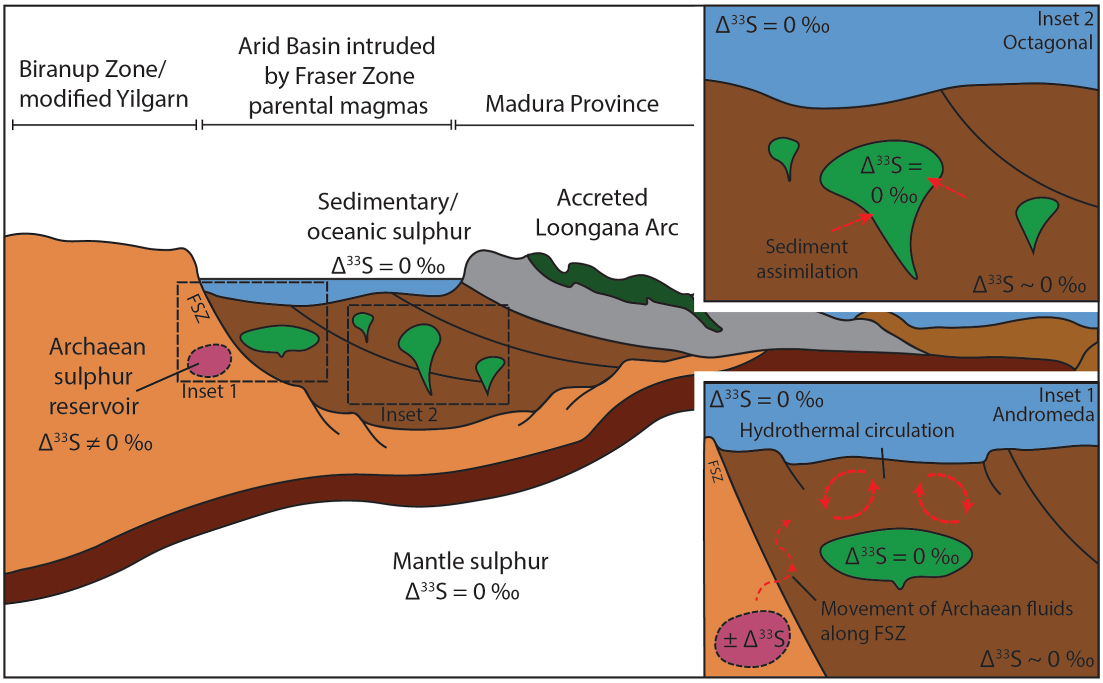

Figure 5.7.3: Proposed model by which a cryptic reservoir of Archaean sulphur preserved within the Biranup Zone, is tapped by fluids moving through the Fraser Shear Zone (FSZ) and incorporated into Andromeda in the Fraser Zone (Inset 1: Andromeda). Inset 2 shows the proposed model of mineralisation at Octagonal (Inset 2) which involves assimilation of sediments stripped of Archaean sulphur (Walker et al., 2019)

5.8 Conclusions

Sulphides from wall rock, sulphide breccia and vein material from the Andromeda prospect in the Fraser Zone were characterised by *in-situ* sulphur isotope analysis and petrography. We conclude that:

- Mineralised horizons in Andromeda consist of pyrrhotite, chalcopyrite, pyrite and sphalerite, which is atypical of magmatic sulphide mineralisation.
- A majority of the *in-situ* δ^{34}S compositions fall within a range of 4.50‰ to 6.70‰. The δ^{34}S values of mineralised material are higher than those of disseminated sulphides in proximal footwall lithologies, which indicates that the footwall lithologies were not a primary source of the sulphur that forms the mineralisation. The observed range of values is characteristic of Archaean and Proterozoic VMS deposits worldwide and, combined with the presence of sphalerite in Andromeda sulphide assemblages, is consistent with a VMS-mineralised protolith.
- The presence of sulphur with a MIF-signature at Andromeda, contrasts with the lack of sulphur with a MIF-signature elsewhere in the Fraser Zone (Walker et al., 2019). To reconcile the results, we propose that fluids that flowed on the FSZ transported sulphur with a MIF-signature from the Biranup Zone to Andromeda.
- Plausible reservoirs in the Biranup Zone include recycled material derived from the regionally extensive, pyrite-bearing Kapai Slate and/or Black Flag Group of the Eastern Goldfields. Archaean MIF signatures borne by Archaean sulphur-bearing pyrite in this material might have been mobilised by hydrothermal fluids and deposited in the sulphides at Andromeda (Fig. 5.8.1).
- The data presented in this study, in addition to those of Walker et al. (2019), describe a dynamic and complex sulphur system within the Fraser Zone. Archaean sulphur was stripped from sediments during weathering and transport prior to assimilation into magmatic sulphides (Walker et al., 2019), while also being incorporated into VMS-style mineralisation within the Fraser Zone from more distal sources via the Fraser Shear Zone.

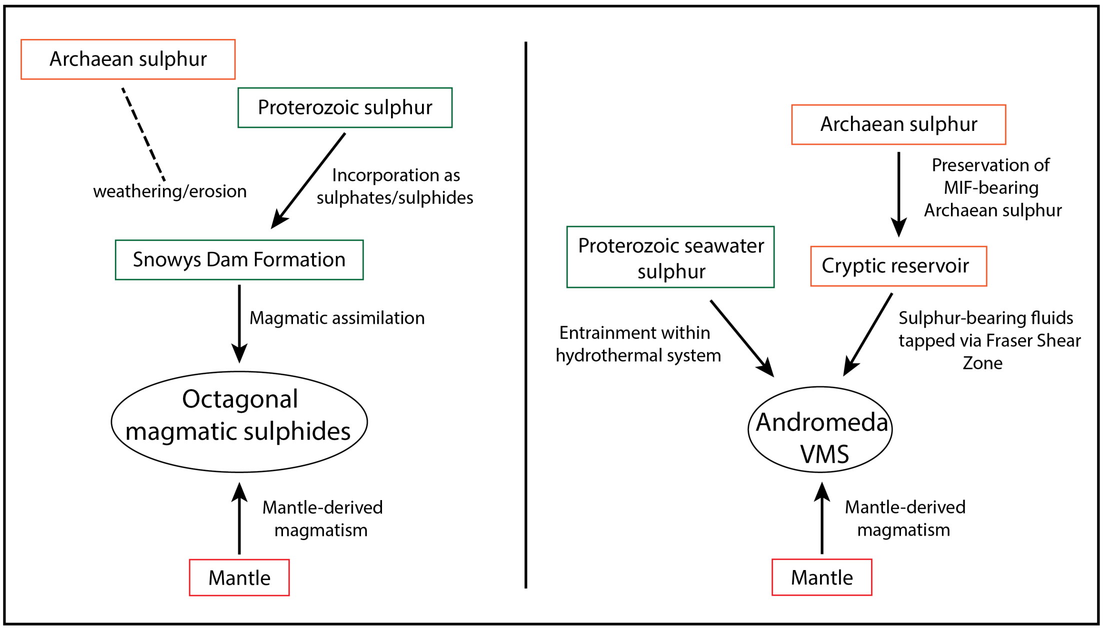

Figure 5.8.1: Proposed models and sources of sulphur incorporated in Andromeda (suspected VMS) versus Octagonal (magmatic sulphide) in the Fraser Zone (after Walker et al., 2019)

5.9 References

Barley, M. E., Brown, S. J., Krapež, B., Kositcin, N., 2008. Physical volcanology and geochemistry of a Late Archaean volcanic arc: Kurnalpi and Gindalbie terranes, Eastern Goldfields superterrane, Western Australia. Precambrian Research 161 (1-2), 53–76.

Barrie, C., Cathles, L., Erendi, A., Schwaiger, H., Murray, C., Hannington, M., 1999. Heat and fluid flow in volcanic-associated massive sulfide-forming hydrothermal systems. Reviews in Economic Geology 8, 201–219.

Brisbout, L., 2015. Determining crustal architecture in the east Albany-Fraser Orogen from geological and geophysical data. Geological Survey of Western Australia.

Brueckner, S. M., Piercey, S. J., Layne, G. D., Piercey, G., Sylvester, P. J., 2015. Variations of sulphur isotope signatures in sulphides from the metamorphosed Ming Cu (- Au) volcanogenic massive sulphide deposit, Newfoundland Appalachians, Canada. Mineralium Deposita 50 (5), 619–640.

Clark, C., Kirkland, C. L., Spaggiari, C. V., Oorschot, C., Wingate, M. T., Taylor, R. J., 2014. Proterozoic granulite formation driven by mafic magmatism: An example from the Fraser Range Metamorphics, Western Australia. Precambrian Research 240, 1–21.

Condie, K. C., Myers, J. S., 1999. Mesoproterozoic Fraser Complex: geochemical evidence for multiple subduction-related sources of lower crustal rocks in the Albany-Fraser Orogen, Western Australia. Australian Journal of Earth Sciences 46 (6), 875–882.

Corfu, F., Hanchar, J. M., Hoskin, P. W., Kinny, P., 2003. Atlas of zircon textures. Reviews in mineralogy and geochemistry 53 (1), 469–500.

de Gromard, R., Spaggiari, C., Munro, M., Sapkota, J., De Paoli, M., 2017. SGTSG 2017 Albany-Fraser Orogen pre-conference field trip: Transect across an Archaean craton margin to a Proterozoic ophiolite. Geological Survey of Western Australia Record 2017/14, 100p.

De Waele, B., Pisarevsky, S., 2008. Geochronology, paleomagnetism and magnetic fabric of metamorphic rocks in the northeast fraser belt, western australia. Australian Journal of Earth Sciences 55 (5), 605–621.

Farquhar, J., Bao, H., Thiemens, M., 2000. Atmospheric influence of earth's earliest sulfur cycle. Science 289 (5480), 756–758.

Farquhar, J., Wing, B. A., 2003. Multiple sulfur isotopes and the evolution of the atmosphere. Earth and Planetary Science Letters 213 (1-2), 1–13.

Franklin, J., Gibson, H., Jonasson, I., Galley, A., 2005. Volcanogenic massive sulfide deposits. Economic Geology 100 (Anniversary volume), 523–560.

Galley, A. G., Hannington, M. D., Jonasson, I., 2007. Volcanogenic massive sulphide deposits. Mineral deposits of Canada: A synthesis of major deposit-types, district metallogeny, the evolution of geological provinces, and exploration methods: Geological Association of Canada, Mineral Deposits Division, Special Publication 5, 141–161.

Glasson, K. J., Johnson, T. E., Kirkland, C. L., Gardiner, N. J., Clark, C., Blereau, E., Hartnady, M. I., Spaggiari, C., Smithies, H., 2019. A window into an ancient backarc? The magmatic and metamorphic history of the Fraser Zone, Western Australia. Precambrian Research 323, 55–69.

Godefroy-Rodríguez, M., Hagemann, S., LaFlamme, C., Fiorentini, M., 2018. The multiple sulfur isotope architecture of the Golden Mile and Mount Charlotte deposits, Western Australia. Mineralium Deposita, 1–26.

Gregory, D. D., Large, R. R., Bath, A. B., Steadman, J. A., Wu, S., Danyushevsky, L., Bull, S. W., Holden, P., Ireland, T. R., 2016. Trace element content of pyrite from the kapai slate, St. Ives Gold District, Western Australia. Economic Geology 111 (6), 1297–1320.

Hulston, J., Thode, H., 1965. Variations in the S33, S34, and S36 contents of meteorites and their relation to chemical and nuclear effects. Journal of Geophysical Research 70 (14), 3475–3484.

Huston, D. L., Pehrsson, S., Eglington, B. M., Zaw, K., 2010. The geology and metallogeny of volcanic-hosted massive sulfide deposits: Variations through geologic time and with tectonic setting. Economic Geology 105 (3), 571–591.

Johnston, D. T., 2011. Multiple sulfur isotopes and the evolution of Earth's surface sulfur cycle. Earth-Science Reviews 106 (1-2), 161–183.

Kirkland, C., Smithies, R., Spaggiari, C., Wingate, M., de Gromard, R. Q., Clark, C., Gardiner, N., Belousova, E., 2017. Proterozoic crustal evolution of the Eucla basement, Australia: Implications for destruction of oceanic crust during emergence of Nuna. Lithos 278, 427–444.

Kirkland, C. L., Spaggiari, C. V., Johnson, T. E., Smithies, R. H., Danišík, M., Evans, N., Wingate, M. T. D., Clark, C., Spencer, C., Mikucki, E., McDonald, B. J., 2016. Grain size matters: Implications for element and isotopic mobility in titanite. Precambrian Research 278, 283 – 302.

Kirkland, C. L., Spaggiari, C. V., Pawley, M. J., Wingate, M. T. D., Smithies, R. H., Howard, H. M., Tyler, I. M., Belousova, E. A., Poujol, M., 2011a. On the edge: U-Pb,Lu-Hf, and Sm-Nd data suggests reworking of the Yilgarn craton margin during formation of the Albany-Fraser Orogen. Precambrian Research 187 (3), 223 – 247.

Kirkland, C. L., Wingate, M. T. D., Spaggiari, C. V., 2011b. 194709: metamonzogranite, Cave Rock; Geochronology Record 985. Geological Survey of Western Australia, 4p.

Kita, N. T., Ushikubo, T., Fu, B., Valley, J. W., 2009. High precision sims oxygen isotope analysis and the effect of sample topography. Chemical Geology 264 (1), 43 – 57.

LaFlamme, C., Fiorentini, M. L., Lindsay, M. D., Bui, T. H., 2018a. Atmospheric sulfur is recycled to the crystalline continental crust during supercontinent formation. Nature communications 9.

LaFlamme, C., Jamieson, J. W., Fiorentini, M. L., Thébaud, N., Caruso, S., Selvaraja, V., 2018b. Investigating sulfur pathways through the lithosphere by tracing mass independent fractionation of sulfur to the Lady Bountiful orogenic gold deposit, Yilgarn Craton. Gondwana Research 58, 27–38.

LaFlamme, C., Martin, L., Jeon, H., Reddy, S. M., Selvaraja, V., Caruso, S., Bui, T. H., Roberts, M. P., Voute, F., Hagemann, S., et al., 2016. In situ multiple sulfur isotope analysis by sims of pyrite, chalcopyrite, pyrrhotite, and pentlandite to refine magmatic ore genetic models. Chemical Geology 444, 1–15.

Leavitt, W. D., Cummins, R., Schmidt, M. L., Sim, M. S., Ono, S., Bradley, A. S., Johnston, D. T., 2014. Multiple sulfur isotope signatures of sulfite and thiosulfate reduction by the model dissimilatory sulfate-reducer, Desulfovibrio alaskensis str. G20. Frontiers in microbiology 5, 591.

MacNamara, J., Thode, H., 1950. Comparison of the isotopic constitution of terrestrial and meteoritic sulfur. Physical Review 78 (3), 307.

Maier, W. D., Smithies, R. H., Spaggiari, C. V., Barnes, S. J., Kirkland, C. L., Kiddie, O., Roberts, M. P., 2016. The evolution of mafic and ultramafic rocks of the Mesoproterozoic Fraser Zone, Albany-Fraser Orogen, and implications for the Ni-Cu sulphide potential of the region. Geological Survey of Western Australia, Record 2016/8, 49p.

Munro, M., de Gromard, R., Spaggiari, C., 2017. Structural evolution of the S-bend region, east Albany-Fraser Orogen. In: GSWA Extended Abstracts, Perth.

Naldrett, A., 2004. Magmatic sulfide deposits: Geology, geochemistry and exploration. Springer Science & Business Media.

Ono, S., Wing, B., Johnston, D., Farquhar, J., Rumble, D., 2006. Mass-dependent fractionation of quadruple stable sulfur isotope system as a new tracer of sulfur biogeochemical cycles. Geochimica et Cosmochimica Acta 70 (9), 2238–2252.

Piercey, S. J., 2011. The setting, style, and role of magmatism in the formation of volcanogenic massive sulfide deposits. Mineralium Deposita 46 (5-6), 449–471.

Seal, II, R. R., 2006. Sulfur isotope geochemistry of sulfide minerals. Reviews in Mineralogy and Geochemistry 61 (1), 633.

Selvaraja, V., Caruso, S., Fiorentini, M. L., LaFlamme, C., 2017. The Global Sedimentary Sulfur Isotope Database.
URL http://www.cet.edu.au/research-projects/special-projects/gssid-global-sedimentary-sulfur-isotope-database

Smithies, R. H., Spaggiari, C. V., Kirkland, C. L., 2015. Building the crust of the Albany-Fraser Orogen: constraints from granite geochemistry. Geological Survey of Western Australia, Report 150, 49p.

Smithies, R. H., Spaggiari, C. V., Kirkland, C. L., Howard, H. M., Maier, W. D., 2013. Petrogenesis of gabbros of the Mesoproterozoic Fraser Zone: constraints on the tectonic evolution of the Albany-Fraser Orogen. Geological Survey of Western Australia, Record 2013/15, 29p.

Spaggiari, C., Kirkland, C., Smithies, R., Occhipinti, S., Wingate, M., 2014a. Geological framework of the albany–fraser orogen. In: Albany–Fraser Orogen seismic and magnetotelluric (MT) workshop 2014: extended abstracts compiled by CV Spaggiari and IM Tyler: Geological Survey of Western Australia, Record. Vol. 6. pp. 12–27.

Spaggiari, C., Smithies, R., Kirkland, C., England, R., Occhipinti, S., Wingate, M., 2015a. Eucla basement results: implications for geodynamics and mineral prospectivity. In: Eucla Basement Stratigraphic Drilling Results Release Workshop: Extended Abstracts, Record. Vol. 10. pp. 53–58.

Spaggiari, C. V., Bodorkos, S., Barquero-Molina, M., Tyler, I. M., Wingate, M. T. D., 2009. Interpreted bedrock geology of the South Yilgarn and central Albany-Fraser Orogen, Western Australia. Geological Survey of Western Australia, Record 2009/10, 84p.

Spaggiari, C. V., Kirkland, C. L., Smithies, R. H., Wingate, M. T. D., 2011. The geology of the East Albany-Fraser Orogen - A Field Guide. Geological Survey of Western Australia, Record 2009/10, 84.

Spaggiari, C. V., Kirkland, C. L., Smithies, R. H., Wingate, M. T. D., 2012. What lies beneath - interpreting the Eucla basement. GSWA extended abstracts, 24–26.

Spaggiari, C. V., Kirkland, C. L., Smithies, R. H., Wingate, M. T. D., 2014b. Tectonic links between Proterozoic sedimentary cycles, basin formation and magmatism in the Albany-Fraser Orogen. Geological Survey of Western Australia, Report 133, 63p.

Spaggiari, C. V., Kirkland, C. L., Smithies, R. H., Wingate, M. T. D., Belousova, E. A., 2015b. Transformation of an Archean craton margin during Proterozoic basin formation and magmatism: The Albany-Fraser Orogen, Western Australia. Precambrian Research 266, 440 – 466.

Spaggiari, C. V., Smithies, R. H., Kirkland, C. L., Wingate, M. T., England, R. N., Lu, Y.-J., 2018. Buried but preserved: The Proterozoic Arubiddy Ophiolite, Madura Province, Western Australia. Precambrian Research 317, 137–158.

Squire, R. J., Allen, C. M., Cas, R. A., Campbell, I. H., Blewett, R. S., Nemchin, A. A., 2010. Two cycles of voluminous pyroclastic volcanism and sedimentation related to episodic granite emplacement during the late Archean: Eastern Yilgarn Craton, Western Australia. Precambrian Research 183 (2), 251–274.

Steadman, J. A., Large, R. R., Meffre, S., Olin, P. H., Danyushevsky, L. V., Gregory, D. D., Belousov, I., Lounejeva, E., Ireland, T. R., Holden, P., 2015. Synsedimentary to early diagenetic gold in black shale-hosted pyrite nodules at the Golden Mile Deposit, Kalgoorlie, Western Australia. Economic Geology 110 (5), 1157–1191.

Tripp, G. I., 2013. Stratigraphy and structure in the Neoarchaean of the Kalgoorlie district, Australia: critical controls on greenstone-hosted gold deposits. Ph.D. thesis, James Cook University.

Urey, H. C., 1947. The thermodynamic properties of isotopic substances. Journal of the Chemical Society (Resumed), 562–581.

Waddell, P.-J. A., Timms, N. E., Spaggiari, C. V., Kirkland, C. L., Wingate, M. T., 2015. Analysis of the Ragged Basin, Western Australia: Insights into syn-orogenic basin evolution within the Albany–Fraser Orogen. Precambrian Research 261, 166–187.

Walker, A., Evans, K., Kirkland, C., Martin, L., Kiddie, O., Spaggiari, C., 2019. Tracking mineralisation with in situ multiple sulphur isotopes: a case study from the Fraser Zone, Western Australia. Precambrian Research 332.

Chapter 6

Conclusions

The overarching objective of this project was to use trace element and sulphur isotopes to constrain the processes that formed and modified mineralisation within the Fraser Zone. Previous research comprised only one study describing the sulphur isotopes and geochemical characteristics of localities hosting magmatic sulphide mineralisation (Maier et al., 2016). The samples used for this project are sulphide-bearing rocks from four localities in the Fraser Zone that host variable degrees and styles of mineralization: Plato, Nova-related material (NRM), Octagonal and Andromeda. The in-situ sulphur isotope work described in Chapters 3 and 5 highlights the relationship between magmatic sulphide mineralisation and assimilation of local sulphur-rich lithologies, and reveals a complex record of mixed sulphur sources, including Archaean sulphur with a MIF-signature, in the Fraser Zone. Furthermore, the image analysis technique that we used for the first time in geological applications enabled quantitative assessment of modification of magmatic sulphides by metamorphic processes, and can be applied widely in geological science to quantify relationships that were previously estimated from qualitative visual assessments. The major findings of this project, the potential limitations and avenues for further research are as follows:

6.1 Contribution of sedimentary sulphur to magmatic sulphide mineralisation

Assimilation of sulphur from sedimentary rocks of the Snowys Dam Formation is a key process in the formation of magmatic sulphide mineralisation in the Fraser Zone (Chapter 3). In-situ sulphur isotope analyses showed that the δ^{34}S signatures of the Plato, NRM and Octagonal magmatic sulphide prospects are different, and different to that of metasediments of the Snowys Dam Formation. A mean δ^{34}S value of 1.05‰ (± 0.85‰) at Plato overlaps accepted δ^{34}S values for mantle sulphur, and in conjunction with weak mineralisation at Plato, implies that assimilation of sedimentary sulphur was limited at that locality. This is consistent with the conclusions of (Maier et al., 2016), who infer that mafic intrusions at Plato were emplaced as a network of narrow sill-like bodies that crystallised rapidly and that did not assimilate much country rock. In contrast, higher mean δ^{34}S values of 2.35‰ (± 0.40‰) at NRM and 4.31‰ (± 0.80‰) at Octagonal, in conjunction with a range of δ^{34}S values between 4.44‰–7.88‰ in local metasedimentary sulphides, are interpreted to represent more extensive assimilation of sedimentary sulphur at NRM and Octagonal.

Two-component mixing models between Fraser Zone parental magmas and Snowys Dam metasediments based on these δ^{34}S data allow the contribution of sedimentary sulphur to mineralisation to be quantified. Assuming comparable sulphur concentrations within assimilated material at each locality, around 5% of the sulphur at Plato is estimated to be assimilated sedimentary sulphur, while sedimentary sulphur provides c. 12% and 30% of the sulphur within the NRM and Octagonal parental magmas, respectively.

Pyrrhotite inclusions inside garnet hosted by metasediments at Octagonal have different δ^{34}S values to pyrrhotite in the matrix; pyrrhotite inside and outside garnet are characterised by mean δ^{34}S values of 4.55‰ and 5.51‰, respectively. This indicates that the pyrrhotite outside the garnet contains a higher proportion of the heavier sulphur isotope. The change in sulphur isotope ratio is attributed to progressive melting of the Snowys Dam Formation during amphibolite to granulite facies metamorphism of the Fraser Zone during Stage I of the Albany-Fraser Orogeny, with preferential loss of the lighter isotope to a mobile phase. Pyrrhotite enclosed within garnet did not lose sulphur and consequently exhibits less positive δ^{34}S values.

6.2 VMS-style mineralisation in the Fraser Zone

Until recently the Fraser Zone was only considered prospective for nickel sulphide mineralisation. However, the Andromeda prospect, discovered in 2018, is atypical of magmatic nickel sulphide deposits because the sulphide assemblages comprise sphalerite, pyrrhotite, pyrite and chalcopyrite. This assemblage, combined with δ^{34}S values of 3.84‰–7.04‰ are more characteristic of VMS-style mineralization than magmatic sulphide mineralisation (Chapter 5). The existence of VMS mineralisation in the Albany–Fraser Orogen has not been reported previously, but is not unexpected. These deposits are generated in extensional tectonic settings, extension-related magmatism is key to their formation (Piercey, 2011), and the Fraser Zone is thought to have formed within a back-arc or continental rift setting (Kirkland et al., 2011; Spaggiari et al., 2011), where large volumes of mantle-derived magmas were emplaced into an extending sedimentary basin. The presence of economic VMS mineralisation would increase the list of metals the Fraser Zone may be prospective for to include Zn, Pb, Au, Ag and critical metals such as In, but further work is required to determine the extent of mineralisation styles other than magmatic nickel sulphide mineralisation within the Fraser Zone.

6.3 Archaean sulphur within Fraser Zone magmatic and VMS sulphides

The Fraser Zone's Archaean heritage has been established, based on Lu–Hf isotopic data and geochemical modelling (Kirkland et al., 2011; Smithies et al., 2015). It is reasonable to expect that the Δ^{33}S data would also record this Archaean heritage, provided by the incorporation and reworking of older (Archaean) sulphur and characterised by positive and negative MIF-S anomalies. However, the Δ^{33}S data of Plato, NRM and Octagonal do not have MIF-S anomalies; Δ^{33}S values from all three localities have a mean value of -0.01‰ (± 0.09‰, 2σ) (Chapter 3). Quantitative calculations show that dilution of Archaean sulphur with a MIF-S signature by Proterozoic sulphur does not explain the observed Δ^{33}S values. Approximately 5%, 12% and 30% of the sulphur at Plato, NRM and Octagonal, respectively, was sourced from potentially MIF-S sulphur-bearing sedimentary rocks of the Snowys Dam Formation according to mixing models; these models also indicate that assimilation of a sedimentary sulphur fraction of less than 10%, with a conservative Δ^{33}S value of 1%, would result in a sulphur mix with a Δ^{33}S value in excess of Δ^{33}S values seen at these three localities. Therefore, we concluded that Archaean sulphur was not present in the sulphur in the sedimentary rock that was assimilated to form the magmatic sulphide deposits. Sulphides are more likely to be dissolved by weathering and erosion than zircon, which would decouple sulphur from the Archaean heritage recorded by zircon-hosted trace elements and isotope. The MIF-S signatures are generally considered to be indelible, so their removal by weathering has significant implications for our understanding of cycling of Archaean sulphur within the crust.

In contrast to the Fraser Zone magmatic sulphides, samples from Andromeda include sulphides with a non-zero MIF-S signature, recording the presence of Archaean sulphur in wall rock and orebody sulphides. The Δ^{33}S are -0.38‰–0.21‰. The conclusions drawn from Plato, NRM and Octagonal Δ^{33}S data preclude the possibility that Archaean MIF-S signatures at Andromeda were inherited from metasedimentary material in the Fraser Zone. However, mineralisation at Andromeda is thought to be different to that at Octagonal and NRM because it is VMS rather than magmatic sulphide mineralization. Therefore, the formation of the Andromeda orebody is likely to have involved hydrothermal activity and extensive fluid-rock interaction between the parent magmatic body, adjacent wall rocks, and seawater. The proximity of the Fraser Shear Zone (FSZ) to Andromeda provides a pathway for fluids, which might plausibly have interacted with Archaean material preserved within the adjacent Biranup Zone. This preserved material may include rocks of the Kapai Slate and Black Flag Group; these lithologies are regionally extensive in the southern and southeastern Yilgarn Craton and contain pyrite with a MIF-S signature, so they might have provided the MIF-S signature identified at Andromeda.

The sulphur isotope results from Plato, NRM, Octagonal and Andromeda reveal a complex system, in which sulphur is incorporated into mineralisation from local lithologies, recycled by sedimentary processes, and introduced into the Fraser Zone from adjacent litho-tectonic domains by fluid flow through lithospheric scale structures such as the Fraser Shear Zone.

6.4 Modification of magmatic sulphides

Advances in LA-ICP-MS technology and analytical methods facilitate precise accurate analysis of sulphide trace element compositions at high spatial resolution (Zhu et al., 2016). In this study, laser ablation was combined with TIMA volumetric mineral mode data to produce high resolution quantitative trace element maps of multiple sulphide phases in variably altered samples of sulphide breccia from Octagonal (Chapter 4).

Quantitative elemental mapping of multiple sulphides is not commonly performed because it requires multiple cycles of reduction of the element data using different internal standards to account for the different compositions of the sulphides, and each quantitative sulphide dataset must be calibrated separately against appropriate standards. The maps produced in this study show that the sulphide breccia material preserves evidence of element remobilisation from the sulphides into adjacent fracture infill material, and vice versa. Advanced co-localisation analysis was applied, for the first time in this research area, to quantify relationships between element concentrations and textural features.

The sulphide breccias include a significant proportion of pyrite. Pyrrhotite + pentlandite + chalcopyrite is the typical assemblage that characterises magmatic sulphide mineralization. Pyrite, based on textural relationships and trace element concentrations is interpreted to have formed by pyrrhotite replacement. Normalised trace element signatures reveal depletions in pyrite trace element concentrations relative to pyrrhotite but broadly similar element patterns. These data, together with the pervasive serpentine that is present in sample material implies a period of extensive fluid activity and element remobilisation.

The co-localisation analysis identifies co-localisation between Mn, Pb, Ag and serpentine- and magnetite-bearing fractures, which is attributed to remobilisation of these metals by fluid flow. However differences in the distributions of Pb, Mn and Ag imply that they may have been remobilised at different times, by fluids of different compositions, or that they were remobilised from different sources. Element mapping also indicates Ag zoning within pentlandite. This is interpreted as a consequence of progressive depletion of Ag in MSS as it partitioned into pentlandite.

The co-localisation technique that was used to support these interpretations is shown here to be a powerful tool for the quantification of spatial relationships between mineral chemistry and petrographic textures, with potential to contribute to the quantification of a wide variety of open system processes including serpentinisation and formation of metasomatic zoning. Many observations of geological relationships are qualitative and based on visual assessments which are susceptible to observer bias. The introduction of more quantitative measurements via techniques including co-localisation analysis can only improve our data and interpretations.

6.5 Limitations and further work

This project focused on the Fraser Zone to provide a detailed picture of the features of sulphur isotope signatures in the region considered most prospective for magmatic sulphide mineralisation. Therefore, this thesis does not address the sources and sulphur isotope signatures of sulphur within other zones of the AFO. These areas are still underexplored, and many more years of work are required to constrain the AFO's mineral potential.

However, the focus on four prospects has provided excellent sulphur isotopic constraints on sedimentary sources of sulphur involved in magmatic sulphide mineralisation in the Fraser Zone and addressed the incorporation of external sulphur that is required in typical models for the formation of magmatic nickel sulpide deposits. Significant accumulations of magmatic sulphides are likely to be found where metasediments of the Snowys Dam Formation are in close proximity to emplaced magmatic bodies. Only a small number of mineralised intervals were sampled at each locality, however, so constraints on the details of assimilation and mixing of sediments with the parent magmatic bodies are limited. The mixing models discussed in preceding chapters oversimplify the incorporation of sedimentary sulphur; incomplete assimilation of sedimentary material or weak convective processes within the magma would result in heterogenous sulphur isotope values throughout the magmatic system. In-situ sulphur isotopic analysis of more sulphide-rich intervals at each locality would allow a better understanding of the mixing process between sedimentary and magmatic sulphur.

Furthermore, sulphide saturation of a magma is only one of several factors involved in the formation of magmatic sulphides; significant quantities of metals are also required, and mechanisms by which the magmatic sulphides are concentrated to form an economic deposit. Research that incorporates extensive whole rock geochemical and sulphide trace element characterisation of localities such as Octagonal would allow modelling of the R factors involved in mineralisation, and, in conjunction with structural models, would enable a more comprehensive understanding of magmatic sulphide formation in the Fraser Zone.

The introduction of sulphur into Andromeda from beyond the Fraser Zone via the Fraser Shear Zone raises questions as to whether this has occurred elsewhere in the Fraser Zone, and if so, whether it could be a significant contributor to sulphide mineralisation proximal to these sulphur pathways. The nature of the mineralisation at Andromeda begets more questions and possible avenues of research. Further work is required to identify whether Andromeda is an example of a VMS orebody, and to characterise the nature of the host stratigraphy; this is likely to be a difficult task due to extensive metamorphism of the wallrock and ore with the majority of any primary features erased by metamorphic overprinting. If Andromeda is a VMS deposit then many questions remain regarding it's formation, and whether other instances of VMS mineralisation within the Fraser Zone can be identified.

6.6 References

Adams, M., 2012. Structural and geochronological evolution of the Malcolm Gneiss, Nornalup Zone, Albany-Fraser Orogen, Western Australia. Geological Survey of Western Australia.

Barley, M. E., Brown, S. J., Krapež, B., Kositcin, N., 2008. Physical volcanology and geochemistry of a Late Archaean volcanic arc: Kurnalpi and Gindalbie terranes, Eastern Goldfields superterrane, Western Australia. Precambrian Research 161 (1-2), 53–76.

Barnes, S.-J., Lightfoot, P. C., 2005. Formation of magmatic nickel-sulfide ore deposits and processses affecting their copper and platinum-group element contents. Economic Geology 100th Anniversary, 179–213.

Barnes, S.-J., Makovicky, E., Karup-Moller, S., Makovicky, M., Rose-Hansen, J., 1994. Partition coefficients for Ni, Cu, Pd, Pt, Rh, and Ir between monosulphide solid solution and sulphide liquid and the implications for the formation of compositionally zoned Ni-Cu sulphide bodies by fractional crystallization of sulphide liquid. Mineralogical Magazine 58, 51–52.

Barnes, S.-J., Makovicky, E., Makovicky, M., Rose-Hansen, J., Karup-Moller, S., 1997. Partition coefficients for Ni, Cu, Pd, Pt, Rh, and Ir between monosulfide solid solution and sulfide liquid and the formation of compositionally zoned Ni–Cu sulfide bodies by fractional crystallization of sulfide liquid. Canadian Journal of Earth Sciences 34 (4), 366–374.

Barnes, S.-J., Prichard, H. M., Cox, R. A., Fisher, P. C., Godel, B., 2008. The location of the chalcophile and siderophile elements in platinum-group element ore deposits (a textural, microbeam and whole rock geochemical study): Implications for the formation of the deposits. Chemical Geology 248 (3-4), 295–317.

Barnes, S.-J., Ripley, E. M., 2016. Highly siderophile and strongly chalcophile elements in magmatic ore deposits. Reviews in Mineralogy and Geochemistry 81 (1), 725–774.

Barnes, S. J., Staude, S., Le Vaillant, M., Piña, R., Lightfoot, P. C., 2018. Sulfide-silicate textures in magmatic Ni-Cu-PGE sulfide ore deposits: Massive, semi-massive and sulfide-matrix breccia ores. Ore Geology Reviews.

Barrie, C., Cathles, L., Erendi, A., Schwaiger, H., Murray, C., Hannington, M., 1999. Heat and fluid flow in volcanic-associated massive sulfide-forming hydrothermal systems. Reviews in Economic Geology 8, 201–219.

Bekker, A., Barley, M. E., Fiorentini, M. L., Rouxel, O. J., Rumble, D., Beresford, S. W., 2009. Atmospheric sulfur in archean komatiite-hosted nickel deposits. Science 326 (5956), 1086–1089.

Bekker, A., Holland, H., Wang, P.-L., Rumble Iii, D., Stein, H., Hannah, J., Coetzee, L., Beukes, N., 2004. Dating the rise of atmospheric oxygen. Nature 427 (6970), 117.

Bennett, M., Gollan, M., Staubmann, M., Bartlett, J., 2014. Motive, means, and opportunity: key factors in the discovery of the Nova–Bollinger magmatic nickel–copper sulfide deposits in Western Australia. Building Exploration Capability for the 21st Century. Society of Economic Geologists, Special Publications 18, 301–320.

Bolte, S., Cordelieres, F., 2006. A guided tour into subcellular colocalization analysis in light microscopy. Journal of microscopy 224 (3), 213–232.

Brisbout, L., 2015. Determining crustal architecture in the east Albany-Fraser Orogen from geological and geophysical data. Geological Survey of Western Australia.

Brueckner, S. M., Piercey, S. J., Layne, G. D., Piercey, G., Sylvester, P. J., 2015. Variations of sulphur isotope signatures in sulphides from the metamorphosed Ming Cu (- Au) volcanogenic massive sulphide deposit, Newfoundland Appalachians, Canada. Mineralium Deposita 50 (5), 619–640.

Buddington, A., Lindsley, D., 1964. Iron-titanium oxide minerals and synthetic equivalents. Journal of petrology 5 (2), 310–357.

Clark, C., Kirkland, C. L., Spaggiari, C. V., Oorschot, C., Wingate, M. T., Taylor, R. J., 2014. Proterozoic granulite formation driven by mafic magmatism: An example from the Fraser Range Metamorphics, Western Australia. Precambrian Research 240, 1–21.

Clark, D. J., Hensen, B. J., Kinny, P. D., 2000. Geochronological constraints for a two-stage history of the Albany-Fraser Orogen, Western Australia. Precambrian Research 102 (3), 155 – 183.

Condie, K. C., Myers, J. S., 1999. Mesoproterozoic Fraser Complex: geochemical evidence for multiple subduction-related sources of lower crustal rocks in the Albany-Fraser Orogen, Western Australia. Australian Journal of Earth Sciences 46 (6), 875–882.

Corfu, F., Hanchar, J. M., Hoskin, P. W., Kinny, P., 2003. Atlas of zircon textures. Reviews in mineralogy and geochemistry 53 (1), 469–500.

Costes, S. V., Daelemans, D., Cho, E. H., Dobbin, Z., Pavlakis, G., Lockett, S., 2004. Automatic and quantitative measurement of protein-protein colocalization in live cells. Biophysical journal 86 (6), 3993–4003.

Craig, J. R., Vokes, F. M., 1993. The metamorphism of pyrite and pyritic ores: an overview. Mineralogical Magazine 57 (386), 3–18.

Czamanske, G. K., Kunilov, V. E., Zientek, M. L., Cabri, L. J., Likhachev, A. P., Calk, L. C., Oscarson, R. L., 1992. A proton microprobe study of magmatic sulfide ores from the Noril'sk-Talnakh District, Siberia. The Canadian Mineralogist 30 (2), 249–287.

de Gromard, R., Spaggiari, C., Munro, M., Sapkota, J., De Paoli, M., 2017. SGTSG 2017 Albany-Fraser Orogen pre-conference field trip: Transect across an Archaean craton margin to a Proterozoic ophiolite. Geological Survey of Western Australia Record 2017/14, 100p.

De Waele, B., Pisarevsky, S., 2008. Geochronology, paleomagnetism and magnetic fabric of metamorphic rocks in the northeast fraser belt, western australia. Australian Journal of Earth Sciences 55 (5), 605–621.

Department of Mines, Industry Regulation and Safety, 2018. Latest statistics release. `http://dmp.wa.gov.au/About-Us-Careers/Latest-Statistics-Release-4081.aspxm`, [Online; accessed 25-July-2019].

Ding, L., Yang, G., Xia, F., Lenehan, C. E., Qian, G., McFadden, A., Brugger, J. L., Zhang, X., Chen, G., Pring, A., 2011. A LA-ICP-MS sulphide calibration standard based on a chalcogenide glass. Mineralogical Magazine 75 (2), 279–287.

Doyle, M. G., Fletcher, I. R., Foster, J., Large, R. R., Mathur, R., McNaughton, N. J., Meffre, S., Muhling, J. R., Phillips, D., Rasmussen, B., 2015. Geochronological Constraints on the Tropicana Gold Deposit and Albany-Fraser Orogen, Western Australia. Economic Geology 110 (2), 355.

Dunn, K. W., Kamocka, M. M., McDonald, J. H., 2011. A practical guide to evaluating colocalization in biological microscopy. American Journal of Physiology-Cell Physiology 300 (4), C723–C742.

Duran, C. J., Barnes, S.-J., Corkery, J. T., 2015. Chalcophile and platinum-group element distribution in pyrites from the sulfide-rich pods of the Lac des Iles Pd deposits, Western Ontario, Canada: Implications for post-cumulus re-equilibration of the ore and the use of pyrite compositions in exploration. Journal of Geochemical Exploration 158, 223–242.

Duran, C. J., Barnes, S.-J., Corkery, J. T., 2016. Trace element distribution in primary sulfides and Fe–Ti oxides from the sulfide-rich pods of the Lac des Iles Pd deposits, Western Ontario, Canada: constraints on processes controlling the composition of the ore and the use of pentlandite compositions in exploration. Journal of Geochemical Exploration 166, 45–63.

Duran, C. J., Barnes, S.-J., Pleše, P., Prašek, M. K., Zientek, M. L., Pagé, P., 2017. Fractional crystallization-induced variations in sulfides from the Noril'sk-Talnakh mining district (polar Siberia, Russia). Ore Geology Reviews 90, 326–351.

Dutrizac, J., 1976. Reactions in cubanite and chalcopyrite. The Canadian Mineralogist 14 (2), 172–181.

Ebel, D., Naldrett, A., 1997. Crystallization of sulfide liquids and the interpretation of ore composition. Canadian Journal of Earth Sciences 34 (4), 352–365.

Farquhar, J., Bao, H., Thiemens, M., 2000. Atmospheric influence of earth's earliest sulfur cycle. Science 289 (5480), 756–758.

Farquhar, J., Wing, B. A., 2003. Multiple sulfur isotopes and the evolution of the atmosphere. Earth and Planetary Science Letters 213 (1-2), 1–13.

Franklin, J., Gibson, H., Jonasson, I., Galley, A., 2005. Volcanogenic massive sulfide deposits. Economic Geology 100 (Anniversary volume), 523–560.

Galley, A. G., Hannington, M. D., Jonasson, I., 2007. Volcanogenic massive sulphide deposits. Mineral deposits of Canada: A synthesis of major deposit-types, district metallogeny, the evolution of geological provinces, and exploration methods: Geological Association of Canada, Mineral Deposits Division, Special Publication 5, 141–161.

Glasson, K. J., Johnson, T. E., Kirkland, C. L., Gardiner, N. J., Clark, C., Blereau, E., Hartnady, M. I., Spaggiari, C., Smithies, H., 2019. A window into an ancient backarc? The magmatic and metamorphic history of the Fraser Zone, Western Australia. Precambrian Research 323, 55–69.

Godefroy-Rodríguez, M., Hagemann, S., LaFlamme, C., Fiorentini, M., 2018. The multiple sulfur isotope architecture of the Golden Mile and Mount Charlotte deposits, Western Australia. Mineralium Deposita, 1–26.

Godel, B., Barnes, S.-J., 2008. Platinum-group elements in sulfide minerals and the whole rocks of the JM Reef (Stillwater Complex): Implication for the formation of the reef. Chemical Geology 248 (3-4), 272–294.

Gonzalez-Alvarez, I., Anand, R. R., Hough, R., Salama, W., Laukamp, C., Ley-Cooper, Y., Sweetapple, M. T., Sonntag, I., Lintern, M., Abdat, T., leGras, M., Walshe, J., 2014. Greenfields exploration in the Albany-Fraser Orogen and on the southeast Yilgarn cratonic margin. GSWA extended abstracts 2014, 26–28.

Gregory, D. D., Large, R. R., Bath, A. B., Steadman, J. A., Wu, S., Danyushevsky, L., Bull, S. W., Holden, P., Ireland, T. R., 2016. Trace element content of pyrite from the kapai slate, St. Ives Gold District, Western Australia. Economic Geology 111 (6), 1297–1320.

Helmy, H. M., Ballhaus, C., Berndt, J., Bockrath, C., Wohlgemuth-Ueberwasser, C., 2007. Formation of Pt, Pd and Ni tellurides: experiments in sulfide–telluride systems. Contributions to Mineralogy and Petrology 153 (5), 577–591.

Holwell, B. D., McDonald, I., 2010. A review of the behaviour of platinum group elements within natural magmatic sulfide ore systems. Platinum Metals Review 54 (1), 26–36.

Holwell, D. A., Adeyemi, Z., Ward, L. A., Smith, D. J., Graham, S. D., McDonald, I., Smith, J. W., 2017. Low temperature alteration of magmatic Ni-Cu-PGE sulfides as a source for hydrothermal Ni and PGE ores: A quantitative approach using automated mineralogy. Ore Geology Reviews 91, 718–740.

Hulston, J., Thode, H., 1965. Variations in the S33, S34, and S36 contents of meteorites and their relation to chemical and nuclear effects. Journal of Geophysical Research 70 (14), 3475–3484.

Huston, D. L., Pehrsson, S., Eglington, B. M., Zaw, K., 2010. The geology and metallogeny of volcanic-hosted massive sulfide deposits: Variations through geologic time and with tectonic setting. Economic Geology 105 (3), 571–591.

Irvine, T., 1976. Crystallization sequences in the muskox intrusion and other layered intrusions—ii. origin of chromitite layers and similar deposits of other magmatic ores. In: Irvine, T. (Ed.), Chromium: its Physicochemical Behavior and Petrologic Significance. Pergamon, pp. 991 – 1020.

Jochum, K. P., Nohl, U., Herwig, K., Lammel, E., Stoll, B., Hofmann, A. W., 2005. Georem: A new geochemical database for reference materials and isotopic standards. Geostandards and Geoanalytical Research 29 (3), 333–338.

Johnston, D. T., 2011. Multiple sulfur isotopes and the evolution of Earth's surface sulfur cycle. Earth-Science Reviews 106 (1-2), 161–183.

Kelly, D., Vaughan, D., 1983. Pyrrhotine-pentlandite ore textures: a mechanistic approach. Mineralogical Magazine 47 (345), 453–463.

Kirkland, C., Smithies, R., Spaggiari, C., Wingate, M., de Gromard, R. Q., Clark, C., Gardiner, N., Belousova, E., 2017. Proterozoic crustal evolution of the Eucla basement, Australia: Implications for destruction of oceanic crust during emergence of Nuna. Lithos 278, 427–444.

Kirkland, C. L., Spaggiari, C. V., Johnson, T. E., Smithies, R. H., Danišík, M., Evans, N., Wingate, M. T. D., Clark, C., Spencer, C., Mikucki, E., McDonald, B. J., 2016.

Grain size matters: Implications for element and isotopic mobility in titanite. Precambrian Research 278, 283 – 302.

Kirkland, C. L., Spaggiari, C. V., Pawley, M. J., Wingate, M. T. D., Smithies, R. H., Howard, H. M., Tyler, I. M., Belousova, E. A., Poujol, M., 2011a. On the edge: U-Pb,Lu-Hf, and Sm-Nd data suggests reworking of the Yilgarn craton margin during formation of the Albany-Fraser Orogen. Precambrian Research 187 (3), 223 – 247.

Kirkland, C. L., Spaggiari, C. V., Smithies, R. H., Wingate, M. T. D., 2014. Cryptic progeny of craton margins: geochronology and isotope geology of the Albany-Fraser Orogen with implications for evolution of the Tropicana Zone. Albany-Fraser Orogen seismic and magnetotelluric (MT) workshop 2014: extended abstracts compiled by CV Spaggiari and IM Tyler, Geological Survey of Western Australia, Record 2014/6, 89–101.

Kirkland, C. L., Wingate, M. T. D., Spaggiari, C. V., 2011b. 194709: metamonzogranite, Cave Rock; Geochronology Record 985. Geological Survey of Western Australia, 4p.

Kirkland, C. L., Wingate, M. T. D., Spaggiari, C. V., 2012. 194711: metamonzogranite, Kent Dam; Geochronology Record 1044. Geological Survey of Western Australia, 4p.

Kirkland, C. L., Wingate, M. T. D., Spaggiari, C. V., Pawley, M., 2010a. 194719: metasyenogranite, Symons Hill; Geochronology Record 848. Geological Survey of Western Australia, 5p.

Kirkland, C. L., Wingate, M. T. D., Spaggiari, C. V., Pawley, M., 2010b. 194736: metasyenogranite, Bartlett Bluff; Geochronology Record 849. Geological Survey of Western Australia, 4p.

Kita, N. T., Ushikubo, T., Fu, B., Valley, J. W., 2009. High precision sims oxygen isotope analysis and the effect of sample topography. Chemical Geology 264 (1), 43 – 57.

Kullerud, G., 1969. Phase relations in the Cu-Fe-S, Cu-Ni-S and Fe-Ni-S system. Magmatic ore deposits, 323–343.

Kullerud, G., Yoder, H. S., 1959. Pyrite stability relations in the Fe-S system. Economic Geology 54 (4), 533–572.

LaFlamme, C., Fiorentini, M. L., Lindsay, M. D., Bui, T. H., 2018a. Atmospheric sulfur is recycled to the crystalline continental crust during supercontinent formation. Nature communications 9.

LaFlamme, C., Jamieson, J. W., Fiorentini, M. L., Thébaud, N., Caruso, S., Selvaraja, V., 2018b. Investigating sulfur pathways through the lithosphere by tracing mass independent fractionation of sulfur to the Lady Bountiful orogenic gold deposit, Yilgarn Craton. Gondwana Research 58, 27–38.

LaFlamme, C., Martin, L., Jeon, H., Reddy, S. M., Selvaraja, V., Caruso, S., Bui, T. H., Roberts, M. P., Voute, F., Hagemann, S., et al., 2016. In situ multiple sulfur isotope analysis by sims of pyrite, chalcopyrite, pyrrhotite, and pentlandite to refine magmatic ore genetic models. Chemical Geology 444, 1–15.

Leavitt, W. D., Cummins, R., Schmidt, M. L., Sim, M. S., Ono, S., Bradley, A. S., Johnston, D. T., 2014. Multiple sulfur isotope signatures of sulfite and thiosulfate reduction by the model dissimilatory sulfate-reducer, Desulfovibrio alaskensis str. G20. Frontiers in microbiology 5, 591.

Li, C., Barnes, S.-J., Makovicky, E., Rose-Hansen, J., Makovicky, M., 1996. Partitioning of nickel, copper, iridium, rhenium, platinum, and palladium between monosulfide solid solution and sulfide liquid: effects of composition and temperature. Geochimica et Cosmochimica Acta 60 (7), 1231–1238.

Liu, Y., Brenan, J., 2015. Partitioning of platinum-group elements (PGE) and chalcogens (Se, Te, As, Sb, Bi) between monosulfide-solid solution (MSS), intermediate solid solution (ISS) and sulfide liquid at controlled fO_2–fS_2 conditions. Geochimica et Cosmochimica Acta 159, 139–161.

MacNamara, J., Thode, H., 1950. Comparison of the isotopic constitution of terrestrial and meteoritic sulfur. Physical Review 78 (3), 307.

Maier, W., Smithies, R., Spaggiari, C., Barnes, S., Kirkland, C., Yang, S., Lahaye, Y., Kiddie, O., MacRae, C., 2016a. Petrogenesis and Ni–Cu sulphide potential of mafic–ultramafic rocks in the Mesoproterozoic Fraser Zone within the Albany–Fraser Orogen, Western Australia. Precambrian Research 281, 27 – 46.

Maier, W. D., Smithies, R. H., Spaggiari, C. V., Barnes, S. J., Kirkland, C. L., Kiddie, O., Roberts, M. P., 2016b. The evolution of mafic and ultramafic rocks of the Mesoproterozoic Fraser Zone, Albany-Fraser Orogen, and implications for the Ni-Cu sulphide potential of the region. Geological Survey of Western Australia, Record 2016/8, 49p.

Makovicky, E., 2002. Ternary and quaternary phase systems with PGE. In: Geology, Geochemistry, Mineralogy and Mineral Beneficiation of Platinum-group Elements. Canadian Institute of Mining, Metallurgy and Petroleum, pp. 131–175.

Manders, E., Verbeek, F., Aten, J., 1993. Measurement of co-localization of objects in dual-colour confocal images. Journal of microscopy 169 (3), 375–382.

Mansur, E. T., Barnes, S.-J., Duran, C. J., Sluzhenikin, S. F., 2019. Distribution of chalcophile and platinum-group elements among pyrrhotite, pentlandite, chalcopyrite and cubanite from the Noril'sk-Talnakh ores: implications for the formation of platinum-group minerals. Mineralium Deposita, 1–18.

Mavrogenes, J. A., O'Neill, H. S., 1999. The relative effects of pressure, temperature and oxygen fugacity on the solubility of sulfide in mafic magmas. Geochimica et Cosmochimica Acta 63 (7), 1173 – 1180.

Mungall, J. E., Andrews, D. R., Cabri, L. J., Sylvester, P. J., Tubrett, M., 2005. Partitioning of Cu, Ni, Au, and platinum-group elements between monosulfide solid solution and sulfide melt under controlled oxygen and sulfur fugacities. Geochimica et Cosmochimica Acta 69 (17), 4349–4360.

Munro, M., de Gromard, R., Spaggiari, C., 2017. Structural evolution of the S-bend region, east Albany-Fraser Orogen. In: GSWA Extended Abstracts, Perth.

Murowchick, J. B., Barnes, H., 1986. Marcasite precipitation from hydrothermal solutions. Geochimica et Cosmochimica Acta 50 (12), 2615 – 2629.

Naldrett, A., 1969. A portion of the system Fe–S–O between 900 and 1080°c and its application to sulfide ore magmas. Journal of Petrology 10 (2), 171–201.

Naldrett, A., 2004. Magmatic sulfide deposits: Geology, geochemistry and exploration. Springer Science & Business Media.

Naldrett, A., Craig, J., Kullerud, G., 1967. The central portion of the Fe-Ni-S system and its bearing on pentlandite exsolution in iron-nickel sulfide ores. Economic Geology 62 (6), 826–847.

Ono, S., Eigenbrode, J. L., Pavlov, A. A., Kharecha, P., Rumble, D., Kasting, J. F., Freeman, K. H., 2003. New insights into archean sulfur cycle from mass-independent sulfur isotope records from the hamersley basin, australia. Earth and Planetary Science Letters 213 (1), 15 – 30.

Ono, S., Wing, B., Johnston, D., Farquhar, J., Rumble, D., 2006. Mass-dependent fractionation of quadruple stable sulfur isotope system as a new tracer of sulfur biogeochemical cycles. Geochimica et Cosmochimica Acta 70 (9), 2238–2252.

Paktunc, A. D., Hulbert, L. J., Harris, D. C., 1990. Partitioning of the platinum-group and other trace elements in sulfides from the Bushveld Complex and Canadian occurrences of nickel-copper sulfides. The Canadian Mineralogist 28 (3), 475–488.

Penarrubia, P. G., Ruiz, X. F., Gálvez, J., 2005. Quantitative analysis of the factors that affect the determination of colocalization coefficients in dual-color confocal images. IEEE transactions on image processing 14 (8), 1151–1158.

Penniston-Dorland, S. C., Mathez, E. A., Wing, B. A., Farquhar, J., Kinnaird, J. A., 2012. Multiple sulfur isotope evidence for surface-derived sulfur in the bushveld complex. Earth and Planetary Science Letters 337-338, 236 – 242.

Peregoedova, A., 1998. The experimental study of the Pt–Pd–partitioning between monosulfide solid solution and Cu–Ni–sulfide melt at 900–840°c. In: The 8th International Platinum Symposium. pp. 325–373.

Piercey, S. J., 2011. The setting, style, and role of magmatism in the formation of volcanogenic massive sulfide deposits. Mineralium Deposita 46 (5-6), 449–471.

Piña, R., Gervilla, F., Barnes, S.-J., Ortega, L., Lunar, R., 2013. Platinum-group elements-bearing pyrite from the Aguablanca Ni-Cu sulphide deposit (SW Spain): a LA-ICP-MS study. European Journal of Mineralogy 25 (2), 241–252.

Ripley, E. M., Li, C., 2003. Sulfur Isotope Exchange and Metal Enrichment in the Formation of Magmatic Cu-Ni-(PGE) Deposits. Economic Geology 98 (3), 635.

Ripley, E. M., Li, C., 2013. Sulfide Saturation in Mafic Magmas: Is External Sulfur Required for Magmatic Ni-Cu-(PGE) Ore Genesis? Economic Geology, v. 108, 45–58.

Rumble, D., 2005. Presidential address to the mineralogical society of america seattle, november 4, 2003: A mineralogical and geochemical record of atmospheric photochemistry. American Mineralogist 90 (5-6), 918.

Savarino, J., Romero, A., Cole-Dai, J., Bekki, S., Thiemens, M. H., 2003. Uv induced mass-independent sulfur isotope fractionation in stratospheric volcanic sulfate. Geophysical Research Letters 30 (21).

Schoonen, M., Barnes, H., 1991. Mechanisms of pyrite and marcasite formation from solution: III. Hydrothermal processes. Geochimica et Cosmochimica Acta 55 (12), 3491–3504.

Seal, II, R. R., 2006. Sulfur isotope geochemistry of sulfide minerals. Reviews in Mineralogy and Geochemistry 61 (1), 633.

Selvaraja, V., Caruso, S., Fiorentini, M. L., LaFlamme, C., 2017. The Global Sedimentary Sulfur Isotope Database.
URL http://www.cet.edu.au/research-projects/special-projects/gssid-global-sedimentary-sulfur-isotope-database

Sinyakova, E., Kosyakov, V., 2009. Experimental modeling of zonality of copper-rich sulfide ores in copper-nickel deposits. In: Doklady Earth Sciences. Vol. 427. Springer, pp. 787–792.

Smith, J., Holwell, D. A., McDonald, I., 2014. Precious and base metal geochemistry and mineralogy of the Grasvally Norite–Pyroxenite–Anorthosite (GNPA) member, northern Bushveld Complex, South Africa: implications for a multistage emplacement. Mineralium Deposita 49 (6), 667–692.

Smithies, R. H., Spaggiari, C. V., Kirkland, C. L., 2015. Building the crust of the Albany-Fraser Orogen: constraints from granite geochemistry. Geological Survey of Western Australia, Report 150, 49p.

Smithies, R. H., Spaggiari, C. V., Kirkland, C. L., Howard, H. M., Maier, W. D., 2013. Petrogenesis of gabbros of the Mesoproterozoic Fraser Zone: constraints on the tectonic evolution of the Albany-Fraser Orogen. Geological Survey of Western Australia, Record 2013/15, 29p.

Smithies, R. H., Spaggiari, C. V., Kirkland, C. L., Maier, W. D., 2014. Geochemistry and petrogenesis of igneous rocks in the Albany-Fraser Orogen. Albany-Fraser Orogen seismic and magnetotelluric (MT) workshop 2014: extended abstracts compiled by CV Spaggiari and IM Tyler, Geological Survey of Western Australia, Record 2014/6, 69–80.

Spaggiari, C., Kirkland, C., Smithies, R., Occhipinti, S., Wingate, M., 2014a. Geological framework of the albany–fraser orogen. In: Albany–Fraser Orogen seismic and magnetotelluric (MT) workshop 2014: extended abstracts compiled by CV Spaggiari and IM Tyler: Geological Survey of Western Australia, Record. Vol. 6. pp. 12–27.

Spaggiari, C., Smithies, R., Kirkland, C., England, R., Occhipinti, S., Wingate, M., 2015a. Eucla basement results: implications for geodynamics and mineral prospectivity. In: Eucla Basement Stratigraphic Drilling Results Release Workshop: Extended Abstracts, Record. Vol. 10. pp. 53–58.

Spaggiari, C. V., Bodorkos, S., Barquero-Molina, M., Tyler, I. M., Wingate, M. T. D., 2009. Interpreted bedrock geology of the South Yilgarn and central Albany-Fraser Orogen, Western Australia. Geological Survey of Western Australia, Record 2009/10, 84p.

Spaggiari, C. V., Kirkland, C. L., Smithies, R. H., Wingate, M. T. D., 2011. The geology of the East Albany-Fraser Orogen - A Field Guide. Geological Survey of Western Australia, Record 2009/10, 84.

Spaggiari, C. V., Kirkland, C. L., Smithies, R. H., Wingate, M. T. D., 2012. What lies beneath - interpreting the Eucla basement. GSWA extended abstracts, 24–26.

Spaggiari, C. V., Kirkland, C. L., Smithies, R. H., Wingate, M. T. D., 2014b. Tectonic links between Proterozoic sedimentary cycles, basin formation and magmatism in the Albany-Fraser Orogen. Geological Survey of Western Australia, Report 133, 63p.

Spaggiari, C. V., Kirkland, C. L., Smithies, R. H., Wingate, M. T. D., Belousova, E. A., 2015b. Transformation of an Archean craton margin during Proterozoic basin formation and magmatism: The Albany-Fraser Orogen, Western Australia. Precambrian Research 266, 440 – 466.

Spaggiari, C. V., Occhipinti, S. A., Korsch, R. J., Doublier, M. P., Clark, D. J., Dentith, M. C., Gessner, K., Doyle, M. G., Tyler, I. M., Kennett, B. L. N., Costelloe, R. D., Fomin, T., Holzschuh, J., 2014c. Interpretation of Albany-Fraser seismic lines 12GA-AF1, 12GA-AF2 and 12GA-AF3: implications for crustal architecture, *in* Albany-Fraser Orogen seismic and magnetotelluric (MT) workshop 2014: extended abstracts *compiled by* CV Spaggiari and IM Tyler. Geological Survey of Western Australia, Record 2014/6.

Spaggiari, C. V., Smithies, R. H., Kirkland, C. L., Wingate, M. T., England, R. N., Lu, Y.-J., 2018. Buried but preserved: The Proterozoic Arubiddy Ophiolite, Madura Province, Western Australia. Precambrian Research 317, 137–158.

Squire, R. J., Allen, C. M., Cas, R. A., Campbell, I. H., Blewett, R. S., Nemchin, A. A., 2010. Two cycles of voluminous pyroclastic volcanism and sedimentation related to episodic granite emplacement during the late Archean: Eastern Yilgarn Craton, Western Australia. Precambrian Research 183 (2), 251–274.

Steadman, J. A., Large, R. R., Meffre, S., Olin, P. H., Danyushevsky, L. V., Gregory, D. D., Belousov, I., Lounejeva, E., Ireland, T. R., Holden, P., 2015. Synsedimentary to early diagenetic gold in black shale-hosted pyrite nodules at the Golden Mile Deposit, Kalgoorlie, Western Australia. Economic Geology 110 (5), 1157–1191.

Sylvester, P., Cabri, L., Tubrett, M., McMahon, G., Laflamme, J., Peregoedova, A., et al., 2005. Synthesis and evaluation of a fused pyrrhotite standard reference material for platinum group element and gold analysis by laser ablation-ICPMS. In: 10th International Platinum Symposium: Oulu, Geological Survey of Finland, Extended Abstracts. pp. 16–20.

Tripp, G. I., 2013. Stratigraphy and structure in the Neoarchaean of the Kalgoorlie district, Australia: critical controls on greenstone-hosted gold deposits. Ph.D. thesis, James Cook University.

Urey, H. C., 1947. The thermodynamic properties of isotopic substances. Journal of the Chemical Society (Resumed), 562–581.

Venables, T., 2014. Enterprise Metals Limited, Fraser Range Project, Exploration Licence 63/1281 Final Drilling Report, Co-funded Drilling Agreement DAG 2014/00384566, 25th July, 2014. WAMEX report A103177.

von Gehlen, K., 1992. Sulfur in the earth's mantle — a review. In: Schidlowski, M., Golubic, S., Kimberley, M. M., McKirdy, D. M., Trudinger, P. A. (Eds.), Early Organic Evolution: Implications for Mineral and Energy Resources. Springer Berlin Heidelberg, Berlin, Heidelberg, pp. 359–366.

Waddell, P.-J. A., Timms, N. E., Spaggiari, C. V., Kirkland, C. L., Wingate, M. T., 2015. Analysis of the Ragged Basin, Western Australia: Insights into syn-orogenic basin evolution within the Albany–Fraser Orogen. Precambrian Research 261, 166–187.

Walker, A., Evans, K., Kirkland, C., Martin, L., Kiddie, O., Spaggiari, C., 2019. Tracking mineralisation with in situ multiple sulphur isotopes: a case study from the Fraser Zone, Western Australia. Precambrian Research 332.

Wohlgemuth-Ueberwasser, C. C., Ballhaus, C., Berndt, J., Stotter née Paliulionyte, V., Meisel, T., Nov 2007. Synthesis of pge sulfide standards for laser ablation inductively coupled plasma mass spectrometry (la-icp-ms). Contributions to Mineralogy and Petrology 154 (5), 607–617.

Zhu, Z.-Y., Cook, N., Yang, T., Ciobanu, C., Zhao, K.-D., Jiang, S.-Y., 2016. Mapping of sulfur isotopes and trace elements in sulfides by la-(mc)-icp-ms: potential analytical problems, improvements and implications. Minerals 6 (4), 110.